

## A Complete Thermal Processing System for Fuels and Polymer Analysis

J.W. Washall, T.P. Wampler and W.A. Bowe,  
Autoclave Engineers - Oxford/CDS Instruments 7000 Limestone  
Rd, Oxford, PA 19363

Thermal Characterization of fuel sources is essential in geochemical exploration. Determining the maturity of source rock and coal beds aids in the processing of these fuel sources. Quantitative assessment of the migratory hydrocarbons ( $P_1$ ), kerogen ( $P_2$ ) and fixed gases ( $P_3$ ) provide vital information about the fuel generating capability of the sample.

Total thermal processing of samples, both geochemical and polymeric, can occur with temperatures up to 1400°C. The system used in this evaluation makes use of both furnace and filament pyrolysis. Samples analyzed included oil shales, polymers and composite materials.

Pyrolysis equipment in general is composed of three major components. First and foremost, a filament, wire or furnace in which the sample is deposited for pyrolysis. The second component is a heated chamber which prevents the pyrolysate from condensing and not reaching the injection port. The final component is a modification, or add-on to the injection port of the gas chromatograph<sup>1,2</sup>. Egsgaard and Carlsen describe a low pressure continuous flow inletting system for Curie Point pyrolysis into a mass spectrometer<sup>3</sup>. In their work they describe three separate inletting systems depending on sample matrix: gas, liquid or solid. Many mass spectrometers, however, can accommodate direct insertion probes for pyrolysis in the source<sup>4,5</sup>. This technique, although valuable for many applications, tends to produce highly complex spectra because there is no chromatographic separation. Cold trapping prior to injecting the pyrolysate onto the GC will improve resolution, however, highly volatile components may tend to breakthrough and go undetected.

The impetus of his work was to provide an analytical system which would provide a full range of thermal processing capabilities, including dynamic headspace, furnace pyrolysis and filament pyrolysis. Previously, thermal treatment of samples involved Curie Point, furnace or filament pyrolysis. Each of these pyrolysis techniques has advantages and limitations.

The system in this study makes use of a programmable furnace pyrolyzer for temperatures up to 600°C and a filament pyrolyzer capable of reaching temperatures up to 1400°C. A major benefit of this system is the programmable furnace in combination with a series of adsorbent traps which enable fractions to be collected prior to chromatographic analysis.

All heated zones in the system are controlled via the systems computer terminal which can accommodate 20 separate methods. As the sample is heated, sample flow passes over the sample and sweeps the volatiles through an adjustable split valve. Part of the sample then moves to a monitor flame ionization detector (FID), the rest of the sample is carried to an adsorbent trap. At that point a second temperature fraction can be collected in the same manner. A molecular sieve trap can also collect any fixed gases which may be evolved from the sample. These gases are then analyzed by a self contained packed column GC with a thermal conductivity detector. This is the first analytical system to employ furnace pyrolysis, filament pyrolysis and trapping capabilities. Heating rate capabilities range from 0.01°C/minute to a maximum rate to 20,000°C/second.

#### Experimental Section

The system described in this paper makes use of existing elements of analytical instrumentation in a unique combination. A CDS Instruments Model 920 Thermal Processing System was used in these experiments. Dynamic headspace/purge and trap, furnace pyrolysis and filament pyrolysis can all be performed during a single experiment.

The thermal processing unit consists of a thermal desorption/furnace pyrolysis chamber mounted on the side of the instrument. For dynamic headspace and/or furnace pyrolysis the chamber has a maximum temperature of 600°C. The heating rate of the furnace is up to 60°C/minute. If higher temperatures or heating rates are required, the Pyroprobe 2000 can be used to heat the sample to a maximum temperature to 1400°C at rates from 0.01°C/minute to 20,000°C/second. As the sample is heated, carrier flow directs the volatiles to the three on-line traps. These traps contain Tenax TA to retain organic fractions or molecular sieve 5A for trapping fixed gases.

Figure 1 shows a flow diagram for this system, which contains three traps, a monitor FID, packed column GC with a TCD and a capillary column GC with an FID. In terms of geochemical analysis, the furnace heats the sample to 300°C, while the migratory hydrocarbons are trapped onto trap A. At the same time part of this fraction goes on to a monitor FID to determine the total P<sub>i</sub> concentration. The sample is then heated to 600°C. The cracked kerogen passes to a split valve where part of the sample is collected onto trap B and the remainder passes on to the monitor FID for P<sub>i</sub> evaluation. After collection of the fixed gases on the molecular sieve trap, the fixed gases are analyzed with a packed column GC and a thermal conductivity detector. After this, the trap containing the migratory hydrocarbons (P<sub>i</sub>) is backflushed through a heated transfer line to a capillary GC with a 50M X 0.25mm SE-54 capillary column. After this analysis, trap B containing the cracked kerogen components is backflushed and analyzed by the capillary GC.

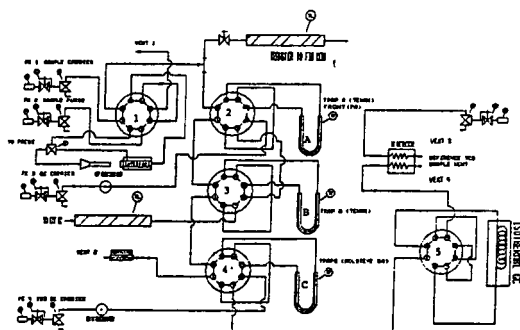


Figure 1: Flow schematic of thermal processing system.

Due to the flexibility and programming capability of this system, any number of thermal treatments can be performed depending on analytical needs.

## Results

Two geochemical samples were compared in this study. The first sample was an Alaskan oil shale, the second sample was from the Green River. The samples were heated to 300°C and then to 600°C using the furnace pyrolyzer. Figure 2 shows the monitor FID composite results of the Alaskan oil shale sample along with the temperature profile. The  $P_1$  composite fraction elutes at approximately 138°C and  $P_2$  elutes at a sample temperature of 530°C. The area ratio of  $P_1/P_2$  was measured to be 0.084.

### TEMPERATURE PROFILE

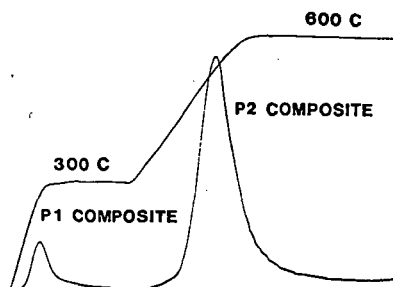


Figure 2: Temperature profile,  $P_1$  and  $P_2$  fractions of an Alaskan oil shale.

Figures 3 and 4 respectively, show the capillary column chromatograms of these two fractions. The  $P_1$  fraction shows the migratory hydrocarbons from pentane to tetradecane. The larger fraction,  $P_2$  displays the cracked kerogen geopolymer. Compounds generated by thermal treatment up to 600°C produces hydrocarbons up to  $C_{30}$ .

### MIGRATORY HYDROCARBONS ( $P_1$ )

#### SAMPLE HEATED TO 300°C

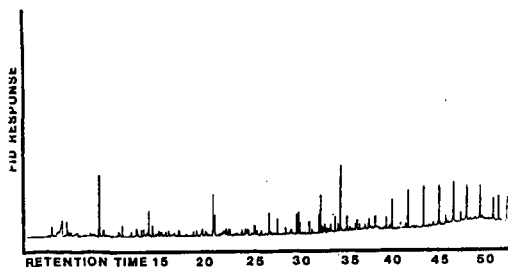


Figure 3: Alaskan oil shale heated to 300°C.

GEOCHEMICAL ANALYSIS

CRACKED KEROGEN (P2)  
SAMPLE HEATED TO 600°C

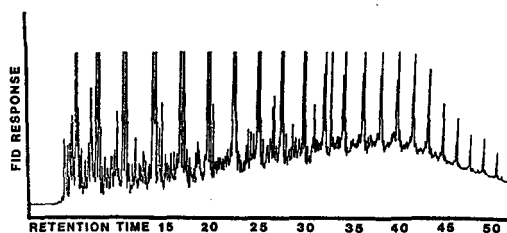


Figure 4: Alaskan oil shale heated to 600 C.

A second application of this instrument is in the field of synthetic polymer analysis. Residual solvent analysis, polymer identification and structural determinations are all possibilities. Figure 5 displays a 10 mg. sample of polystyrene which was heated to 300°C. The chromatogram shows primarily solvents used in the processing of this polymer and especially residual styrene monomer.

DYNAMIC HEADSPACE OF POLYSTYRENE AT 300 C

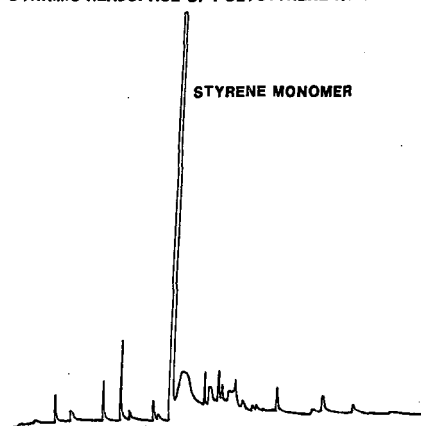


Figure 5: Polystyrene heated to 300 C for 10 minutes.

After residual solvent analysis, a portion of the residue (approximately 500 micrograms) was pyrolyzed at 750°C for 10 seconds. Figure 6 shows the results of this procedure. Styrene monomer, dimer and trimer are all products of this thermal treatment.

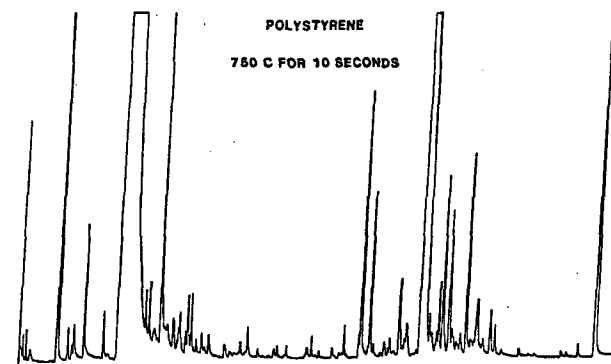


Figure 6: Pyrolysis/GC analysis of polystyrene at 750 C.

Finally, the most complex type of analysis involves composite materials which contain many components of varying volatilities. Cosmetics are a group of materials which fit ideally into this category. Mascara samples frequently contain solvents, pigments, polymers and inorganics which can hinder the analysis. A mascara sample was heated to 300°C and then pyrolyzed at 700°C for 10 seconds. The solvent analysis of the mascara sample is shown in figure 7. This chromatogram reveals solvents and the black pigments used in this commercial product. Subsequent pyrolysis of the residue, figure 8, shows the presence of an acrylate polymer which was identified as polymethylmethacrylate.

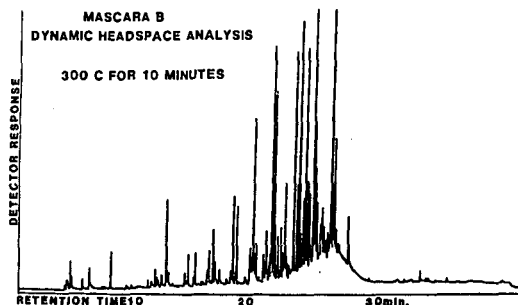


Figure 7: Dynamic headspace of mascara at 300 C.

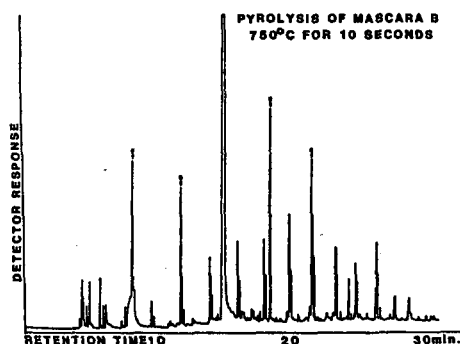


Figure 8: Pyrolysis/GC analysis of mascara residue.

### Conclusions

The analytical system described in this paper proves to be versatile instrument for the thermal processing of a diverse range of samples. Due to the trapping capabilities of the system, several temperature dependent fractions can be collected and subsequently analyzed by GC, GC/MS or GC/FT-IR.

### References

- (1) Hickman, D.S.; Jane, I., *Analyst*, 1979, 104, 334
- (2) Ohtani, H.; Nagaya, T.; Sugimura, Y, Tsuge, S. J. *Anal. Appl. Pyrol.*, 1982, 4, 117.

- (3) Washall, J.W.; Wampler, T.P. J. Chromatogr. Sci. 1989, 27, 144.
- (4) Egsgaard, H.; Carlsen, L. J. Anal. Appl. Pyrol. 1984, 7, 1.
- (5) Westall, W.A.; Ridduck, A.J. J. Anal. Appl. Pyrol. 1987, 11, 3.
- (6) Montaudo, G. J. Anal. Appl. Pyrol. 1988, 13, 1.
- (7) Whiton, A.S.; Morgan, S.L. Anal. Chem. 1985, 57, 778.



## Thermal Degradation of Polyarylethersulfones 1. Review of Underlying Chemistry

C. Libanati, C. LaMarca, M. T. Klein\*, S. M. Andrews<sup>1</sup>,  
and R. J. Cotter<sup>1</sup>

Center for Catalytic Science and Technology  
Department of Chemical Engineering  
University of Delaware  
Newark, DE 19716

**KEYWORDS:** polymer, pyrolysis, mechanisms.

The development of composite materials and the appearance of new applications in the aerospace and automotive industries have revived interest in high performance organic polymers, identified as possible matrices for fiber/polymers composites. Polyarylethers, which were some of the first commercialized plastics, are among the polymers being considered. They form a class of polymers that are tough, have a high softening temperature and maintain their mechanical properties for extended periods of time at temperatures over 150°C [1,2,3].

Sulfone-containing polyarylethers generally include one or more aromatic rings linked together by ether and sulfone groups. One class of these polymers also contains isopropylidene linkages. The nature and proportions of the different linkages determine the physical properties of each polymer. Herein we focus attention on polymers with phenyl ether (Ph-O-Ph) and phenyl sulfone (Ph-SO<sub>2</sub>-Ph) bonds; we will consider polymers containing the propylidene linkage in a follow-up paper.

The thermoplastic behavior of polyarylethersulfones makes them very attractive for injection molding, forming, pultrusion and other manufacturing techniques in which the raw material is softened by heating in order to be processed. Due to their high softening temperature (glass transition temperature > 195°C), these polymers require processing temperatures of 350 to 400°C. At these temperatures, the chemical bonds within the macromolecules are thermally labile, which can lead to changes in the structure of the polymer. Structural changes can also occur when the polymers are maintained at high operational temperatures (150 to 200°C) for an extended period of time.

The foregoing manufacturing and operational issues have motivated studies of the thermal behavior of the polyarylethersulfones since the early stages of development, and elucidation of the mechanism of degradation has been pursued. The literature in this area is largely experimental and suggests that the thermal decomposition chemistry can cause topological changes leading to altered polymer properties, such as the formation of a gel from a linear polymer. This literature motivated the present work aimed at the development of a molecular model of polymer reaction and diffusion using our recently formulated Monte Carlo approach to the simulation of the reaction of macromolecules.

Most of the experimental work on thermal and radiolytic stability has recently been reviewed by Verma [1]. As is evident in the literature, there is no objective measure of the thermal stability of polyarylethersulfones. If the maximum decomposition temperature is the important parameter, polymers align in the order of increasing stability in one way [5,6,7]. On the other hand, if gel formation is to be avoided (e.g. during injection molding), then stability is ordered in another way [6]. Thus, thermal or radiative stability must be considered in relation to one or more of the polymer's properties when exposed to heat or radiation.

The properties of interest are directly linked to the applications for which the polymers are intended. Polymers may have good stability for certain applications while performing poorly in others. For example, a polymer with a high degradation temperature may exhibit rapid gel formation at processing temperature. The following have been used as a measure of thermal stability: lowest degradation temperature and weight percent loss in vacuum or in air obtained from TGA analysis [5,6,7,10,11,16,17], gel and gas formation [6,7,8,10,11,12,13,18], intrinsic and limiting viscosity of the sol fraction [8,9,10,18,12,13,15], modulus [9], tensile flexural strength [9,13,15] and molecular weight distribution of sol fraction [14,20,21]. Some properties studied in the literature have no direct link to properties necessary for use or manufacturing, but provide clues towards the determination of the underlying phenomena. They include optical density [19], infrared and nmr spectra [6,10,17,18,20] and bond scission and crosslinking rates [8,9].

<sup>1</sup> Amoco Performance Products, Inc., Research & Development Center, 4500 McGinnis Ferry Rd., Alpharetta, GA 30202-3944.

The behavior of the polymer depends not only on its chemical composition but on the physical structure as well. Only one recent publication by Nakron and coworkers [19] addresses the influence of initial molecular weight distributions on the thermal reaction of polyarylethersulfones. They show marked differences in the optical densities and oxygen uptake in the degradation of different molecular weight fractions of the chemically identical polyarylethersulfones. Also, Brown et al. [13] have shown large differences in the gel formation during radiolytic degradation of polyarylethersulfones when the reaction temperature is above and below the glass transition temperature.

This explicit relationship between reactivity and structure has prompted the development of the present molecular model of polymer degradation. This model, which incorporates fundamental information concerning the reaction of the polymers' reactive moieties and mobility of the polymer segment, explicitly links the structure of the system to its reactivity and reaction path. The model consists of a Monte Carlo simulation, within a percolation grid, of reaction and segmental mobility of polymer chains.

The framework for this model is the underlying basic chemistry on which it rests. We present the development of the model in two parts. Part 1, the present manuscript, delineates the controlling elementary steps of pyrolysis. These are assembled into a prediction of the reactivity of a model polysulfone in Part 2, when the mechanics of the Monte Carlo simulation of structure, reaction, and diffusion are presented.

Thus our present focus is on basic chemistry. What follows is a result of a thorough review of not only the polyarylethersulfone literature but also the physical and organic chemistry literature of the reactions of polyarylethersulfone-related moieties. Our objective was to discern reaction pathways and kinetics parameters. The former would provide Monte Carlo allowable "transitions" while the latter would provide transition probabilities.

## THE THERMAL CHEMISTRY OF POLYETHERSULFONE SYSTEMS

The thermal degradation of polyarylethersulfones was postulated in the original study by Hale et al. [7] to be free radical in nature. This has been probed since in numerous thermal and radiative degradation studies with different formulations of related polyarylethersulfones [4,6,8,10,21]. An important publication by Lyons et al. [22] on the radiative effects on polyarylethersulfones and related model compounds confirmed such an assumption by identifying the presence of several free radicals during ESR monitoring of the reaction.

Although they formulated the main hypothesis behind the degradation process, namely that the "weaker" link breaks and generates radicals, Hale et al. [7] did not account for crosslinking reactions. Their study reports thermal gravimetric experiments that mask the extent of the structural changes occurring in the melt. Their proposed mechanism includes only bond breaking through initiation and bond forming through termination.

Davis [8] was the first to obtain explicit evidence of crosslinking reactions by measuring the gel fraction in the reaction products as a function of time. The experimental curve was similar to the gelation results obtained during copolymerization of polyfunctional monomers [44]. He concluded that crosslinking must occur by addition of polymer radicals to other polymer chains, but did not advance a mechanism for such a process.

A mechanism for crosslinking, involving cyclohexadienyl-type radicals observed by Lyons et al. [22], was later proposed by Danilina et al. [6]. It involves the addition of phenyl radicals, produced by initiation, to the benzene rings in the polymer chains, followed by elimination of hydrogen atoms. More recent publications by Narkon et al. [18] and Kuroda et al. [21] calculate crosslinking and bond scission rates from experimental results, using the Charlesby method for the former and their own novel method for the latter. Their calculations, however, do not take into account the nature of the crosslinking process and only schematic mechanisms of reaction are presented.

It is clear from the literature that structurally significant reactions involved in the radical chains include not only initiation and termination reactions, but also addition steps that can lead to crosslinking. Herein, we reduce the enormous complexity of these types of reactions via their organization into reaction families. Reactions involving radicals are classified into three main groups:

- Initiation reactions, which create radicals from stable molecules;
- Propagation reactions, in which the number of radicals is conserved;
- Termination reactions, which consume radicals.

### INITIATION REACTIONS

Hale [7] first proposed that the scission of the "weaker" bonds were responsible for the generation of radicals. Bond dissociation energies identify the carbon-sulfur bond (66 kcal/mole) in the sulfone group.

Although the nature of the initiation has been widely accepted, the mechanism remains a subject of discussion. The dominant view, proposed by Hale et al. [7], consist of a two step initiation mechanism, where the carbon-sulfur bond breaks to produce a phenyl radical and a sulfonyl radical. The  $\text{Ph-SO}_2^\bullet$  radical can further decompose to  $\text{Ph}^\bullet$  and  $\text{SO}_2$  or react with other molecules. This view is shared by Lyons et al. in their radiation damage studied, but no conclusive evidence has been provided in the literature [22].

Ayscough [23] proposed a concerted mechanism in which simultaneous cleavage of adjacent carbon-sulfur bonds occurs.

The fission to  $\text{Ph}^\bullet$  and  $\text{Ph-SO}_2^\bullet$  described above occurs with  $\log_{10} A_1 (\text{s}^{-1}) = 15$  and an activation energy equal to the dissociation energy of the carbon-sulfur bond,  $E_1 = 65 \text{ kcal/Mole}$ . For reaction of  $\text{Ph-SO}_2^\bullet$  to  $\text{Ph}^\bullet$  and  $\text{SO}_2$ ,  $\log_{10} A_2 (\text{s}^{-1}) = 15$  and  $E_2 = 45 \text{ kcal/Mole}$  is equal to the enthalpy of reaction, for the unimolecular decomposition<sup>†</sup>.

The phenyl radicals produced in the initiation steps can either terminate or react with other molecules generating new radicals, which propagate a pseudo kinetic chain. The list of possible radicals participating in radical-molecule reactions is limited to  $\text{H}^\bullet$ ,  $\text{Ph}^\bullet$ ,  $\text{R-O}^\bullet$ ,  $\text{R-SO}_2^\bullet$ , Cyclohexadienyl radicals, cyclohexenyl radicals and cyclohexyl radicals.

### PROPAGATION REACTIONS

Three types of propagation reactions are present in the degradation mechanism: Addition of a radical to benzene rings and double bonds; elimination or  $\beta$ -scission; and hydrogen abstraction by a radical from a stable molecule. We consider each in turn.

#### Addition Reactions

The work of Danilina et al. [6] suggest that addition reactions to the polymer's benzene ring is the vehicle for crosslinking. Radicals can add to a substituted benzene ring to yield a substituted cyclohexadienyl radical.

These reactions are very fast when the attacking radical is a phenyl radical [24,27,29,30,31,32,34,35,36,39] or a hydrogen atom [25,26,28,37,38]. In the case of phenyl radicals, at  $450^\circ\text{C}$  the addition to a benzene ring is 40 times faster than abstraction of hydrogen by the radical from benzene.

Rate constants for addition of hydrogen atoms and phenyl radicals to substituted benzenes have been reported in the synthetic organic chemistry literature [24-39]. Jansen [27] provides a value of  $7.8 \times 10^4 \text{ M}^{-1} \text{ s}^{-1}$  for the rate constant of addition of phenyl radicals to benzene. Pryor [25] estimated the rate constant for addition of hydrogen to benzene at  $10^9 \text{ M}^{-1} \text{ s}^{-1}$  at  $35^\circ\text{C}$ . The activation energy for the latter reaction is known to be  $3.8 \text{ kcal/mole}$  [24,26,37], which implies a  $\log_{10} A (\text{M}^{-1} \text{ s}^{-1}) = 11.7$ . Modelling the transition state for the addition of phenyl radicals provides an estimate of  $\log_{10} A (\text{M}^{-1} \text{ s}^{-1}) = 7.7$ . Combined with the reported rate constant, the activation energy is calculated at  $E^* = 3.83 \text{ kcal/moles}$ . This value is very close to the hydrogen value and is consistent with the energetics of the reaction; the estimated enthalpy of reaction for hydrogen and phenyl additions are essentially equal at  $\Delta H_R^\circ = -24.9 \text{ kcal/moles}$  and  $25.1 \text{ kcal/mole}$  respectively [25,26].

For all other radicals, the rate constant for addition, in its Arrhenius form, has been estimated from an Evans-Polanyi relationship relating activation energies to heats of reaction. The Evans-Polanyi relationship was used to estimate activation energies ( $E^* = E_0^\circ + \alpha \Delta H_R^\circ$  for exothermic reactions and  $E^* = E_0^\circ + (1-\alpha) \Delta H_R^\circ$  for endothermic reactions).

$\Delta H_R^\circ$  is the enthalpy of reaction,  $E_0^\circ = 16.3 \text{ kcal M}^{-1}$ , and  $\alpha = 0.56$ .  $\Delta H_R^\circ$  is calculated from the heat of formation of reactant and products determined from literature information or group additivity [41]. Estimated heats of formation are summarized in Table 1. The parameters  $E_0^\circ$  and  $\alpha$  were determined from the values of the activation energies for the addition of phenyl radicals and the addition of cyclohexadienyl radicals [27,42]. This procedure is described in detail elsewhere.

The pre-exponential factors are assumed to be  $5 \times 10^7 \text{ M}^{-1} \text{ s}^{-1}$ , equal to the one for phenyl radical addition.

The rate constant for addition can also be affected by electronic effects due to the presence of substituents on the reactant molecules. This is particularly true for addition at different positions in substituted benzenes. According to the extensive literature on radical addition to substituted benzene rings [25-39], neutral radicals, such as phenyl radicals, preferentially add to the benzene ring at non-substituted positions. The reasons for such behavior are unclear. A possible ex-

<sup>†</sup> The heat of formation of the sulfonyl radical was calculated from the heat of formation of diphenyl sulfone,  $\Delta H_f^\circ = -30.98 \text{ Kcal/Mole}$ , and the bond dissociation energy of the C-S bond. Substituent effects, generated by the ether linkages at the para position to the sulfone linkage, have been neglected here.

planation is that for large radicals, the substituent may present an important steric hindrance to ipso-substitution reactions. Because of their size, small hydrogen atoms are assumed to be an exception and are allowed in our reaction scheme to substitute at occupied positions on a benzene ring. For any of the electro-neutral radicals that participate in the reaction mechanism, including the hydrogen atom, the preferred position for addition is ortho to a substituent, followed by the para position and, finally, the usually much less reactive meta position [24,29]. The relative selectivity toward each position is influenced by the electronic characteristics (electron donating or electron withdrawing) of the substituent and the attacking radical [24,29,31].

As an example, the rate constant for addition of a phenyl radical at an ortho position from an  $\text{NO}_2$  group is 9 times greater than the rate of addition of the same radical on an unsubstituted benzene [24]. Values of the estimated relative activation energy and rate constant for addition of phenyl radicals, at  $425^\circ\text{C}$ , at every position of a substituted benzene to the rate constant of addition to any position in an unsubstituted benzene are summarized in Table 2 for all the possible substituents in the polymer systems considered in this work. Similar studies with other radicals show qualitatively the same results, for electro-neutral radicals [24,29,39]. Quantitatively, the values reported show a stronger influence of the substituents present on the neutral molecule rather than of the nature of the attacking radical. Consequently, the ratios reported in Table 2 are assumed to be the same for all other radicals present during polysulfone degradation.

An analogous reaction is the addition of radicals to the double bonds of cyclohexadiene and cyclohexene, which are not present in the original polymer but can be formed during reaction. Additions to double bonds are similar in nature to the addition to benzenes and consequently the same Evans-Polanyi relation was used to estimate activation energies.

#### Elimination Reactions.

The reverse reaction to additions are eliminations reactions. They are  $\beta$ -scission reactions in which hydrogen or a substituent are eliminated. The pre-exponential factors for these reactions were estimated at  $5 \times 10^{13}$  when hydrogen is eliminated and  $5 \times 10^{12}$  for elimination of a bulkier substituent. The activation energy,  $E_\beta$ , can be calculated from  $E_A^\ddagger$ . The activation energy of the reverse addition reaction (from section IV.2.2.1), and the heat of reaction  $\Delta H_R$ ,  $E_\beta = E_A^\ddagger - \Delta H_R$ , already determined from Table 1.

#### Hydrogen Abstraction

The last family of radical-molecule reactions is hydrogen abstraction from a stable molecule by any of the radicals. There is very little easily extractable hydrogen in the initial polymer. When the benzyl hydrogen is the one exchanged in this reaction, the rate for the fastest abstraction (by phenyl radicals or  $\text{H}^\bullet$ ) is already several orders of magnitude slower than that for addition to the benzene ring. The only easily abstractable hydrogen in the initial polyethersulfone systems is the phenoxy-H. As the reaction progresses, however, more-saturated cyclohexadienes, cyclohexenes and cyclohexene, as well as a higher number of hydroxy and possible  $-\text{SO}_2\text{H}$  groups form and bring an extra source of abstractable hydrogen.

The pre-exponential factor for these reactions was estimated from modelling the transition state at  $10^{10} \text{ M}^{-1} \text{ s}^{-1}$  when  $\text{R}^\bullet = \text{H}^\bullet$  and  $10^8 \text{ M}^{-1} \text{ s}^{-1}$  otherwise. It is comparable with literature values [43]. The activation energy was calculated using the Evans-Polanyi relation.

In this case,  $\Delta H_R = d_{\text{R-H}}^0 - d_{\text{R}^\bullet\text{-H}}^0$ . The bond energies  $d_{\text{R-H}}^0$  and  $d_{\text{R}^\bullet\text{-H}}^0$  were found in the literature [[56]] or estimated from group contribution methods. They are summarized in Table 3.

#### TERMINATION REACTIONS

Radical-radical reactions consume two radical chain carriers. These very fast reactions are responsible for the termination of the kinetic chain. They have kinetics implications, because they eliminate the chain carriers from the reaction mixture, and also structural implications, because they can create bonds.

#### Recombination Reactions

Recombination of two radicals is the simplest case of termination. Recombination is assumed to be non-activated and with  $\log_{10} A (\text{M}^{-1} \text{ s}^{-1}) = 10$  when  $\text{R}_1$  or  $\text{R}_2$  are hydrogen atoms and  $\log_{10} A (\text{M}^{-1} \text{ s}^{-1}) = 9$   $\text{M}^{-1} \text{ s}^{-1}$  otherwise.

Recombination reactions produce an increase in molecular weight but can only be responsible for crosslinking when one of the terminating radicals is a central radical in the polymer chain, such as a phenyl or cyclohexadienyl radical linked to two other benzene rings.

### Disproportionation Reactions

Disproportionation reactions can occur, in competition with recombination, when one of the radicals has a donatable hydrogen at the  $\alpha$  position. This is the case for cyclohexadienyl, cyclohexenyl or cyclohexyl radicals. From product yields reported in literature [24,26], the rate constant for disproportionation appears to be 3 times smaller than the one for recombination.

### SUMMARY

The observed chemistry is the combination of these simultaneous reactions. Their quantitative contributions to the degradation process is a function of their relative rates and their structural significance in the complex mechanism of reaction. The model developed in the following sections incorporates the complete set of elementary steps into a quantitative molecular representation of the polymeric melt. We conclude here with a more quantitative description of the kinetically and structurally significant chemistry.

The thermal reaction begins by fission of the weak Ph-SO<sub>2</sub>-Ph bond. The net result is the formation of SO<sub>2</sub> gas and two polymeric phenyl radicals.

The phenyl radicals begin the propagation steps. Phenyl radical addition to a benzene ring affords a substituted cyclohexadienyl (CHD) radical, the key intermediate in the overall chemistry. The CHD radical can add to a neighboring benzene ring, creating a crosslink and a different CHD radical. The CHD radical can also revert to the original phenyl radical and benzene ring, or eliminate a substituent as a radical that can continue the propagation cycle. The CHD radical can also terminate which, when by recombination, will generally lead to another crosslink.

The complexity of this system is that at least seven (7) different radicals can participate in this chemistry. Moreover, the importance of a given reaction depends on whether the radical is at the terminus, or interior of a linear chain, a free low molecular weight radical, or part of a crosslinked polymeric arm. This motivates the use of structure-explicit computer models to track the reaction rates and structural significance. This is the topic of our companion paper to follow.

### REFERENCES

1. Rose, J. B., *Polymer*, **15**, 456, 1974.
2. Gotham, K. V. and S. Turner. *Polymer*, **15**, 1974.
3. Johnson, R. N., A. G. Farnham, R. A. Clendinning, W. F. Hale, and C. N. Marriam. *J. Polym. Sci.: Part A-1*, **5**, pp. 2375-2398, 1967.
4. Verma, A. K. *Prog. Polym. Sci.*, **12**, pp. 219-228, 1986.
5. Crossland, B., G. J. Knight, and W. W. Wright. *Brit. Polymer J.* **18**, p. 3, 1986.
6. Danilina, L. I., E. N. Teleshov, and A. N. Pravednikov. *Vysokomol. soyed.*, **A16**(3), pp. 581-587, 1974.
7. Hale, W. F., A. G. Farnham, R. N. Johnson, and R. A. Clendinning. *J. Polym. Sci.: Part A-1*, **5**, pp. 2399-2414, 1967.
8. Davis, A. *Die Makromolekulare Chemie*, **128**, pp. 242-251, 1969.
9. Davis, A., M. H. Gleaves, J. H. Golden, and M. B. Huglin. *Die Makromolekulare Chemie*, **129**, pp. 62-72, 1969.
10. Levantovskaya, I. I., G. V. Dralyuk, O. A. Mochalova, I. A. Yurkova, M. S. Akutin, and B. M. Kovarskaya. *Vysokomol. soyed.*, **A13**(1), pp. 8-15, 1971.
11. Davis, A. *Die Makromolekulare Chemie*, **132**, pp. 23-33, 1970.
12. *Polymer Letters*, **8**, pp. 121-126, 1970.
13. Brown, J. R. and J. H. O'Donnell. *J. Appl. Polym. Sci.*, **23**, pp. 2763-2775, 1979.
14. Levantovskaya, I. I., A. L. Narkon, O. V. Yershov, V. V. Gur'yanova, L. I. Reitburd, M. P. Radetskaya (dec.), L. M. Bolotina, A. B. Blyumenfel'd, A. V. Pavlov, and M. A. Morotina. *Polymer Science U.S.S.R.*, **27**(2), pp. 404-411, 1985.
15. Brown, J. R. and J. H. O'Donnell. *J. Appl. Polym. Sci.*, **19**, pp. 405-417, 1975.
16. Mikityayev, A. K., G. B. Shustov, A. M. Kharayev, V. V. Korshak, B. I. Kunizhev, and V. T. Dorofeyev. *Polym. Sci. U.S.S.R.*, **26**(1), pp. 83-87, 1984.
17. Wu, Z., R. Yokota, M. Kochi, and H. Kambe. *Kobunshi Ronbunshu*, **38**(7), pp. 479-484, 1981.

18. Narkon, A. L., I. I. Levantovskaya, Y. L. Kotov, B. Y. Konovalova, L. I. Reitburd, L. M. Bolotina, and A. B. Blyumenfel'd. *Polymer Science U.S.S.R.*, **26**(8), pp. 1917-1923, 1984.
19. Narkon, A. L., I. I. Levantovskaya, V. V. Gur'yanova, L. I. Reitburd, O. V. Yerшов, G. V. Dralyuk, M. A. Motorina, Y. I. Metelkina, L. M. Bolotina, A. B. Blyumenfel'd, and A. V. Pavlov. *Polym. Sci. U.S.S.R.*, **28**(3), pp. 562-567, 1986.
20. Coulter, D. R., M. V. Smith, F.-D. Tsay, and A. Gupta. *J. Appl. Polym. Sci.*, **30**, pp. 1753-1765.
21. Kuroda, S.-I, K. Terauchi, K. Nogami, and I. Mita. *Eur. Polym. J.*, **25**(1), pp. 1-7, 1989.
22. Lyons, A. R., M. C. R. Symons, and J. K. Yandell. *Die Makromolekulare Chemie*, **157**, pp. 103-109, 1972.
23. Ayscough, P. B., K. J. Ivin, J. H. O'Donnell. *Trans. Faraday Soc.*, **61**, 1110, 1965.
24. Kochi, J. K., *Free Radicals*, VII, Vol I. Wiley-Interscience, 1973.
25. Henderson, R. W., Pryor W. A., *J. Am. Chem. Soc.*, **97**:26, December 24, 1975.
26. James, D. G. L., R. D. Stuart. 2735-2751, 1966.
27. Janzen, E. G., C. A. Evans. *J. Am. Chem. Soc.*, **97**:1, January 8, 1975.
28. Benson, S. W., R. Sherv. *J. Am. Chem. Soc.* **89**:21, October 11, 1967.
29. Hey, D. H. *Adv. Free Radical Chem.* **V2**, 1967.
30. Ito, R., T. Migita, N. Morikawa, O. Simamura. *Tetrahedron*, **21**, 955-961, 1965.
31. Tietz, M. *Accounts of Chemical Research*, **13**, 1980.
32. Hey, D. H., M. J. Perkins, Gareth, H. Williams. *J. Chem. Soc.*, 3412-3418, 1969.
33. Gill, G. B., Gareth. *J. Chem. Soc.*, 995-1002, 1965.
34. Detar, D. F., R. A. J. Long, J. Rendleman, J. Bradley, P. Duncan. *J. Am. Chem. Soc.*, **89**:16, August 2, 1967.
35. Detar, D. F. *J. Am. Chem. Soc.* **89**:16, Aug 2, 1967.
36. Pryor, W. A., J. T. Echols, K. Smith. *J. Am. Chem. Soc.* **88**:6, March 20, 1968.
37. James, D. G. L., R. D. Stuart. 2752-2769, 1966.
38. Brett, C.L., V. Gold. *Chemical Communications*, 1971.
39. Pryor, W. A., F. Y. Tony, R. H. Tony, D. F. Chuch. *J. Am. Chem. Soc.*, **104**, 2885-2891, 1982.
40. Bevington, J. C. and J. Toole. *J. Polymer Science*, Vol. **XXVIII**, 413-410, 1958).
41. McMillen, D. F. and D. M. Golden. *Am. Rev. Phys. Chem.*, **33**, 493-532, 1982.
42. Shelton, J. R., C. W. Uzelmeier. *J. Am. Chem. Soc.*, **88**:22, Nov. 20, 1966.
43. Sundarom, K. M., G. F. Froment. *Ind. Eng. Chem. Fundm.*, **17**:3, 179-180, 1978.
44. Flory, P. J. *Principles of Polymer Chemistry*, Cornell University Press, Ithaca and London, 1953.

Table 2. Substituent Effects for Phenyl Radical Addition to Substituted Benzenes

Substituents	Ortho	Meta	Para
-SO <sub>2</sub> -†	2.3	1.0	2.1
-O -††	1.2	1.0	1.1
Others†††	1.0	1.0	1.0

† Reactivity towards -SO<sub>2</sub>- substituted benzenes was estimated from values for NO<sub>2</sub> substituted benzenes.

†† Reactivity towards -O- substituted benzenes was estimated from values from -O-CH<sub>3</sub> substituted benzenes.

††† Estimated from the values for saturated hydrocarbon.

Table 1. Heat of Formation of Molecules and Radicals [kcal/mol]


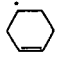

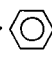
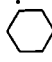
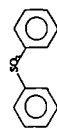
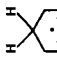
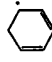
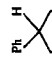
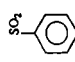
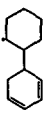
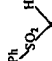
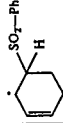
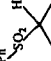
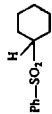
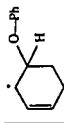
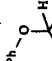

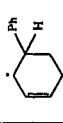

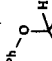
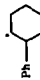
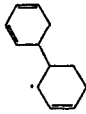

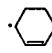
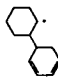
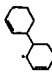
H <sub>2</sub>	0	H <sup>•</sup>	52.1		-29.3		40.4
	19.8		78.6				13
	-30.98		43.9	SO <sub>2</sub>	-70.9		47
Ph-O-Ph	8.2		80.4		-40.9		45.33
Ph-Ph	42.92		0.65	Ph-O <sup>•</sup>	12.1		-23.12
					-38.16		12.99
SO <sub>2</sub> -H	-97.27		43.24		3.35		53.17
	26				38.98		58.94
	-0.8		30		45.33		24.42

Table 1. Heat of Formation of Molecules and Radicals [kcal/mol]

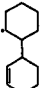
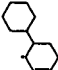
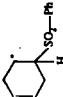
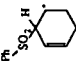
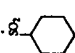

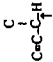
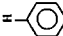
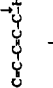
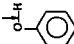
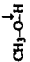
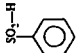



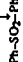

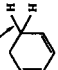

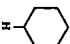

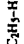
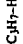


	18.52		3.39
	-10.76		
	40.4		
	-69.37		
	-40.24		

Table 3. Bond Dissociation Energies [kcal/mol]

104.2			82.5±1.3
110.9			83.±3
86.5			104.4±1
			103.4±1
			102.4±1
-66			104.7±1
66			104.7
86			86
			65
73±5			80
95.5			
98.2±1			
95.1±1			
88±1			
86.3±1.5			



## Thermal Degradation of Poly(arylether sulfones)

### 2. Monte Carlo Simulation of Polymer Structure, Reaction, and Diffusion

C. Libanati, C. LaMarca, M. T. Klein\*, S. M. Andrews<sup>1</sup>,  
and R. J. Cotter<sup>1</sup>

Center for Catalytic Science and Technology  
Department of Chemical Engineering  
University of Delaware  
Newark, DE 19716

**keywords:** polymer, pyrolysis, modelling

#### INTRODUCTION

Sulfone-containing polyarylethers generally include one or more aromatic rings linked together by ether and sulfone groups. One class of these polymers also contains isopropylidene linkages. They form a class of polymers that are tough, have a high softening temperature, and maintain their desirable properties for extended periods of time.

The neat poly(arylether sulfones) are softened by heating for processing. The literature [38] suggests that some of the challenges to this processing are engendered by the valuable properties of the polymers themselves. The same desirable high temperature softening point for end-use applications is also high enough that some thermal degradation can occur during front-end processing. This can lead to gas evolution and viscosity increase, the latter presumably owing to the formation of a gel.

These literature reports motivated the present work aimed at applying our previously developed reaction modelling technique using Monte Carlo simulation to the reactions of poly(arylether sulfones). The particular appeal was that the literature suggested the thermal reactions have structural implications (e.g., gel formation), and our Monte Carlo technique is structurally explicit. There thus appeared to be a good match.

Our model therefore sought an explicit link among polymer structure, reactivity and properties. The link between polymer structure and reactivity was formed by basing the reaction pathways and kinetics on model compound chemistry. Part 1 of this series described the elementary steps modelled to control the thermal degradation of poly(arylether sulfones). The link between the thus-changing polymer structure and properties was established by phrasing the model in terms of a three-dimensional lattice, on which lattice sites represented monomer units and lattice site connections represented bonds. Polymer diffusion on this lattice was described by the movement of monomers to adjacent empty lattice sites. Polymer reaction was described by the destruction or formation of bonds between lattice sites, the nature and probabilities of which being described by model compound pathways and kinetics.

This percolation model of gelation allowed determination of gel, sol and gas fractions as a function of reaction time. Other relationships or models linking properties of the material to its structure (e.g., viscosity from molecular weight distribution or modulus from number of crosslinks and degree of polymerization between crosslinks) can be used to determine the adequacy of the polymer to the application for which it is intended.

The input to the model consists of the chemical and physical structure of the polymer of interest, an assumed mechanism of segmental mobility and associated transport constants, and the postulated mechanism of thermal reaction and its associated rate constants. The output is a prediction of the structure and chemical identity of the system as a function of time. Because the model describes the system at the molecular level, at which all polymers share structure and chemistry, the simulation parameters, such as reaction and transport time constants, are independent of the system modelled, and can be determined from other sources such as experiments with model compounds. Thus this model is envisioned as a tool for the understanding of the underlying fundamentals and for the determination and design of optimal systems.

Although models have been frequently used to improve qualitative understanding, any significant quantitative use of a model's prediction is achieved through comparison with laboratory experimental results. However, the lack of precise characterization of the starting material renders difficult quantitative comparisons between experimental studies and simulation results, especially when the polymers studied were synthesized for a particular study. In particular, a frequent omission in the studies reported in the literature is the molecular weight distribution of the original polymers studied. For the purpose of obtaining pertinent experimental data, we have developed our own experimental procedure which will be reported upon in a follow-up paper. Herein we focus on only the development and operation of the Monte

<sup>1</sup> Amoco Performance Products, Inc., 4500 McGinnis Ferry Rd., Alpharetta, GA 30202-3944.

Carlo simulation of polymer degradation. We begin by considering the basic issue of gelation, which controls the present structure-property link sought.

## GELATION AND PERCOLATION.

Part I described the basic chemistry of poly(arylether sulfone) degradation. Occurring in the polymer, these elementary steps have structural significance. We need to account for more than just the net bond formation/bond breaking; we need to account for crosslinking and longer-range connectivity. This requires a model of the gelation process. Gelation involves the formation of indefinitely large polymer structure, which will extend through the volume of the polymer sample and, on the molecular scale, may be considered essentially infinite.

Gelation is always the result of crosslinking. Its main characteristic is the existence of a gelation point or threshold. This point is akin to the critical point in thermodynamics. As conversion increases during the polymerization of a system containing multi-functional monomers, a point is reached where the system suddenly changes from a viscous homogeneous fluid to a two-phase system, containing an insoluble cluster, the gel, and a soluble portion, the sol [1-8,11, 12,20]. The existence of a gelation point has also been demonstrated in systems where initial constituents are not monomers but linear polymers [1,9-16].

Models of gelation address the connectivity of the system. An early analytical model was developed by Flory and Stockmayer [1,11,12]. Their approach is based on three main assumptions: functional groups react independently of one another; identical functional groups have the same reactivity; no intramolecular reactions occur. Also, any functional group can react with any other functional group, independent of position, and excluded volume effects are neglected.

Based on these assumptions, the system can be represented as a Bethe lattice [5] of functionality equal to the functionality of the monomers. A statistical analysis on this network provides information on the size of the clusters and the connectivity of the monomers as a function of conversion,  $p$  being defined as the number of bonds formed over the total number of possible bonds. This approach correctly describes the gelation transition and the critical conversion value  $p_c$  for the existence of an infinite cluster, calculated as  $p_c = 1/(f-1)$ , for monomer of functionality  $f$  [1]. The same approach has also been used to describe the crosslinking of linear polymer chains in the vulcanization of rubber [9,10,13-16].

The assumptions stated earlier limit the quantitative use of the analytical approach to but a handful of simple systems. For instance, neglecting intramolecular reaction is probably unreasonable when the initial condition is a set of large linear molecules rather than a collection of monomers. Also, excluded volume effects become important as the reaction proceeds, generating isolated sites, and the equal accessibility rule breaks down in strongly transport-limited systems. Percolation models of gelation are considered to account for the deficiencies of the analytical approach.

The central concept in percolation is the discrete description of space. Space is spanned by a lattice of dimensionality  $N$ . The lattice sites can be occupied by monomers, and are connected to neighboring sites by a certain number  $f$  of bonds, corresponding to the functionality of the monomers. It can be noted here that the Flory-Stockmayer approach is equivalent to a percolation of infinite dimensionality.

Percolation models are usually implemented numerically and grids of finite size are used to describe a representative fraction of the system. The boundaries of the grid are then considered to be periodic. In these instances, gelation is attained when percolation occurs. In other words, a cluster becomes infinite when it spans the length of the lattice. Based on the state of the lattice a slate of statistical quantities, regarding the composition of the system, can be calculated. The reaction network and kinetics determine the rules by which bonds are formed, linking  $p$  to reaction time.

In the case of poly(arylether sulfone) degradation, crosslinking occurs as a consequence of breaking and forming linkages within an initially linear polymeric system. The grid percolation models offer the advantage, over the analytical model, of describing the physical and chemical environment of a reactant. A reactive intermediate has a certain number of nearest neighbors with which it can react. Therefore, reactions can be considered at the elementary step level, where bond breaking and bond forming occur. These were presented in Part I and can be organized, from a topological point of view, into three main classes:

- |                           |   |
|---------------------------|---|
| Bond-breaking reactions:  | Initiations and eliminations from cyclohexadienyl, cyclohexyl or cyclohexenyl radicals. |
| Bond-forming reactions:   | Additions and terminations.   |
| "Bond-neutral" reactions: | Hydrogen abstractions and disproportionations.  |

In the next section, the Monte Carlo simulation of poly(arylether sulfone) degradation is presented, using a three-dimensional square-grid percolation model that incorporates the entire set of elementary steps described earlier.

## MONTE CARLO MODEL DEVELOPMENT.

The Monte Carlo simulation of degradation of poly(arylether sulfones) is summarized in terms of major modules of the overall simulation scheme. The initial polymer configuration is constructed from structural information. Once an original configuration is determined, radicals are generated within the grid using an event-space algorithm. The time  $t_i$  and nature of the initiating event (initiation reaction or diffusion into the lattice) are calculated. The new state of the system is determined, and time is updated (time = time +  $t_i$ ). Once radicals are present in the lattice, polymer segments are moved, and all radicals present are tested for reaction with their environment during a fixed time interval

$\Delta t$ . If, after that time interval, radicals are still present in the lattice, the total time is updated (time = time +  $\Delta t$ ), and the previous step is repeated. If, on the contrary, all radicals have disappeared from the lattice (via termination or by diffusing out through a grid boundary), new radicals are generated within the lattice. Then time is updated and the same movement/reaction process described above is repeated. Results are stored at desired reaction times. Once the final reaction time is reached, a new initial configuration is generated for each subsequent run. The results of all runs are averaged to yield statistically significant quantities.

The following subsections present in detail the features of each unit of the overall simulation, starting with the simulation of structure, including the initial configuration and the dynamic simulation of structure, followed by simulation of initiation and propagation reactions. The mechanics of the program developed are detailed elsewhere [39].

## SIMULATION OF STRUCTURE

The polymeric melt is represented by a three dimensional square grid of dimension  $N \times N \times N$ . Polymer chains are represented by monomers occupying grid sites connected by bonds. Each grid site has six nearest neighbors with which to interact through linkages or reaction. This representation of the system allows the description of the chemical environment of each site, as well as the global connectivity of the system. It also allows for spatial movement of the monomers, from site to site according to specified rules, to account for diffusion.

In poly(arylether sulfone) systems, the grid sites represent substituted benzene rings, and the bonds represent the linkages between aromatic units. For the system considered here, these bonds are sulfonyl linkages, ether linkages or carbon-carbon bonds (arising from thermal reaction).

### Initial configuration

The initial configuration of the system is determined by randomly placing molecules in the grid. Polymer molecules are initially linear. They are represented by self-avoiding random walks in the cubic lattice [1,20,17-19,21]. The degree of polymerization (chain length) of each molecule is randomly chosen from the initial degree of polymerization distribution. The molecule is then placed in the percolation grid, by placing monomers one by one, until the pre-determined length is attained. Where structure is concerned, the boundaries of the grid are periodic. This means that a polymer chain that exits the grid through one face reenters it through the opposite face. This procedure is repeated with new polymer chains until a fraction of the lattice, corresponding to the polymer's density, is filled.

In order to calculate the occupied fraction of the grid, the Van der Waals volume of the polymer, estimated by optimizing the structure of the polymer's building blocks (in this case diphenylsulfone and diphenyl ether), was compared with the total volume of the lattice, assumed to be the total volume occupied by the polymer. The estimation of the polymer molecular volume was achieved by optimizing structure using extended Hückel molecular orbital calculations. The occupied fraction was obtained by dividing the molar Van der Waals volume of the polymer's building block by the molar density of the polymer. In the case of poly(arylether sulfone), the density is 1.06 g/cc, and an average volume of diphenylsulfone and diphenylether was estimated at  $130 \text{ \AA}^3$ . The occupied fraction in this case is 75%.

The initial polymer configuration gives the complete connectivity of the polymeric melt, the free volume that will allow polymer movement and the chemical identity of each lattice site and bond. Reaction and movement of polymer units can then be explicitly addressed at the molecular level.

### Dynamic structure simulation.

The transport characteristics of the medium in which radical reactions occur have a strong influence on pathways and kinetics. The radical reactions involved in the degradation mechanism are very fast. Fast reactions have been shown to be affected by the ability of the reactant to move [22-24,28,30,32-36]. The time scale of these reactions is often comparable to that for molecular movement, especially in restricted systems like polymer melts. Also, the connectivity of the network can affect or be affected by transport limitations, as is apparent in the work of Brown in the radiolitic degradation of poly(arylether sulfone) at temperatures above and below the glass transition temperature [22]. It is therefore important to introduce mechanisms that account for the movement of the monomers.

The approach taken follows the idea that a polymer molecule diffuses through the movement of its smaller segments, in a wormlike fashion [39]. In simulation, a number of movements, equal to the number of monomers present in the medium, are attempted in a time step  $\Delta t$ . Since the CPU requirement to move every possible segment in the system becomes prohibitively large with grid size, only polymer segments within three lattice sites of a given radical were moved in one step. This local diffusion model captured the environment about a reactive site while still allowing reasonable computational demand. The model has been described in detail elsewhere [39].

### Simulation of Reaction

Reactions are simulated according to the stochastic algorithm described elsewhere [39]. Two classes of events are distinguished: The initiation events, creating active centers (radicals) within the lattice, and propagation events, carrying the radical chain reactions.

**Initiation Events.** Radicals responsible for the degradation of poly(arylether sulfone) are formed in initiation reactions. The sulfonyl linkages break to give two radicals, a phenyl radical and a sulfonyl radical. These radicals can propagate the reaction by interacting with stable monomers, or they can terminate.

An event-space algorithm is used to generate radicals. The initiation possibilities include the breaking of any of the  $N_{SO_2}$  sulfonyl linkages present in the lattice. Each one of them represents an event that can happen with rate constant  $k_{init}$ . However, due to the finite size of the grid, an extra initiation event was included: radicals generated elsewhere in the melt and outside of the lattice were allowed to diffuse into the grid. The necessity for such an event was prompted by the relative values of initiation and termination rate constants. Rate constants for initiation are usually orders of magnitude smaller than those for propagation reactions and up to  $10^{15}$  times smaller than termination rate constants. Concentrations of radicals in this system are of the order of  $10^{-8}$ – $10^{-10}$  times the concentration of initiating linkages. Memory availability and CPU requirement limit grid sizes to values well below the  $10^8$  sites necessary to simulate a representative sample of polymer melt. This means that periodic boundary conditions cannot be applied regarding the movement of radical intermediates. If a radical moves out of the percolation grid, it disappears. Having it reenter the grid through the opposing face would artificially increase the concentration of radicals. Including this second (transport) component to the "initiation" or generation of radicals involved the evaluation of the rate of "diffusion" of radicals into the lattice. This was accomplished by calculating the number of radicals that will cross the lattice boundaries inwards per unit time. A radical will move a distance equal to one lattice unit in an average time  $\tau = \pi l^2 / 16 D$ , where  $D$  is the effective diffusion coefficient and  $l$  is the size of a lattice unit. There are 6 neighboring sites to which the radical can move. If a radical is positioned one lattice site outside the lattice boundary, only one of its neighboring sites is part of the lattice. Thus, on average, 1/6 of the radicals in those positions will move into the lattice. The number of radicals diffusing into the lattice per unit time is then  $n_{rad} = C_{rad} \times V / 6 \tau$ , where  $C_{rad}$  is the global concentration of radicals in the melt and  $V = 6(Nl)^2$  is the volume represented by a slab one-lattice-site thick around the outside of the lattice boundaries. Estimations of  $C_{rad}$  and  $D$  were required in order to calculate  $n_{rad}$ .

The effective diffusion coefficient of radicals is a result of the combined effect of the mobility of polymer chains and segments and the reaction of radicals with occupied neighboring sites. The diffusing species is the radical reactive center and can move from molecule to molecule by reaction. This means that a radical center can "diffuse" even when the molecules bearing it are fixed.

The effective diffusion coefficient was therefore related not only to the physical characteristics of the system, through its transport properties (i.e. viscosity, molecular weight, crosslinks) but to its chemical structure as well. It was evaluated by placing a radical in the center of the reactive lattice and performing the simulation disabling initiation and termination chemistry. The average distance travelled,  $\bar{d}$ , by the radicals in a time  $t = 1$  second was recorded, and the diffusion coefficient was calculated by assuming the radical performed a random walk. In such a case,  $D = \pi \bar{d}^2 / 16 t$  or  $\bar{d}^2 / 6 t$ .

Finally, the evaluation of the rate of radicals diffusing into the lattice requires the knowledge of  $C_{rad}$ , the global concentration of radicals in the melt. The theory of reactions in solution as well as the pseudo-steady state approximation were applied to evaluate  $C_{rad}$  *a priori*, as described in detail elsewhere [39].

The final result is shown in Eq. 1, where  $[SO_2]$  is the concentration of unreacted  $SO_2$  linkages.

$$C_{rad} = \left( \frac{k_{init} k_d}{k_{term}} [-SO_2] \right)^{1/2} \quad (1)$$

The rate of diffusion of radicals into the lattice was thereby determined as a function of the physical and chemical characteristics of the real system and of the simulation parameters (i.e. grid size).

An event-space simulation is performed to calculate the time and nature of the next initiation event. The list of possible events includes the scission of any of the  $N_{SO_2}$  sulfonyl linkages and the diffusion of a radical into the lattice. The total rate constant for radical generation is then  $k_{rg} = N_{SO_2} k_{init} + n_{rad}$ . The time interval between the present time and the next event,  $\tau$ , is determined according to the algorithm described elsewhere [36]. A random number, RN, is then drawn to determine which event occurred. If  $RN < N_{SO_2} k_{init} / k_{rg}$ , a sulfonyl linkage, chosen at random, breaks, generating two radicals. Otherwise, an occupied position selected at random on the lattice boundary is modified to become a radical (i.e. if the occupied position is a benzene ring, it is changed to a phenyl radical or a cyclohexadienyl radical, or to a phenoxy radical if it has phenoxy substituents), to represent the generation of an active center via diffusion. The reaction time was at this point updated by adding  $\tau$  to the current time.

Once reactive intermediates appeared in the lattice they could undergo a series of faster radical-molecule, radical-radical or  $\beta$ -scission reactions.

**Propagation reactions.** Propagation reactions can be strongly affected by segmental mobility. A fixed time step approach [37, 39] was used to simulate the reactions of radicals with their environment. A radical can react with any of its nearest neighbors to which it is not connected.

In the general case  $n$  reactions will be possible for a given radical. The probability for reaction  $i$  to occur is given by Equation (2):

$$P_i = \frac{k_i}{\sum_j k_j} \left( 1 - \exp \left( - \sum_j k_j \Delta t \right) \right) \quad (2)$$

The possible transitions and their associated probabilities are computed according to the environment of the radical and the energetics of elementary steps listed in Part 1. However, for bimolecular reactions, the reactants must come within one lattice unit of each other before they can react. Following the "reactions in solution" formalism, it is justified to say that they must form an encountered pair of reactant, A:B\*, for them to react. Chemical transformation of this pair is best described by a first-order process, the disappearance of the species identified as "an encountered pair of reactants". In short, the rate constants of Part 1 and the "reactions in solution" formalism [23,25,28] were reconciled

[39] to determine the transition probability for this first order process. The final result is  $k_{\text{first Order}} = \nu \rho \pi e^{-E^*/RT} = \frac{4}{3} \pi \rho^3 L A_{\text{second Order}} e^{-E^*/RT}$ , where the second order reaction and that of the encountered pair have the same activation energy.

To implement the simulation, the occurrence and nature of a reaction was determined through the algorithm for parallel reactions [37,39]. A random number,  $RN_i$ , was compared to the probability  $P_i = \left( 1 - \exp \left( - \sum_j k_j \Delta t \right) \right)$  that a radical  $i$  reacts. If reaction occurs a second random number determines its nature. The state of the lattice is then updated, and the random number  $RN_i$ , the rate constant of the reaction that did occur and  $\sum_j k_j$  are kept in memory. The same procedure is applied to all the radicals present in the lattice. The formalism of reactions in series [37,39] was used to account for the fact that several reactions in series can occur in  $\Delta t$ . If radical  $i$  reacts in the time interval to yield another radical (it does not terminate or "escape" from the grid), the new radical is tested for reaction. This procedure is repeated until no further reaction occurs.

Once all radicals have been checked for reaction in  $\Delta t$ , the reaction time is updated by adding  $\Delta t$  to the current time. A new time step is allowed to pass or new radicals are generated in the lattice depending on the status of the lattice. When the reaction time reaches predetermined output times, the status of the grid is recorded. Results of several Markov Chains are averaged to yield statistically significant numbers.

#### OUTPUT OF THE SIMULATION

The simulation results are recorded to allow for comparison with laboratory kinetics experiments. The computer "experiment" is the average of the results of  $N$  Markov Chains, for which results were recorded after 0-30 minutes of simulated reaction time.

The output of the simulation summarizes the detailed chemical structure and connectivity of the polymeric system as a function of reaction time. The attributes of the system are described in fractions (sol fraction, gel fraction, fraction of crosslinked monomers), averages (average molecular weight, average number of OH groups per monomer) or distributions (sol fraction molecular weight distribution, distribution of number of linkages per monomer).

The choice of attributes is often determined by the desired comparison with laboratory experiments, as is the case for the gel, sol and gas fractions. However, attributes unavailable from laboratory experiments may present considerable importance in the understanding of the underlying fundamentals. For example, the fraction of crosslinked monomers can be used to evaluate the validity of the Flory-Stockmayer model assumptions.

The quantities recorded for the present simulations were: distribution of monomer types (benzene rings, cyclohexadienes, cyclohexenes, cyclohexanes); total number of linkages; fraction of sulfonyl, ether and biphenyl linkages; fraction of monomers with one, two, three, and four linkages; gas, sol and gel fractions; number-average and weight-average molecular weight and degree of polymerization of the sol fraction; sol fraction molecular weight distribution; gas fraction composition; number of OH groups per monomer; number of chain ends; number of  $\text{SO}_2\text{H}$  groups per monomer; total number of radicals generated in the lattice.

Most of the foregoing quantities are determined by simple inspection of the lattice. Determination of gel, sol and gas fractions from the simulated pyrolysis requires more attention. Experimentally, these fractions are related to the solubility protocol used: the gas fraction is the portion of the mixture that is volatile at room temperature and one atmosphere total pressure; the gel fraction is the portion insoluble in a suitable solvent or any molecule unable to pass through a 5  $\mu$  micro-fiberglass filter; the sol fraction is the rest of material. The determination of the gel fraction was by making the conceptual link that the gel fraction corresponded to the portion of polymer that is insoluble in a solvent that dissolves linear polymers of same chemical compositions. The existence of a gel implies, according to Flory [1], the presence of an infinite network of crosslinked material.

#### SIMULATION RESULTS

Model predictions are presented in terms of temporal variation of average structural parameters and the yields of solubility-based product fractions from simulated poly(arylether sulfone) pyrolyses. The results presented here are the output of the simulation performed on a three-dimensional square grid of dimension 40 x 40 x 40.

## PRODUCT FRACTIONS

The determination of products belonging to the gel fraction, the sol fraction or the gas fraction was made according to the rules described above. Calculating the weight of each monomer and its associated linkages, summing these for the gel and sol fractions, and dividing by the total weight of all particles in these two fractions enabled prediction of the weight yield of the sol and gel fractions from simulated pyrolyses.

Figure 1 presents the temporal variations of the sol and gel product fractions for simulated pyrolysis at 425°C. The gel fraction shows a general increase with time, and the sol fraction shows the complementary decrease with time. A small fraction of gel is formed at times < 500 s, but a dramatic increase occurs at 500 s, where the gel fraction increases sharply to slightly greater than 20%. This can be qualitatively likened to the existence of a gelation point which has been reported during experimental polymer pyrolyses. The small fluctuations in the gel fraction prior to the dramatic increase can be attributed to computational factors. The simulation allows for bond-breaking initiations at all time steps. Chains already considered to be a part of the gel fraction can undergo chain scission at later reaction stages and therefore may no longer satisfy the percolation and crosslinking requirements for gelation. The frequency of this occurring is very small, however, and, in any event, dampens as the number of Markov Chains increases.

The yields of sulfur-containing product gases, H<sub>2</sub>S and SO<sub>2</sub>, from the simulated pyrolysis are shown in Figure 2. The percent yield is based on the amount of sulfone linkages contained in the reactant poly(arylether sulfone). The yield of SO<sub>2</sub> increases linearly with time and reaches an ultimate value of 4% after 1100 s of simulated reaction time. The percentage of H<sub>2</sub>S formed is much lower and achieves a value of only 0.1% after 1100 s of reaction time. The balance of the sulfur would remain in the gel or sol fraction as SO<sub>2</sub> linkages between monomers.

## STRUCTURAL PARAMETERS

The model explicitly monitored the length of each chain (number of monomeric units) and the type and number of links for each of the monomers. This information could be assembled to specify values of average structural parameters for the entire polymer or any of its product fractions.

The number average degree of polymerization,  $\bar{x}_n$ , for the sol product fraction as a function of time is presented in Figure 3. The value of  $\bar{x}_n$  is defined in the simulation as:

$$\bar{x}_n = \frac{\sum_i \text{number of chains of degree of polymerization } i \times i}{\text{total number of chains}}$$

where  $i=1$  would represent one unit in the polymer chain where a unit is taken to be a single benzene-derived ring or, in simulation terms, one grid point. Note that the value of  $\bar{x}_n$  continually decreases, exhibiting a value of 108 at the initial time and decreasing to an ultimate value of 20 at 1100 s. Chain scission and crosslinking have opposing effects on the value of  $\bar{x}_n$ . However,  $\bar{x}_n$  is particularly sensitive to the proportion, by number, of shorter chain lengths, and therefore exhibits the generally decreasing trend.

In the region of 500 s, there is a marked decrease in the value of  $\bar{x}_n$ . This is the point when a significant portion of gel fraction forms and the large, crosslinked chains no longer contribute to the value of  $\bar{x}_n$  for the sol fraction. The time at which this occurs is simultaneous with the point considered to be the gelation point in the gel fraction versus time curve presented above.

The temporal variation of the weight average degree of polymerization,  $\bar{x}_w$ , is shown in Figure 4. The definition of  $\bar{x}_w$  used in the simulation is:

$$\bar{x}_w = \frac{\sum_i \text{number of chains of degree of polymerization } i \times i^2}{\sum_i \text{number of chains of degree of polymerization } i \times i}$$

The value of  $\bar{x}_w$ , in contrast with the value of  $\bar{x}_n$ , increases with time in the initial stages of reaction. The weight average degree of polymerization is particularly sensitive to the presence of larger chain lengths, and therefore, the effect of crosslinking dominates over chain scission. The sharpest rise occurs in the region of 450 s followed by a sharp decline. This corresponds to the region, identified earlier as a gelation point. Here the infinite chains in the gel no longer contribute to any parameters measured in the sol fraction. In the later stages of reaction, more of the material is contained in the gel fractions, and the sol fraction is composed of small chains which gives rise to a small ultimate value of  $\bar{x}_w$ .

All of the results presented are for the reaction at 425°C of a poly(arylether sulfone) with a single initial degree of polymerization. We are just beginning to use the model to explore other polymers and conditions. The object of this report was to describe and record the approach and methodologies used. The agreement between model predictions and experimentally observed temporal variations of the yields of product fractions and the values of structural parameters will be assessed quantitatively in a follow-up communication.

## CONCLUSIONS

1. Poly(arylether sulfone) structure, reactions, and diffusion can be described quantitatively in terms of a dynamic reaction lattice.
2. Model compound kinetics provide a basis for modelling the bond-breaking and bond-forming reactions of poly(arylether sulfones).
3. Gelation was associated with the attainment of a spanning cluster on the lattice. The gel fraction was sensitive to the fraction of bonds formed, as in polymerization.
4. The model represents a flexible computer experiment for testing the influence of processing conditions.

## REFERENCES

1. Flory, P. S., *Principles of Polymer Chemistry*, Cornell University Press, Ithaca and London, 1953.
2. de Gennes, P. G., *Phys. Lett. A*, **38**, pp. 339-42, 1972.
3. de Gennes, P. G., *J. Physique*, **36**, pp. 1049-54, 1975.
4. Stauffer, D., *J. Chem. Soc. Faraday Trans II*, **72**, pp. 1354-64, 1976.
5. Stauffer, D., *Introduction to Percolation Theory*, Taylor and Francis, London and Philadelphia, 1985.
6. Coniglio, A., Starly, H. E., Klein, W., *Phys. Rev. Lett.*, **42**, pp. 518-22, 1979.
7. Earnoux, B., *Ann. Phys. Paris* **1**, pp. 73-141, 1976.
8. Lubensky, T. C. and Isaacson, S., *Phys. Rev. Lett.*, **41**, pp. 829-32, 1978.
9. Coniglio, A., Daout, M., *J. Phys. A: Meth. Gen.*, Vol. **12**, No. **10**, 1979.
10. Gonzalez, A. E., Daout, M., *J. Phys. A: Meth. Gen.*, **14**, pp. 2441-2457, 1981.
11. Stockmayer, W. H., *J. Chem. Phys.*, **11**, 45, 1943.
12. Stockmayer, W. H., *J. Chem. Phys.*, **12**, 125, 1944.
13. Gordon, M., *Proc. R. Soc. A.*, **268**, 240, 1962.
14. Gordon, M. and Malcolm, G. N., *Proc. R. Soc. A.*, **295**, 29, 1966.
15. Gordon, M. and Ross-Murphy, S. B., *Pure and Appl. Chem.*, **43**, **1**, 1975.
16. Gordon, M. and Scontlebury, G. R., *Proc. R. Soc.*, **292**, 380, 1966.
17. Weiss, G. H. and Rubin, R. J., "Random Walks: Theory and Applications," *Advances in Chemical Physics*, **52**, 1983.
18. Domb, C., *Adv. Chem. Phys.*, **15**, 229, 1969.
19. McKenzie, *Phys. Rep.*, **27C**, 35, 1976.
20. de Gennes, P. G., *Scaling Concepts in Polymer Physics*, Cornell University Press, Ithaca, N.Y., 1979.
21. Rudnick, J. and Graspari, G., *Science*, **237**, 1987.
22. Brown, J. R. and O'Donnell, J. H., "Effects of Gamma Radiation on Two Aromatic Polysulfones. II. A Comparison of Irradiation at Various Temperatures in Air-Vacuum Environments," *J. Appl. Polym. Sci.*, **23**, pp. 2763-2775, 1979.
23. Moore, J. W. and Pearson, R. G., *Kinetics and Mechanics*, John Wiley and Sons, New York, 1981.
24. Troe, J., *J. Phys. Chem.*, Vol. **90**, no. **30**, 1980.
25. Rabinowitch, E., *Trans Faraday Soc.*, **32**, 1381, 1936.
26. Fowler, R. H. and Slatev, N. B., *Trans Faraday Soc.*, **33**, 1185, 1937.
27. North, A. M., *The Collision Theory of Chemical Reactions in Liquids*, Methuen, London, 1964.
28. Smoluchowski, M. V., *Phys. Z.*, **17**, 1917.
29. Moelign-Hughes, E. A., *The Kinetics of Reactions in Solutions*, The Clarendon Press, Oxford, 2nd ed., 1947.
30. Noyes, R. M., *J. Am. Chem. Soc.*, **86**, 4529, 1964.
31. Noyes, R. M., *Prog. React. Kinet.*, **1**, 129, 1961.
32. Caldin, E. F. and Hasinoff, B. B., *J. Chem. Soc., Faraday Trans. I*, **71**, 515, 1975.
33. Trommsdorff, E., Kohle, H., Lagelly, P., *Makromolec. Chem.*, **1**, 169, 1948.
34. Tulig, T. J. and Tinell, M., *Macromol.*, **15**, 459, 1982.
35. Tulig, T. J. and Tinell, M., *Macromol.*, **14**, 1501, 1981.
36. Rohr, D. and Klein, M. T., *I&EC Research*, **29**, 1210, 1990.
37. McDermott, J. B., Libanati, C., LaMarca, C. and Klein, M. T., *I&EC Research*, **29**, p. 22, 1990.
38. Rose, J. B., "Preparation and Properties of polyarylene ether sulphones," *Polymer*, **15**, pp. 456-465, 1974.
39. Libanati, C., Ph.D. Thesis, University of Delaware, Newark, DE, 1990.

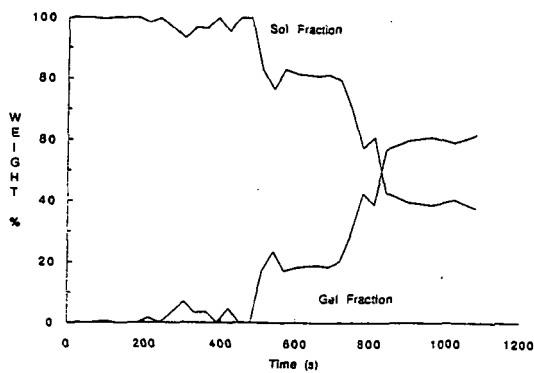


Figure 1. Temporal variation of gel and sol product fractions at 425°C from simulated poly(arylether sulfone) pyrolysis.

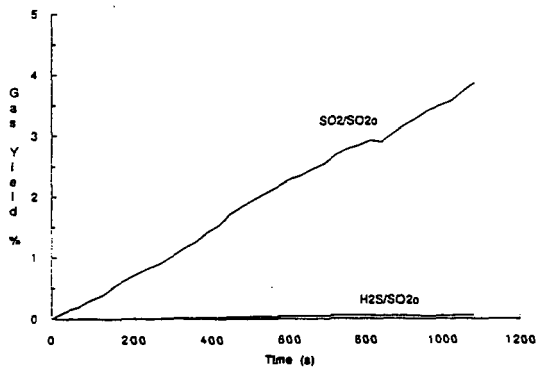


Figure 2. Temporal variation of sulfur-containing gas fraction at 425°C from simulated poly(arylether sulfone) pyrolysis.



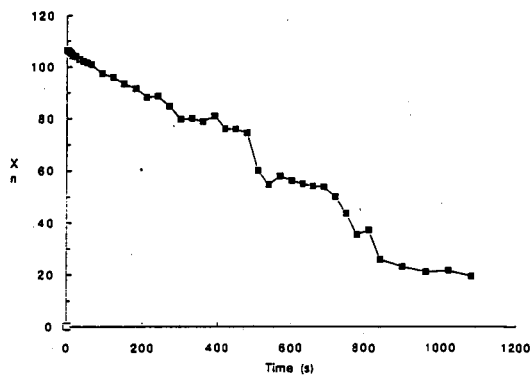


Figure 3. Temporal variation of number average degree of polymerization of sol fraction at 425°C from simulated poly(arylether sulfone) pyrolysis.

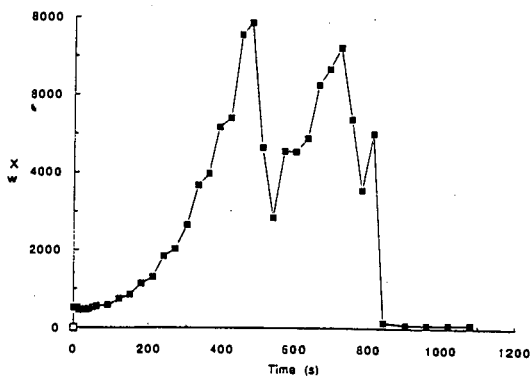


Figure 4. Temporal variation of weight average degree of polymerization of sol fraction at 425°C from simulated poly(arylether sulfone) pyrolysis.

## PYROLYSIS OF PHENOL-FORMALDEHYDE RESIN: EXPERIMENTS AND MODELING

Michael A. Serio, Sylvie Charpenay, Rosemary Bassilakis, and Peter R. Solomon

Advanced Fuel Research, Inc.  
87 Church Street  
East Hartford, CT 06108

**Keywords:** Pyrolysis, Phenol-Formaldehyde Resin, Modeling

### INTRODUCTION

Fires kill nearly 10,000 people each year in the U.S. and cause nearly 300,000 injuries and over 6 billion dollars in property damage (1). Consequently, there is a great need for additional research on fires and fire safety. While non-polymeric materials (e.g., cooking fat) are the main sources of ignition, natural and synthetic organic polymers are most frequently the materials which are primarily responsible for the propagation of fires (2). To describe the pyrolytic degradation of a burning polymer, one needs to know the chemical reactions and rates for the bridge breaking (depolymerization) and crosslinking (repolymerization) reactions. But these reactions typically occur within a crosslinked macromolecular network, so their effects in fragmenting the macromolecule must be treated statistically. In addition, the effects of heat and mass transport within a material undergoing phase changes (solid to liquid and gas) must also be included. While statistical methods have been applied to the polymerization processes (3,4), such models have not been as well developed for the degradation processes, particularly for charring polymers.

This study is based on two techniques, one theoretical and one experimental which have resulted from research during the past ten years by Advanced Fuel Research, Inc. (AFR) on the pyrolysis of coal, a natural polymer. This work has led to development of a macromolecular network model to describe the thermal decomposition of coal (5-10). To develop this model, we have determined the rates and mechanisms for depolymerization, crosslinking, and the formation of char, tar, and gases. These processes are imposed upon a sample macromolecular network constructed in a computer, and Monte Carlo (or Percolation Theory) methods are used to determine the molecular weight of the network fragments as the population of bonds and crosslinks changes. The model includes a model for viscosity (melting) based on the molecular weight distribution of the macromolecular fragments. In addition to predicting the molecular fragments, the evolution of gas species is predicted from the thermal decomposition of peripheral functional groups in the network. The combined model has been called the FG-DVC model, which stands for Functional Group - Depolymerization, Vaporization and Crosslinking model. The FG-DVC model has been validated using literature data and data obtained in our laboratory (8-10).

The work on coal pyrolysis has also led to the development of a new instrument called the TG-FTIR which integrates a thermogravimetric analyzer (TGA) with an FT-IR for enhanced gas analysis (11-13). The TG-FTIR system provides kinetic information on the weight loss and volatile products used for validation of the FG-DVC model.

The modeling (FG-DVC) and experimental (TG-FTIR) techniques were applied to pyrolysis of phenol-formaldehyde (P-F) resin, which is an example of a charring polymer. Currently, these types of polymers present the most difficulty as far as predicting their behavior in a fire. Charring polymers are also of increasing importance because they have inherently higher flame retardance properties than non-charring polymers. The thermal decomposition of P-F has been the subject of numerous literature studies because of its commercial importance, which also makes it a good candidate for development of new models and techniques (14-24). Finally, the behavior of P-F is similar to coal in many respects and it has been used as a model system for coal (25-29).

## EXPERIMENTAL

### Apparatus

Details of the TG-FTIR method appear elsewhere (11-13). The apparatus consists of a sample suspended from a balance in a gas stream within a furnace. As the sample is heated in a helium flow, the evolving volatile products are carried out of the furnace directly into a 5 cm diameter gas cell (heated to 150°C) for analysis by FT-IR. The FT-IR can obtain spectra every 0.2 s to determine quantitatively the evolution rate and composition of several hydrocarbon compounds. The system allows the sample to be heated on a pre-programmed temperature profile at rates between 3°C min<sup>-1</sup> and 100°Cs<sup>-1</sup> up to a temperature between 20 and 1000°C and held for a specified time. The system continuously monitors: 1) the time-dependent evolution of the gases (including specific identification of the individual species such as, CH<sub>4</sub>, C<sub>2</sub>H<sub>6</sub>, C<sub>2</sub>H<sub>4</sub>, C<sub>2</sub>H<sub>2</sub>, C<sub>3</sub>H<sub>8</sub>, benzene, etc.; 2) the heavy liquid evolution rate and its infrared spectrum with identifiable bands from the functional groups; and 3) weight of the non-volatile material (residue). An analysis of C, H, N and S in the residue at the end of the pyrolysis experiment can be obtained by introducing oxygen to burn the residue and analyzing the combustion products.

### Sample

Phenol-Formaldehyde (P-F) resins are products of the condensation of phenols with aldehydes (usually formaldehyde) and represent an important group of thermosetting resins. The synthesis procedure for P-F resins is illustrated in Fig. 1a, along with a representative structure. The structure used in the simulation of P-F behavior in the FG-DVC model is shown in Fig. 1b.

These resins are classified in two basic types: novolaks (produced with acid catalysts and an excess of phenol) and bakelites or resols (produced with basic catalysts and an excess of aldehyde). Novolaks are linear polymers with molecular weights of 1000-1500 amu. These are not initially crosslinked and are fusible and soluble. Conversely, bakelites have short chains and are highly crosslinked insoluble resins. An advantage to working with bakelites is that, by adjusting the ratio of phenol to formaldehyde, non-linear polymers with different degrees of crosslinking can be obtained.

The sample of phenol-formaldehyde resin used in the current study was a bakelite and was obtained from Professor Eric Suuberg of Brown University. It was synthesized using NH<sub>4</sub>OH catalyst, with a formaldehyde-to-phenol ratio of 4.33. The curing procedure was done in three stages: a) 2 hours at 60°C in vacuum; b) 12 hours at 120°C in vacuum; c) 2 hours at 300°C in helium.

### Analysis

The FG-DVC model inputs require information from elemental, FIMS, solvent swelling/extraction and TG-FTIR, as shown in Fig. 2. The P-F resin was subjected to elemental analysis at Huffman Laboratories (Golden, CO). The results on a daf basis were C: 76.6, H: 5.5, O: 17.8, N: 0.1.

A sample of the P-F resin was sent for analysis in the Field Ionization Mass Spectrometer (FIMS) apparatus at Stanford Research Institute (30). The Field Ionization induces little fragmentation and so provides a determination of the sample's molecular weight. The FIMS analysis is done by a programmed pyrolysis of the material into the inlet of the mass spectrometer (held at vacuum). The mass spectra are taken at regular intervals so that the evolution of individual compounds can be tracked as a function of temperature. The FIMS technique provides detailed insight into the tar formation (and indirectly the char formation) processes. The formation of tar is key to the prediction of polymer combustion properties since it impacts the ignition, soot formation, smoke formation, and char formation.

The sample of P-F resin was extracted with pyridine at the boiling point to obtain the amount and composition of the extract. A portion of the dried, extracted solids was also swelled in pyridine in order to determine the volumetric swelling ratio (VSR). This solvent swelling measurement was carried out according to the method of Green, Kovac and Larsen (31,32). The value of the VSR can be used in the FG-DVC model to determine the starting value of the molecular weight between

crosslinks. However, this requires an assumption of the monomer molecular weight. It is more convenient to use the pyridine extractables amount which is determined from the same experiment.

## RESULTS

Pyrolysis experiments were performed on the P-F sample using the TG-FTIR apparatus (11-13) over a range of heating rates (3-100°C/min). Figure 3a illustrates the weight loss, the sum of the evolved products, and the temperature history for a 20 mg sample taken on a 30°C/min temperature excursion, first to 150°C to dry for four minutes and then to 900°C for pyrolysis.

During the excursion, infrared spectra are obtained once every 41 s. The spectra show absorption bands for CO, CO<sub>2</sub>, CH<sub>4</sub>, H<sub>2</sub>O, SO<sub>2</sub>, COS, C<sub>2</sub>H<sub>4</sub>, and NH<sub>3</sub>. The spectra above 250°C also show aliphatic, aromatic, hydroxyl, carbonyl, and ether bands from tar. The evolution of gases derived from the IR absorbance spectra are obtained by a quantitative analysis program that employs a database of integration regions and calibration spectra for different compounds (11-13). Figure 3b through 3f illustrate the evolution rates and integrated amounts evolved for H<sub>2</sub>O, tars, CO<sub>2</sub>, CH<sub>4</sub>, and CO respectively. Because the data are quantitative, the sum of the evolved products matches the weight loss as determined by the TGA balance.

Pyrolysis of phenol formaldehyde resin in the TG-FTIR apparatus led to the formation of tar, CO, CO<sub>2</sub>, CH<sub>4</sub>, and H<sub>2</sub>O as illustrated in Fig. 3. The product mix and evolution profiles are consistent with previous studies on the thermal degradation of this material (14-24). CO evolved in two distinct peaks, one before tar evolution (450°C at 30°C/min), the other after tar evolution (620°C at 30°C/min). The CO<sub>2</sub> evolution rate peaked at approximately the same temperature as the first CO peak, while the CH<sub>4</sub> evolution rate was a maximum at roughly the same temperature as the second CO peak. Water evolution occurred at the same time as tar evolution for all heating rates. A composite species evolution plot from the TG-FTIR analysis of phenol formaldehyde at 30°C/min is shown in Fig. 4a.

The overall pyrolysis behavior of phenol formaldehyde is very similar to that of Wyodak subbituminous coal. The elemental compositions of these materials are similar although the bridging groups between the aromatic rings are different. A composite species evolution plot from the TG-FTIR analysis of Wyodak coal is shown in Fig. 4b. In both cases, there is a CO<sub>2</sub> peak prior to tar evolution, a CH<sub>4</sub> peak following tar evolution, and a water peak at the same temperature as tar. The amount of tar is also comparable: about 12% for phenol formaldehyde and 9% for Wyodak. The only significant difference between the gas evolution of the two samples is for CO, since all of the CO evolves after the tar peak for Wyodak while there is an early peak before tar evolution in the case of phenol formaldehyde. The similarity of the evolution profiles and the char yields for the two materials provides support for the idea of using a model developed for coal (FG-DVC) to describe a synthetic polymer (P-F). Of course, it is also true that the similarity in the product yields does not guarantee that the decomposition mechanisms are the same. However, the model has the flexibility to incorporate these different mechanisms, as discussed below.

## MODELING

The FG-DVC model was originally developed based on a polymeric representative of coal which is aromatic clusters connected by weak (ethylene) bridges and which also include functional groups such as carboxyl or methoxy which promote crosslinking and/or lead to gas evolution. The depolymerization occurs by random, homolytic cleavage of the weak bridges (8-10).

Phenol-formaldehyde resin is also a charring polymer which decomposes by random degradation with crosslinking. The system does not produce many volatile products, and there is formation of char after complex crosslinking reactions. It is the nature of the depolymerization and crosslinking reactions which is different for P-F resin than for coal.

### Model Implementation

The implementation of the FG-DVC model for a specific polymer system requires the specification of several parameters, some of which are constrained by the known polymer structure and some of

which are constrained by experimental characterization data. A flow diagram of the model inputs and outputs is given in Fig. 2. The basic idea is to validate the model using simple small scale experiments like TG-FTIR, FIMS, solvent swelling, and elemental analysis and then use the model to make predictions for conditions where experimental data are not readily available such as at high heating rates. This approach has been highly successful in using the FG-DVC model to make predictions for pyrolysis of coal under combustion conditions at high heating rates using a model that was validated using low heating rate TG-FTIR and fluidity data (33).

**Network Polymers** - First, the polymer network has to be defined. This requires specification of the following parameters: monomer units and subunits, the types of bridges and the fraction of breakable vs. unbreakable bridges, the number and type of peripheral groups, and number of initial crosslinks (unbreakable linkages at branch points in the polymer chains). Since synthetic polymers usually have a regular and repetitive structure, they can often be represented in the model by monomers (a monomer being the smallest repetitive unit) linked by a single type of bridge. Depending on their complexity, monomers can be described as being composed of submonomers of different types, which are linked together by either labile (breakable) or unbreakable bridges. The reason for including submonomers is to describe more accurately the structure.

In the case of polymer resins like phenol formaldehyde, the structure is not necessarily a unit which repeats over a short length scale as shown in Fig. 1a. Consequently, some average structures must be written (as shown in Fig. 1b). This is even more true in the case of coal where the repeating unit is purely a statistical quantity.

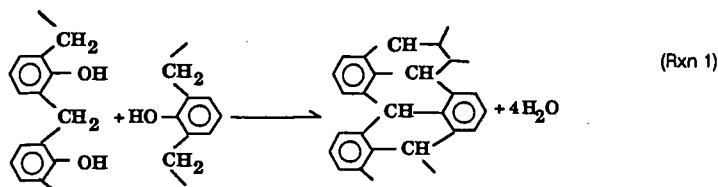
Once the monomer units and subunits have been established, the parameters of the network are then defined through the mass of monomers, submonomers, labile bridges, and unbreakable bridges. Once the polymer network has been specified, the next step is to specify the depolymerization reactions, crosslinking reactions, and gas forming reactions. This is done based on the known polymer structure and literature work.

**Depolymerization Reactions** - Phenol-formaldehyde is an example of a polymer constructed by joining aromatic units with labile (methylene) bridges. Usually, single atom bridges between aromatic rings are not very labile. However, the ortho situated hydroxyl group activates the decomposition of the methylene linkage due to a keto-enol tautomerism (34).

The depolymerization process, done by breaking labile bridges, can be performed with hydrogen abstraction from either other labile bridges, if those can give hydrogen, or other possible hydrogen donor species in the polymer, such as the aromatic rings. In the latter case, all the bridges can be broken, while in the former case, only part of them are actually broken. The choice of depolymerization process is based on the hydrogen availability in the polymer. Currently, the model does not include hydrogen transfer along the chain since this is not usually important for aromatic polymers. The weight of the evidence from the literature suggests that, for the depolymerization of phenol-formaldehyde, hydrogen donation occurs from other methylene bridges (14-24).

**Crosslinking Reactions** - In the case of charring polymers, an important reaction to model is the crosslinking of the polymer. In the version of the FG-DVC model used for coal, crosslinking reactions are related to gas evolution, in particular  $\text{CO}_2$  and  $\text{CH}_4$  (8,9,35). It seems obvious that, in the case of polymers, these gases might also be related to crosslinking events, along with other gases as well. As discussed above, phenol formaldehyde has a behavior very close to coal. The same types of gases evolve ( $\text{CO}_2$ ,  $\text{CH}_4$ ,  $\text{CO}$ ,  $\text{H}_2\text{O}$ ) and the total weight loss is comparable to coal's weight loss. However, the most probable crosslinking reaction in phenol formaldehyde involves  $\text{H}_2\text{O}$  evolution (16) as discussed below and in Ref. 36. The crosslinking efficiency, i.e., the number of crosslinks introduced per mole of gas evolved, is an adjustable parameter of the model.

In the case of phenol formaldehyde, one of the possible crosslinking reactions involves elimination of a labile bridge at the crosslink site.



In our nomenclature, we reserve the term crosslinks to refer to bonds which cannot be broken during the preliminary pyrolysis stages ( $< 600^{\circ}\text{C}$ ) such as C-C aryl linkages. For example, the methylene linkages between the phenolic groups in phenol-formaldehyde would not be considered crosslinks in our model because these can be broken at relatively low temperatures because of the activating mechanism of the ortho situated hydroxyl groups, discussed above. Conversely, the formation of an ether link by the reaction of two hydroxyls (discussed below) may act as a crosslink under primary pyrolysis conditions because the reaction also removes this activating mechanism.

The difference between crosslinks and unbreakable bonds in the model is as follows: crosslinks are unbreakable bonds which act as branch points (divergence of two chains) while unbreakable bonds are part of a linear chain. This distinction is made in Fig. 1b where examples of a crosslink (X.L.) and hardbond (H.B.) are shown.

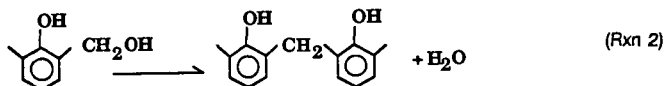
**Gas Evolution** - For aromatic polymers, the gas evolution occurs from decomposition of peripheral groups including bridge structures. In the FG-DVC model, these groups are distributed based on the known polymer composition using a mixture of functional group sources (6,7). This is the "FG" part of the model. The specific mechanisms of gas evolution have not been input into the model with the same level of detail as the char and tar formation (treated in the "DVC" part of the model). It has been found that the absence of detailed gas formation mechanisms has not prevented us from accurately predicting gas formation from coal over a wide range of heating rates ( $0.05^{\circ}\text{C/s}$  -  $20,000^{\circ}\text{C/s}$ ) (9,33). It is expected the same will be true of phenol-formaldehyde, although we do not yet have the high heating rate data to verify this assumption.

**Experimental Inputs** - The next step in setting up the model is to use experimental data to further constrain the model. This is shown schematically in Fig. 2. For polymers, with a regular repeating structure, there are obviously no adjustments required to match the elemental analysis data. However, for polymers with an irregular repeating structure, like phenol formaldehyde, the peripheral groups and bridge structures are distributed statistically and must be in agreement with known structures based on FT-IR and elemental analysis data.

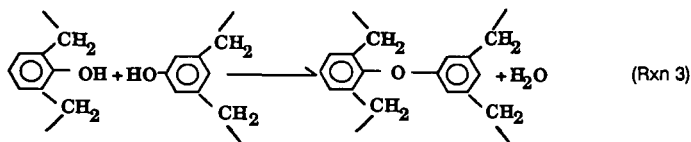
A second experimental input required for polymers which have an indefinite structure is the number of starting crosslinks. This can be based on either the volumetric swelling ratio or the pyridine extractables as discussed above.

### Simulations of Phenol-Formaldehyde Pyrolysis

A literature review showed that several reactions involving water elimination might lead to the formation of crosslinks. The fact that we observe in the TG-FTIR analysis a water peak at  $200\text{-}300^{\circ}\text{C}$  (see Fig. 3b) (which is a temperature range too high for moisture) might indicate that crosslinking reactions have occurred during low temperature pyrolysis. Reaction 2 is a curing reaction which occurs at low temperature and forms water.



However, a methylene bridge formed ortho to a hydroxyl group would not act as a crosslink under primary pyrolysis conditions. Reaction 1 (see above) is a possible pathway to produce crosslinks at low temperatures (16). Reaction 3 is also thought to occur at relatively low temperatures, although the extent of the reaction and its temperature range are subject to debate between researchers.



An ether linkage formed in this manner could act as a crosslink under primary pyrolysis conditions.

Since several reactions can lead to the production of water, it is not likely that every water molecule evolved corresponds to a crosslink. Different test cases showed that a value of 0.5 for the crosslinking efficiency of  $\text{H}_2\text{O}$  seems to be the best choice. One of the crosslinking reactions (Reaction 1) takes place between the  $-\text{OH}$  of a phenol and a methylene bridge, thus removing a labile bridge. To take this into account, we also included in the model, for every new crosslink formed, a reaction transforming a labile bridge next to the crosslink into an unbreakable bridge. Since it was not known *a priori* if Reaction 1 is the important pathway for crosslinking, simulations were done with this reaction and also with Reaction 3 as the main crosslinking reaction.

The network parameters (amount of available hydrogen, initial crosslink density, and starting oligomer length) were chosen to match the experimental value of pyridine extractables (0.8%) and the amount of tar from TG-FTIR experiments (12%). Although we did not make any fluidity (inverse viscosity) measurements on phenol formaldehyde, the network parameters were input into the fluidity model and the predictions are consistent with the fact that no melting was observed during pyrolysis of this material at low heating rates.

Two sets of assumptions were used in the pyrolysis simulations of phenol-formaldehyde. These assumptions are summarized in Table 1 as Case 1 and Case 2.

TABLE 1  
SUMMARY OF ASSUMPTIONS USED IN PHENOL-FORMALDEHYDE  
PYROLYSIS SIMULATIONS

	Number of Hard Bonds	Number of Initial Crosslinks	Crosslinking Reaction
Case 1	0	320	1
Case 2	600	320	3

For the first case, we considered that relatively few hard bonds were present in the original resin, since there is probably no condensation yet. A significant number of starting crosslinks was also necessary in order to have a 3-dimensional network, and also to limit vaporization of dimers, trimers, etc., since these are not present in the FIMS spectra (36). While there are no real crosslinks in the original phenol-formaldehyde structure (see Fig. 1a), these must be introduced during the curing process, perhaps by Reaction 1, since the curing is done up to relatively high temperatures (300°C). Having included the reaction transforming a labile bridge into unbreakable bridges when a crosslink is formed, we found that no initial hard bonds and approximately one branch point for every three monomers gave the best fit to the TG-FTIR data (see Figs. 5 and 6 and Table 1). The solid lines in Figs. 5 and 6 are the FG-DVC model predictions while the experimental data are represented as symbols connected by lines. Using an alternative crosslinking reaction (Reaction 3), more initial hard bonds (approximately one for every four bridges) were necessary, keeping the same crosslink density. This is Case 2 in Table 1. This rather high value of hard bonds (while we expect few original bonds) might indicate that there is a process of consumption of labile bridges in the polymer during curing or in the early stages of pyrolysis, since these would not be expected in the original structure. In both of these two cases, a narrow range in the network parameters was found to give the best fit. When either set of parameters was used in the model, the main features of the tar FIMS spectra were simulated (36).

The kinetic parameters for gases and tar were selected by fitting TG-FTIR evolution curves for different heating rates. The tar evolution was found to correspond to an activation energy of 51.4 kcal, which is very close to activation energies found in the case of coals (8-10). The overall rate is, however, lower than that for coals since the tar peak for phenol formaldehyde occurs at higher temperatures. A comparison of the product evolution data with the model predictions is given for two different heating rates in Figs. 5 and 6. Excellent agreement was obtained. Similar results were obtained for the Case 2 parameters. The gas predictions are not very sensitive to the choice of network parameters while the tar and char yields are sensitive. Case 1 is thought to be more realistic since it does not require the assumption of a large amount of starting hard bonds. Additional analysis of the cured P-F resin, such as by solid state  $C^{13}$ -NMR, would be required in order to definitely rule out Case 2.

Once the model has been fully validated, it can be used to make predictions for a different range of network parameters or a different range of experimental conditions. An example of this is shown in Fig. 7 where the effect of changing the starting number of crosslinks on the predictions for weight loss, tar evolution rate, and tar molecular weight distributions (MWD) are shown. The model predicts the correct trend in the change in the tar molecular weight distribution, tar yield, and weight loss with increasing initial crosslink density based on the results that have been obtained for coal (35).

## CONCLUSIONS

The main conclusions from this effort can be summarized as follows: 1) The TG-FTIR method can provide information on several aspects of polymer thermal decomposition behavior including kinetics and degradation mechanisms; 2) The FG-DVC model can be generalized to predict kinetics, product evolution, tar yields, and tar molecular weight distributions for phenol formaldehyde and other charring polymers over a wide range of conditions; 3) The key inputs required to model the decomposition of a charring polymer are the network parameters, depolymerization reactions, crosslinking reactions, and gas formation reactions; 4) The choice between two alternative crosslinking reactions may lead to a different choice of network parameters.

## ACKNOWLEDGEMENTS

This work was supported by the National Science Foundation under Phase I SBIR Grant No. ISI-8961476. The authors also acknowledge helpful discussions with Professor Eric Suuberg of Brown University, who also provided the phenol-formaldehyde resin sample.



## REFERENCES

1. Gann, R.G. and Dipert, R., "Polymer Flammability", Encyclopedia of Polymer Science and Engineering, John Wiley & Sons, NY, 1986.
2. Cullis, C.F. and Hirschler, M.M., The Combustion of Organic Polymers, Clarendon Press, Oxford, 1981.
3. Rodriguez, F.R., Principles of Polymer Systems, McGraw-Hill, New York, 1982.
4. Polymerization Kinetics and Technology, (N.A.J. Platzer, Ed.), American Chemical Society, Washington, 1973.
5. Solomon, P.R., "New Approaches in Coal Chemistry", ACS Symposium Series 169, American Chemical Society, Washington, DC, 1981, pp 61-71.
6. Solomon, P.R. and Hamblen, D.G., in Chemistry of Coal Conversion, (R.H. Schlosberg, Ed.), Plenum Press, NY, 1985, Chapter 5, pg. 121.
7. Serio, M.A., Hamblen, D.G., Markham, J.R., and Solomon, P.R., *Energy & Fuels*, 1(2), 138, (1987).
8. Solomon, P.R., Hamblen, D.G., Carangelo, R.M., Serio, M.A., and Deshpande, G.V., *Combustion and Flame*, 71, 137, (1988).
9. Solomon, P.R., Hamblen, D.G., Carangelo, R.M., Serio, M.A., and Deshpande, G.V., *Energy & Fuels*, 2, 405, (1988).
10. Solomon, P.R., Hamblen, D.G., and Yu, Z.Z., *Fuel*, 69, 754, (1990).
11. Carangelo, R.M., Solomon, P.R. and Gerson, D.J., *Fuel*, 66, 960 (1987).
12. Whelan, J.K., Solomon, P.R., Deshpande, G.V., and Carangelo, R.M., *Energy and Fuel*, 2, 65, (1988).
13. Solomon, P.R., Serio, M.A., Carangelo, R.M., Bassilakis, R., Gravel, D., Baillargeon, M., Baudais, F., and Vail, G., *Energy & Fuel*, (1990).
14. Symposium on Phenolic Resins, Parts I and II; Rept. Org. Coatings and Plastic Chem., 26, 85, (1966); and 27, 84, (1967).
15. Monographs in Macromolecular Chemistry: Thermal Stability of Polymers, (R. Conley, Ed.), Marcel Dekker, Inc., New York, 1970, Volume 1.
16. Yamashita, Y. and Ouchi, K., *Carbon*, 19, 89, (1981).
17. Honda, H. and Sanada, Y., *Fuel*, 36, 403, (1957).
18. Shulman, G.P. and Lochte, H.W., *J. Appl. Polymer Sci.*, 10, 619, (1966).
19. Ouchi, K. and Honda, H., *Fuel*, 38, 429, (1959).
20. Jackson, W.M. and Conley, R.T., *J. Appl. Polymer Sci.*, 8, 2163, (1964).
21. Conley, R.T. and Bieron, J.F., *J. Appl. Polymer Sci.*, 7, 103 and 171, (1963).
22. Conley, R.T., *J. Appl. Polymer Sci.*, 9, 1117, (1965).
23. Lochte, H.W., Strauss, E.L., and Conley, R.T., *J. Appl. Polymer Sci.*, 9, 2799, (1965).
24. Ouchi, K., *Carbon*, 4, 59, (1966).
25. van Krevelen, D.W., Coal, Elsevier, Amsterdam, 1961.
26. Suuberg, E.M., Wojtowicz, M., and Calo, J., 22nd Symposium (Int) on Combustion, The Combustion Institute, 1988, pg. 79.
27. Suuberg, E.M., Calo, J.M., and Wojtowicz, M., ACS Div. of Fuel Chem. Preprints, 31(3), 186, (1986).
28. Wojtowicz, M., Ph.D. Thesis, Brown University, (1988).
29. Wolfs, P.M., van Krevelen, D.W., and Waterman, H.I., *Fuel*, 39, 25, (1960).
30. St. John, G.A., Buttrill, Jr., S.E. and Anbar, M., ACS Symposium Series, 71, p. 223, (1978).
31. Green, T.K., Kovac, J., and Larsen, J.W., *Fuel*, 63, 935, (1984).
32. Green, T.K., Kovac, J., and Larsen, J.W., in Coal Structure, (R.A. Meyers, Ed.), Academic Press, NY, 1982.
33. Serio, M.A., Solomon, P.R., Charpenay, S., Yu, Z.Z., and Bassilakis, R., ACS Div of Fuel Chem. Preprints, 35(3), 808, (1990).
34. van Krevelen, P.W., *Chimia* 1974, 28, 504.
35. Solomon, P.R., Serio, M.A., Deshpande, G.V., and Kroo, E., *Energy & Fuels*, 4(1), 42, (1990).
36. Serio, M.A., Charpenay, S., Bassilakis, R., and Solomon, P.R., "A Statistical Network Model for Polymer Degradation", Final Report under NSF Grant No. ISI-8961476, (October 1990).

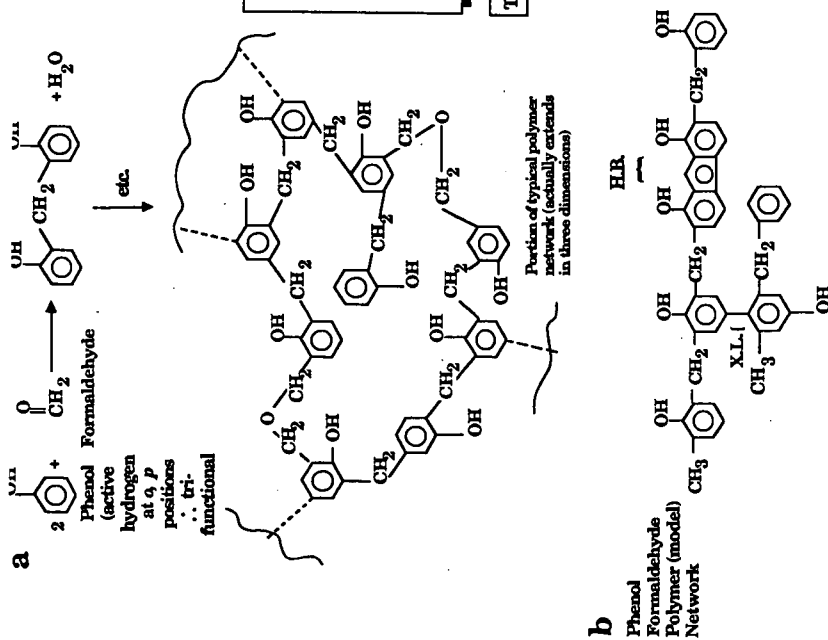


Figure 1. Phenol-Formaldehyde Structures.

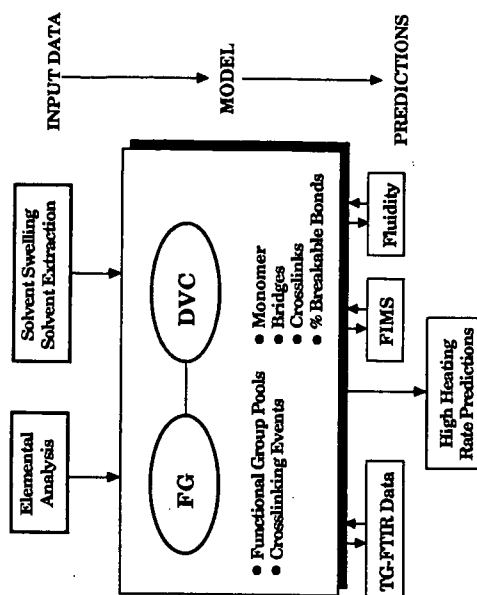


Figure 2. Structure of FG-DVC Model and Major Inputs and Outputs.

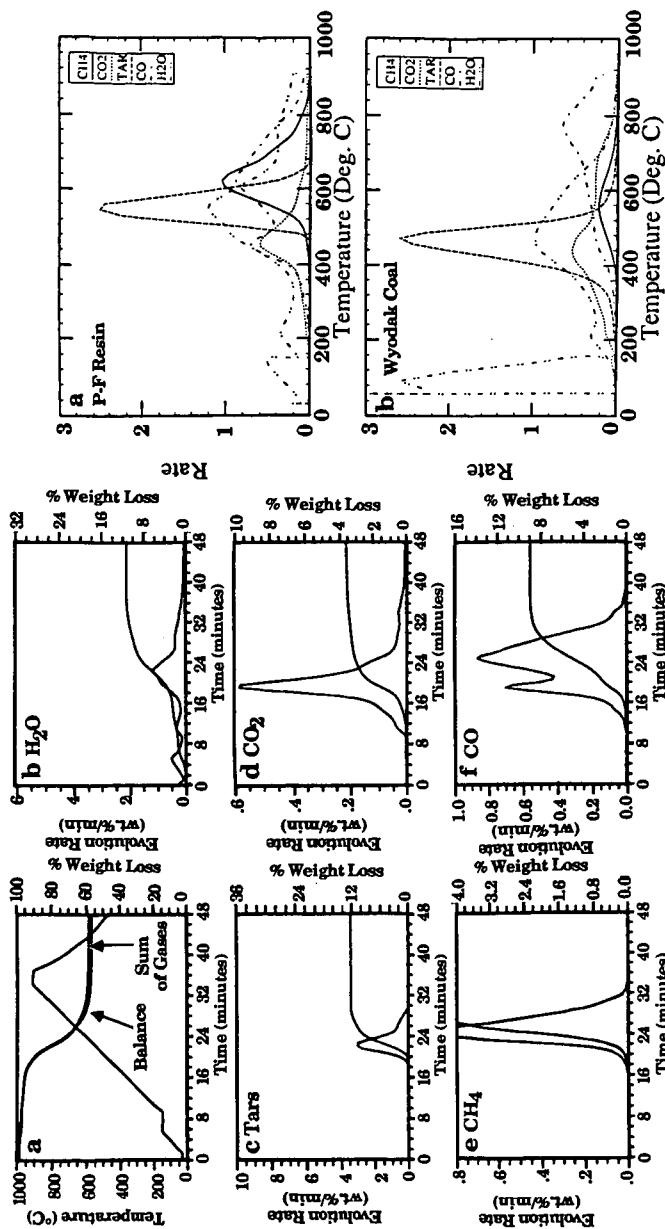


Figure 3. TG-FTIR Analysis of Phenol-Formaldehyde at 30°C/min.

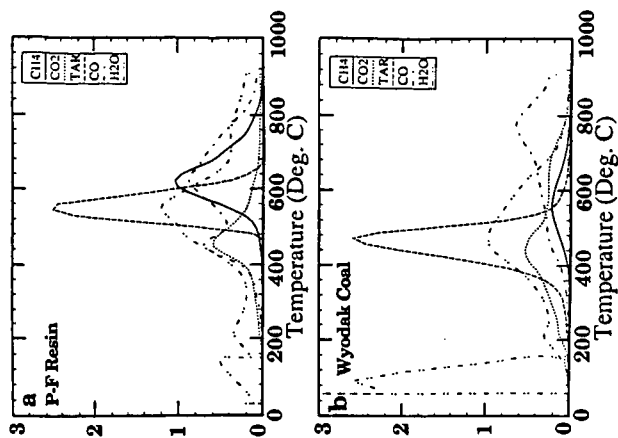


Figure 4. Composite TG-FTIR Evolution Plots for a) Phenol-Formaldehyde Resin; b) Wyodak Subbituminous Coal.

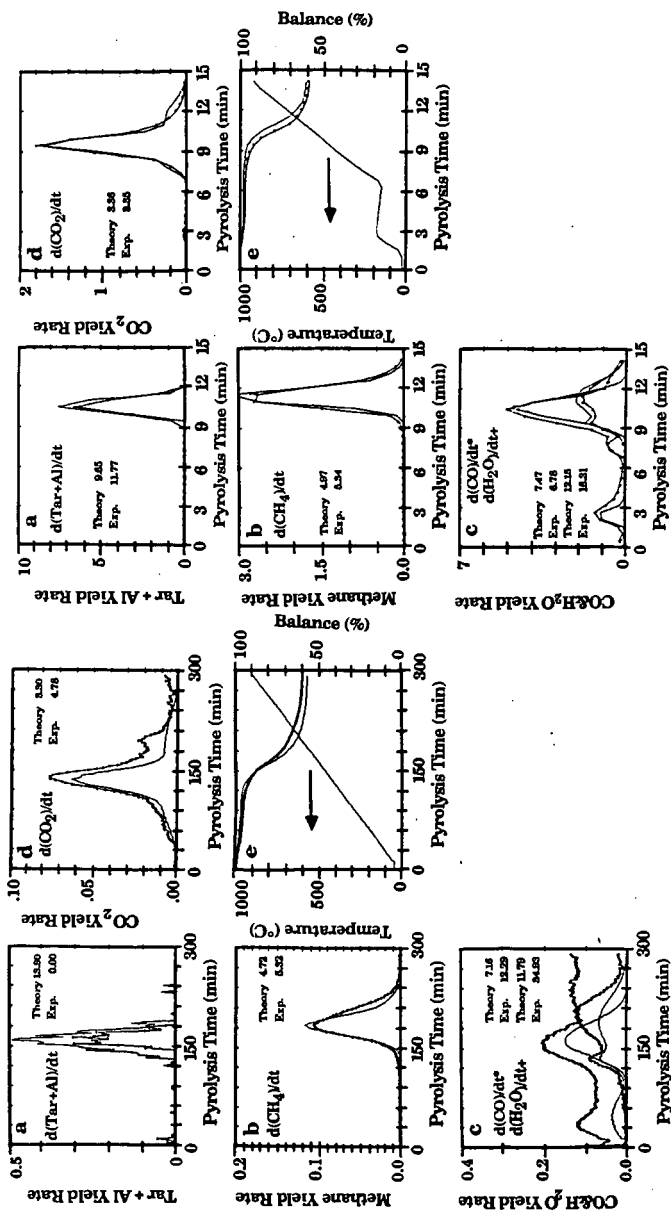


Figure 5. Comparison of FG-DVC Model Predictions (solid lines) with Pyrolysis Data (at 3°C/min) for Phenol-Formaldehyde Resin. Case 1.

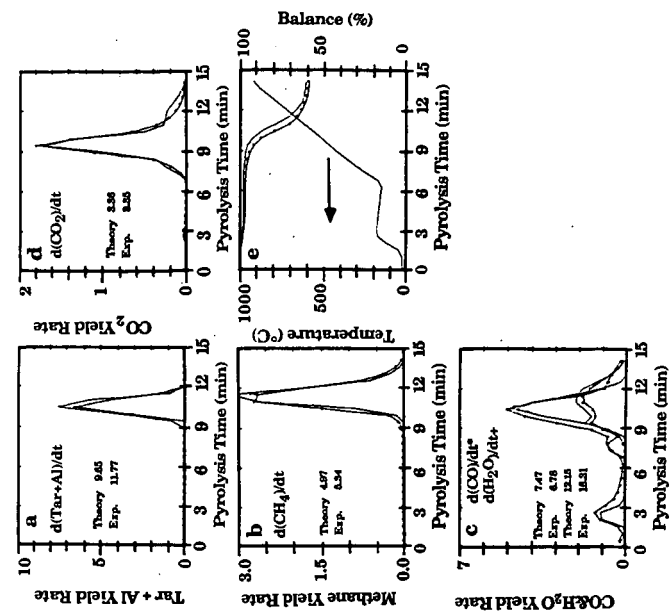


Figure 6. Comparison of FG-DVC Model Predictions (solid lines) with Pyrolysis Data (at 100°C/min) for Phenol-Formaldehyde Resin. Case 1.

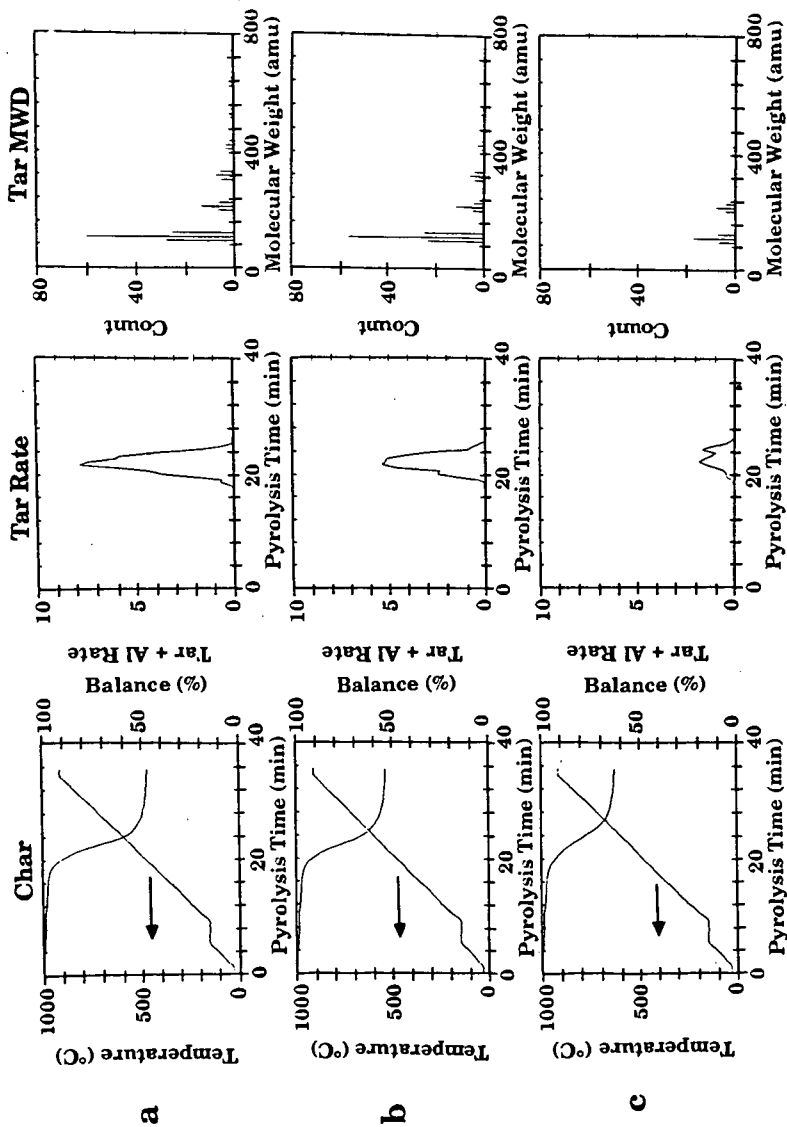


Figure 7. Simulation of Results for Weight Loss, Tar Evolution Rate and Tar Molecular Weight Distribution for Three Different Initial Crosslink Densities.  
a) 50 Crosslinks; b) 150 Crosslinks; c) 450 Crosslinks.

## Thermolysis of 2,2-Diphenylpropane and 4-Cumyl Phenol

Concetta LaMarca, Cristian Libanati and Michael T. Klein\*  
Robert J. Cotter<sup>1</sup> and Stephen M. Andrews<sup>1</sup>

Center for Catalytic Science and Technology  
Department of Chemical Engineering  
University of Delaware  
Newark, DE 19716

**KEYWORDS:** polymer, pyrolysis, model compounds.

### ABSTRACT

The thermal reactivity of 2,2-diphenylpropane is relevant to the stability of a broad class of polymers which are made using bisphenol A. Consequently, the pyrolysis of 2,2-diphenyl propane and 4-cumyl phenol, its analog containing a hydroxy substituent, have been studied at 450 and 500°C. 2,2-DPP is observed to react to 1,1-diphenylethane, 1,1-diphenylethylene, toluene, ethylbenzene, 2-phenyl propene diphenylmethane, benzene and cumene. 4-Cumyl phenol reacts to an analogous spectrum of products, but at faster reaction rates indicating activation by the hydroxy substituent. A free-radical mechanism consistent with experimental results has been proposed herein together with the associated rate parameters for elementary steps.

### INTRODUCTION

Polymer thermal stability is important for purposes of recycling and in regards to degradation during end-use applications and high temperature processing. A broad class of these polymers (e.g., polycarbonate, polysulfone, polyarylate, polyetherimide) are prepared using bisphenol A, and therefore the thermal reaction of materials containing this moiety are of interest.

This reactivity can be probed directly in experiments with the polymeric materials themselves. These experiments can provide much relevant but system-specific information. A second, complementary approach is in experiments using pure component, model compounds, which provide a great deal of fundamental information about the reaction pathways, kinetics and mechanisms. This information can be used in the prediction of the reaction of polymeric materials beyond the range of experiments with the actual polymers.

In this work we follow the second tact to study the reactivity of materials containing the isopropylidene linkage. We present results of pyrolysis experiments of 2,2-diphenylpropane [2,2-DPP] and its hydroxy substituted analog, 4-cumyl phenol [4-CP].

The reaction pathways and kinetics of 2,2-diphenylpropane have not been thoroughly studied. Previous experimental work [1] indicates the bond homolysis activation energy as  $E_a=65.7$  kcal/mol and  $\log_{10}A=15.7$ . Pryor, Gleicher and Church [2] studied ring ozonation of 2,2-DPP at 25°C. Duty, Geier and Harwood [3] demonstrated resistance of 2,2-DDP to oxidation by dichromate when reacted in an aqueous solution at 250°C and 18 hrs. Schanne and Haenel [4] used potassium to cleave the phenyl ring to form benzene and 2-phenylpropane by what they propose to be a radical ion mechanism. Golden [5] irradiated 2,2-DPP at 1000 megarads using electron beam radiation. The reaction products were primarily methane and hydrogen, with little  $CO$ ,  $CO_2$  and hydrocarbon gases found.

Herein we extend this previous literature through more comprehensive study of the reaction pathways, kinetics and mechanisms for the pyrolysis of 2,2-diphenylpropane and 4-cumyl phenol.

### EXPERIMENTAL SECTION

2,2-DPP and 4-cumyl phenol were pyrolysed at 450°C and 500°C for batch holding times of 2-120 min. Initial concentrations were nominally 60 mM.

<sup>1</sup> Amoco Performance Products, Inc., Research & Development Center, 4500 McGinnis Ferry Rd., Alpharetta, GA 30202-3944

## Materials

2,2-DPP was obtained from Aldrich and subsequently distilled and collected at 113–117°C and 3 mm Hg. 4-Cumyl phenol was obtained from Aldrich and recrystallized before use. Dibenzyl ether, used as an external standard for GC analysis, was obtained from Aldrich. Gold band ampules (Wheaton) were used to fabricate batch reaction vessels.

## Procedure

The reactors were loaded by weight with a typical charge of 25 mg of reactant. One reactor was prepared for each desired reaction time. The ampules were purged with argon to avoid oxidation and then immediately sealed using a propane/O<sub>2</sub> flame. These reactions were then immersed into a constant-temperature, fluidized sand bath (Techne) for the desired reaction time. The reaction was quenched by immersion in a cold, room-temperature fluidized sand bath. Reactors were checked for leaks by weighing both before and after reaction.

Reactant conversion and product yields were quantified by use of the external standard, dibenzyl ether, added to the reaction mixture after reaction. All materials were then recovered in methylene chloride. Analysis was performed by GC (Hewlett-Packard 5880) equipped with an FID to quantify yields and GC/MSD (Hewlett-Packard 5890 GC/H-P 5970 MSD) to identify products.

## RESULTS AND DISCUSSION

2,2-Diphenylpropane pyrolysis at 450°C was at holding times ranging from 2.0–120.0 minutes; reaction at 500°C was for holding times ranging from 5–60 min. The detailed product spectrum, shown in Table 1 as product molar yields vs. time, includes benzene, toluene, ethylbenzene, styrene, cumene, 2-phenylpropene, 1,1-diphenylethane, 1,1-diphenylethene and diphenylmethane. At 450°C, a 32% conversion of 2,2-DPP was observed at 120 min, where the products in most significant yields were 1,1-diphenylethane and 1,1-diphenylethene, followed by benzene, toluene and ethyl benzene.

The Delplot technique [6] is a data analysis approach which reveals reaction path information allowing discrimination between primary, secondary and higher order products. For example, in a first-rank Delplot, product selectivity (yield/conversion) is examined as a function of conversion. In extrapolation to zero conversion, primary products have finite y-intercepts, while that for higher order products goes to zero. In a second-rank Delplot (yield/conversion<sup>2</sup> vs. conversion), primary products diverge as  $\chi \rightarrow 0$ , while secondary products have finite intercepts.

First-rank Delplots for 2,2-DPP pyrolysis at 450°C indicate that all products except diphenylmethane, toluene, ethyl benzene and styrene were clearly primary. Delplots for 2,2-DPP pyrolysis at 500°C suggest all products but diphenylmethane to be primary. This may indicate that at 500°C the intermediates that lead to toluene, ethyl benzene and styrene may be very short lived.

4-Cumyl phenol was pyrolysed at both 450 and 500°C to final holding times of 101 and 60 min, respectively. Table 2 summarizes the reaction products, namely benzene, toluene, ethyl benzene, cumene, phenol, 2-phenylpropene, methylpropyl benzene, 4-methyl phenol, 4-ethyl phenol, 4-hydroxy diphenylmethane, 4-hydroxy-(1,1-diphenylethane) and 4-hydroxy-(1,1-diphenylethene). These are analogous to the products observed from 2,2-DPP pyrolysis. 4-hydroxy diphenylethane and 4-hydroxy diphenylethene were observed in the highest yields, with relatively large amounts of phenol. The first-rank Delplots for 4-cumyl phenol pyrolysis at 500°C suggest most products to be primary with the exception of methylpropyl benzene, 4-ethyl phenol and hydroxydiphenylmethane.

The foregoing information suggests the 2,2-DPP and 4-CP pyrolysis pathways to be straightforward. Primary pyrolysis provides most of the products, with secondary reactions accounting for only diphenylmethane (for 2,2-DPP) and methylpropyl benzene, 4-ethyl phenol, and hydroxy diphenylmethane (for 4-CP). Pseudo-first-order rate constants for the reaction of both 2,2-DPP and 4-cumyl phenol to their primary products are shown in Table 3. The suggested Arrhenius parameters (two temperatures only) for primary 2,2-DPP pyrolysis are also listed in Table 3. 4-Cumyl phenol pyrolysis was much faster than that of 2,2-DPP. For example, for reaction at 500°C and 60 min, the 4-cumyl phenol conversion was 93%, whereas only 80% conversion was observed for 2,2-DPP.

A set of elementary steps consistent with the observed product spectra is shown in Figure 1. For 2,2-DPP, initiation by unimolecular decomposition can proceed through fission of two different bonds, leading to

the production of either methyl and diphenyl ethyl radicals (which subsequently become methane and 1,1-diphenylethane following hydrogen abstraction) or to phenyl and isopropyl benzene radicals (similarly leading to benzene and cumene). The former is expected to be more facile since the controlling bond dissociation energy is ~66 kcal/mol, 14 kcal/mol lower than that of ~80 kcal/mol for the latter. Propagation is by hydrogen abstraction by any radical from 2,2-DPP. The thus-derived 2,2-DPP radical has two  $\beta$ -scission pathways available. One leads to a methyl radical and diphenylethene and has a lower heat of reaction than the second, leading to a phenyl radical and 2-phenyl propene. A thermodynamically favorable phenyl shift can ultimately lead to toluene and ethyl benzene. Termination is by combination of any two radicals. An analogous set of steps could lead to the observed 4-CP products.

In summary, the structure and thus-derived thermochemical properties of 2,2-DPP and 4-CP control their pyrolysis activity. No evidence for a significant kinetic chain was found. The main products all appear to be primary and are explained nicely by elementary steps in strict accord with thermochemical estimates.

#### ACKNOWLEDGEMENT

The authors gratefully acknowledge financial support from Amoco Performance Products, Inc. We are also thankful for the laboratory assistance of Ken Crovetto and Wendy Rise.

#### REFERENCES

1. Robaugh, D. A. and S. E. Stein. "Stabilities of highly conjugated radicals from bond homolysis rates". *J. Am. Chem. Soc.*, **1986**, *108*, 3224-3229.
2. Pryor, W. A., G. J. Gleicher, and D. F. Church. "Relative reactivities of alkylbenzenes and related compounds toward ozone. The mechanism of ozonation at benzylic positions." *J. Org. Chem.*, **1984**, *49*, 2574-2578.
3. Duty, R. C., M. Geier and J. Harwood. "Precursors to aromatic units in coal." *Fuel*, **1985**, *64*, March, 421-423.
4. Schanne L. and M. W. Haenel. "Cleavage of carbon-carbon-bonds by solvated electrons." *Tetrahedron Letters*, **1979**, *44*, 4245-4248.
5. Golden, J. H. "Degradation of Polycarbonates II. Effect of radiation on model compounds." *Die Makromolekulare Chemie*, **1963**, *66*, 73-81.
6. N. A. Bhore, M. T. Klein and K. B. Bischoff. "The Delplot technique: a new method for reaction pathway analysis." *Ind. Eng. Chem. Res.*, **1990**, *29*, 313-316.



Table 1 - Product Molar Yields for Pyrolysis of 2,2-Diphenylpropane  
Reaction at 450°C

Time (min)	0.00	2.00	5.00	10.00	15.00	20.00	30.00	45.00	60.00	120.00
2,2-DPP	1.0000	0.9715	1.0157	0.9604	0.9932	0.9124	0.9106	0.8427	0.8121	0.6812
Benzene	0.0000	0.0005	0.0012	0.0047	0.0067	0.0079	0.0094	0.0102	0.0125	0.0130
Toluene	0.0000	0.0004	0.0006	0.0027	0.0067	0.0104	0.0160	0.0202	0.0253	0.0383
Ethylbenzene	0.0000	<0.0001	<0.0001	0.0018	0.0042	0.0067	0.0103	0.0132	0.0173	0.0245
Styrene	0.0000	<0.0001	<0.0001	0.0006	0.0012	0.0018	0.0026	0.0032	0.0043	0.0052
Cumene	0.0000	<0.0001	0.0008	0.0026	0.0033	0.0037	0.0043	0.0046	0.0056	0.0060
2-PhenylPropene	0.0000	0.0004	0.0010	0.0032	0.0044	0.0051	0.0057	0.0061	0.0080	0.0071
DiPEthane	0.0000	0.0002	0.0017	0.0068	0.0122	0.0175	0.0262	0.0367	0.0542	0.0931
DP Ethylene	0.0000	0.0003	0.0014	0.0063	0.0124	0.0191	0.0295	0.0419	0.0668	0.0990
DPM	0.0000	<0.0001	0.0002	0.0003	0.0007	0.0009	0.0015	0.0021	0.0030	0.0073

Reaction at 500°C

Time (min)	0.00	5.00	15.00	45.00	60.00
2,2-DPP	1.0000	0.8872	0.6547	0.3302	0.2020
Benzene	0.0000	0.0131	0.0185	0.0237	0.0278
Toluene	0.0000	0.0176	0.0419	0.0823	0.1067
Ethylbenzene	0.0000	0.0122	0.0238	0.0393	0.0445
Styrene	0.0000	0.0035	0.0069	0.0107	0.0115
Cumene	0.0000	0.0061	0.0070	0.0087	0.0093
2-PhenylPropene	0.0000	0.0098	0.0120	0.0116	0.0109
DiPhenylEthane	0.0000	0.0334	0.0983	0.2070	0.2487
DP Ethylene	0.0000	0.0403	0.1274	0.2359	0.2582
DPM	0.0000	0.0013	0.0083	0.0414	0.0730

Table 2 - Product Yields for Pyrolysis of Cumyl Phenol  
Reaction at 450°C

time/min	0.00	2.00	5.00	10.00	20.00	47.58	60.00	101.02
Cumyl Phenol	1.0003	0.8909	0.8753	0.8217	0.7247	0.614	0.5636	0.4699
benzene	0.0157	0.0150	0.0154	0.0157	0.0164	0.0191	0.0193	0.0242
toluene	0.0004	0.0009	0.0020	0.0043	0.0086	0.0183	0.0219	0.0402
et. benzene	0.0000	0.0003	0.0013	0.0031	0.0061	0.0129	0.0155	0.0297
cumene	0.0000	0.0015	0.0038	0.0076	0.0122	0.0232	0.0279	0.0469
phenol	0.0000	0.0030	0.0059	0.0148	0.0211	0.038	0.0472	0.0834
2pp	0.0000	0.0062	0.0088	0.0163	0.0197	0.0251	0.0283	0.0369
4mp	0.0000	0.0003	0.0012	0.0030	0.0062	0.0127	0.0154	0.0272
4ep	0.0000	<0.0001	0.0008	0.0024	0.0055	0.0113	0.0132	0.0218
HDPM	0.0000	<0.0001	<0.0001	<0.0001	0.0007	0.0029	0.0049	0.0124
hdpethane	0.0000	0.0005	0.0044	0.0108	0.0214	0.0493	0.0681	0.1145
hdpethene	0.0000	0.0014	0.0063	0.0159	0.0329	0.0594	0.0707	0.0825

Reaction at 500°C

time/min	0.00	5.00	15.00	30.00	45.00	60.00
Cumyl Phenol	1.0000	0.8222	0.5018	0.2472	0.1570	0.0665
benzene	0.0000	0.0020	0.0043	0.0068	0.0092	0.0127
toluene	0.0000	0.0085	0.0226	0.0429	0.0574	0.0852
et. benzene	0.0000	0.0058	0.0148	0.0303	0.0448	0.0665
cumene	0.0000	0.0109	0.0235	0.0352	0.0572	0.0569
phenol	0.0000	0.0148	0.0407	0.0760	0.1380	0.1737
2pp	0.0000	0.0178	0.0315	0.0398	0.0565	0.0536
methylpropbenz	0.0000	0.0021	0.0022	0.0028	0.0036	0.0038
4mp	0.0000	0.0062	0.0164	0.0307	0.0354	0.0512
hdpethane	0.0000	0.0329	0.0859	0.1400	0.1405	0.1390
hdpethene	0.0000	0.0621	0.1390	0.1614	0.1387	0.1380

Table 3: Reaction Pathway Parameters; 2,2-Diphenylpropane and 4-Cumyl Phenol

a) 2,2-Diphenylpropane

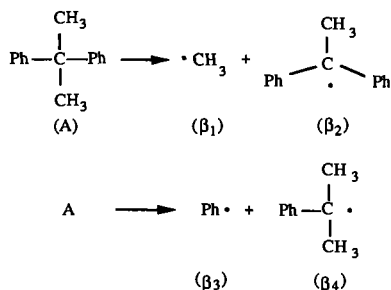
Reactant/Product	$k_1(450^\circ\text{C})$ [1/min]	$k_1(500^\circ\text{C})$ [1/min]	$E_a$ [kcal/mol]	$\log_{10} A$
DPP	3.31E-03	2.61E-02	45.8	9.6
Benzene	1.86E-04	9.82E-04	37.0	9.2
Toluene	4.23E-04	3.33E-03	45.9	8.7
Ethyl Benzene	2.75E-04	1.53E-03	38.1	6.2
Styrene	6.94E-05	4.00E-04	38.9	5.8
Cumene	8.06E-05	6.16E-05		
2-Phenyl Propene	1.10E-04	4.21E-06		
1,1-DP Ethane	9.38E-04	8.02E-03	47.7	9.6
1,1-DP Ethene	1.04E-03	8.82E-03	47.5	9.6

a) 4-Cumyl Phenol

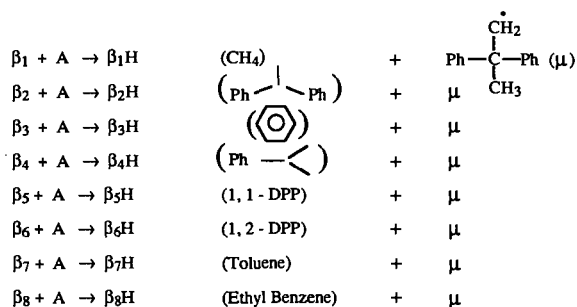
Reactant/Product	$k_1(450^\circ\text{C})$ [1/min]	$k_1(500^\circ\text{C})$ [1/min]	$E_a$ [kcal/mol]	$\log_{10} A$
4-Cumyl Phenol		4.46E-02		
Benzene		1.07E-08		
Toluene		3.70E-03		
Ethyl Benzene		6.40E-04		
Cumene		2.98E-04		
Phenol		6.60E-03		
2-Phenyl Propene		2.82E-03		
4-Methyl Phenol		2.45E-03		
4-Hydroxy(1,1-DP Ethane)		6.24E-03		
4-Hydroxy(1,1-DP Ethene)		7.58E-03		

Figure 1  
Elementary Steps for Reaction of 2, 2 - DPP

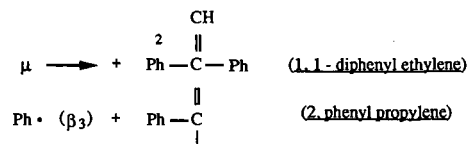
Bond Fission



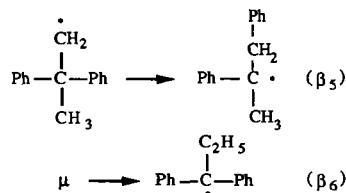
Hydrogen Transfer



$\beta$  - scission



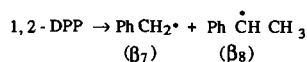
Radical Isomerization



Recombination

All combinations

Secondary Reactions



## PYROLYSIS OF BIOMASS AND POLYMER MIXTURES - MUNICIPAL SOLID WASTE AS AN EXAMPLE

Wei-chuan Lai and Prof. Barbara Krieger-Brockett  
Chemical Engineering, University of Washington  
Benson Hall BF-10, Seattle, WA 98195.

Keywords: refuse-derived fuel, pyrolysis, heat transfer, composition and particle size effects

### ABSTRACT

Incineration and thermal conversion of municipal solid waste are receiving considerable attention from both a political and scientific viewpoint. Polymers are present, both natural and manmade, representing about 80 weight % of the waste. Little quantitative reaction data is available and potential pollution problems have been identified when the polymeric mixtures contain chlorine and are reacted or incinerated at high temperature. The purpose of this work is to provide a quantitative basis for the engineering design of reactors to recover hydrocarbons from this waste. We have performed experiments under controlled conditions on a reasonably well-characterized "model" for municipal solid waste, that is, commercially available densified refuse-derived fuel (d-RDF), made by sorting, drying and compressing municipal solid waste. The resulting relatively uniform composition and density pellets have, however, low thermal conductivity, making the apparent reaction rate limited by the local heat transfer rate. This pyrolysis study employs single, "macro"-particle experiments where particle non-isothermality can be measured and its effect on product slate can be understood. A variety of polymeric substrates as well as commercial RDF have been heated under well-controlled conditions spanning those of industrial importance. The devolatilization behavior, such as time-temperature history and evolved gas composition, has been measured in detail. The results have been used to develop correlations applicable to reactor design and pollution control. Specialized statistical methods are used to quantify the contribution of a single mixture constituent to pyrolysis behavior. Conclusions from the experiments have aided in the development of a mathematical model of the devolatilization process and have increased our understanding of the role of reactant composition, as well as particle mass and heat transfer, during gasification and combustion.

### INTRODUCTION

The ongoing work described in this preprint is a portion of a study (1) of the transport rates and chemical reaction behavior during thermal conversion of a particular form of municipal solid waste (MSW), namely densified refuse-derived fuel (d-RDF). It is made commercially by removing recyclables and non-combustibles, drying and compressing the remaining mixture (manmade and natural polymers as well as other materials) into pellets of relatively uniform size and density (~1-2 cm diameter, 2-3 cm long cylinders, specific gravity between 1 and 2). The resulting material is considerably more compact, has approximately the heating value of coal, and can be economically transported to a central site for thermal conversion. It is envisaged that this central site could then be expected to have a larger, more advanced design thermal conversion process with potentially the flexibility to optimize certain products, and certainly the capability of pollution control and monitoring.

While some work has been performed on d-RDF and MSW (1-3), it remains to be determined what reaction conditions optimize particular products, what are the effects of pellet moisture, size and density on conversion rate and products, and in particular, what changes in the waste stream polymeric mixture result in desirable or undesirable pyrolysis products. Reactor design will require devolatilization kinetics data on the d-RDF constituents, and a knowledge of whether constituents co-react when confined to the interior of the relatively non-porous particle of d-RDF, or whether the constituents react independently. By studying the behavior of single particles as in other studies (4), we can direct the efforts in mathematical modeling of the pellet behavior, provide a basis for judging adequate kinetic models, and make suggestions regarding appropriate reactor configurations.

### EXPERIMENTAL ASPECTS

The experimental apparatus consists of a single particle reactor which allows determination of particle temperature and gas evolution history, heat transfer rates, and total product analysis. It is described elsewhere (1,5). The d-RDF compositions studied span the range found in practice (Table 1) as interpreted by the standard deviation of the 10 composition studies available in the recent literature. To

understand the role of composition, laboratory-fabricated pellets as well as commercial pellets are studied under the well-controlled reaction conditions likely to occur in industrial practice (Table 2).

As in other studies where sample size must remain constant while composition is changed, in this study the weight fractions of waste constituents sum to unity, making the composition variables correlated and the interpretation of results ambiguous unless special experimental designs and biased regression methods are employed. Consider a 1 gram sample of say 4 equal concentration components (25% by weight). Its reaction behavior is to be compared to another 1 gram sample (so sample temperature history remains constant) with a different composition. In the second sample, it is desired to determine the pyrolysis product slate change when one of the constituents is reduced to say 10% by weight. Owing to the constant sample size, this change necessitates that one of the other constituents make up the remaining 15%. Changes in behavior cannot be unambiguously attributed to a reduction in the former, but rather to either a reduction in the former or increase in the latter constituent. This difficulty is lessened when one constituent predominates as in the case of paper-like components of MSW. In Table 1 it can be seen that components 1-4, 7, and perhaps 6 can be approximated by paper such as newsprint with a lignin content close to that of native wood. Daugherty et al. (6) have studied the stability of d-RDF with respect to biological degradation and long term integrity of the pellets. They found a well-behaved d-RDF pellet can be made when  $\text{Ca}(\text{OH})_2$  is used as a binder comprising approximately 1-8% by weight. The binder is similar to the inorganic material that accompanies the combustible fraction in actual MSW. For a number of reasons (1), we were able to justify reducing the composition classes in d-RDF to four: paper as exemplified by newsprint, plastics as equal fractions PVC and polyethylene, non-combustibles as exemplified by metal and glass, and inorganic substances as exemplified by binder. The ranges over which these four components were varied are shown in Table 2. The combination of compositions and reaction conditions actually run in our experimental program was a special mixture design (1,7), and ridge regression as well as other biased regression methods were used to calculate the effects of composition changes.

The procedure consists of heating the sample one-dimensionally with a constant radiative heat flux for a fixed pyrolysis time of 12 min. The constant heating time can be rationalized as analogous to the constant time-at-temperature (residence time) a particle experiences in a moving bed reactor. Particle size is varied as are initial particle moisture, composition, and the intensity of the heat flux, all in systematic combinations dictated by the experimental design (1,7). During the pyrolysis, time-temperature profiles are measured at several depths (Fig. 1) and gas evolution rate and composition are also measured as functions of time (Fig. 2). Hydrocarbons are measured as well though only carbon oxides and total gas yield are shown in Fig. 2. The overall pyrolysis product yields are measured as integrated batch yields as well; Table 3 reports typical yields of interest for this paper. In addition, though not the subject of this paper, tar composition is measured in detail as are char surface area and composition by FTIR. To narrow the focus, this paper will concentrate on the composition history of the gases since it is seen to be an indicator of the pyrolysis chemistry occurring in the large, non-uniform temperature particle. The gas composition is measured semi-continuously using a computer controlled automatic sampling valve and a gas chromatograph.

## RESULTS

The d-RDF pellets were pyrolyzed and the time-temperature histories (at 2, 6 and 9 mm into the particle) and gas flux histories are shown in Figs. 1 and 2 respectively. A temperature plateau at about 100°C can be seen to occur at interior thermocouple locations owing to the constant temperature evaporation of water as the heating front passes. The gases are released (Fig. 2) with the peak in the rate controlled by the heating rate applied at the surface, as well as the size and moisture content of the particle. Using data similar to Fig. 2, this paper will present a limited discussion on the comparison of pyrolysis behavior between d-RDF samples with high and low fractions of plastics.

Direct comparisons will be presented in which the only difference between 2 experiments is the fraction of plastics (the remainder being made up by paper (newsprint)). In these, it is useful to *subtract* the yields, or subtract the gas flux histories and report the difference as a function of time. That is, the data analogous to Fig. 2 for an experiment with low fraction plastics are subtracted from the data resulting when a high fraction plastics pellet is pyrolyzed. The *fractional* difference provides perhaps more insight when concentrations are small as in our pyrolyses, and this is shown in Figs. 3 and 4 for carbon oxides and hydrocarbons respectively (the low plastics result is the reference or denominator). Thus Figs. 3 and 4 report fractional difference in gas composition as a function of pyrolysis (reaction) time for the cases of high and low plastics content in d-RDF. It is important to keep in mind the sample-to-

sample variation expected in such a heterogeneous reactant and we have studied this by replicate experiments. For replicates, the difference between measured gas concentrations expressed as a fraction of one of them is less than approximately two-fold over the entire time interval; thus fractional concentration variations greater than 3 in Figs. 3 and 4 represent probable composition effects in the pyrolysis behavior. It can be seen that the hydrocarbons, especially  $C_2H_4$  and  $CH_4$ , appear to be sensitive to the concentration of plastics. This is to be expected judging from the thermal degradation products measured for polymers (8-16).

The time-dependent pyrolysis behavior is to likely represent data with a high degree of noise or uncertainty in them. A more robust measurement, though revealing less kinetic and reaction information, is the comparison of overall (time-integrated) yields from a plastics-rich compared to a plastics-poor sample of d-RDF. In Table 4 are presented three direct comparisons of overall yields, and as before, the pyrolysis component concentrations in the product gas are subtracted for the two cases, and the result expressed as a fractional difference. The three direct comparisons represent different values of other experimental conditions. It can be seen in Table 3 that even replicate d-RDF (laboratory fabricated) pyrolyses exhibit variations in measured product concentrations of about 20%. Thus only differences in overall yields exceeding 25-30% in columns 5,9, and 13 (Table 4) can be interpreted as actual composition effects attributable to the high plastics content. This high a difference is observed for all gases except  $CO_2$ , and in some cases such as ethylene, the difference is over a 200% increase in yield in the product.

## DISCUSSION

The composition effects presented here are direct comparison experiments, that is, only one pair of compositions is varied at a time. Other data (1) indicate that the magnitude of these enhanced pyrolysis product yields is dependent in a complex way on all the other reaction condition variables, namely particle size, initial moisture, heating rate experienced, and in particular, on the amount of inorganic material (binder) present. It is interesting to note that the experimentation to date, and the regression of the results indicate that the d-RDF constituents can be assumed to react independently. Current work is focused on mathematical modeling of the independent reactions, prediction of the effect of such a high moisture content as is typical of MSW (Table 1) and prediction of the coupled processes of heat transfer and reaction rate in the non-isothermal RDF particle.

### Comparison to Pyrolysis of Polymers

It is well known that thermal degradation of Poly(vinyl chloride) (PVC) releases HCl. Hydrogen Chloride generation begins at temperatures as low as  $130^\circ C$ . Up to 99% of the chlorine contained in PVC is lost as HCl, with very little vinyl chloride monomer formed. In inert atmospheres, and at temperatures ranging from 160 to  $700^\circ C$ , more than 75 pyrolysis degradation products have been identified and they included olefinic hydrocarbons, benzene, toluene, xylenes, ethylbenzenes, aliphatic, naphthalenes, and methylated species. Sometimes condensed aromatics such as biphenyl and anthracene were also identified (13). Although many products have been identified, the major products of PVC pyrolysis were hydrogen chloride gas and benzene. In some cases, chlorinated compounds were also identified at higher temperatures; for example, ethylene chloride at  $400^\circ C$ , chlorobenzene, di- and trichlorobenzenes at  $500-700^\circ C$ , and vinyl and ethyl chloride at  $550^\circ C$  (14). For these reasons, we believe that HCL should have been produced in our RDF pyrolyses.

Degradation of polyethylene (PE) under varying oxidative conditions ( $500-800^\circ C$ ) has also long been carried out. The products identified consisting of olefin and n-hydrocarbon with chain lengths of 8 to 23 carbons, in addition to lower molecular weight species such as acetaldehyde, acrolein and benzene (15). It was found that when oxygen in the gas stream was reduced, the amount of carbon dioxide product decreased and hydrocarbon production increased (16). These findings are consistent with our RDF pyrolyses in that (recall no oxygen is present) few hydrocarbons and relatively more condensable volatiles are in the product slates, consistent with the degradation of plastic components. Our carbon dioxide concentration is greater than from pure plastic degradation, attributable to the cellulose decarboxylation from the paper fraction in RDF.

Since HCl is highly soluble in water, HCl gas produced from pyrolysis of PVC is believed to be trapped in the cold tar trap in the form of hydrochloric acid. The trap tar sample collected was analyzed for water and low molecular weight tar components such as Methanol, Acetaldehyde, Acetone, and Acetic acid, by GC using a Supelco 80/100 mesh Porapak Q column. Using the same column, the

response to HCl was calibrated. Calibration results show that the retention time of HCl is 0.71 minute and therefore does not interfere in a major way with any other peak, but that the Porapak Q column is not sensitive enough to detect HCl unless it has a concentration of at least  $3.65 \times 10^{-6}$  g/ $\mu$ l in our sample. Due to this low HCl sensitivity, we detected no HCl in all our pyrolysis product samples. The HCl analysis is currently in progress.

#### ACKNOWLEDGMENTS

The authors would like to acknowledge the financial support of the Department of Energy through the Solar Energy Research Institute, Contract No. XK-7-07224-1.

#### REFERENCES

- 1) Lai, Wei-chuan, Ph.D. thesis, Dept. of Chemical Engineering, U. of Washington, 1991.
- 2) Levie, Benjamin Eli, Ph.D. Thesis, "Pyrolysis of Refuse Derived Fuel Pellets", University of Colorado, Dept. of Chemical Engineering, 1988.
- 3) Agrawal, Ravindra K., F. Gandhi, and R. J. McCluskey, "Low-Pressure Pyrolysis of Newsprint: Product Formation", J. of Analytical and Applied Pyrolysis, **6** (1984), 325-338.
- 4) Russel, W.A., Saville, D., and Greene, M.I., "Model for Short Residence Time Hydropyrolysis of Single Coal Particles," 1979 AIChE J., **25** 65.
- 5) Chan, W. C. Ricky, Marcia Kelbon and B. Krieger-Brockett, "Single-Particle Biomass Pyrolysis: Correlations of Reaction Products with Process Conditions", Ind. Eng. Chem. Res., **27**, 2261-2275 (1988).
- 6) Daugherty, K. E., O. Ohlsson, A. Safa, and B. J. Venables, "Densified Refuse Derived Fuel as a Power Source", Proceedings of the American Power Conference, **45**, pp 930-935, 1986.
- 7) Cornell, John A., Experiments with Mixtures (Designs, Models, and the Analysis of Mixture Data). Second Edition. N.Y.: John Wiley & Sons, Inc. (1990).
- 8) Hodgkin, J. H., M. N. Galbraith, and Y. K. Chong, "Combustion Products from Burning Polyethylene", J. of Macromol. Sci. - Chem., **A17**(1), 35-44 (1982).
- 9) Iida, Takeo, Motoharu Nakanishi, and Kunio Goto, "Investigations on Poly(vinyl Chloride). II. Pyrolysis of Chlorinated Polybutadienes as Model Compounds for Poly(vinyl Chloride)", J. of Polymer Science: Polymer Chemistry Edition, **13**, 1381-1392 (1975).
- 10) Ishihara, Yumiko, Hidesaburo Nanbu, Tadashi Ikemura, and Tomoyuki Takesue, "Catalytic Decomposition of Polyethylene Using a Tubular Flow Reactor System", Fuel, **69**, 978-984 (1990).
- 11) Khalturinskii, N. A., "High-Temperature Pyrolysis of Polymers", J. of Thermal Analysis, **32** (1987), 1675-1682.
- 12) Mallya, Narayani and James E. Helt, "Effects of Feedstock Components on Municipal Solid Waste Pyrolysis", in Research in Thermochemical Biomass Conversion, edited by A. V. Bridgewater and J. L. Kuester, pp113-126, New York: Elsevier Applied Science, 1988.
- 13) Chang, E. P. and R. Salovey, "Pyrolysis of Poly(vinyl Chloride)", J. of Polymer Science: Polymer Chemistry Edition, **12**, 2927-2941 (1974).
- 14) Lattimer, Robert P. and William J. Kroenke, "The Formation of Volatile Pyrolyzates from Poly(vinyl Chloride)", J. of Applied Polymer Science, **25**, 101-110 (1980).
- 15) Hodgkin, J. H., M. N. Galbraith, and Y. K. Chong, "Combustion Products from Burning Polyethylene", J. of Macromol. Sci. - Chem., **A17**(1), 35-44 (1982).
- 16) Boettner, E. A. and Gwendolyn L. Ball, "Combustion Products of Plastics and Their Contribution to Incineration Problems", in Chemical Engineering Applications in Solid Waste Treatment. Edited by Guy E. Weismantel. AIChE Symposium Series, No. 122, Vol. 68 (1972).



**Table 1**

MSW Composition, wt % (Analyses from 10 studies)

	Average	standard deviation
MSW Fraction:		
1. Paper	40.1	6.6
2. Yard Waste	13.7	5.1
3. Food Waste	11.5	4.7
4. Wood	3.1	1.1
5. Plastics	4.9	3.4
6. Rubber & leather	1.9	0.9
7. Textiles	2.1	0.8
Subtotal	77.3	2.5
8. Metal	9.5	1.7
9. Glass	9.9	1.6
10. Misc. Inorganics	3.3	2.6
Total	100.0	
Moisture Content	25.6	3.1

**Table 2**

Experimental Conditions Studied

Process variables	Symbol	Range		Comments
Heat flux	q	$12.6 \times 10^{-4}$	to	$21.0 \times 10^{-4}$ W/m <sup>2</sup>
Moisture content	MC	5.0%	to	30.0% dry basis
Particle thickness	L	1.0	to	2.0 cm
Composition variables				
Paper	X <sub>1</sub>	0.57	to	0.95 weight fraction
Plastics	X <sub>2</sub>	0.00	to	0.20 weight fraction
Metal/Glass	X <sub>3</sub>	0.05	to	0.15 weight fraction
Binder	X <sub>4</sub>	0.00	to	0.08 weight fraction

Table 3

Replicate Runs: Reaction Conditions and Integrated Gas Yields over Pyrolysis Time

	Replicates:			fractional difference of Run 24
	Run 24	Run 25	difference	
X1(PAPER)	0.76	0.76	0	
X2(PLASTICS)	0.1	0.1	0	
X3(MET&GLASS)	0.1	0.1	0	
X4(Binder)	0.04	0.04	0	
Q(cal/cm2-s)	4	4	0	
MC(%)	17.5	17.5	0	
L(CM)	1.5	1.5	0	
GAS(%)2	5.473	4.454	1.0187	19.0%
CO(%)2	1.746	1.313	0.4322	25.0%
CO2(%)2	3.135	2.830	0.3044	10.0%
CH4(%)2	0.245	0.183	0.0621	25.0%
C2H2(%)2	0.012	0.010	0.0017	14.0%
C2H4(%)2	0.058	0.050	0.0081	14.0%
C2H6(%)2	0.053	0.068	-0.015	-29.0%
			average:	19.0%

Table 4

Integrated Gas Yields over Pyrolysis Time for  
Comparison Experiments: High Versus Low Plastics Content

	Hi/lo plastics comparison for experiments with high binder, low metal/glass content, and 2 cm thick				Hi/lo plastics comparison for experiments with low binder, high metal/glass content, and 2 cm thick				Hi/lo plastics comparison for experiments with high binder, low metal/glass content, and 1 cm thick			
	Run 18	Run 51	18-51	18-51 /51	Run 33	Run 21	33-21	33-21 /21	Run 54	Run 55	54-55	54-55 /55
X1(PA)	0.71	0.82	-0.102		0.70	0.81	-0.102		0.71	0.82	-0.102	
X2(PL)	0.15	0.05	0.102		0.15	0.05	0.102		0.15	0.05	0.102	
X3(M&G)	0.07	0.07	0		0.13	0.13	0		0.07	0.07	0	
X4(BI)	0.06	0.06	0		0.02	0.02	0		0.06	0.06	0	
Q	5	5	0		5	5	0		5	5	0	
MC(%)	5	5	0		5	5	0		5	5	0	
L(CM)	2	2	0		2	2	0		1	1	0	
GAS(%)2	6.91	7.83	-0.92	-12.0%	5.85	8.42	-2.58	-31.0%	10.66	12.27	-1.60	-13.0%
CO(%)2	1.62	1.88	-0.26	-14.0%	1.62	2.61	-1.00	-38.0%	2.36	2.92	-0.56	-19.0%
CO2(%)2	4.63	5.56	-0.93	-17.0%	3.36	5.12	-1.76	-34.0%	7.69	8.74	-1.05	-12.0%
CH4(%)2	0.31	0.21	0.09	45.0%	0.20	0.36	-0.17	-46.0%	0.32	0.41	-0.09	-21.0%
C2H2(%)2	0.01	0.01	-0.002	-20.0%	0.02	0.02	0.003	20.0%	0.02	0.01	0.01	56.0%
C2H4(%)2	0.16	0.05	0.11	238.0%	0.05	0.10	-0.05	-52.0%	0.09	0.09	-0.001	-1.0%
C2H6(%)2	0.12	0.09	0.03	30.0%	0.10	0.07	0.03	37.0%	0.18	0.07	0.11	161.0%

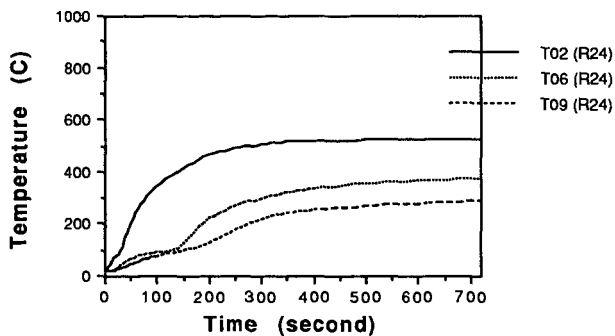


Fig. 1 - Time-Temperature Profiles at 3 different depths from the heated surface (average composition and reaction conditions, centerpoint of range studied, Run 24, conditions shown Table 3)

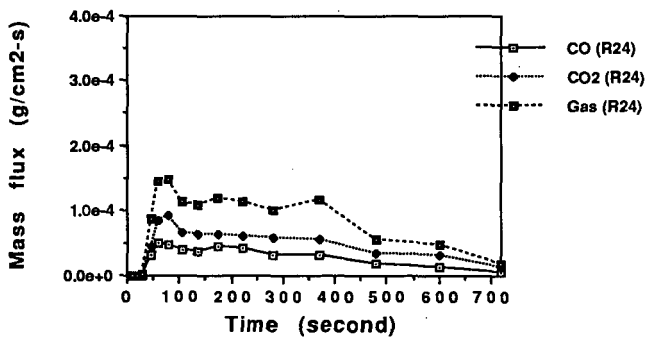


Fig. 2 - Gas Release Histories (Run 24) for Experimental Conditions shown in Table 3

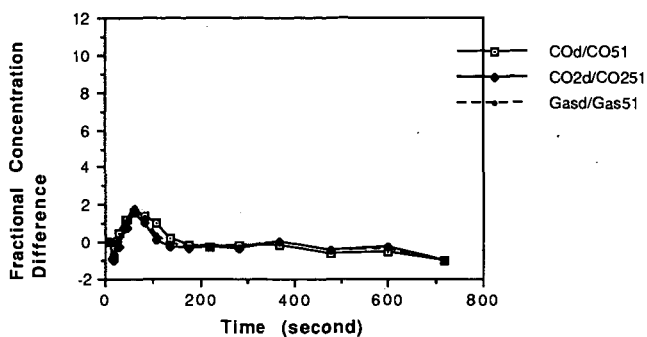


Fig. 3 - Difference in Carbon Oxide and Total Gas Concentration between two direct comparison Runs (Runs 18 and 51) - Normalized by Concentrations in Run 51 (low plastics content)

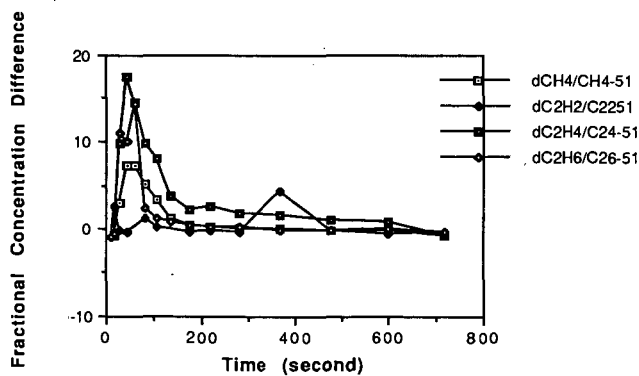


Fig. 4 - Difference in Hydrocarbon Gas Concentration between two direct comparison Runs (Runs 18 and 51) - Normalized by Concentrations in Run 51 (low plastics content)

PY-GC-ION TRAP DETECTION OF SORGHUM GRAIN POLYPHENOLS (*syn.*  
VEGETABLE TANNINS): PRELIMINARY RESULTS

Guido C. Galletti  
Centro di Studio per la Conservazione dei Foraggi - C.N.R.  
via Filippo Re, 8  
40126 Bologna, Italy

Keywords: pyrolysis-gas chromatography-ion trap detector mass spectrometry; polyphenol analysis; sorghum analysis.

ABSTRACT

Polyphenols (tannins) from sorghum grains with a high tannin content were analyzed by pyrolysis-gas chromatography-ion trap detector mass spectrometry (PY-GC-MS). Pyrolysis at 600 °C produced high relative percentages (around 50%) of catechol (1,2-dihydroxybenzene), and minor amounts of other phenolic compounds. Catechol was also the main fragment in the pyrogram of catechin (a monomeric unit of tannins). The absence of significant levels of catechol in the pyrogram of non-tannin polyphenols (such as lignin), and its relative lower abundance in that of low-tannin containing sorghum grains suggests the use of catechol as a remarkable characteristic fragment for qualitative-quantitative analysis of tannins by PY-GC-MS.

INTRODUCTION

Polyphenols (*syn.* vegetable tannins) can be divided into two classes, namely hydrolyzable and condensed or non-hydrolyzable tannins. The hydrolyzable tannins are esters of mainly glucose with hydroxyphenolic acids such as gallic acid. The condensed tannins are polymers of flavanoid precursors such as catechin (scheme 1) (1).

Vegetable tannins influence the characteristics of many plant products - their taste, palatability, nutritional value, pharmacological and toxic effects, and their microbial decomposition - because of their ability to complex strongly with proteins, carbohydrates, nucleic acids, alkaloids and minerals (2,3,4).

Structure elucidation of monomeric and oligomeric (up to 5-6 units) procyanidins has been accomplished by <sup>1</sup>H- and <sup>13</sup>C-NMR (5), and Fast Atom Bombardment Mass Spectrometry (6). Classical methods for routine quantitative analysis have included colorimetric (7,8) and protein precipitation assays (9), but their validity has been questioned (10).

Tannins have been chromatographed by HPLC (11) and gel permeation (12). Gas chromatography (GC) is unfeasible due to their large molecular weight, polarity and thermal lability. However, molecules with these chemical features are in principle suitable to be degraded by pyrolysis (PY), an effective technique for the study of complex, non-volatile samples, which can be integrated with a gas chromatograph-mass spectrometer (PY-GC-MS) to provide a rapid analysis of the degradation products, and hence the characterization of the original sample.

This paper reports on the GC-MS analysis of the pyrolysis products of tannins isolated by gel permeation from sorghum grain, and of catechin as a reference compound. It is anticipated that these preliminary results indicate whether pyrolysis

can provide characteristic fragments of diagnostic significance for the recognition of the non-volatile tannins by gas chromatography without the need for off-line degradation and derivatization or mass spectrometry.

## EXPERIMENTAL

### Extraction and gel permeation.

A detailed procedure for tannin extraction and purification has been described elsewhere (12). Briefly, a 100-g sample of ground sorghum grain was defatted in Soxhlet with diethyl ether. The residue was transferred into a dark bottle and extracted overnight at +1 °C under rotary shaking with acetone (3x300 ml). The residue was extracted under the same conditions with methanol (3x300 ml). The methanolic extracts were combined and the solvent was distilled off under vacuum in a rotary evaporator (T: 35 °C). A 500-mg aliquot of this crude extract was suspended in methanol (7 mL) and the slurry was applied onto a column packed with Sephadex LH 20 (35x3 cm). The column was eluted at 2 mL/min (detection 340 nm) with 95% ethanol (800 mL) to remove some coloured non-phenolic substances, then with acetone/water (7/3, 640 mL) to collect the brown polyphenolic fraction retained at the top of the column. The acetone/water solvent was evaporated in rotary evaporator under reduced pressure (T: 40 °C). The tannin was dried over P<sub>2</sub>O<sub>5</sub> and stored at - 25 °C until analysis.

### Pyrolysis-gas chromatography-mass spectrometry (PY-GC-MS).

About 1 mg of tannin was pyrolyzed using a CDS Pyroprobe 100 equipped with a platinum coil probe and a quartz sample holder. Catechin was pyrolyzed by applying 10 µL of a methanolic solution (10 mg/mL) in the quartz tube. The pyrolyzer was interfaced with a GC-MS system consisting of a Varian 3400 gas chromatograph coupled to a Finnigan MAT Ion Trap Detector (ITD) model 800 mass spectrometer and operating under the following conditions: injector (split 1/120) at 220 °C; SPB-5 column (30 m x 0.32 mm i.d.) programmed from 50 to 300 °C at 10 °C/min (He: 1 mL/min); transfer line at 220 °C; mass spectra recorded at 70 eV under the usual ITD software release 4.0 conditions.

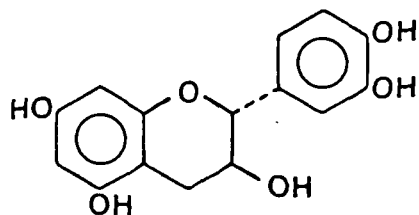
## RESULTS AND DISCUSSION

Two sorghum grain commercial cultivars, i.e. Arval and Argence representative of high- and low tannin content, respectively, were used for the present work. According to the vanillin test (8), Arval tannin content was 5.30 (expressed as catechin equivalent percentage of original sample dry matter) and that of Argence was 0.10. Table 1 collects these figures, and the yields of crude extract and tannin after gel permeation expressed as percentage of original sample dry matter and crude extract, respectively.

The total ion chromatograms (TIC) of the Arval and Argence tannin fractions after pyrolysis at 600 °C are shown in figures 1 and 2, respectively. Table 2 collects the eight most abundant ions in the mass spectra of the main peaks. The identification proposed for most of the pyrolysis fragments is reported in table 3. The fragmentation under pyrolysis was similar for the two samples, but the quantitative analysis (relative percentages) was substantially different (table 3). Catechol (identified by both mass spectrometry and injection of pure standard) was the main fragment (55.4%) in the pyrogram of Arval tannin (fig. 1, peak no. 24), whereas it was only 4.58% in that of

Table 3. Relative percentage and proposed identification of the main pyrolysis peaks in the two sorghum tannins Arval and Argence.

#	Arval	Argence	Compound
1	9.00	14.15	carbon dioxide
2	trace	trace	unknown
3	0.82	-	acetone
4	5.28	6.88	unknown
5	6.47	17.40	propylacetate
6	5.95	-	3-methylfuran
7	0.56	4.75	2-furanol, tetrahydro-2,3-dimethyl
8	0.34	0.94	unknown
9	0.67	0.27	3-furaldehyde
10	0.94	1.42	pyridine
11	0.20	0.15	toluene
12	1.28	0.71	unknown
13	1.16	-	unknown
14	0.33	-	unknown
15	0.30	0.39	unknown
16	1.51	17.69	phenol
17	1.09	0.88	unknown
18	0.22	1.17	unknown
19	0.51	1.80	4-methylphenol
20	0.62	3.81	guaiacol
21	0.45	0.28	unknown
22	0.17	0.36	unknown
23	0.52	2.53	ethylphenol
24	55.4	4.58	catechol
25	0.10	7.06	2-ethenylphenol
26	7.25	1.89	dihydroxytoluene



Scheme 1. Catechin (flavan-3-ol).

Table 1. Polyphenol estimation using the vanillin test (% of catechin equivalents (CE)), crude extract yield (% of original sample dry matter), and polyphenol yield (% of crude extract).

	CE	crude extract	polyphenol
Arval	5.30	2.40	43.0
Argence	0.10	1.81	3.4

Table 2. Eight-peak mass spectra of the pyrolysis fragments of Arval sorghum tannin.

#	scan	MW	m/z (%)							
1	142	44	44(100)	45(40)	43 (1)	-	-	-	-	-
2	147	-	43(100)	41(68)	42(38)	49(38)	45(36)	47(33)	48(30)	55(17)
3	151	58	58(100)	59(45)	42(44)	60(13)	44(12)	57(9)	40(7)	45(5)
4	155	-	43(100)	59(36)	42(13)	58(10)	41(4)	40(3)	44(3)	60(2)
5	169	102(0.2)	43(100)	61(25)	45(19)	42(15)	44(4)	41(1)	71(1)	59(1)
6	177	82	82(100)	53(91)	81(78)	50(43)	51(41)	52(18)	83(14)	54(12)
7	192	116	43(100)	75(12)	42(11)	57(7)	41(6)	44(6)	45(3)	40(2)
8	201	-	43(100)	45(58)	57(45)	74(34)	42(29)	73(27)	75(23)	41(22)
9	211	96	96(100)	95(94)	53(75)	51(56)	50(48)	43(39)	67(25)	52(22)
10	231	79	52(100)	79(91)	50(66)	43(62)	51(55)	80(37)	78(12)	53(11)
11	245	92	91(100)	92(50)	63(19)	65(18)	43(15)	41(11)	45(10)	50(10)
12	251	-	43(100)	85(25)	101(18)	100(14)	42(10)	45(4)	72(4)	44(3)
13	261	-	55(100)	43(60)	41(55)	83(48)	53(18)	42(17)	99(17)	98(13)
14	269	-	41(100)	55(76)	70(47)	43(36)	42(29)	69(25)	53(18)	56(12)
15	406	-	41(100)	53(53)	96(47)	42(44)	67(44)	55(38)	69(34)	81(34)
16	417	94	94(100)	66(65)	65(38)	63(23)	50(21)	40(17)	51(14)	53(12)
17	461	-	57(100)	41(99)	55(40)	43(39)	56(29)	70(27)	105(21)	83(20)
18	492	-	91(100)	45(83)	77(78)	128(72)	107(61)	108(61)	79(56)	69(50)
19	510	108	107(100)	108(85)	77(58)	79(50)	51(38)	50(31)	53(27)	63(23)
20	527	124	109(100)	81(99)	124(72)	53(54)	51(34)	52(33)	50(29)	63(14)
21	559	138	81(100)	43(40)	41(39)	54(30)	64(28)	42(25)	53(20)	138(10)
22	585	-	43(100)	55(30)	42(27)	107(15)	44(14)	51(13)	101(12)	69(12)
23	600	122	107(100)	77(43)	122(34)	41(22)	51(22)	53(17)	79(15)	50(14)
24	631	110	110(100)	63(38)	64(35)	53(30)	81(25)	51(18)	50(17)	82(17)
25	647	120	120(100)	91(97)	69(78)	41(48)	42(42)	57(23)	119(23)	73(22)
26	718	124	124(100)	78(75)	123(50)	51(42)	77(33)	67(20)	53(20)	106(18)



Argence tannin (fig. 2). In the latter, the main fragment was phenol (peak no. 17, 17.7%), which accounted for only 1.51% of Arval tannin TIC. Total phenolic content was also different in the pyrograms of the two tannins, i.e. 65.91% in Arval and 40.23% in Argence. The relative quantities of catechol were consistent with the results of the tannin colorimetric assay of the two sorghum cultivars reported in table 1, i.e. high percentage of catechol in Arval and low in Argence. In another work (13), it was also observed that catechol was present in non-significant amounts in the pyrogram of a non-tannin polyphenol such as lignin. The pyrolysis of catechin under the same conditions of tannins yielded catechol as the single degradation product (fig. 3). A black residue was observed in the quartz sample holder after pyrolysis, probably due to some polymerization reactions undergone by the other moiety of the molecule, which might explain the lack of other pyrolysis fragments. Increasing the temperature of pyrolysis up to 900 °C did not change the fragmentation. The reproducibility of triplicate pyrolysis of catechin was good (fig. 4).

## CONCLUSION

PY-GC-MS analysis of condensed tannins containing catechin-like monomeric units shows catechol as main fragment. This compound is of diagnostic significance for condensed tannins not only because it is originated by a simple cleavage of one of its monomeric units, but also because it is peculiar of this class of polyphenols and not, for instance, of another class of polyphenols widespread in nature such as lignin, and because its formation under pyrolysis is quantitatively reproducible. Further studies are underway to screen a larger set of samples, to establish a quantitative correlation between the amount of catechin subjected to pyrolysis and the quantity of produced catechol, and to determine its range of linear response. If the preliminary results of the present work will be confirmed on a more quantitative basis, pyrolysis affords the prospect of a rapid and specific analysis of tannins by gas chromatography, a technique so far neglected for tannins, without the need of cumbersome sample preparation and derivatization.

## REFERENCES

1. Haslam, E. (1966) *Chemistry of Vegetable Tannins*, Academic Press, London and New York.
2. Goldstein, J.L., Swain, T. (1963) *Phytochemistry* 2, 371.
3. Goldstein, J.L., Swain, T. (1965) 4, 185.
4. Bate-Smith, E.C., Swain, T. (1953) *Chem. Ind.* April 18, 377.
5. Gujer, R., Magnolato, D., Self, R. (1986) *Phytochemistry* 25, 1431.
6. Self, R., Eagles, J., Galletti, G.C., Mueller-Harvey, I., Hartley, R.D., Lea, A.G.H., Magnolato, D., Richli, U., Gujer, R., Haslam, E. (1986) *Biomed. Environ. Mass Spectrom.* 13, 449.
7. Price, M.L., Butler, L.G. (1977) *J. Agric. Food Chem.* 25, 1628.
8. Price, M.L., Van Scoyoc, S., Butler, L.G. (1978) *J. Agric. Food Chem.* 26, 1214.
9. Hagerman, A.E., Butler, L.G. (1980) *J. Agric. Food Chem.* 28, 947.
10. Maxson, E.D., Rooney, L.W. (1972) *J. Cereal Chem.* 49, 719.
11. Chiavari, G.C., Vitali, P., Galletti, G.C. (1987) *J. Chromatogr.* 392, 426.
12. Galletti, G.C., Self, R. (1986) *Ann. Chim. (Rome)* 76, 195.
13. Piccaglia, R., Galletti, G.C., Traldi, P. (1990) *J. High Res. Chrom.* 13, 52.

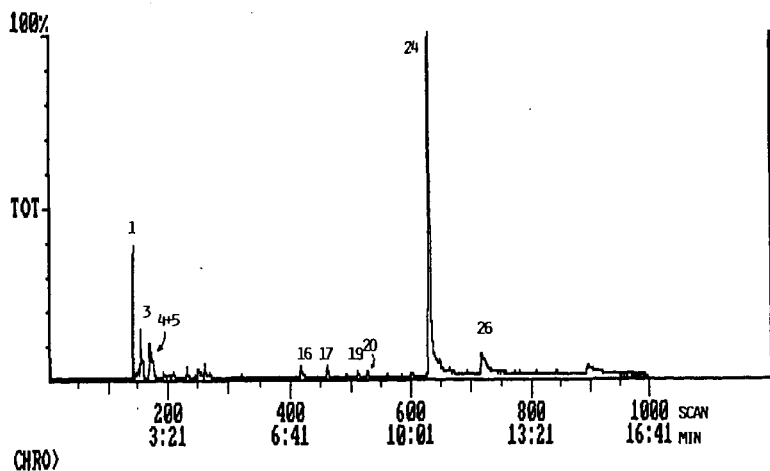


Fig. 1. Total ion chromatogram of Arval sorghum tannin after pyrolysis at 600 °C.

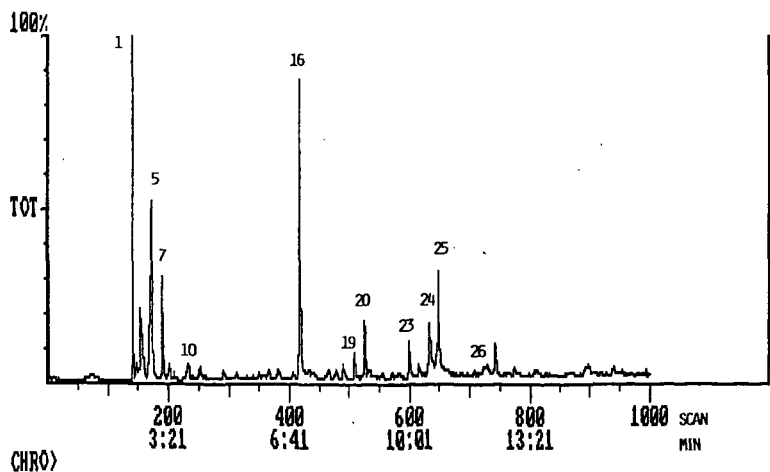


Fig. 2. Total ion chromatogram of Argence sorghum tannin after pyrolysis at 600 °C.

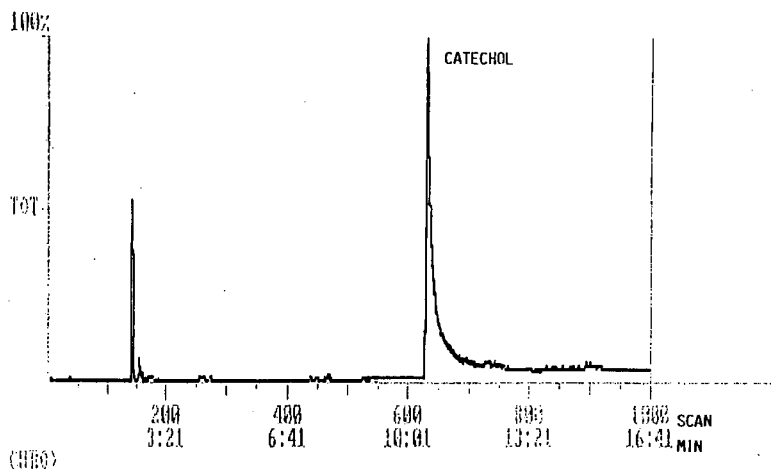


Fig. 3. Total ion chromatogram of catechin after pyrolysis at 600 °C.

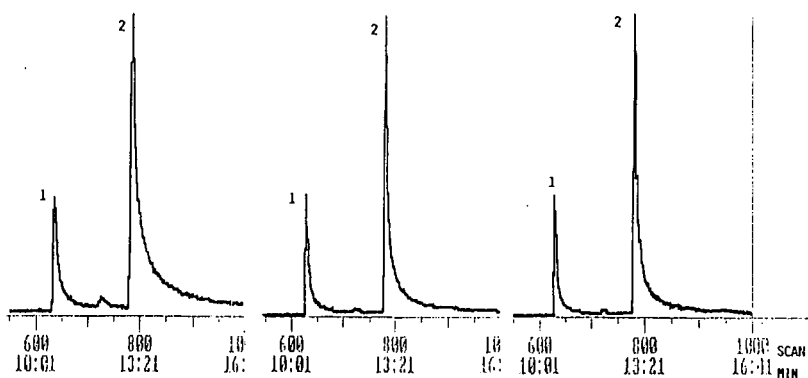


Fig. 4. Replicate pyrolysis of catechin under the same conditions of figure 1-3. (1) catechol, (2) p-hydroxybenzaldehyde which was added in view of its possible use as an internal standard in future quantitative experiments.

## A NOVEL POLYPHENOL BIOPOLYMER ISOLATED FROM FOSSIL SEEDS: AN ALTERNATIVE SOURCE FOR (ALKYL)PHENOL MOIETIES IN COALS.

Pim F. van Bergen<sup>\*,\*</sup>, Margaret E. Collinson<sup>\*</sup>, Jaap S. Sinninghe Damsté<sup>\*</sup> and Jan W. de Leeuw<sup>\*</sup>.

<sup>\*</sup>Organic Geochemistry Unit, Delft University of Technology,  
De Vries van Heystplantsoen 2, 2628 RZ Delft, The Netherlands.

<sup>\*</sup>Biosphere Sciences Division, King's College London,  
Kensington Campus, Campden Hill Road, London, W8 7AH, UK.

Keywords: Polyphenol biopolymer, fossil seeds, selective preservation

### INTRODUCTION

During the last years several papers have been published on the chemical composition of recognizable higher plant remains in sediments (e.g. spores, pollen<sup>1</sup>, cuticles<sup>2,3</sup>, bark<sup>4,5</sup>, wood remains<sup>6</sup>). It is thought that these tissues have survived in the geological record because they are comprised of highly resistant biopolymers such as cutan<sup>3</sup>, suberan<sup>4</sup> and lignin<sup>6</sup>, whose chemical structures are only slightly modified during sediment diagenesis.

Within this context seeds have hardly been studied. To some extent this is remarkable since they are often produced in large amounts. Alternatively, if few seeds are produced they can be of large size. Extremes in this respect are orchids with produce over one million seeds per fruit per year (each weighing 5 µg) and the Seychelles coconut with a production of perhaps ten seeds in a lifetime weighing 20 kg each. Perhaps more important from a geochemical point of view, seeds possess protective envelopes derived from the integuments of the ovule. They comprise the seed coat and include the testa and tegmen at least one layer of which often becomes tough and sclerotic at biological maturity. The testa is a product of the outer integument whereas the tegmen is produced by the inner integument occurring inside the testa. On morphological features the tegmen is comparable to a cuticle. The protective layers represent only a few percent of the total biomass of the produced seed. However, in most cases it are only the seed coats that are found in the geological record, because the outer layers of seeds contain resistant compounds to protect the genetic material against physical and chemical processes such as temperature and humidity changes and bacterial and fungal attacks. Hence, seeds, and particularly their resistant layers, have a large potential to enter the geosphere and may become selectively enriched.

In this study outer and inner layers (testae and tegmens, respectively) of Late Eocene seeds of *Stratiotes* (water soldier) and *Sabrenia* (fossil water lily) were analyzed by means of flash pyrolysis-gas chromatography-mass spectrometry and flash pyrolysis-gas chromatography in order to test the above mentioned hypothesis. The testa of the studied seeds is a sclerotic layer, whereas the tegmen is a translucent tissue comparable to a cuticle. The *Sabrenia* seeds are obtained from the Brembridge Marls Member, Bouldnor Formation, Hamstead Ledge, Isle of Wight. The *Stratiotes* seeds are obtained from the Totland Bay Member, Headon Hill Formation, Hordle Cliff, Hampshire. In addition a comparison is made between the pyrolysate of the *Sabrenia* testae and the Beulah Zap lignite<sup>7</sup>. This coal sample was obtained from the Sentinel Butte Formation of the Fort Union Group (Upper Palaeocene), Mercer County, North Dakota.

### EXPERIMENTAL

The fossil testae and tegmens were dissected by hand. The samples were ultrasonically extracted with methanol. The residues were dried in a vacuum stove at 30°C.

Curie-point pyrolysis-gas chromatography (PY-GC) analyses were performed with a Hewlett-Packard 5890 gas chromatograph using a FOM-3LX unit for pyrolysis. The samples were applied to a ferromagnetic wire. The Curie temperature was 610°C. The gas chromatograph, equipped with a cryogenic unit, was programmed from 0°C (5 min) to 320°C (20 min) at a rate of 3°C/min. Separation was achieved using a fused-silica capillary column (25m x 0.32mm) coated with CP Sil-5 (film thickness 0.4 µm). Helium was used as the carrier gas.

The Curie-point pyrolysis-gas chromatography-mass spectrometry (PY-GC-MS) analyses were performed using the same equipment and conditions as described above for the PY-GC connected with a VG 70S mass spectrometer operated at 70 eV with a mass range  $m/z$  40-800 and a cycle time of 1.8 s.

## RESULTS AND DISCUSSION

The pyrolysates of the fossil tegmens of both *Stratiotes* and *Sabrenia* seeds are dominated by series of  $n$ -alkanes and  $n$ -alk-1-enes. In addition, the pyrolysate of the *Sabrenia* tegmens shows the distinct presence of isoprenoids. *Prist-1-ene* is the most abundant compound. Since  $\delta$ -tocopherol was also detected, this compound is thought to be the precursor of the observed isoprenoids<sup>8</sup>. The  $n$ -alk-1-enes and  $n$ -alkanes detected in pyrolysates of the tegmens are thought to be derived from a highly aliphatic biopolymer comparable to cutan<sup>3</sup>.

On the contrary, the main compounds in the pyrolysate of the fossil testae of *Stratiotes* and *Sabrenia* are phenol and  $C_1$  and  $C_2$  alkylated phenols (Table 1). In addition, some methoxyphenols and benzenediols (mainly benzene-1,2-diols) are present. The abundance of these latter compounds is very low in the pyrolysate of the *Stratiotes* testae. The identification of these compounds was confirmed by comparison of mass spectra and relative retention times with those of authentic standards. The methoxyphenols present in these pyrolysates are not derived from lignin, since the distribution of these compounds in lignin pyrolysates is completely different<sup>6</sup>. The phenols and benzenediols detected are thought to be pyrolysis products of a novel polyphenol biopolymer.

The seeds of *Stratiotes* as well as *Sabrina* are produced under or near the water surface. In these environments fungal activities are prominent. Since phenols are known to possess fungicidal properties<sup>9</sup>, it is thought that the outer layer (testa) contains a polyphenol biopolymer as an additional protective shield for the genetic material. Hence, physical as well as chemical protection is conferred by the sclerotic testa.

As mentioned earlier the tegmen occurs inside the testa as a cuticle based on biological features. This similarity of tegmen and cuticle is supported by pyrolysis data since a highly aliphatic biopolymer comparable to cutan has been recognized as a constituent of tegmens.

The distribution patterns of the phenols and benzenediols in the pyrolysates of the testae are remarkably similar to those in the pyrolysate of the Beulah Zap lignite (Table 1; Fig. 1). This indicates that selective preservation of this novel biopolymer may be an alternative for the proposed demethoxylation of lignins<sup>10</sup> to explain the presence of phenol moieties in coals. Whether these phenol moieties in coal are derived from testae only remains to be seen, because this novel biopolymer may also occur in other tissues of water plants not yet investigated.

## CONCLUSIONS

The two anatomically different seed layers of fossil *Stratiotes* and *Sabrenia*, tegmen and testa, respectively, show remarkable differences in chemical composition. The tegmens are mainly comprised of an aliphatic biopolymer comparable to cutan whereas the sclerotic testae contain a novel polyphenol biopolymer.

The highly similar distribution pattern of phenols and benzenediols observed in both pyrolysates of testae and lignites strongly indicates that selective preservation of the novel biopolymer may be an alternative for the proposed demethoxylation of lignins to explain the presence of phenol moieties in coals.

## REFERENCES

1. Schenck, P.A., de Leeuw, J.W., Van Graas, G., Haverkamp, J. and Bouman, M. (1981), In: Organic Maturation Studies and Fossil Fuel Exploration 1981 (ed. J.Brooks), Academic Press, London. 225-237.
2. Nip, M., Tegelaar, E.W., Brinkhuis, H., de Leeuw, J.W., Schenck, P.A. and Holloway, P.J. (1986), *Org.Geochem.*, **10**: 769-778.
3. Tegelaar, E.W., de Leeuw, J.W., Largeau, C., Derenne, S., Schulten, H-R., Muller, R., Boon, J.J., Nip, M. and Sprenkels, J.C.M. (1989), *J.Anal.Appl.Pyrolysis*, **15**: 29-54.
4. Tegelaar, E.W., Hollman, G., Van der Vegt, P., de Leeuw, J.W. and Holloway, P.J. (1990), In: Resistant biomacromolecules in morphologically characterized constituents of kerogen: a key to the relationship between biomass and fossil fuels (ed. E.W.Tegelaar). PhD thesis, University of Utrecht.
5. Wilson, M.A. and Hatcher, P.G. (1988), *Org.Geochem.*, **12**: 539-546.
6. Saiz-Jimenez, C. and de Leeuw, J.W. (1986), *Org.Geochem.*, **10**: 869-876.
7. Smith, K.L. and Smoot, L.D. (1990), *Prog.Energy Combust.Sci.* **16**: 1-53.
8. Goossens, H., de Leeuw, J.W., Schenck, P.A. and Brassell, S.C. (1984), *Nature*, **312**: 440-442.
9. Waller, G. (1987), Allelochemicals: Role in agriculture and forestry. *Am.Chem.Soc.Symp.Series* **330**.
10. Senftle, J.T., Larter, S.R., Bromley, B.W. and Brown, J.W. (1986), *Org.Geochem.* **2**: 345-350.

Table 1: Major identified peaks in pyrolysates of *Sabrenia testae* and the Beulah Zap lignite (Fig. 1)

---

1.	Phenol
2.	2-Methylphenol
3.	2-Methoxyphenol
4.	3-Methylphenol and 4-Methylphenol
5.	2,4-Dimethylphenol
6.	4-Ethylphenol
7.	4-Methyl-2-methoxyphenol
8.	Benzene-1,2-diol
9.	C <sub>8</sub> -phenol
10.	4-ethyl-2-methoxyphenol
11.	4-methyl-benzene-1,2-diol

---

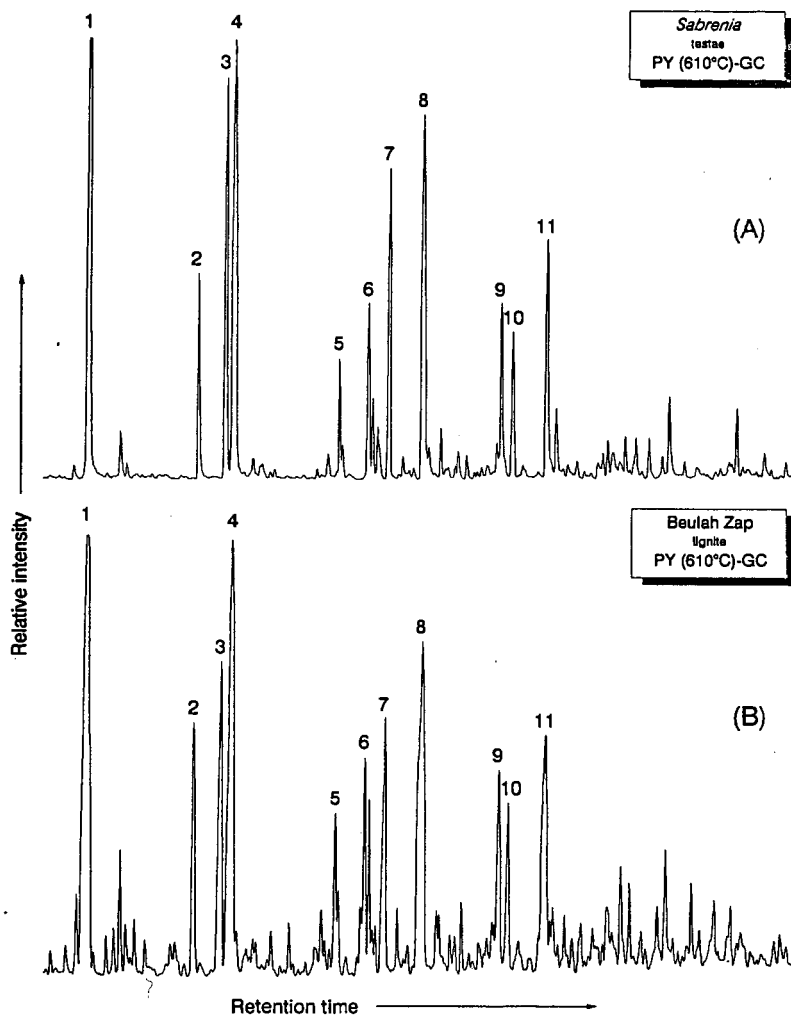


Fig. 1: Partial gas chromatogram of flash pyrolysates of *Sabrenia testae* (A) and the Beulah Zap lignite (B).

## PYROLYSIS OF NATURAL RUBBER, WAXES AND RESINS WITH ZEOLITIC CATALYSTS.

Sara Gnecco, Ruby Cid, Victoria Caamano and Attila E. Pavlath\*

Laboratorio de Recursos Renovables. Facultad de Ciencias, Universidad de Concepcion, Casilla 3-C, Concepcion-Chile and \*Western Regional Research Center, U.S.D.A., 800 Buchanan St., Albany, C.A. 94710. U.S.A.

### INTRODUCTION

In recent year there has been considerable interest in developing renewable resources, as alternatives to petroleum based substances. Oil and hydrocarbon producing plants, mostly growing in arid regions, are especially promising candidates to produce important chemical intermediates and fuels. (1-4).

In previous work (5,6), we have evaluated chemically the potential of some Chilean species growing in arid lands as hydrocarbon producing crops. Among the studied species, Euphorbia lactiflua, Euphorbia copiapina, Tessaria absinthioides and Bulnesia chilensis turned out to be promising sources of polyisoprene and/or n-paraffins. Their extracts are potential starting materials for fuels and/or chemicals through pyrolytic reactions. However, it is necessary to study the effect of various catalysts on the pyrolysis and identify the most promising ones, in order to utilize economically these plants.

Most of the work on the pyrolytic reactions of biomass were carried out with the carbohydrates. (8). There is very little known on the influence of catalysts, pretreatments and other reaction conditions on the compounds obtainable through the pyrolysis of the extracts from latex producing plants. It has been reported that mixtures of ethylene, propylene, toluene, xylenes, C<sub>5</sub> through C<sub>20</sub> nonaromatics, and C<sub>1</sub> to C<sub>4</sub> alkanes can be obtained when these extracts are pyrolyzed in the presence of ZSM-5, a molecular shape-selective zeolitic catalyst developed by Mobil Oil Corporation (7).

It is difficult to tailor-make "a priori" a catalyst for all the types of reaction that take place in converting biomass extracts to valuable chemicals. However, we theorize that owing to their acidic and structural properties, such as larger pore size and central cavity size than those of



ZSM-5, thermostable zeolitic faujasites would be appropriate. Some bi-functional catalysts, e.g. Pt/faujasite, would be also good candidates to improve reduction of carbonyl groups and to diminish the formation of coke which deactivates the catalyst.

To assess the possibility of obtaining fuels, the main components of  $\text{CH}_2\text{Cl}_2$  extracts from Chilean species, i.e., polyisoprene, n-paraffins and resins, were pyrolyzed with various zeolitic catalysts, utilizing different heating rates and substrate/catalyst (S/C) ratio. Conversion degree and best conditions of pyrolysis were estimated by means of thermogravimetry and differential scanning calorimetry.

## EXPERIMENTAL

### Extraction, fractionation and analysis.

Plant species were collected from the wild, in the North of Chile (III and IV Regions). Voucher specimens were kept at the University of Concepcion Herbarium (Conc.). Samples of latex from Euphorbia lactiflua were collected by tapping wild plants.

Dried milled samples were extracted in a Soxhlet apparatus with  $\text{CH}_2\text{Cl}_2$  for 40 hours. After the evaporation of the solvent, the solids were again extracted using acetone to obtain acetone-soluble and acetone-insoluble fractions. Representative fractions were characterized by quantitative analysis, IR,  $^1\text{H}$  and  $^{13}\text{C}$  NMR spectroscopy, TLC and GC (5,6). Results are given in Table 1.

### Isolation and Characterization of main components.

#### n-Paraffins.

Acetone-insoluble fractions were refluxed in a suspension of activated carbon, Johns-Manville cellite and hexane, filtered and dried to obtain the fractions of refined hydrocarbons which were analyzed by IR,  $^1\text{H}$  NMR,  $^{13}\text{C}$  NMR, and GC. (5).

NMR and IR spectra of refined hydrocarbons from different species revealed almost exclusively the presence of n-paraffins. The identification of hydrocarbons was carried out by the comparison of RRT data with those of authentic standards. The results revealed the presence of n-alkanes mixtures with chain lengths varying from n-nonadecane (n-C<sub>19</sub>) to n-tritriacontane (n-C<sub>33</sub>). In the mixture, n-heptaeicosane (n-C<sub>27</sub>), n-

nonaeicosane (n-C<sub>29</sub>) and n-hentriacontane (n-C<sub>31</sub>) were the dominant alkane components.

### Rubber

Fresh latex from *E. lactiflua* was mixed with C<sub>2</sub>Cl<sub>4</sub>. After removing the azeotrope, the solid was dried at 50°C for 12 hours. Dry latex was dissolved in CH<sub>2</sub>Cl<sub>2</sub>, then filtered, and the solution was added drop by drop to methanol. The precipitate was centrifuged, dried in a vacuum oven at 50°C for 2 hours and weighed. The yield was 8.05% in dry latex weight basis. The characterization was done by IR, NMR spectroscopy (<sup>13</sup>C and <sup>1</sup>H) and TLC. All the data obtained agreed with those given in literature for *cis*-1,4-polyisoprene.

### Resins

Resins isolated through successive fractionation of dry latex from *E. lactiflua* and CH<sub>2</sub>Cl<sub>2</sub> extract from *C. odorifera* were characterized by I.R., <sup>13</sup>C NMR and TLC with standards (5). The main components were: sterols (B-sitosterol-type), fatty alcohols (oleic-type), fatty acids (oleic-type).

### Preparation and Characterization of Catalysts

Series of HNaY, MNaY and M<sub>1</sub>M<sub>2</sub>NaY (M = Pt, Co, Mo) zeolites were prepared by impregnation or partial sodium exchange of a NaY zeolite faujasite-type (Linde, Si/Al = 2.4) with NH<sub>4</sub><sup>+</sup> or suitable metallic ions. The degree of ionic exchange was determined by atomic absorption sodium analysis in the filtrate. Dehydration, deamination and dehydroxilation were carried out at 110°C, 250-420°C and 480-550°C respectively. Reduction of PtNaY catalyst was carried out with H<sub>2</sub> at 520°C (9-10).

The crystallinity of the exchanged zeolites was determined by X-ray diffraction using the powder method (11). The specific areas of the prepared zeolites were determined by the absorption method of N<sub>2</sub>. The analysis were performed in a volumetric BET conventional equipment at -196°C (12). The number of acid centers and their relative strengths were determined by a potentiometric method (13). Results are given in Table 2.

### Thermogravimetric analysis.

*C. odorifera* n-paraffins, *E. lactiflua* polyisoprene and *E. copiapina* resins were selected as model substrates. The rate of weight loss, and the

weight of the residue of each substrate, catalyst, and mixtures S/C, were determined in a T.G.A. under  $N_2$ . A temperature range of 50-550°C and heating rates of 20, 40 and 80 degrees/min were used. The results for samples S/C = 1/1 (wt/wt) are given in Table 3. Percents of total weight loss (substrate + catalyst) were corrected and are given in percent of weight loss of the substrate.

### DSC analysis

Calorimetric studies were carried out on a DSC-system, upon heating from 30 to 500°C at 80°C/min. The samples were sealed in aluminum pans with a pinhole on top for the escape of volatiles, which were flushed out of the reaction zone with a constant flow of  $N_2$ .

## RESULTS AND DISCUSSION

According to the results of Table 3, as the heating rate increases, the  $T_{infl}$  also does. The  $T_{infl}$  is around 330 to 390°C and it is higher for the substrates without catalyst. The percent of weight loss at this point is from 37 to 64%, therefore it could be assumed that most of the pyrolytic products are formed around 400°C.

Results for samples S/C = 9/1 (wt/WT) are not given because were not reproducible. This may be due to the fact that it is very difficult to obtain homogeneous samples with this ratio, and a small error in the quantity of catalyst may cause a large error in the results.

In the DSC analysis, the pyrolysis of the mixtures S/C = 1:1 (wt/wt) could be separated into two large and broad peaks: one endothermic, with maxima around 200°C, the other, exothermic, with maxima around 430°C.

Below 300°C a minimal amount of volatile material is generated (Table 3), and the first range endothermic peak is probably due to melting and minor scissions. On the other hand, the second range temperature, exothermic peak, is located, within the experimental error, in the zone of maxima volatilization rate (Table 3), therefore, an extensive decomposition seems to take place around 400°C.

The temperature of the maxima of the exothermic peak is lower for most of mixtures S/C than for the substrates without catalyst showing that they speed up the pyrolysis.

## CONCLUSIONS

General conclusions emerging from the results are:

- The catalysts speed up the process of pyrolysis and enhances the percent of conversion of all substrates.
- The better conditions for the catalytic pyrolysis would be temperatures around 400°C and higher heating rate.
- Regarding the percentage of conversion (% wt final), the catalysts that seem to direct more efficiently the pyrolysis of the extracts of hydrocarbon producing plants to mixtures with low C/H ratio, besides ZSM-5, were: Co(1)NaY, Mo(2)NaY and Co(1) Mo(0.5)NaY.

## Continuing work.

The composition of pyrolytic volatile products and theirs combustion heats are being investigated to make the final conclusions about the most suitable pyrolytic conditions. Further results from these studies will be reported in the near future.

## ACKNOWLEDGEMENTS.

The authors wish to thank to Research Office, University of Concepcion (DI 20.13.70), FONDECYT (Proj. 687/89) and Program in Science and Technology Cooperation, Agency for International Development (Grant DPE-5542-G-SS-8029-00) for financial support.

## REFERENCES

1. M. Calvin, Science, **219**, 24 (1983).
2. G.E. Wickens, J.R. Gooding, D.V. Field Eds. "Plant for arid lands", London (1985).
3. M.E. Carr et. al. J.A.O.C.S., **62**, 136/ (1985).
4. E.A. Davis, J.L. Kuester, M.O. Bagby, Nature, **307**, 726 (1984).
5. S. Gnecco, J. Bartulin, C. Marticorena, A. Ramirez, Biomass **15**, 165-173 (1988).
6. S. Gnecco, J. Bartulin, C. Marticorena, J. Becerra, Phytochemistry, **28** (4) 1254-1256 (1989).
7. P.W. Weisz, W.O. Haag and P.G. Rodewald, Science, **206**, 57 (1979).
8. M.J. Antal, Advances in Solar Energy, American Solar Energy Society, Boulder, Colorado 1983, p. 61.
9. R. Cid, M.E. Konig, R. Arriagada, Applied Catalysis, **2**, 189-194 (1982).
10. R. Cid, R. Arriagada, F. Orellana, J. Catal. **80**, 228-230, (1983).
11. R. Cid, R. Arriagada, F. Orellana, Bol. Soc. Chil. Quim. **30** (2), 63-67 (1985).
12. R. Cid, F. Orellana and A. Lopez-Agudo, Applied Catalysis **32**, 327-336 (1987).
13. R. Cid, G. Pecchi, Applied Catalysis, **14**, 15-21 (1985).

**TABLE 1**  
**YIELD, MOLAR RATIO C/H OF REPRESENTATIVE FRACTIONS AND**  
**POLYMERIC HYDROCARBON TYPE FROM SOME CHILEAN SPECIES**

SPECIES	CH <sub>2</sub> Cl <sub>2</sub>	EXTRACT	ACETONE-INSOLUBLE POLYMERIC		HYDROCAR- BON TYPE <sup>C</sup>
	YIELD <sup>A</sup>	C/H RATIO <sup>B</sup>	YIELD <sup>A</sup>	C/H RATIO <sup>B</sup>	
<u>E. LACTIFLUA</u>	10.80	0.52	2.90	0.48	NR, WAXES
<u>E. COPIAPINA</u>	11.70	0.57	3.10	0.51	NR <sup>D</sup> , WAXES
<u>C. ODORIFERA</u>	4.50	0.54	2.20	0.48	NR <sup>D</sup> , WAXES
<u>C. SALICIFOLIA</u>	5.30	0.55	1.60	0.49	NR <sup>D</sup> , WAXES
<u>T. ABSINTHIOIDES</u>	7.40	0.57	1.32	0.52	WAXES

A. Given as a percentage of plant dry weight; average value of extracts from 2-3 plant samples

B. C/H molar ratio calculated from quantitative analysis data

C. NR=natural rubber (cis-1,4-polyisoprene) identified by spectroscopic data

D. Traces.

**TABLE 2. CHARACTERISTICS OF THE PREPARED ZEOLITES**

DEGREE OF I.E. OR IMPREGNATION	SOLID DENOMINA- TION	CRYSTAL- LINITY %	S BET (M <sup>2</sup> G <sup>-1</sup> )	RELATIVE ACID STRENGTH
40% NH <sub>4</sub>	H(40)-NAY	100	726	STRONG
64% NH <sub>4</sub>	H(64)-NAY	100	713	STRONG
0.5 Wt % Pt	Pt (0.5)-NAY	100	680	WEAK
1Wt% Co(AS CO <sub>3</sub> O <sub>4</sub> )	Co (1)-NAY	100	722	MODERATE
2Wt% Mo(AS MoO <sub>3</sub> )	Mo (2) NAY	85	615	MODERATE
1Wt% Co (ASCO <sub>5</sub> O <sub>4</sub> )	Co (1) Mo (0.5)-NAY	90	710	MODERATE

I.E. =Ionic exchange

TABLE 3. THERMOGRAVIMETRIC ANALYSIS FOR MIXTURES S/C=1/1  
wT/wTD.

n	CATALYST	HEATING RATE (DEGREE/min.	T. INF. (°C)	%W. L. INF.	T <sub>F</sub> (°C)	%WL. F.
P	-	20	370	64.0	430	95.4
A	ZSM-5	20	350	50.6	480	91.0
R	H(40)NAY	20	320	51.8	460	93.5
A	H(64)NAY	20	330	46.6	450	92.5
F	Pt(0.5)NAY	20	315	23.9	450	68.7
F	Co(1)NAY	20	310	39.1	450	89.7
I	Mo(2)NAY	20	325	38.5	450	98.2
N	Co(1)Mo(0.5)NAY	20	320	41.8	450	94.8
S	-	40	390	55.2	480	85.9
	ZSM-5	40	360	46.2	480	84.4
	H(64)NAY	40	350	45.4	470	94.6
	Pt(0.5)NAY	40	330	24.5	460	61.8
	Co(1)NAY	40	330	37.6	450	90.8
	Mo(2)NAY	40	350	38.1	450	91.5
	Co(1)Mo(2)NAY	40	340	37.8	490	88.3
	-	80	420	53.0	490	82.9
	ZSM-5	80	390	40.0	470	89.7
	H(40)NAY	80	380	43.9	460	89.5
	H(64)NAY	80	360	46.7	480	92.2
	Mo(2)NAY	80	390	45.0	510	92.0
R	-	20	350	46.1	450	82.1
	ZSM-5	20	310	41.6	350	84.4
E	H(40)NAY	20	310	37.5	450	77.4
S	H(64)NAY	20	295	38.2	400	75.4
I	Pt(0.5)NAY	20	270	27.9	400	60.0
N	Co(1)NAY	20	300	36.9	450	75.0
S	Mo(2)NAY	20	320	48.4	450	98.4
	Co(1)Mo(0.5)NAY	20	300	43.7	400	83.6
	-	40	380	41.4	450	78.3
	ZSM-5	40	350	44.8	460	80.5
	H(40)NAY	40	330	40.9	420	81.8
	H(64)NAY	40	310	40.2	400	82.4
	Pt(0.5)NAY	40	300	34.8	450	77.0
	Co(1)NAY	40	300	43.9	450	95.2
	Mo(2)NAY	40	330	49.6	450	97.4
	Co(1)Mo(0.5)NAY	40	330	38.9	450	87.3

Continuation of TABLE 3.

CATALYST	HEATING RATE (DEGREE/min.	T <sub>INF.</sub> (°C)	%W. L. INF.	T <sub>F</sub> (°C)	%WL. F.
P -	20	390	42.9	460	82.9
O ZSM-5	20	385	50.0	450	91.5
L H(40)NAY	20	375	49.8	450	78.4
Y H(64)NAY	20	370	38.1	480	72.4
I Pt(0.5)NAY	20	400	36.6	470	57.4
S Co(1)NAY	20	350	31.5	450	91.9
O Mo(2)NAY	20	350	29.2	450	71.9
P Co(1)Mo(0.5)NAY	20	370	48.4	450	87.4
R					
E -	40	406	33.1	490	88.4
N ZSM-5	40	390	42.8	500	96.1
E H(40)NAY	40	390	47.3	470	88.6
H(64)NAY	40	370	40.3	480	80.8
Pt(0.5)NAY	40	340	25.3	500	75.0
Co(1)NAY	40	380	34.2	500	96.2
Mo(2)NAY	40	370	37.3	450	88.6
Co(1)MO(0.5)NAY	40	385	48.1	450	89.8
-	80	425	51.1	510	93.3
ZSM-5	80	400	46.6	500	97.7
H(40)NAY	80	390	42.5	460	86.0
H(64)NAY	80	400	39.2	480	79.4
Mo(2)NAY	80	410	45.0	510	82.1

T<sub>INF.</sub> = Temperature at inflection point%WL INF. = % of weight loss at T<sub>INF.</sub>I<sub>F</sub> = Temperature where no more weight loss occurs%WL<sub>F</sub> = % of weight loss at T<sub>F</sub>.

**ALKYLPYRROLES IN KEROGEN PYROLYSATES:  
EVIDENCE FOR ABUNDANT MACROMOLECULARLY-BOUND  
TETRAPYRROLE PIGMENTS**

Jaap S. Sinninghe Damsté\*, Timothy I. Eglinton\*# and Jan W. de Leeuw\*

\*Delft University of Technology, Faculty of Chemical Engineering  
and Materials Science, Organic Geochemistry Unit, De Vries van  
Heystplantsoen 2, 2628 RZ Delft, The Netherlands.

#Fye Laboratory, Department of Chemistry, Woods Hole  
Oceanographic Institution, Woods Hole, MA 02543, U.S.A.

Keywords: alkylpyrroles, kerogen pyrolysates, macromolecularly-bound tetrapyrrole pigments

## INTRODUCTION

Porphyrins and related compounds are well known biological markers often applied in geochemistry.<sup>1,2</sup> These tetrapyrrole pigments also occur in kerogen since upon off-line pyrolysis of kerogen DPEP- and ETIO-porphyrins are released.<sup>3</sup> Recently, Barakat and Yen reported that major amounts of 3-ethyl-4-methyl-1*H*-pyrrole-2,5-dione and, to a lesser extent, 3,4-dimethyl-1*H*-pyrrole-2,5-dione were formed upon controlled stepwise oxidation of a Monterey kerogen from the Santa Maria basin and Green River shale kerogen.<sup>4</sup> These compounds are thought to be derived from oxidation of entrapped ETIO-porphyrins.

Here we report the identification of C<sub>1</sub>-C<sub>8</sub> alkylpyrroles as major pyrolysis products of a Miocene kerogen from the Monterey Formation (CA, USA) and provide evidence that they are derived from macromolecularly-bound tetrapyrrole structures. A more detailed and expanded account of this work will be presented elsewhere.<sup>5</sup>

## SAMPLE

The kerogen sample studied is from an immature outcrop in the Santa Barbara basin of the Miocene Monterey Formation (CA, USA). Kerogen isolation was performed by HCl/HF treatment of the solvent-extracted sediment and yielded a kerogen isolate with the elemental composition: C, 60.31%; H, 6.45%; N, 3.55%; S<sub>tot.</sub>, 9.81%; ash, 4.62%; O (by difference), 15.26%.

## EXPERIMENTAL

Flash pyrolysis-gas chromatography-mass spectrometry (Py-GC-MS; 610°C, 10 s) was performed using a Curie point pyrolyser mounted on an Hewlett-Packard 5890 gas chromatograph equipped with a 25 m x 0.32 mm i.d. capillary column coated with CP Sil-5 (film thickness 0.45 µm). The gas chromatograph was connected with a VG-70s mass spectrometer operated at 70 eV with a cycle time of 1.8 s and a mass range *m/z* 50-800 at a resolution of 1000.

Flash pyrolysis-mass spectrometry (Py-MS) was performed using the FOM autoPYMS system. Pyrolysis (770°C) was performed *in vacuo* (180°C) and the products were transferred *via* an expansion chamber (200°C) to a Baltzers QMA 150/QMG 511 quadrupole mass spectrometer. The following MS conditions were employed: electron impact ionization, 15 eV; mass range, *m/z* 25-250; scan rate, 10 scans.s<sup>-1</sup>.

## RESULTS AND DISCUSSION

GC-MS of a flash pyrolysate of a kerogen isolated from an immature (R<sub>o</sub> = ca. 0.30%) Monterey sediment revealed the abundance of a number pyrroles with alkyl side-chains containing 1-6 carbon atoms. Figure 1 shows a part of the total ion current and a summed mass chromatogram of *m/z* 80.07 + 81.08 +



94.08 + 95.09 + 108.10 + 109.11 + 122.11 + 123.12 + 136.13 + 137.13 + 150.14 + 151.14 of the flash pyrolysate, indicating the abundance of the C<sub>1</sub>-C<sub>6</sub> alkylpyrroles. This was also evident from the Py-low voltage MS data (Figure 2) which show the abundance of *m/z* 81, 95, 109, 123 and 137, the molecular ions of the C<sub>1</sub>-C<sub>5</sub> alkylpyrroles.

The alkylpyrrole composition in the flash pyrolysate is dominated by a small number of specific alkylpyrroles: 2,3,4-trimethylpyrrole, 3-ethyl-4-methylpyrrole, 2,3-dimethyl-4-ethylpyrrole, 2,4-dimethyl-3-ethylpyrrole and 3-ethyl-2,3,5-trimethylpyrrole (Table 1). Most of these compounds were identified by using authentic standards.

A similar alkylpyrrole composition was found to be present in the flash pyrolysate of the asphaltene fraction isolated from the bitumen of the same Monterey sediment sample. This lends further support to the hypothesis that asphaltenes can be thought of as small, "soluble" parts of kerogen.<sup>6</sup>

The very specific alkyl substitution pattern of the major alkylpyrroles (i.e. with an ethyl and a methyl group at position 3 and 4 and 0-2 methyl group(s) at the other positions) strongly suggest that they are derived from tetrapyrrole pigments (e.g. chlorophyll-*a*, bilirubin).

Therefore, the linear tetrapyrrole bilirubin was flash pyrolysed under the same conditions as the kerogen sample. Indeed, C<sub>1</sub>-C<sub>6</sub> alkylpyrroles were formed and their distribution is dominated by the same structural isomers as in case of the Monterey kerogen pyrolysate (Figure 3). Similar results were obtained for chlorophyll-*a* and protoporphyrin-IX dimethyl ester. These results are in good agreement with literature data.<sup>7</sup>

These results suggest that the Monterey kerogen contains significant amounts of macromolecularly-bound tetrapyrrole units. Quantitative pyrolysis of the kerogen and bilirubin using a polymer internal standard indicate that the kerogen on a weight for weight basis contains ca. 15% "bilirubin equivalents". This very high amount of tetrapyrrole pigments suggests either an abundant algal contribution to the sediment (probably related to upwelling conditions) or unique preservation characteristics associated with this deposit or a combination of both factors.

## REFERENCES

1. Baker, E.W. and Louda, J.W. (1986), In: "Biological Markers in the Sedimentary Record", R.B. Johns (ed). Elsevier, Amsterdam. pp 125-225.
2. Filby, R.H. and Van Berkel, G.J. (1987), In: "Metal Complexes in Fossil Fuels", R.H. Filby and J.F. Branthaver (eds). ACS Symp. Ser. 344, ACS, Washington. pp 2-39.
3. Van Berkel, G.J. and Filby, R.H. (1987), In: "Metal Complexes in Fossil Fuels", R.H. Filby and J.F. Branthaver (eds). ACS Symp. Ser. 344, ACS, Washington. pp 110-134.
4. Barakat, A.O. and Yen, T.F. (1989), *Energy Fuels*, **3**: 613-616.
5. Sinninghe Damsté, J.S., Eglinton, T.I. and de Leeuw, J.W. (1991), *Geochim. Cosmochim. Acta* (submitted).
6. Behar, F. and Pelet, R. (1985), *J. Anal. Appl. Pyrol.*, **7**: 121-135.
7. Whitten, D.G., Bentley, K.E. and Kuwada, D. (1966), *J. Org.Chem.* **31**: 322-324.

TABLE I. Alkylpyrroles identified in the pyrolysates.

peak number	compound(s)
1	C <sub>1</sub> alkylpyrroles
2	C <sub>2</sub> alkylpyrroles
3	C <sub>3</sub> alkylpyrroles
4	2,3,4-trimethylpyrrole
5	3-ethyl-4-methylpyrrole
6	2,3-dimethyl-4-ethylpyrrole
7	2,4-dimethyl-3-ethylpyrrole
8	3-ethyl-2,3,5-trimethylpyrrole

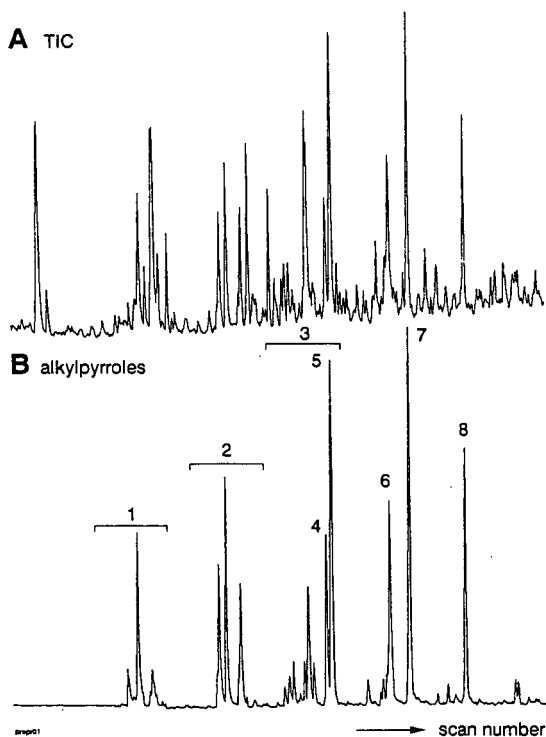
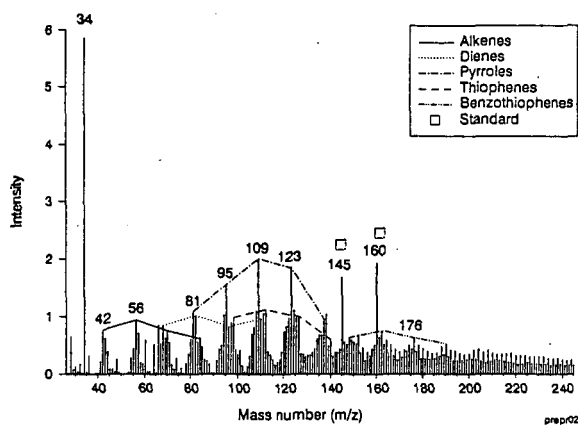
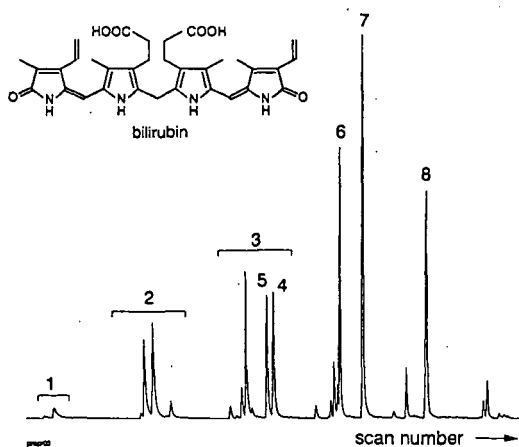


Figure 1. Partial Total Ion Current (TIC; A) of the flash pyrolysate (610°C) of the Monterey-25 kerogen and accurate mass chromatograms (mass window 0.01 amu) of  $m/z$  80.07 + 81.08 + 94.08 + 95.09 + 108.10 + 109.11 + 122.11 + 123.12 + 136.13 + 137.13 + 150.14 + 151.14 showing the distributions of the C<sub>1</sub>-C<sub>8</sub> alkylpyrroles (B). Peak numbers refer to alkylpyrroles listed in Table I.



**Figure 2.** Py-MS spectra of Monterey-25 kerogen. For quantitation poly-4-*t*-butylstyrene was co-pyrolysed, which gives rise to its monomer, 4-*t*-butylstyrene ( $m/z$  160, 145).



**Figure 3.** Accurate (mass window 0.01 amu) summed mass chromatograms of  $m/z$  80.07 + 81.08 + 94.08 + 95.09 + 108.10 + 109.11 + 122.11 + 123.12 + 136.13 + 137.13 + 150.14 + 151.14 for the flash pyrolysate (610°C) of bilirubin. Peak numbers refer to alkylpyrroles listed in Table 1.

## NEW APPROACHES TO THE STUDY OF CELLULOSE PYROLYSIS

R. J. Evans, F. A. Agblevor, H. L. Chum  
Chemical Conversion Research Branch  
Solar Energy Research Institute  
Golden, Colorado 80401

J. B. Wooten, D. B. Chadwick and S. D. Baldwin  
The Philip Morris Company  
Richmond, Virginia 23261

**KEY WORDS:** Pyrolysis, Cellulose, Mass Spectrometry, Labeled Cellulose

### INTRODUCTION

Cellulose pyrolysis presents some unique questions that include the effect of polymer secondary structure, (e.g., crystallinity), the intrinsic mechanism of pyrolysis by homolytic or heterolytic pathways, the role of alkali-metal catalysis, and the existence of major pathways, other than levoglucosan formation by "transglycosylation."<sup>1-4</sup> Most of the advances in the last five years have resulted from new analytical information. Piskorz et al.<sup>5</sup> and Richards<sup>6</sup> have published papers in recent years that describe hydroxyacetaldehyde formation as a major product and have speculated on the mechanism of this newly recognized, important product. These workers have used bench-scale pyrolysis units with physical collection of samples and employed chromatographic analysis of the products. Another approach is to perform pyrolysis with on-line analytical capability, either gas chromatography (Py-GC or Py-GC-MS) or mass spectrometry (Py-MS). Pouwels et al.<sup>7</sup> have recently reported a detailed analysis of cellulose pyrolysis products using Py-GC-MS analysis. The major disadvantage of the GC approach is the collection of products on the head of the column where thermal degradation or other reactions can occur for some of the pyrolyzate constituents. The advantages of Py-MS are complete product collection and time-resolved analysis, but ambiguities arise due to the nature of the ionization method and the detection of products with the same nominal mass. The typical approach is to use low-voltage, electron ionization (12-25 eV) to preserve the parent ions as much as possible.<sup>8</sup> When this approach is coupled with multivariate data analysis, it is often possible to deconvolute the major components among the products.<sup>9</sup>

We report here the implementation of several new tools for the study of cellulose pyrolysis using molecular beam mass spectrometry (MBMS).<sup>10</sup> The new tools for py-MBMS investigations include systematic catalytic additions to identify correlated products, tandem mass spectrometry for identifying the contribution of specific compounds to nominal masses, preliminary rate analysis techniques for time-resolved data, and the growth and purification of <sup>13</sup>C labeled cellulose using *Acetobacter xylinum* to be used in the study of cellulose pyrolysis.

### EXPERIMENTAL

The MBMS and pyrolysis procedures have been previously described.<sup>10</sup> A sample (1- 30 mg) contained in a quartz holder or "boat" is inserted into flowing (13 l/min at reactor temperature), preheated (typically 500°C) helium carrier gas. The hot gases are expanded through an orifice on the apex of a sampling cone into a low pressure chamber. The pressure difference is sufficient for free-jet expansion, which quenches the products and allows light gases, high-molecular-weight compounds, and reactive products to be simultaneously sampled and analyzed. A molecular beam, collimated through a second expansion, enters an ion source, where approximately 20 eV electron impact ionization is used to form ions. The mass range of interest (typically 15-300 amu) is scanned each second throughout the time for complete pyrolysis product evolution. Data are processed by integrating the spectra over the time of pyrolysis (10 to 90 s, depending on the sample and gas temperature), and by subtracting the background. If time-resolved data analysis is to be performed, each individual spectrum in a pyrolysis experiment is background-corrected. Factor analysis was used to analyze the results, either on a set of spectra from

related pyrolysis experiments to determine common behavior, or on time-resolved data to deconvolute different groups of products. The techniques used for factor analysis have been adapted from the methods of Windig and Meuzelaar<sup>9</sup> that have been recently described by Windig.<sup>11</sup> The software package was the ISMA program<sup>11</sup> (Interactive Self-modeling Multivariate Analysis).

Avicel microcrystalline cellulose (FMC Corp., PH-102) was used throughout this work. Catalytic additions of salts were made by adding an appropriate amount of aqueous solution to just form a slurry and then allowing the material to dry completely in air at room temperature. Additions are reported as wt % cation relative to sample weight.

Cellulose was prepared with <sup>13</sup>C at the C-1 position by growing cultures of *Acetobacter xylinum* on media that included D-[1-<sup>13</sup>C]-glucose. The cellulose sheets, or pelicles, were allowed to grow in media and then were thoroughly cleaned to remove other biopolymers and metal contamination. This cleaning procedure included autoclaving the pelicles in a solution of Alconox detergent followed by exhaustive washings in deionized water (resistivity = 10<sup>7</sup> ohm). The pelicles were analyzed by C-13 NMR and found to be free of non-cellulosic carbon signals. The level of <sup>13</sup>C<sub>1</sub> enrichment was 14%.

## RESULTS AND DISCUSSION

The pyrolysis of cellulose is shown in figs. 1 and 2 for samples treated with different levels of KOH to demonstrate the two major product groups known to form: anhydrosugars and hydroxyacetaldehyde and their related compounds. The sample treated with 0.001% K has a product slate dominated by levoglucosan as shown by the average spectrum in fig 1B. Levoglucosan ionization fragment ions contribute to the intensity at m/z 144, 98, 73, 70, 60, and 57. The evolution profiles for m/z 43 and 144 are shown in fig. 1A as key markers for the two major product groups. In most natural cellulosic material, the yield of levoglucosan is less than that obtained from pure, isolated cellulose, such as Avicel. The average spectrum and time-resolved profiles for the pyrolysis products from cellulose treated with 0.5% K is shown in fig. 2. Hydroxyacetaldehyde, at m/z 60, fragments in the ion source to give fragment ions at m/z 31 and 32 and acetyl compounds give a major fragment ion at m/z 43. These masses are good indicators for the other major product slate. These data support the hypothesis that the level of alkali metals determine the relative amounts of these two major cellulose pyrolysis products. This point will be further demonstrated below.

A major question in cellulose pyrolysis is the existence of other "product classes" in cellulose pyrolysis. The systematic addition of catalytic alkali metal salt has been used to simulate the range of product groups encountered in cellulosic biomass pyrolysis. Salts investigated include NaCl, NaOH, KOH, and K<sub>2</sub>CO<sub>3</sub> at the 0.001 to 0.1 wt. % level. Multivariate analysis of the average pyrolysis spectra was used to deconvolute three main groups of products. These catalysts show different mechanistic effects at various levels of addition. The factor score plot, the mass variable loading projections, and the variance diagram are shown in fig. 3. The score plot reveals a systematic effect from the catalytic addition with two trends and three main product groups. The three product groups are controlled by the level of salt addition. The mass-variable axes projections (fig. 3B) show that the masses are fanned out, which indicate that most masses belong to more than one of the three groups. The variance diagram (fig. 3C), which provides visual insight into the weighted average of the mass vectors, shows the three main maxima that indicate the direction of the component axes. The pure mass method is used to determine the vector coordinates that best represent the major, independent, real chemical "components." Chemical components in this application means suites of products that have correlated abundances in the spectra and hence appear to be controlled by the same chemical pathways. In this data set, three components were determined as represented by the pure masses, m/z 31, 144, and 191. The mathematically derived spectra of these three resolved components are shown in figs. 4-6, along with the relative amounts of these components for each sample.

The component spectrum 1 (fig. 4B) shows the key fragment ions at m/z 31, 32 and 43 that are due to the aldehyde and related structures. The plot of the relative concentration of component 1 for each sample as a function of wt % cation shows a systematic trend with higher yields at higher levels of alkali

metal. Six biomass samples (pine, fir, beech, maple, wheat straw, and bagasse) were analyzed along with the treated cellulose and were projected into the factor-analyzed cellulose results. These samples are included in fig. 4-6 as a function of their analyzed alkali metal concentrations. The resolved spectrum of component 2 in fig. 5B matches levoglucosan and shows higher relative concentrations in the samples with low levels of alkali metals that decreases monotonically with increased alkali-metal concentration. The biomass samples fit within this curve. Recent work<sup>5,6</sup> has established that these two groups are the major products of cellulose pyrolysis, and our work shows that their relative amounts are controlled by alkali catalysis, which promotes the formation of the aldehydes at the expense of anhydrosugars. The results indicate a third product class that is also a function of alkali catalysis at low levels and that product group is shown in the component spectrum in fig. 6B. The peak at  $m/z$  191 is of great interest since it is higher than the anhydrosugar weight of 162 and because it is an odd mass ion indicating either a protonated  $m/z$  190 or a fragment ion of a higher mass, such as  $m/z$  192. The peaks at  $m/z$  173 and 163 and 145 are correlated with the intensity of  $m/z$  191. The other major product is  $m/z$  126, which could be 5-hydroxymethyl furfural, or hydroxybenzenes.<sup>12</sup> This will be discussed in relation to the CID of  $m/z$  126. The peak at  $m/z$  114 and fragment ion  $m/z$  85 are common products from pentosan pyrolysis products and are thought to be due to a lactone.<sup>10</sup> The relative concentration of component three shows a maximum at intermediate levels of cation concentration and the biomass samples show good agreement with the trends for the cellulose samples. These results imply that the pyrolytic behavior in biomass samples can be largely explained by these three product groups and that the effect of alkali-metal catalysis is sufficient to explain the control of the pyrolysis of cellulose in these materials.

Time-resolved data analysis can be used to estimate the relative kinetic rates for these different classes. As an initial application of this idea, the two sets of time-resolved spectra for the pyrolysis of cellulose treated with .001 and .5% K (as KOH) (shown in figs. 1A and 2A) were combined in the same data set and subjected to factor analysis to deconvolute the major trends as a function of reaction time. Only two significant chemical components were derived by this process in contrast to the three from the alkali-metal experiment. There are two possible reasons for this: 1) the third pathway was not active because these samples are from the two extremes of the sample distribution in fig. 3A, or 2) the two sets of time-resolved spectra did not contain sufficient variation to allow independent expression of the intermediate product group. The masses associated with the third product slate are divided between the other two. The mathematically derived spectra of the two components are shown in fig. 7 and clearly represent aldehyde and anhydrosugar product groups.

Using the relative yields of these two components in each spectrum the data are analyzed by plotting three calculated values that represent tests for zero, first, and fractional order rate behavior.<sup>13</sup> The test for zero order is a plot of fractional conversion to products, expressed as

$$X_i = \left( \sum_{j=0}^i S_{ij} \right) / \left( \sum_{j=0}^n S_{nj} \right)$$

where  $S$  is the score for the  $j$  component ( $j=1$  to 2, in this case) at time  $i$ , and  $n$  is the time for complete conversion. This can be subsequently converted to a first order test by plotting  $-\ln(1-X_i)$  and as a fractional order test by plotting  $(1-X_i)^{1/n}$ , where  $n$  is the fractional order of reaction.<sup>13</sup> The slope of the line can be converted to the rate constant when these values are plotted versus time, and straight line behavior is observed. In these experiments, there is a nonisothermal period while the sample is heated to the reactor temperature. The initial portion of the time-resolved behavior is therefore ignored. This method should be considered a screening technique since there are several uncontrolled factors (e.g., temperature of reacting solid, mass transfer, etc.) that prevent the calculation of intrinsic chemical kinetics with certainty. However, this rapid analytical approach is a way of comparing samples that sheds light on the chemical processes and utilize data that in the past were ignored. The use of factor analysis to deconvolute chemically specific information from time-resolved data is an improvement over weight loss rate analysis. Plots of these calculated values versus time are shown in fig. 8 for the evolution of the aldehydes component from the 0.5% K-treated cellulose and the anhydrosugar component for the 0.001% K-treated cellulose. In both the 0.001% K and 0.5% K samples, a reaction order of .8 and a rate constants of  $0.17(\pm 0.02) \text{ s}^{-1}$  were calculated for the anhydrosugars. For the aldehydes, a reaction order of 0.4 and rates of 0.07 to  $0.11 \text{ s}^{-1}$  were obtained for the 0.001% and 0.5% samples, respectively. The

difference in rates for the aldehydes, if statistically significant, is not unreasonable if one assumes a more "zero-order nature" for the formation of hydroxyacetaldehyde, which is dependent on catalytic activity. The reproducibility of the reaction order for the two reactions under extremes of reaction is illustrative of the insight that this rate analysis of time-resolved data can provide.

Collision induced dissociation (CID) of selected ions has been used to deconvolute ambiguous peaks in pyrolysis-mass spectrometry of cellulose, such as  $m/z$  60, 126, 144, and 162, which are known to be due to more than one product, and  $m/z$  191, 163, and 145, which appear to have new significance in light of results reported above. The results are presented in table 1 for a variety of materials. The species at  $m/z$  191 gives rise to fragments at  $m/z$  173 and 163, due to a loss of 18 and 28, respectively. The series of daughter ions of  $m/z$  191, at  $m/z$  163, 145, and 127, resemble the dehydration series from the electron ionization fragment ions of levoglucosan at  $m/z$  162, 144, and 126. This may imply that the parent of  $m/z$  191 ( $m/z$  192?) may be a derivative from an anhydrosugar. The peak at  $m/z$  163 may be an electron ionization fragment of the same species that gives rise to  $m/z$  191 and it also has daughter ions at  $m/z$  145 and 127, but with a new daughter at  $m/z$  85. Comparing  $m/z$  162 from levoglucosan and cellulose indicates some dramatic differences with the cellulose ion giving rise to a daughter at  $m/z$  73 that is not produced from levoglucosan. The parent at  $m/z$  145 from cellulose pyrolysis is also different from the  $m/z$  145 ion from levoglucosan, which again may be due to the  $m/z$  145 being derived from the same species that gives rise to  $m/z$  191. The daughters of  $m/z$  144 are also more complicated from cellulose than levoglucosan. The model compounds at  $m/z$  126 show relatively unique daughters for each (1,2,3-trihydroxybenzene -  $m/z$  108; 1,3,5-trihydroxybenzene -  $m/z$  85; 5-HMF -  $m/z$  97; levoglucosenone -  $m/z$  98). Untreated Avicel yields  $m/z$  97 as a daughter of  $m/z$  126, which indicates the 5-HMF and no hydroxybenzenes. The presence of salts lowers the overall daughter ion abundance from  $m/z$  126, and the presence of  $m/z$  108 would indicate the trihydroxybenzene in addition to 5-HMF. It is not generally recognized that the furfurals can arise from alkali metal catalysis, but these data support that hypothesis. The daughters of  $m/z$  60 are also fairly unique for the model compounds and show that the daughters from treated cellulose can be resolved into the relative amounts of levoglucosan, hydroxyacetaldehyde, and acetic acid by the relative amounts of  $m/z$  42, 32, and 45. Factor-analysis-based methods are being developed for deconvoluting CID spectra due to multiple products present at the nominal mass of interest.

Recent pyrolysis MBMS experiments of *Acetobacter* cellulose, grown on D-[1- $^{13}\text{C}$ ]-glucose media are reported here and this is a most exciting new tool for PY-MS studies of cellulose pyrolysis. The selectively enriched, labeled and unlabeled *Acetobacter* cellulose samples were prepared and purified by the same methods to remove potential metal ion contaminants and to insure that both samples could be compared. The regular and  $^{13}\text{C}_1$  *Acetobacter* cellulose samples were pyrolyzed in triplicate at 520°C in flowing helium. The sample size was approximately 5 mg. Since  $m/z$  145 and 127 are associated with another product group (that is alkali-catalyzed) in addition to being the isotope peaks of  $m/z$  144 and 126, respectively, the enrichment effect can be masked by the differences between samples in the level of inorganic contamination. The ratio of  $m/z$  126/144 is a sensitive indicator of the relative amounts of these different product groups. The data in table 2 show that the ratios of  $m/z$  126/144 are 0.53 and 0.50 for the regular and enriched *Acetobacter* cellulose samples, respectively. This leads to the conclusion that there is no significant difference between the two samples in the relative amounts of the major pyrolysis product groups. Therefore, the differences in table 2 that are statistically significant are due to the isotope enrichment at the  $\text{C}_1$  position. The average spectrum for the replicates of regular cellulose pyrolysis is indicative of anhydrosugar formation (there was a low abundance of  $m/z$  43, which is a confirmation that these are clean samples). Therefore, isotope effects from this sample will only be relevant to part of the range of cellulose pyrolysis products. An analysis of variance (ANOVA) was performed for the triplicate runs for the two samples. The results are presented as the F-ratio, which is a statistical parameter used to estimate the probability of significant differences between two or more classes of replicated samples. For this experiment, an F-ratio of 7.71 indicates 95% confidence that the measured difference is significant and an F-ratio of 21.2 implies 99% confidence. The ions with an F-ratio greater than 3.5 are included in tables 2 and 3. The F-ratio test shows significant enrichment at  $m/z$  144 with an F-ratio of 87 for  $m/z$  145 and 69 for  $m/z$  144. Since this ion is a six carbon product, which must contain  $\text{C}_1$ , this verifies that the enrichment can be detected for  $\text{C}_1$  containing species. Simulation

data are included in the tables that assume 14% enrichment and the presence of C<sub>1</sub> in the products at every mass. Note that the peak intensities are very close for m/z 144 and 145 for the labeled Acetobacter average and those in the simulated enrichment. The products at m/z 126 also contain six carbon atoms and again the enrichment values for m/z 126 and 127 closely match the simulated values. Of the lower molecular weight products, only m/z 98 is significantly higher.

To force the distribution of pyrolysis products to the aldehyde product slate, samples of the Acetobacter cellulose were treated with 0.1% KOH and treated similarly to the samples described above. In this sample, m/z 126 shows significant enrichment, but no low-molecular-weight products are higher in the enriched cellulose. This indicates that the m/z 60 products that are present under these alkali-catalyzed conditions are not formed from the C<sub>1</sub> position in cellulose, and glycolaldehyde must come from the C2 to C6 positions. This work is continuing with labeled cellulose at other carbon positions.

In summary, the use of systematic catalytic additions to promote formation of product groups, the use of rate analysis of time-resolved data, and the use of CID for characterization, improves the application of Py-MS as a tool for studying the chemistry of cellulose pyrolysis. The most exciting new development is the use of <sup>13</sup>C-labeled cellulose that has specifically labeled positions and allows the source of each pyrolysis product to be traced to the exact position in the cellulose structure.

#### ACKNOWLEDGMENTS

The assistance of Carolyn Elam, David Gratson, Dingneng Wang, and Kuni Tatsumoto in experimental work, and of Willem Windig in discussions of multivariate analysis and use of the ISMA program is greatly appreciated.

#### REFERENCES

1. Antal, M. J., Jr. In Advances in Solar Energy; Boer, K. W.; Duffier, J. A., Eds.; Plenum: New York, 1985, vol.2, pp 175-728.
2. Shafizadeh, F. Applied Polymer Symposium 1975, 28, 153-174.
3. Kilzer, F. J.; Broido, A. Pyrodynamics 1965, 2, 151-163.
4. Golova, O. P. Russian Chemical Reviews, 1975, 44(8), 687-697.
5. Piskorz, J.; Radlein, D.; Scott, D. S. J. Anal. Appl. Pyrol. 1986, 9, 121-137.
6. Richards, G. N. Ibidem. 1987, 10, 251-255.
7. Pouwels, A. D.; Eikje, G. B.; Boon, J. J. Ibidem. 1989, 14, 237-280.
8. Meuzelaar, H. L. C.; Kistemaker, P. G. Anal. Chem. 1973, 45, 587-590.
9. Windig, W.; Meuzelaar, H. L. C. Ibidem. 1984, 56, 2297-2303.
10. Evans, R. J.; Milne, T. A. Energy Fuels 1987, 1, 123-137.
11. Windig, W.; Lippert, J. L.; Robbins M. J.; Kresinske, K. R.; Twist, J. P.; Snyder, A. P. Chemometrics and Intelligent Laboratory Systems, 1990, 9, 7-30.
12. Richards, G. N.; Shafizadeh, F.; Stevenson, T. T. Carbohydr. Res. 1983, 117, 322-327.
13. Carlson, L.; Feldthus, A.; Bo, P. J. Anal. Appl. Pyrol. 1989, 15, 373-381.



Table 1. Results of CID-MS on key masses from the pyrolysis of cellulose and selected model compounds. Conditions for CID were Argon collision gas and ion energies of approximately 20 eV. The intensities are relative to a parent ion intensity of 1000.

Parent	Material	Daughter Ions: m/z(intensity)
191	Avicel	127(168) 173(134) 145(113) 163(31)*
163	Avicel	145(112) 85(62) 127(36) 91(24)*
162	Avicel	73(44) 98(42) 144(42) 89(26)*
162	Levogluconan	98(273) 116(114) 70(57) 106(52)
145	Avicel	85(77) 127(47) 99(34)* 73(31)*
145	Levogluconan	73(223) 98(89)* 74(79)*
144	Avicel	72(92) 98(70) 73(57)*
144	Levogluconan	73(144) 98(123)*
126	1,2,3-THB <sup>1</sup>	108(26) 80(26) 125(7)
126	1,3,5-THB <sup>1</sup>	85(20) 98(7) 125(7)
126	5-H-M-Furfural	97(486) 69(45) 125(11)
126	Levogluconone	98(281) 95(53) 80(48) 70(42) 97(41)
126	Avicel	97(121) 98(46) 80(41) 69(18) 81(11) 70(11)
126	cel+.05%Na <sub>2</sub> CO <sub>3</sub>	97(34) 80(21) 98(12) 108(12)*
126	cel+.5%K <sub>2</sub> CO <sub>3</sub>	98(20) 80(16) 97(14) 125(9)* 108(7)*
126	cel+.05%NaCl	97(59) 98(22) 80(13) 125(10) 108(7)*
126	Aceto. Cel#1	97(179) 98(45) 80(35) 69(33)
126	Aceto. Cel#2	97(109) 98(61) 69(25) 80(24) 70(16) 111(15)
60	Acetic Acid	45(533) 43(259) 42(48) 16(36) 15(12)
60	Hydroxyacetal.	32(1200) 31(873) 45(88) 43(35) 29(34) 42(32)
60	MeFormate	31(650) 32(477) 30(298) 29(75) 45(8) 15(6)
60	2-propanol	45(1700) 44(381) 31(202) 32(142) 43(80)
60	Levogluconan	42(124) 31(60) 30(11)
60	Cel+.05%Na <sub>2</sub> CO <sub>3</sub>	42(108) 31(73) 32(32) 45(16) 43(9) 30(8)*

\*These peaks have low signal-to-noise and their identification as daughters should be considered tentative.

<sup>1</sup>trihydroxybenzene

Table 2. Significant differences in the relative yields of pyrolysis products in regular ( $I_{(m/z)R}$ ) and  $^{13}C_1$ -enriched ( $I_{(m/z)E}$ ) *Acetobacter xylinum* cellulose. Each sample was run in triplicate and analysis of variance was performed to determine the degree of statistical significance (F-ratio, Level of Significance: 21.2, 1%; 12.2, 2.5%; 7.71, 5%). The difference between these values shows the effect of enrichment. Simulated values ( $I_{(m/z)S}$ ) are presented as if each mass was enriched by 14% in  $^{13}C_1$ .

m/z	Experimental				Simulated	
	$I_{(m/z)R}$	$I_{(m/z)E}$	F-ratio	$(I_{(m/z)R} - I_{(m/z)E})$	$I_{m/zS}$	$(I_{(m/z)R} - I_{(m/z)S})$
43	1.37	1.19	37.8	0.18	1.33	0.04
55	1.37	1.25	6.3	0.12	1.23	0.14
68	1.16	1.08	5.1	0.08	1.00	0.16
90	0.39	0.51	7.5	-0.11	0.48	-0.09
99	1.35	1.52	19.0	-0.16	2.38	-1.03
101	0.86	0.72	6.2	0.13	0.78	0.08
103	0.50	0.61	4.9	-0.11	0.57	-0.08
113	1.36	1.18	23.8	0.18	1.22	0.14
114	2.02	1.87	6.4	0.16	1.93	0.09
116	1.37	1.52	9.8	-0.15	1.41	-0.04
126	2.90	2.38	4.8	0.52	2.53	0.38
127	0.56	0.91	37.7	-0.35	0.89	-0.33
142	0.31	0.22	3.6	0.10	0.27	0.04
144	5.50	4.72	68.5	0.78	4.76	0.75
145	0.84	1.46	87.8	-0.62	1.49	-0.65
146	0.20	0.29	39.2	-0.09	0.29	-0.09
163	0.30	0.37	3.6	-0.07	0.30	0.00
167	0.22	0.15	4.1	0.07	0.20	0.02
192	0.16	0.23	22.0	-0.07	0.17	-0.01

Table 3. Significant differences in the relative yields of pyrolysis products in regular and  $^{13}C_1$ -enriched *Acetobacter xylinum* cellulose treated with 0.1% KOH. See Table 2 caption for details.

m/z	Experimental				Simulated	
	$I_{(m/z)R}$	$I_{(m/z)E}$	F-ratio	$(I_{(m/z)R} - I_{(m/z)E})$	$I_{m/zS}$	$(I_{(m/z)R} - I_{(m/z)S})$
29	1.49	1.65	5.3	-0.16	1.50	-0.01
45	0.96	1.26	5.4	-0.30	1.44	-0.48
57	3.14	2.83	21.1	0.31	2.87	0.27
68	1.00	0.86	19.7	0.14	0.91	0.09
74	1.43	1.30	18.2	0.13	1.60	-0.17
85	2.52	2.36	19.0	0.16	2.43	0.09
97	1.80	1.60	6.0	0.19	1.71	0.08
98	3.58	3.32	18.1	0.25	3.33	0.25
126	3.35	2.60	11.8	0.74	2.93	0.41
127	0.59	0.95	34.4	-0.36	0.97	-0.39
142	0.26	0.21	41.7	0.04	0.24	0.02
144	0.80	0.48	20.5	0.32	0.71	0.09
145	0.43	0.33	5.3	0.10	0.48	-0.05
190	0.15	0.20	7.9	-0.06	0.14	0.01
191	0.14	0.17	120.	-0.04	0.14	-0.00

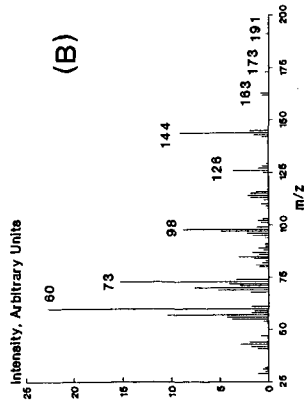
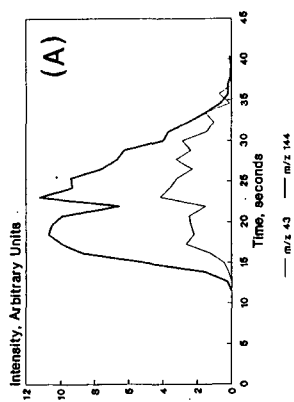


Fig. 1. The pyrolysis of Avicel cellulose treated with .001% K (as KOH) at 540 °C: (A) time-resolved evolution profile of  $m/z$  43 and 144. (B) the average, background-corrected spectrum of pyrolysis products.

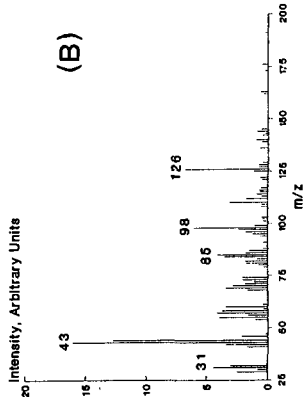
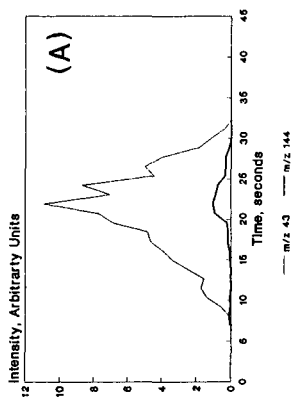


Fig. 2. The pyrolysis of Avicel cellulose treated with .5% K (as KOH) at 540 °C: (A) time-resolved evolution profile of  $m/z$  43 and 144. (B) the average, background-corrected spectrum of pyrolysis products.

# Effect of Salts on Cellulose Pyrolysis

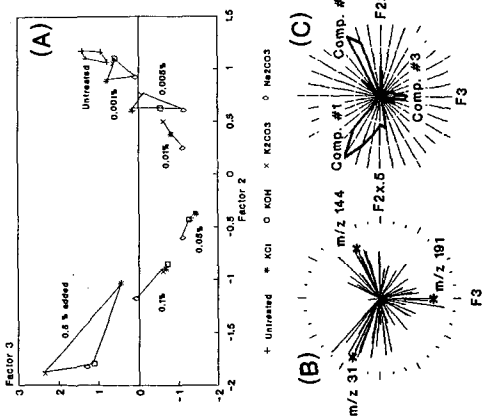


Fig. 3. The results of factor analysis of pyrolysis-mass spectra of avicel cellulose treated with different levels of salts. (A) plot of Factor 3 vs Factor 2 showing trajectories for different salt concentrations in the data set; (B) mass variable loading projections showing underlying distribution of data set; and (C) the variance diagram, which is a weighted display of the mass axes projections and shows the maxima of clustering, which indicate the direction of component change. The delineate component axis, are noted with asterisk in B.

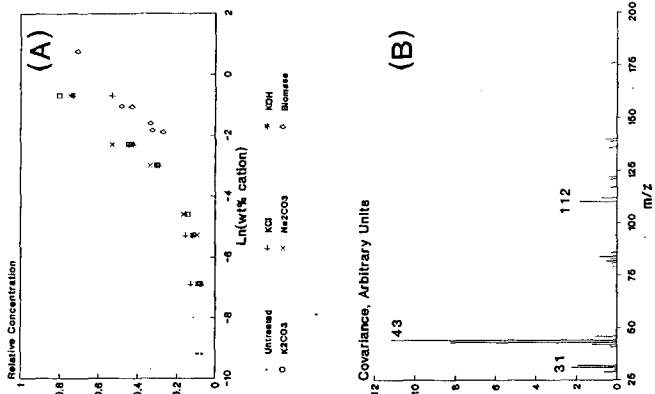


Fig. 4. The first component mathematically resolved from the data set in Fig. 3 (pure mass m/z 31) showing its relative concentration in the samples (A) and the reconstructed spectrum (B).

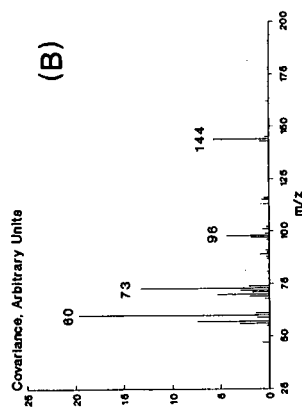
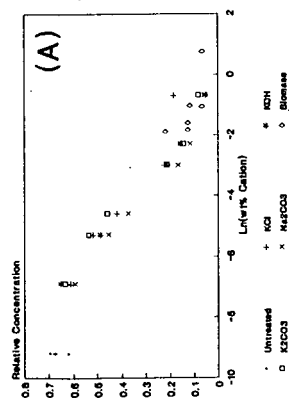


Fig. 5. The second component mathematically resolved from the data set in Fig. 3 (pure mass  $m/z$  144) showing its relative concentration in the samples (A) and the reconstructed spectrum (B).

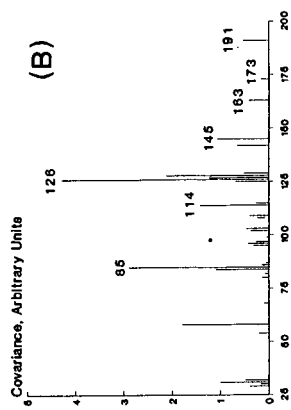
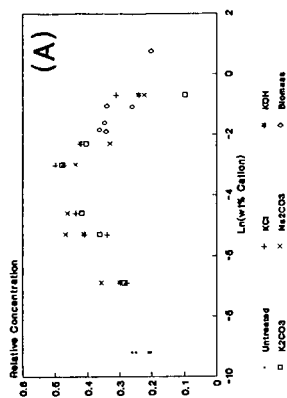
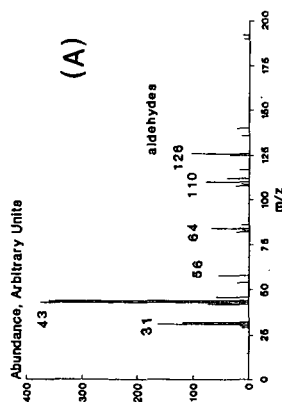


Fig. 6. The third component mathematically resolved from the data set in Fig. 3 (pure mass  $m/z$  191) showing its relative concentration in the samples (A) and the reconstructed spectrum (B).

Component Spectrum 1



Component Spectrum 2

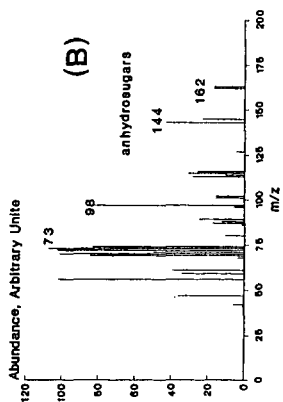


Fig. 7. The results of factor analysis on time resolved data for the .001% and .5% K-treated cellulose data sets, which were combined in one data set to deconvolute the major product states: (A) component spectrum 1, which represents the aldehydes; (B) component spectrum 2, which represents the anhydrosugars.

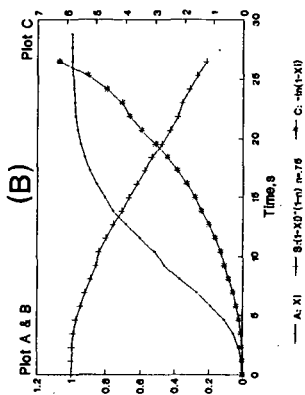
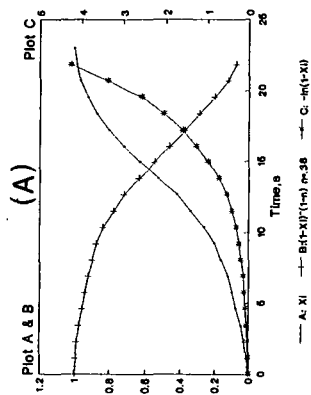


Fig. 8. Examples of the analysis of the rate of formation of the resolved components that are shown in fig. 7: (A) aldehydes from .5% K-treated cellulose and (B) anhydrosugars from .001% K-treated cellulose.

## CHARACTERIZATION OF LIGNOCELLULOSIC MATERIALS AND MODEL COMPOUNDS BY COMBINED TG/(GC)/FTIR/MS

Jacek P. Dworzanski, Richard M. Buchanan, John N. Chapman  
and Henk L.C. Meuzelaar

Center for Micro Analysis and Reaction Chemistry  
The University of Utah, Salt Lake City, UT 84112

**Key words:** thermogravimetry, gas chromatography, mass spectrometry, infrared spectrometry, lignins, wood

### INTRODUCTION

Thermal analytical methods have been widely used during the last two decades in the study of biomass thermochemical conversion processes [1-4]. Biomass, which represents a renewable energy resource, consists primarily of plant cells differentiated into characteristic tissues and organs. Lignins, hemicelluloses and cellulose, as the main components of the cell walls, were therefore extensively analyzed, especially from the point of view of their thermochemical reactivity, which is of basic importance for industrial processing of biomass [3].

All types of cellulose microfibrils are composed of linearly linked  $\beta$ -(1 $\rightarrow$ 4)-D-glucopyranose units and differ only by the degree of polymerization. The remaining polysaccharides are known collectively as hemicelluloses and exhibit species related composition. These amorphous, complex heteropolymers characterized by a branched molecular structure exhibit a lower degree of polymerization than cellulose. Xylan is the predominant hemicellulose component of angiosperms ("hardwoods") whereas mannan forms the main hemicellulose of gymnosperms ("softwoods"). The third principal component of biomass, viz. lignin, is an irregular, high MW polymer formed by enzyme-initiated, free-radical polymerization of coniferyl alcohol (in hardwoods), coniferyl plus sinapyl alcohols (in softwoods), or coumaryl alcohol plus both above mentioned alcohols (in grasses) [5]. Lignins act as binding agents for the cellulose and hemicellulose fibers through a variety of linkages involving ether and carbon-carbon bonds of aromatic rings and propyl side chains.

Thermochemical conversion processes of lignocellulosic materials have been studied using mainly thermogravimetry (TG) [6] or flash pyrolysis (Py) followed by gas chromatographic (GC) separation and identification of the reaction products [1]. Modern analytical techniques based on coupled Py-GC/mass spectrometry (Py-GC/MS) [7] or direct Py-MS [2,8] as well as TG/MS or TG/infrared spectroscopy (TG/IR) [4] have proved to be especially useful for elucidating the relationships between biomass structure and pyrolysis/devolatilization mechanisms.

A novel TG/(GC)/FTIR/MS system developed at the University of Utah, Center for Micro Analysis and Reaction Chemistry [9] provides the opportunity for combining accurate weight loss measurements with precise information about composition and evolution rates of gaseous and liquid products as a function of temperature. In this paper, the usefulness of TG/FTIR/MS, TG/GC/MS and TG/GC/FTIR for thermochemical characterization of wood, lignins and cellulose will be discussed.

## EXPERIMENTAL

The TG/FTIR/MS system consists of a Perkin Elmer model 7 Thermogravimetric Analyzer with high temperature furnace controlled by an IBM compatible PC and interfaced to a Hewlett-Packard GC/IRD/MSD system (GC - model 5890A, IRD - model 5965A and MSD - model 5971A) controlled by HP 9000 computers (Figure 1). As shown in Figure 1 a specially constructed, heated transfer line assembly allows direct coupling of the TG system to the GC injection port with the GC oven acting as a convenient heated coupling and flow distribution module. In order to make an efficient TG/GC interface, a 0.53 mm I.D. ("megabore") deactivated fused silica capillary column is used to transfer TG effluents to the GC oven. On the TG side this column protrudes several centimeters into a 1 mm i.d. quartz tube which, in turn, extends into the high temperature furnace to within 1 cm of the sample crucible. Both the outlet of the ceramic furnace tube and the quartz tube are vented by means of needle valves. The quartz tube may be also backflushed with helium to prevent air from entering the MSD vacuum system when the TG furnace is open or not yet purged. Inside the GC oven this capillary terminates with a splitter which provides 90 % of the total flow to the IRD and 10% to the MSD instrument. In order to enable GC separations of the TG effluent the capillary transfer line terminates within a specially designed repetitive vapor sampling inlet inside the GC oven. This inlet leads, in turn, to either (or both!) the IRD or MSD modules via a short (ca. 2 m) capillary column. The switching action of the repetitive sampling inlet causes diversion of the "protective" helium gas flow (see Figure 1) allowing only a short (1-2 sec long) burst of TG effluent to enter the column for further GC separation of the various components and subsequent spectroscopic (MS and/or IR) identification.

**Samples** A steam explosion lignin prepared from Yellow Poplar wood (Liriodendron tulipifera) was isolated by extraction with sodium hydroxide followed by acid precipitation. This sample was donated by Professor Wolfgang Glasser of the Biobased Materials Center at Virginia Tech., in Blacksburg, VA. Douglas fir wood was air dried and analyzed as tiny particles obtained by scratching a piece of wood with a blade.

## RESULTS AND DISCUSSION

Figure 2 summarizes some of the results obtained by TG/FTIR/MS analysis of steam explosion Yellow Poplar lignin. In Figures 2b and h the TG weight loss and the differential thermogravimetric (DTG) curves are presented at a heating rate of 15 C/min in helium atmosphere. These graphs reveal the onset of weight loss near 150 C, with a peak of maximum rate of weight loss at 350 C which follows two shoulders at 160 C and 230 C and preceeds a third around 420 C. Averaged mass spectra and infrared spectra of all products evolved during the course of the TG experiment are shown in Figures 2a and g, respectively. Inspection of the MS spectrum indicates the presence of components associated with the monomethoxy series: guaiacol {m/z 124 ( $M^+$ ) and m/z 109 ( $M^+ - 15$ )}, 4-methylguaiacol {m/z 138 ( $M^+$ ) and m/z 123 ( $M^+ - 15$ )}, 4-vinylguaiacol {m/z 150 and m/z 135}, vanillin {m/z 152} and isoeugenol {m/z 164}. The components associated with the dimethoxy series are syringol {m/z 154 ( $M^+$ ) and m/z 139 ( $M^+ - 15$ )}, 4-methylsyringol {m/z 168 and m/z 153}, 4-vinylsyringol {m/z 180}, syringaldehyde {m/z 182} and 4-(1-propenyl)-syringol {m/z 194}. These series of ions are typical for thermal degradation products obtained by pyrolysis of hardwoods or their lignin components [2]. In Figures 2e and f the comparative rates of evolution of guaiacol and syringol are shown as well as 4-methylguaiacol and 4-methylsyringol, respectively. The trace shown in Figure 2k demonstrates the profile of the components exhibiting characteristic alkyl-aryl ether



stretching vibration in the 1260-1290  $\text{cm}^{-1}$  region, typical for mono- and di-methoxy phenols, e.g., building blocks of lignin. Our technique enables also the detection of minor contaminants in lignin samples and profiles of the ion  $m/z$  114 (Figure 2d) as well as the trace at 1184  $\text{cm}^{-1}$  (Figure 2j), characteristic for C-O stretching vibrations of lactones, strongly suggest the presence such structures as 3-hydroxy-2-penteno-1,5-lactone (M.W. 114) a carbohydrate "marker" from thermal dissociation of xylanes [10] which may be utilized for quantification of hemicellulose residues in lignin preparations. The total ion current (Figure 2b - TIC) and total absorption (Figure 2h - TAP) profiles of the thermal breakdown products released during the TG experiment reveal substantial differences in shape compared to the recorded DTG curve. This is primarily due to the tuning of the MSD instrument for higher masses as well as due to the fact that a high percentage of the weight loss is caused by low molecular weight components ( $\text{H}_2\text{O}$ ,  $\text{CO}$ ,  $\text{CO}_2$ ,  $\text{MeOH}$ ) as demonstrated by the averaged IR spectrum shown in Figure 2g. Nevertheless, the rate of evolution profiles are virtually the same (compare curves in Figures 2c and i for  $\text{CO}_2$ ), hence stronger responses for higher masses facilitate monitoring of high MW components.

Any ambiguities which inevitably arise in regard to the identity of particular components may, to a large extent, be overcome by GC pre-separation of thermal decomposition products. The TG/GC/MS/IR system is capable of separating major products, while still allowing characterization of the evolution profile for particular components, as illustrated in Figures 3 and 4. This enables inspection of selected spectra, providing the way for unequivocal identification and chemical interpretation of thermal processes occurring during the TG experiment. In the TG/GC/MS run of Douglas fir wood vapor samples were taken at 1 minute intervals, so profiles for each GC peak can be followed by identifying peaks with the same GC retention time. This task is greatly facilitated by the selection of characteristic ions at  $m/z$  114, 98, 109 and  $m/z$  138, as shown in Figures 3 b-e. The mass spectrum of the component eluting at 8.31 min is shown in Figure 3f and contrasted with a library spectrum of 3-hydroxy-2-penteno-1,5-lactone (Figure 3j), a typical thermal fragment of the pentose moieties. The mass spectrum of the component taken 11.21 min (Figure 3g) shows spectra of polyhexose pyrolysis products, viz. furanone-2 (M.W. 84) and 5-methylfuranone-2 (M.W. 98) which are the products of depolymerization and further decomposition of cellulose [11]. For the temperature range 350-450 C profiles taken at  $m/z$  109 and  $m/z$  138 can be fully confirmed as representing guaiacol and methylguaiacol fragment and molecular ions, respectively, derived from lignin. This is clearly shown by comparison of the mass spectra taken at 11.53 min and 12.99 min with library spectra (Figure 3).

Results of the TG/GC/IR analysis of Douglas fir wood are reported in Figure 4. In Figure 4 a TG and DTG curves are contrasted with total absorption chromatogram (TAC) profiles recorded at 1 minute intervals each minute after "injection" of the TG vapors, whereas the averaged FTIR spectrum of all volatile components is shown in Figure 4b. This spectrum reflects the complex composition of the pyrolysis products and is dominated by gases with strong absorption coefficients, such as  $\text{CO}_2$ ,  $\text{CO}$  and  $\text{H}_2\text{O}$ , thereby complicating individual band assignments and chemical interpretations concerning any additional minor components. In Figure 4c a detailed view of an expanded section of the chromatograms shown in Figure 4a is presented (8-24 mins) and the presence of numerous series of peaks is demonstrated. At 24 s retention time a set of chromatographic peaks exists which reach maximum intensity at 11 min. TG run time (265 C). The spectrum of this component contains a strong absorption band at 1184  $\text{cm}^{-1}$ , the selected wavenumber chromatograms of which are shown in Figure 4d, indicating the presence of the C-O stretching vibrations of lactones. In addition to the profiles of these main components, showing the correspondence to the 3-hydroxy-2-penteno-1,5-

lactone from hemicelluloses, there are also two additional sets of peaks at retention time 7 s and maximum rate of evolution at 13 min. (295 °C) as well as at 40 s and maximum evolution rate at 16 min. (340 °C). The last profile clearly exhibits an evolution maximum that is coincident with a profile shown in Figure 4e. The components characterized by retention times approx. 30 s and strong absorption at 1810  $\text{cm}^{-1}$ , typical for carbonyl absorption of unsaturated lactones, confirm the presence of 2-furanones generated during the thermal breakdown of cellulose. Finally, the third major stage in the pyrolysis of wood is seen in the occurrence of components reaching peak evolution rates in the 17-18 min run time (355-370 °C) range and decreasing relatively slowly afterwards. Strong absorption bands near 1500  $\text{cm}^{-1}$  and just below 1300  $\text{cm}^{-1}$  indicate the presence of phenol and aryl-alkyl ethers functionalities, as would be expected from the breakdown products of lignin. An infrared spectrum of such component taken at 42 s after sampling (marked with asterisk in Figure 4f) is shown in Figure 4g and is contrasted with a FTIR reference spectrum of guaiacol, presented in Figure 4h.

Characteristics of this technique combine precise temperature information and accurate weight loss with detailed MS and IR response profiles thereby providing detailed information about the mechanisms and kinetics of thermal degradation processes. Chemical interpretations of the components evolved during heating of lignocellulosic materials under a helium atmosphere are greatly facilitated by inspection of the infrared and mass spectra, if necessary after GC pre-separation.

## ACKNOWLEDGEMENTS

Financial support of the work reported here was provided by the Advanced Combustion Engineering Research Center (funded by NSF, the State of Utah, 23 industrial participants, and the U.S. DOE), as well as The Consortium for Fossil Fuel Liquefaction Science (UKRF-4-23576-90) and by Hewlett-Packard Corporation.

## REFERENCES

1. Antal, M.J., Jr. In Boer, K.W.; Duffie, J.A., Eds., Advances in Solar Energy, ASES Publication, New York, 1985, Vol 2, p. 175.
2. Evans, R.J.; Milne, T.A.; Soltys, M.N. J. Anal. Appl. Pyrol. 1986, 9, 207.
3. Shafizadeh, F. J. Anal. Appl. Pyrol. 1982, 3, 283.
4. DeGroot, W.F.; Pan, W-P.; Rahman, M.D.; Richards, G.N. J. Anal. Appl. Pyrol. 1988, 13, 221.
5. Graham, R.G.; Bergougnou, M.A.; Overend, R.P. J. Anal. Appl. Pyrol. 1984, 6, 95.
6. Shafizadeh, F.; McGinnis, G.D. Carbohydr. Res. 1971, 16, 273.
7. Martin, F.; Saiz-Jimenez, C.; Gonzalez-Vila, F.J. Holzforschung, 1979, 33, 210.
8. Windig, W.; Meuzelaar, H.L.C.; Shafizadeh, F.; Kelsey, R.G. J. Anal. Appl. Pyrol. 1984, 6, 233.
9. Holbrook, K.M.; Buchanan, R.M.; Meuzelaar, H.L.C.; Proc. of the 38th ASMS Conf. on Mass Spectrometry and Allied Topics, Tucson, Arizona, June 3-8, 1990, p. 900.
10. Evans, R.J.; Milne, T.A. Energy Fuels 1987, 1, 123.
11. Pouwels, A.D.; Tom, A.; Eijkel, G.B.; Boon, J.J. J. Anal. Appl. Pyrol. 1987, 11, 417.

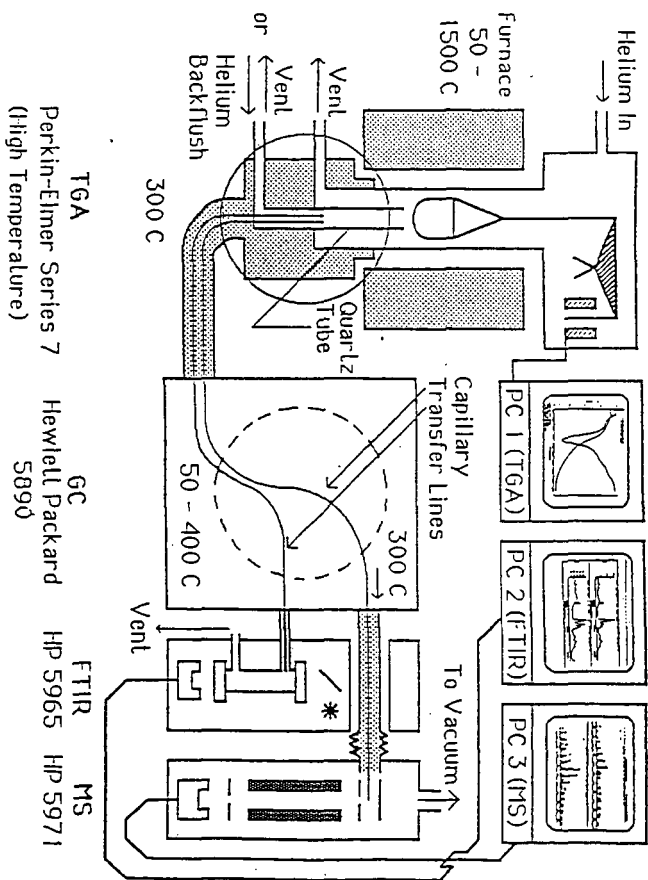


Figure 1. TG/GC/IR/MS instrument configuration.

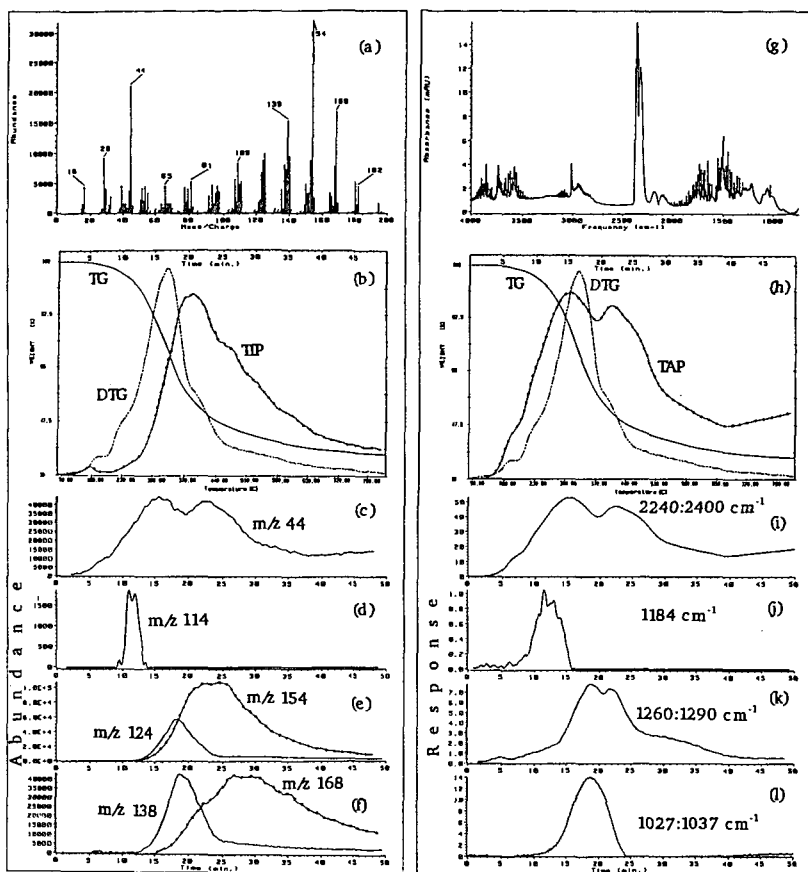
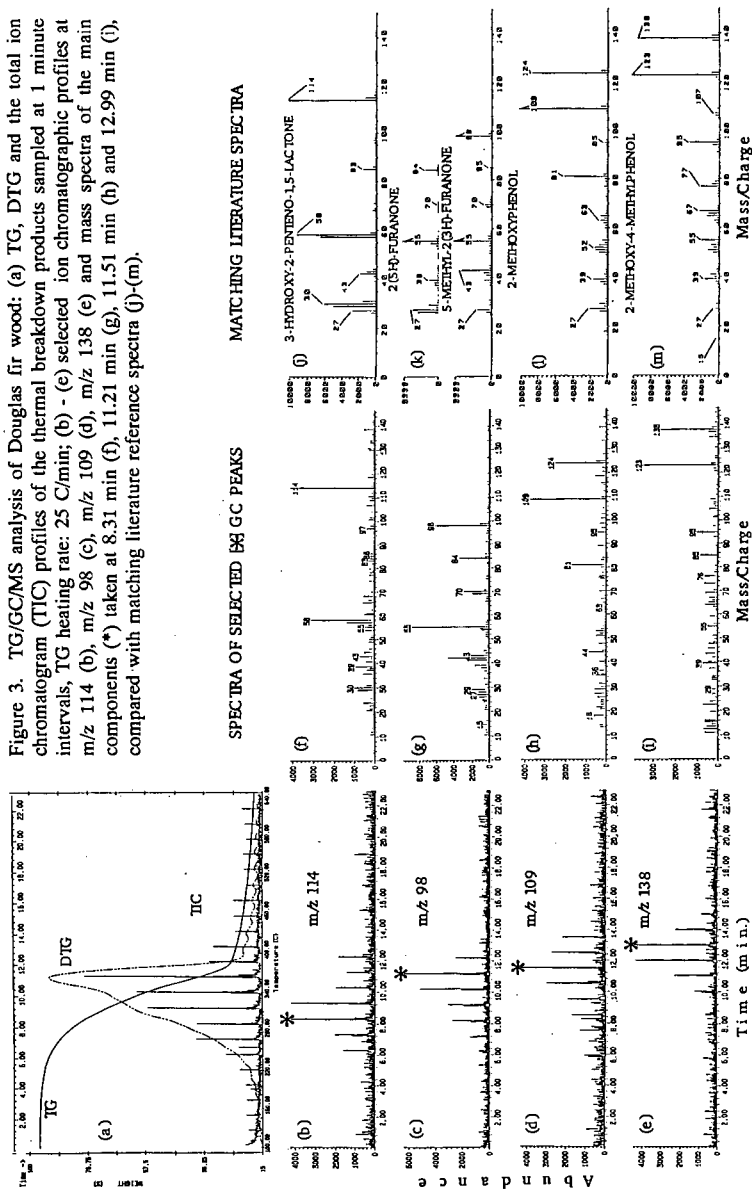


Figure 2. TG/FTIR/MS analysis of steam explosion lignin from Yellow Poplar wood: (a) the averaged MS spectrum of thermal degradation products; (b) TG, DTG and total ion profiles (TIP) of the degradation products; TG heating rate: 15 C/min; (c)-(f) selected ion profiles indicating the evolution of CO<sub>2</sub> (c); 3-hydroxy-2-penteno-1,5-lactone (d); guaiacol ( $m/z$  124) and syringol ( $m/z$  154) (e); 4-methylguaiacol ( $m/z$  138) and 4-methylsyringol ( $m/z$  168) (f); (g) the averaged FTIR spectrum of thermal degradation products; (h) TG, DTG and the total absorption profiles (TAP) of the thermal degradation products; (i)-(l) selected wavenumber profiles indicating the evolution of CO<sub>2</sub> (i), lactones (j), alkyl-aryl ethers (k) and methanol (l).

Figure 3. TG/GCMS analysis of Douglas fir wood: (a) TG, DTG and the total ion chromatogram (TIC) profiles of the thermal breakdown products sampled at 1 minute intervals, TG heating rate: 25 C/min; (b) - (e) selected ion chromatographic profiles at m/z 114 (b), m/z 98 (c), m/z 109 (d), m/z 138 (e) and mass spectra of the main components (\*) taken at 8.31 min (f), 11.21 min (g), 11.51 min (h) and 12.99 min (i), compared with matching literature reference spectra (j)-(m).



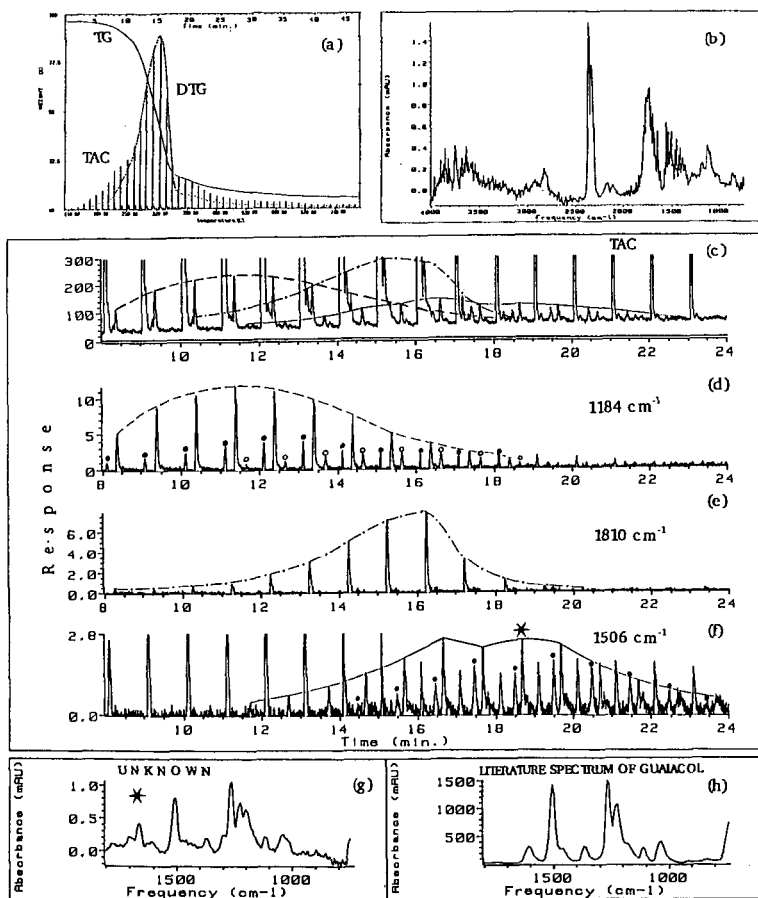


Figure 4. TG/GC/IR analysis of Douglas fir wood: (a) TG, DTG and the total absorption chromatogram (TAC) profiles of the thermal breakdown products sampled at 1 minute intervals, TG heating rate: 15 C/min; (b) the averaged FTIR spectrum of all volatile degradation products; (c) the expanded section of the total absorption chromatogram shown in (a); degradation products from hemicellulose (---), cellulose (---) and lignin (—); (d) - (f) selected wavenumber chromatographic profiles [(d) at 1184 cm<sup>-1</sup> (lactones derived from hemicellulose), (e) at 1810 cm<sup>-1</sup> (furanones derived from cellulose), (f) at 1506 cm<sup>-1</sup> (phenols derived from lignin)]; (g) FTIR spectrum of the unknown component (\*) taken at 18.70 min and corresponding to the phenols derived from lignins (---) compared with the reference spectrum of guaiacol (h).

# **LASER PYROLYSIS GAS CHROMATOGRAPHY/MASS SPECTROMETRY OF SINGLE SPHEROCARB PARTICLES IMPREGNATED WITH BITUMINOUS AND POLYMERIC SUBSTANCES**

Waleed S. Maswadeh, Huaying Huai and Henk L.C. Meuzelaar  
Center for Micro Analysis & Reaction Chemistry, University of Utah  
214 EMRL, Salt Lake City, UT 84112

**Keywords:** coal devolatilization, laser pyrolysis, mass spectrometry

## **INTRODUCTION**

A major bottleneck in the development of novel coal characterization methods, such as laser pyrolysis GC/MS, capable of analyzing individual coal particles, is the unavailability of suitable standard samples. Although carefully homogenized and characterized standard coals are now available through the Argonne National Laboratory Premium Coal Sample Program (ANL-PCSP) such "statistically homogeneous" coal powders are of limited value as reference materials for single particle analysis methods. Even if it would be feasible to prepare particles of closely similar chemical composition and size, e.g., by using highly concentrated coal maceral fractions and careful sieving, remaining variations in shape, density, porosity or thermal conductivity could still introduce an unacceptably high level of uncertainty for most optimization and calibration purposes.

In an attempt to find model coal char particles with well defined chemical [1,2] and physical properties, e.g., for the purpose of modeling char oxidation reactions, several authors have used Spherocarb® particles. Flagan et al [3] have even prepared spherical char particles spiked with mineral matter components in order to more closely mimic actual coal char particles. Although Spherocarb particles still show considerable variability with regard to size (rel. s.d. ~20% on a volume basis), other characteristics such as shape, density, porosity, thermal conductivity and chemical composition are assumed to be quite constant.

Unfortunately, Spherocarb particles are of little value for modeling coal devolatilization reactions due to their very low volatile matter yields. This prompted us to think of ways to increase volatile matter yields by introducing a variety of model compounds, ranging from low molecular weight, bitumen-like components to polymeric materials such as soluble lignins or resins. To the best of our knowledge this article represents the first reported use of bitumen and polymer impregnated Spherocarb particles for modeling devolatilization processes in individual coal particles.

## **EXPERIMENTAL**

Bitumen-like low MW compounds, consisting of a mixture of alkylnaphthalenes prepared by open column LC subfractionization of a coal pyrolyzate, [4] with additional 1-3 ring alkylaromatics and hydroxyaromatics added in later were impregnated into a small batch of Spherocarb particles, in the 125-150 µm dia. size range from a 8 mg/ml solution in methanol, followed by evaporation of the solvent at room temperature. The average amount of bitumen adsorbed by each particle was estimated to be approx. 70 ng. Soluble polymeric materials, such as steam-exploded cottonwood lignin and fossil resin derived from Utah (Blind Canyon seam)

coal were impregnated from 8 mg/ml solutions in 2:1 methanol/dichloromethane and toluene, respectively. Assuming complete absorption of the polymers into the Sphero carb particles the maximum average amount of polymer per particle was estimated at 70 ng. Experiments with actual coal particles in the 100-150  $\mu\text{m}$  size range, prepared by careful sieving, involved Illinois #6 coals from the ANL-PCSP program.

Laser pyrolysis gas chromatography/mass spectrometry (laser Py-GC/MS) experiments were performed with two different experimental configurations as shown in Figures 1a and 1b respectively. The first experimental set-up (Figure 1a) has been described before in more detail [5] and consists of an EDB (electrodynamical balance), a 50 W cw  $\text{CO}_2$  laser and a Finnigan MAT ITMS system. The EDB type particle levitation cell was constructed in such a way as to provide line-of-sight access to the center of the cell for the two opposing  $\text{CO}_2$  laser beams as well as for a stereo microscope and a two-color optical pyrometer. Typical cell operating parameters for levitating a 120  $\mu\text{m}$  dia. Sphero carb particle are: ring electrode 3000 V (60 Hz ac), upper end cap +100 V dc, lower end-cap -100 V dc. A second, novel experimental set-up (Figure 1b) uses copper electron microscopy grids with 45 x 45  $\mu\text{m}$  openings separated by 5  $\mu\text{m}$  thick bars (78% open, see Figure 2) to support individual coal particles in a downward directed flow of air or inert gas in the center of two  $\text{CO}_2$  laser beams crossing at a 37° angle. Since the grids are mounted directly against the mouth of the sampling inlet, yields of volatile products are maximized. Furthermore, introducing, positioning, stabilizing and retrieving individual particles is greatly simplified compared to the set-up in Figure 1a, while conductive heat losses may be assumed to be minimal in view of the light construction of the grid.

The cw  $\text{CO}_2$  laser (Apollo 3050 OEM) is capable of electronic pulsed beam operation. The 8 mm dia. beam is split equally into 2 separate beams focussed at the center of the levitation cell or grid (beam waist ca. 400  $\mu\text{m}$ , typical power densities 4-10  $\text{MW}/\text{m}^2$ ). A co-linear, parafocal HeNe laser beam permits positioning of the particle in the center of the  $\text{CO}_2$  laser beam. Two IR detectors measure integrated pulse energy and time-resolved pulse energy, respectively.

Finally, a heated fused silica capillary GC column (2m x .18 mm DB5) equipped with a special air sampling inlet enables intermittent sampling of volatiles from the center of the levitation cell or grid into the ITMS vacuum system while providing a highly useful degree of GC separation. During a typical run the GC column is ballistically heated from 50 C to 200 C in approx. 2 minutes.

## RESULTS AND DISCUSSION

The novel laser pyrolysis GC/MS configuration shown in Figure 1b, in which coal and Sphero carb particles are supported on ultralight electron microscopy grids (Figure 2), promotes efficient collection of volatile pyrolysis products. As shown in Figure 3, this results in high quality Py-GC/MS profiles of single coal particles. Nevertheless, due to the inherent heterogeneity of individual coal particles with regard to physical and chemical characteristics, marked differences in absolute and relative yields of pyrolysis products are observed during successive analyses of actual coal particles, e.g. for the purpose of kinetic studies, as shown in Figure 4.



This prompted us to use Spherochar particles spiked with known quantities of low MW bitumen-like substances (Figures 5 and 6) or soluble polymeric substances, such as lignin (Figure 7) and fossil resin (Figure 8). Laser desorption studies of bitumen-like substances, composed of alkynaphthalenes and other 1-3 ring alkylaromatics (Figures 5 and 6), are relevant in view of the well known presence of significant quantities of thermally extractable bitumen in many low or medium rank coals [6]. As illustrated in Figure 5, kinetic studies of bitumen release rates from Spherochar particles as a function of laser pulse length do indeed show a markedly constant relative abundance of major bitumen components.

Since the bulk of the coal components undergoing devolatilization reactions consists of nonvolatile, macromolecular compounds which undergo bond scission reactions in addition to the thermal desorption behavior exhibited by low MW, bitumen-like compounds, it is desirable to work with polymeric materials when modeling coal devolatilization processes. Ideally, one would like to introduce high MW coal components, e.g., obtained by solvent extraction of suitable coals into the Spherochar particles. Unfortunately, it tends to be quite difficult to remove effective solvents such as pyridine from these extracts, let alone from a strongly adsorbing Spherochar matrix. These considerations led us to focus on soluble model polymers rather than on high MW vitrinite components. Because of its chemical resemblance to vitrinite components in peats and low rank coals, we chose a soluble lignin. Secondly, we selected a fossil coal resin, which appears to be the only high MW coal component readily soluble in common organic solvents.

Both the lignin and the resin are known to depolymerize readily under typical pyrolysis conditions, thus producing mixtures of characteristic building blocks. As expected from a hardwood lignin [7] the cottonwood lignin sample produces both guaiacylic (e.g.,  $m/z$  124, 138, 152) and syringylic (e.g.,  $m/z$  154) building blocks (see Figure 7). Similarly, the Blind Canyon seam resin, known to consist primarily of polymeric sesquiterpenoids [8], produces a characteristic series of sesquiterpenoid building blocks as shown in Figure 8, ranging from cadinenes ( $m/z$  204) through the partially aromatized calamenes ( $m/z$  202) to the fully aromatized cadalene ( $m/z$  198). It should be noted here that the resinite pyrolysis patterns shown in Figure 8 appear to be more simple than those obtained by conventional pyrolysis GC/MS techniques. Whether this is due to selective loss of less stable pyrolysis products in the Spherochar particles or to differences in primary pyrolysis mechanisms at the much higher heating rates achieved by the  $\text{CO}_2$  laser ( $10^4$ - $10^5$  K/sec) needs to be investigated further.

Although the experiments with polymer impregnated Spherochar particles are still in a relatively early stage, the selected ion chromatograms in Figures 7 and 8 demonstrate that it is indeed possible to introduce readily detectable amounts of such polymers. Unknown at present, however, are the answers to the following fundamental questions:

- (1) what is the maximum weight % of polymeric materials that can be introduced;
- (2) how can the amount of polymeric material adsorbed into each Spherochar be conveniently controlled and measured;
- (3) to what extent does the Spherochar matrix influence the devolatilization mechanisms and kinetics; and
- (4) are polymer impregnated Spherochar particles well enough defined to achieve the desired reduction in interparticle heterogeneity during devolatilization experiments?

The primary objective of several experiments currently underway in our laboratory is to find answers to the above questions.

## CONCLUSIONS

The feasibility of producing bitumen and polymer impregnated Spherocarb particles for coal devolatilization modeling experiments has been established. Bitumen-impregnated Spherocarb particles show a markedly decreased level of interparticle heterogeneity compared to actual coal particles. Spherocarb particles impregnated with (soluble) polymeric materials produce readily detectable volatile products thought to represent characteristic building blocks produced by bond scission reactions. Although the "volatile matter enhanced" Spherocarb particle approach appears to offer promise for modeling coal devolatilization reactions, several fundamental questions regarding the quantitative and qualitative behavior of such systems remain to be answered before this approach can be recommended as a general tool for devolatilization studies in individual coal particles.

## ACKNOWLEDGEMENTS

This work was sponsored by the Advanced Combustion Engineering Research Center. Funds for this Center are received from the National Science Foundation, the State of Utah, 23 industrial participants, and the U.S. Department of Energy.

## REFERENCES

1. Spjut, R.E., Sarofim, A.F., Longwell, J.P., "Laser Heating and Particle Temperature Measurement in an Electrodynamic Balance," *Langmuir*, Vol. 1, #3, 1985.
2. Phuoc, T.X., Maloney, D.J., "Laser Pyrolysis of Single Coal Particles in An Electrodynamic Balance," 22nd Symp. (Intl.) on Combustion (The Combustion Institute), 1988, pp. 125-134.
3. Levendis, Y.A., Flagan, R.C., "Synthesis, Formation and Characterization of Micro Sized Glassy Carbon Spheres of Controlled Pore Structure", *Carbon* 27, 265-283, 1989.
4. Hoesterey, B.L., Windig, W., Meuzelaar, H.L.C., Eyring, E.M., Grant, D.M., Pugmire, R.J., "An Integrated Spectroscopic Approach to the Chemical Characterization of Pyrolysis Oils" in *Pyrolysis Oils from Biomass: Producing, Analyzing and Upgrading*, 1988, ACS Symp. Series 376, J. Soltes and T.A. Milne (eds.), pp. 189-202.
5. Maswadeh, W., Arnold, N.S., Meuzelaar, H.L.C., "Laser Pyrolysis-transfer Line Chromatography/Mass Spectrometry of Single, Levitated Coal Particles", *ACS Preprints, Div. of Fuel Chem.*, Vol. 35(3), August 1990, pp. 713-720.
6. Yun, Y., Meuzelaar, H.L.C., "Simultaneous Thermogravimetric and Mass Spectrometric Observations on Vacuum Pyrolysis of Argonne PCSP Coals," *ACS Preprints, Div. of Fuel Chem.*, Vol. 33, #3, Sept. 1988, pp. 75-84.
7. Saiz-Jimenez, C.S., Boon, J.J., Hedges, J.I., Hessels, J.K.C., deLeeuw, J.W., "Chemical Characterization of Recent and Buried Woods by Analytical Pyrolysis", *J. Anal. Appl. Pyrol.*, 11 (1987) 437-450.
8. Meuzelaar, H.L.C., Huai, H., Lo, R., Dworzanski, J. "Chemical Composition and Origin of Fossil Resins from Utah Wasatch Plateau Coal", submitted to *Fuels Processing Technology* (1990).

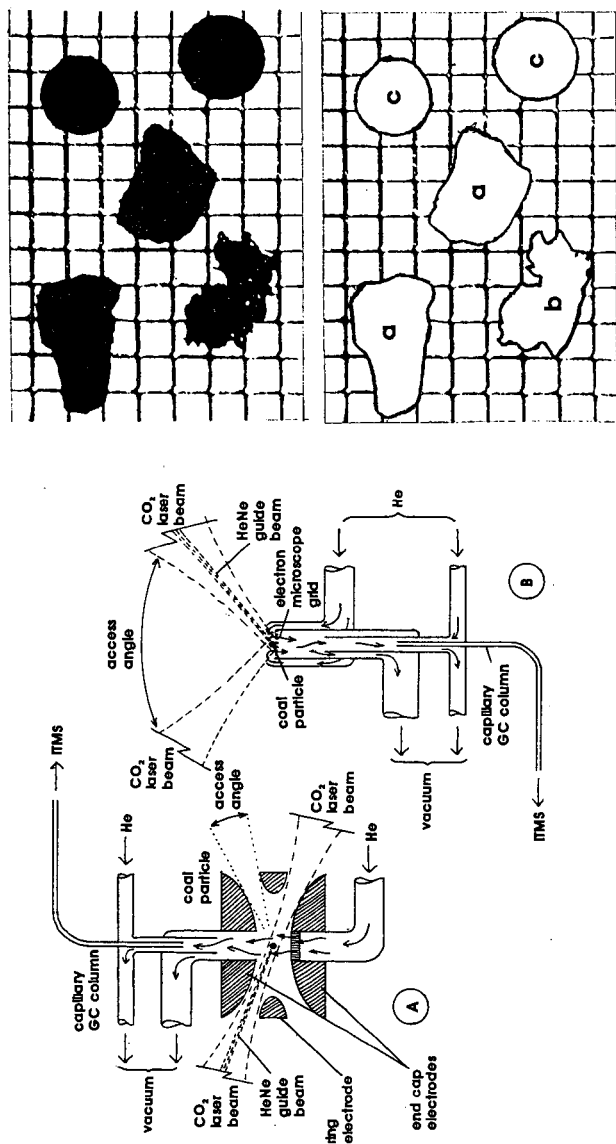


Figure 1. Laser Py-GC/MS configurations used: (a) electrodynamic balance (EDB) with opposing laser beams; (b) electron microscope grid with crossed laser beams. Note special sample inlet and capillary GC transfer line connection to ion trap mass spectrometer (ITMS).

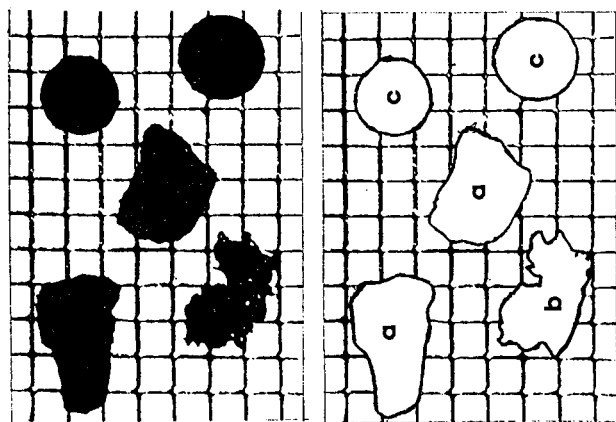


Figure 2. Microscopic view of coal and char particles on 400 mesh copper electron microscope grid; (a) fresh particles of Illinois #6 coal, (b) char particle, (c) Spherochar particles. (a) and (c) were added later. Note degree of size and shape variation present.

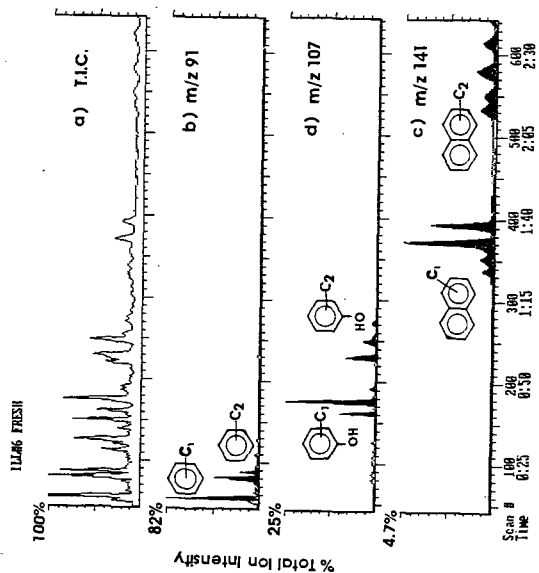


Figure 3. Laser Py-GC/MS profiles of single Illinois #6 coal particle obtained with system configuration shown in Figure 1b. Note good signal-to-noise ratio and useful degree of chromatographic separation. Highly similar patterns can be obtained with the system configuration shown in Figure 1a as well as by conventional Curie-point Py-GC/MS.

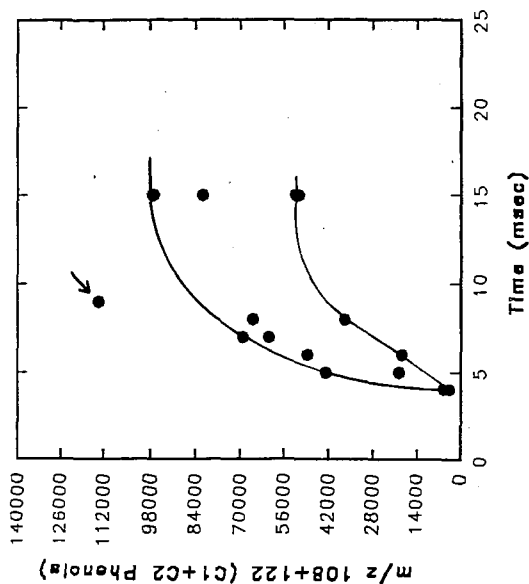


Figure 4. Relationship between laser pulse time and yield of specific pyrolysis products ( $C_1$  and  $C_2$  alkylphenols) during 14 consecutive laser Py-GC/MS runs on individual Illinois #6 coal particles. Note large variations in yield. Curves fitted to maximum and minimum values only. Arrow indicates outlier with anomalous GC/MS pattern. Experimental conditions as in Figure 1b.

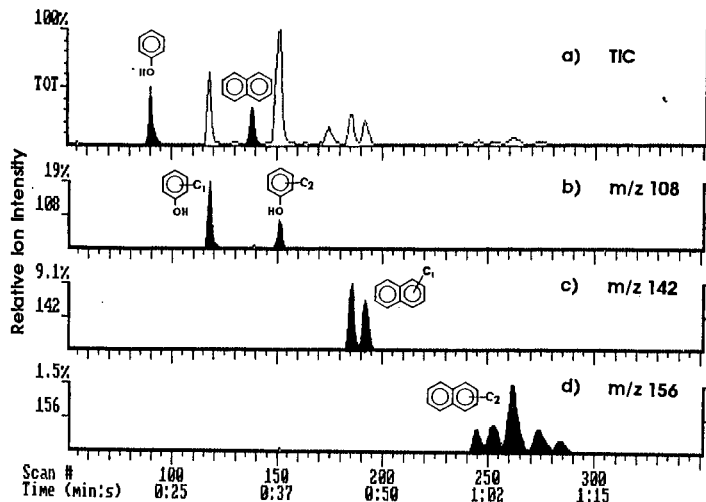


Figure 5. Laser desorption GC/MS profiles of a single Sphercarb particle impregnated with a mixture of bitumen-like compounds. Note separation of various alkylaromatic isomers. Experimental configuration as in Figure 1a.

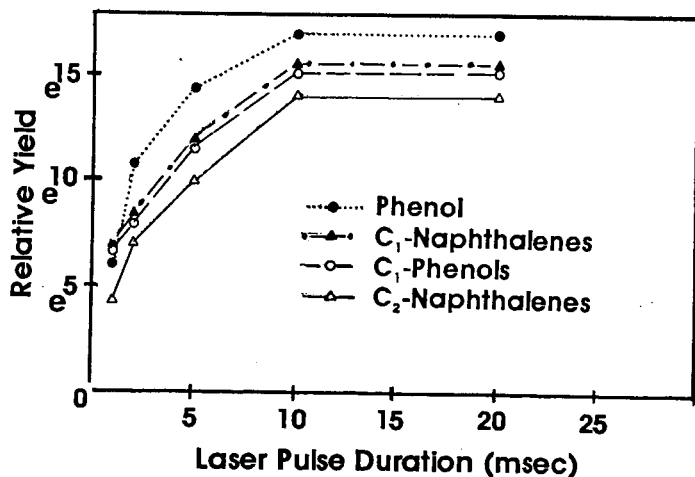


Figure 6. Relationship between laser pulse time and desorption yields of some of the model compounds shown in Figure 5. Each dot represents the average of 2 different laser desorption GC/MS analyses. Note closely similar relative abundances at all pulse durations, except for phenol.

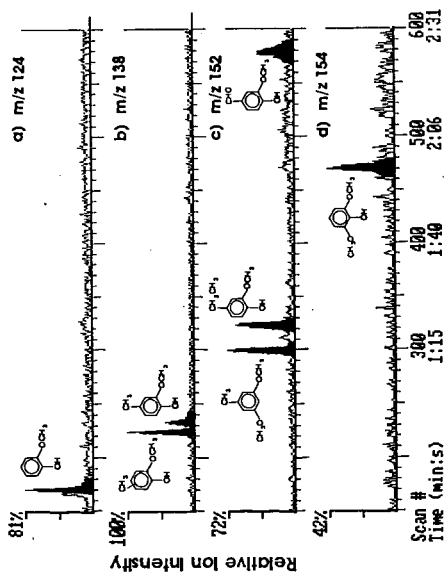


Figure 7. Selected ion chromatograms obtained by Laser Py-GC/MS analysis of a single, lignin impregnated Spherocharb particle. Note presence of characteristic hardwood lignin building blocks. Experimental conditions as in Figure 1b.

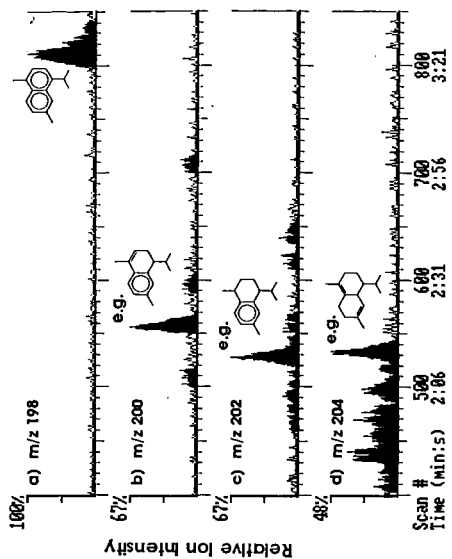


Figure 8. As Figure 5 but using a single, fossil resin impregnated Spherocharb particle. Note characteristic sesquiterpenoid building blocks. It should be noted here that a minor portion of the signals at m/z 198 (cadalene) and 202 (calamenes) represents low MW (monomeric) rather than polymeric components. Experimental conditions as in Figure 1b.

## IDENTIFICATION OF CHEMICAL MARKERS FOR BACTERIA BY PYROLYSIS-TANDEM MASS SPECTROMETRY

Kent J. Voorhees and Stephan J. DeLuca  
Department of Chemistry and Geochemistry  
Colorado School of Mines  
Golden, CO 80401

**Keywords:** Pyrolysis, Tandem Mass Spectrometry, and Bacteria

### INTRODUCTION

There is a substantial body of literature concerning the identification of microorganisms by mass spectrometry (1-11), however, little has been done to identify bacteria in complex variable backgrounds. Several sample introduction and ionization methods have been used for mass-spectrometric analysis of bacteria. Sampling methods may be classified as either direct or indirect, depending on whether whole organisms or extracts are used in the analysis. Of the direct sampling methods, pyrolysis is the most frequently used, although recently FAB methods utilizing whole cells have been shown to be useful for identifying microorganisms (12-13). Pyrolysis has been used with direct introduction of pyrolysate to the ionizer (Py-MS, i.e., pyrolysis *in vacuo*) and also in conjunction with gas chromatography (Py-GCMS). Both electron ionization and chemical ionization have been used in Py-MS and Py-GCMS analyses.

The simplest and most rapid of these methods is direct Py-MS with electron ionization. The Py-mass spectra, however, are generally quite complex and do not easily lend themselves to chemical interpretation. On the other hand, Py-GCMS allows identification of the chemical components of cellular material, hence, specific biomarkers may be found (1,10,14). The presence of such compounds may be used to unambiguously identify target materials, even in complex backgrounds.

Tandem mass spectrometry adds a dimension to traditional Py-MS which permits identification of specific compounds in a pyrolysate (5,11). The purpose of the present research was to determine the feasibility of using Py-MS/MS to detect bacterial biomarkers in complex backgrounds of particulate material.

### EXPERIMENTAL

Measurements were obtained with an Extrel Model EL-400 triple quadrupole mass spectrometer fitted with a Curie-point pyrolysis inlet (11). Daughter ion spectra were collected for  $m/z$  79, 111, 117, 126, and 135. These ions were chosen based on our experience with the samples. The samples used are described in Table 1. All samples were suspended in methanol at about 1mg/ml. Approximately 10  $\mu$ L of each suspension was applied to 610°C Curie-point wires, and the solvent evaporated under a stream of hot air.

Multivariate statistical analyses were carried out with the RESOLVE program (15). Each Py-MS spectrum was collected as a set of raw intensities. Prior to principal components analysis, the data were normalized to constant length. The results, displayed as Karhunen-Loeve (K-L) or principal components plots, show the distribution of the samples in the multivariate mass spectral space. Factor spectra for the components were also derived. Factor spectra show the correlations (positive and negative) of mass spectral peaks with directions in the principal component space.

## RESULTS AND DISCUSSION

In previous experiments (unpublished), we found that the Py-MS patterns of bacteria could vary more within strains of a given species than between different species. For example, the intensities of  $m/z$  52 and 79 varied drastically among strains of *B. subtilis* and *B. licheniformis*. Strains showing large  $m/z$  79 and 52 peaks were sporulated, while other strains were vegetative cells. We postulated that the  $m/z$  79 and 52 peaks were markers for sporulation. The daughter ion spectra of  $m/z$  79 for the test samples (Figure 1) showed that  $m/z$  52 is a strong daughter of  $m/z$  79 for the bacteria, while samples such as fog oil and diesel smoke showed virtually no  $m/z$  52 as a daughter of  $m/z$  79.

The principal components plot shown in Figure 2a separates the *B.g.* spores and *B. subtilis* from the rest of the samples. The factor spectrum generated for principal component 2 (Figure 2b) shows peaks at  $m/z$  52 and 79 positively correlated with the *B.g.* and *B. subtilis* samples, while peaks at  $m/z$  51 and 77 are positively correlated with the remainder of the samples.

Sporulating bacteria produce large quantities of picolinic acid (2-pyridine-carboxylic acid) which forms the hardened "shell" of the spores. The EPA/NIH library spectrum (16) of picolinic acid (virtually identical to that of pyridine) shows large peaks at  $m/z$  79 (i.e., pyridine molecular ion) and  $m/z$  52. Because the mass spectra of pyridine and picolinic acid are so similar, it is not possible to determine which of these species is liberated upon pyrolysis. It is clear, however, that the presence of picolinic acid in the spores is responsible for the separation seen in the K-L plot.

The negative correlation of peak  $m/z$  77 with the sporulated organisms indicates that this peak is more intense (relatively) in the other samples as is obvious by inspection of Figure 1. In order to determine the chemical species responsible for the peak at  $m/z$  79 in samples other than sporulated bacteria, parent ion spectra of  $m/z$  79 were collected. The parent ion spectrum of  $m/z$  79 for diesel smoke is shown in Figure 3. This spectrum is quite complicated and it appears that at least three compound classes are present. The peak at  $m/z$  94 appears to be due to alkylcyclocladienyl hydrocarbons (e.g., methylcyclohexadiene). The  $m/z$  105 peak may be due to alkyl benzaldehydes (e.g., 2,6 dimethylbenzaldehyde) and the series of peaks at  $m/z$  107, 121, 135 and 149 are probably produced by a series of alkyl phenols. Although these identifications are tentative (based on a comparison of EPA/NIH library spectra with the parent and daughter spectra) each of the compound types listed above show a significant  $m/z$  77 peak as well as an  $m/z$  79



peak. It is clear that many compounds contribute to the peak at  $m/z$  79, however, sporulated bacteria are easily identified by the presence of large quantities of picolinic acid, as reflected in the intense  $m/z$  52 peak in the daughter spectrum of  $m/z$  79.

Representative spectra of daughter ions of  $m/z$  117 are illustrated in Figure 4. The major peaks appearing in these spectra are  $m/z$  89, 90, 91, 115 and 117. The K-L plot in Figure 5a shows scores of the samples on the first two principal components. The fog oil, wood smoke, and diesel smoke samples are clearly separated from the other samples, all of which contain protein. The factor spectrum associated with this separation (Figure 5b) shows two distinctive patterns; one correlated with the fog oil and smokes shows large peaks at  $m/z$  91 and 115 while the other pattern (negative direction) has strong peaks at  $m/z$  89 and 90. The spectrum in the negative direction is that of indole, a known pyrolysis product of proteins containing the amino acid tryptophane. The peaks at  $m/z$  91 and 115 are probably due to unsaturated alkyl aromatic compounds, for example, 2-methylbutenylbenzene. The daughter ion spectrum of  $m/z$  117 appears to contain markers for the presence of protein in a sample.

We have observed that the base adenine (MW 135) is liberated by pyrolysis of DNA. It was postulated that adenine could be used as a marker for organisms since all living material contains nucleic acids. The daughter ion spectra in Figure 6 are representative of the sample set. The K-L plot in Figure 7a shows a distribution of samples in the Component 2 direction with wood smoke, fog oil, and diesel smoke at one extreme and *E. coli* and MS-2 coliphage at the other. The factor spectrum associated with Component 2 (Figure 7b) indicates the presence of adenine ( $m/z$  108) in the negative direction, and a series of alkyl phenols ( $m/z$  107, 93, 79, etc.) in the positive direction. The parent ion scan of  $m/z$  135 for diesel smoke shows a homologous series of alkyl chain lengths (of an alkyl phenol) extending up to at least 290 amu (a C14 alkyl group).

The daughter ion spectrum of  $m/z$  135 indicates the presence of nucleic acids by the appearance of an  $m/z$  108 peak. This suggests that the daughter ion spectrum of  $m/z$  135 may be used to determine the presence of living material (or recently living material) in an aerosol sample. This would provide a useful branch point for a decision tree; if adenine is not present, there is no bacterial threat.

Daughter ion spectra were also collected for  $m/z$  111, 126, and 128. In each case there were clear separations of background materials (i.e., fog oil, diesel and wood smoke) from the targets (i.e., MS-2 coliphage, *E. coli*, *B.g.* spores, etc.). The factor spectra associated with these separations, however, were quite complex and could not be interpreted chemically with a high degree of confidence. For example, factor spectra for the daughters of  $m/z$  126 showed correlations of peaks with fog oil that indicated the presence of unsaturated hydrocarbons (probably nonene). The spectra associated with other samples, however, could contain contributions from nucleic acids (thymine), proteins, and carbohydrates (methylhydroxypyranone).

## CONCLUSIONS

The feasibility of using pyrolysis-tandem mass spectrometry to identify biomarkers in complex backgrounds has been demonstrated. Three markers for biological substances have been identified. Adenine, a marker for nucleic acids and hence all living material, is detected in the daughter ion spectrum of  $m/z$  135. The presence of protein in a sample may be inferred from the daughter ion spectrum of  $m/z$  117, which indicates the presence or absence of indole, a product of pyrolysis of proteins containing the amino acid tryptophane. Pyridine, from picolinic acid, is seen in the daughter ion spectrum of  $m/z$  79. This is a marker for the presence of sporulated bacteria. These ions obviously do not solve the problem of identifying specific organisms in ambient samples. There are however hundreds more ions to be studied, and if biomarkers are present in the pyrolysates, Py-MS/MS has the capability of finding them.

## REFERENCES

1. Fox, Alvin; Morgan, Stephen L.; Larsson, Lennart; and Odham, Goran; Eds.; *Analytical Microbiology Methods*. 1989 Plenum Press, NY.
2. Anhalt, John P. and Fenselau, Catherine, *Anal. Chem.* 1975, 47(2), 219-255.
3. Voorhees, Kent J.; Harrington, Peter B.; Street, Thomas E.; Hoffman, Stephen; Durfee, Steven L.; Bonelli, Joseph E. and Firnhaber, Cynthia S. from "Computer-Enhanced Analytical Spectroscopy, V. 2, H.L.C. Meuzelaar, Ed., 1990, 257-275.
4. Voorhees, Kent J.; Durfee, Steven L.; and Updegraff, David M., *J. Microbiol. Meth.* 1988, 8, 315-325.
5. Voorhees, Kent J.; Durfee, Steven L.; Holtzclaw, James R.; Enke, C.G.; and Bauer, Mark R., *J. Anal. Appl. Pyrol.*, 1988, 14, 7-15.
6. Tas, A.C.; Van Der Greef, J.; DeWaart, J.; Bouwman, J.; and Teu Noever de Braw, M.D., *J. Anal. Appl. Pyrol.*, 1985, 7, 249-255.
7. Tas, A.C.; DeWaart, J.; Bouwman, M.C.; Teu Noever de Braw, M.C.; and Van Der Greef, J. *J. Anal. Appl. Pyrol.*, 1987, 11, 329-340.
8. Van der Greef, J.; Tas, A.C.; and Teu Noever de Brauw, M.C. *Biomed. Env. Mass Spec.*, 1988, 16, 45-50.
9. Tas, A.C.; Bastiaanse, H.B.; Van Der Greef, J.; and Kerkenaar, A. *J. Anal. Appl. Pyrol.*, 1989, 14, 309-321.
10. Morgan, Stephen L.; Fox, Alvin; and Gilbert, James. *J. Microbiol. Meth.*, 1989, 9, 57-69.

11. DeLuca, Stephan; Sarver, Emory W.; Harrington, Peter de B.; and Voorhees, Kent J. *Anal. Chem.* 1990, 62, 1465-1472.
12. Heller, D.N.; Feusclau, C.; Cotter, R.J.; Demirev, P.; Olthoff, J.K.; Honovich, J.; Uy, M.; Tanaka, T. and Kishimoto, Y. *Biochem. Biophys. Res. Comm.*, 1987, 142(1), 194-199.
13. Seid, Robert C., Jr.; Bone, William M.; and Phillips, Lawrence R. *Anal. Biochem.*, 1986, 155, 168-176.
14. Holzer, G.; Bourne, T.F.; Bertsch, W. *J. Chromatog.* 1989, 468, 181-190.
15. Harrington, P. de B.; Street, T.E.; Voorhees, K.J.; Radicati di Brozolo, F.; Odom, R.W. *Anal. Chem.* 1989, 61, 715-719.
16. Heller, S.R. and Milne, G.W.A. *EPA/NIH Mass Spectral Data Base*, 1978, Nat. Stand. ref. data ser.; NSRDS-NBS 63.

#### ACKNOWLEDGMENT

The authors wish to thank Teledyne-CME and the U.S. Army CRDEC for their support of this project.

Table 1. Samples used in the study

Substance	Category
Fog oil	f
Wood smoke	w
Diesel smoke	d
Grass pollen ( <i>Secale cereale</i> )	p
Dry Yeast	y
Aldolase	a
MS-2 coliphage	m
<i>E. coli</i>	e
<i>B. subtilis</i> (sporulated)	b
<i>B. globigii</i> spores ( <i>B. subtilis</i> var. <i>niger</i> )	g

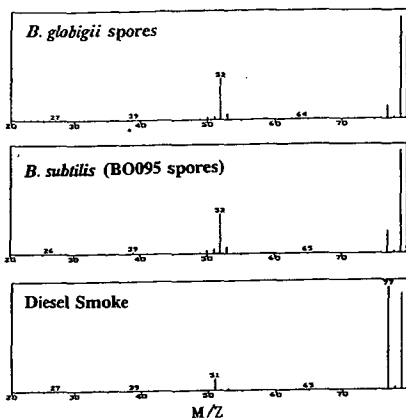


Figure 1. Selected daughter ion spectra for  $m/z$  79.

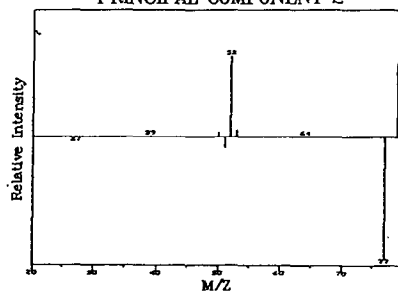
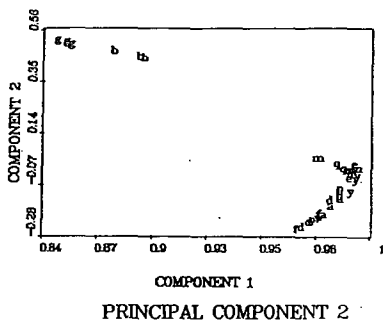


Figure 2. Principal components plot (a) and factor spectrum (b) for daughters of  $m/z$  79.

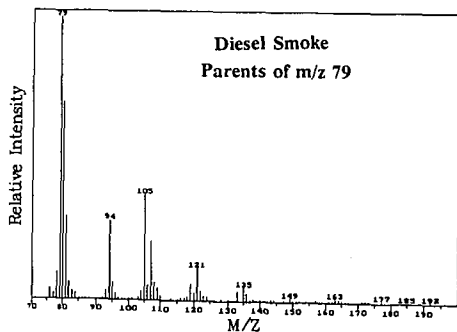


Figure 3. Parent ion spectrum of diesel smoke for  $m/z$  79.

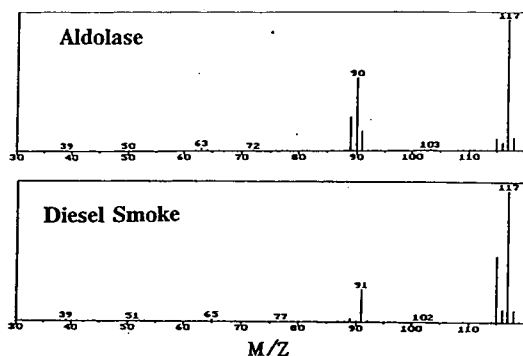


Figure 4. Selected daughter ion spectra for  $m/z$  117

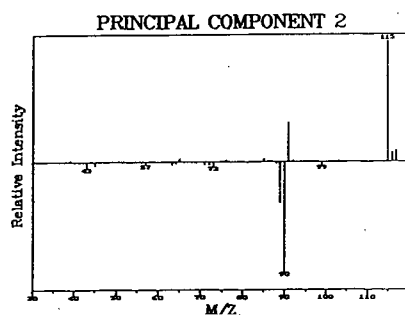
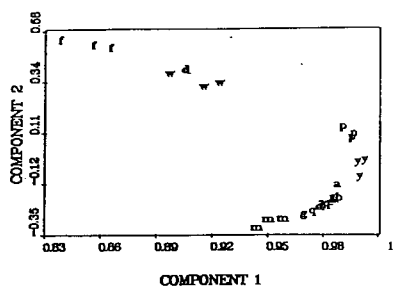


Figure 5. Principal components plot (a) and factor spectrum (b) for daughters of  $m/z$  117.

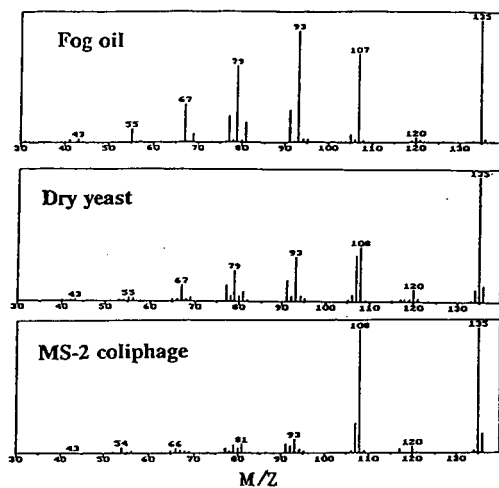


Figure 6. Selected daughter ion spectra for  $m/z$  135.

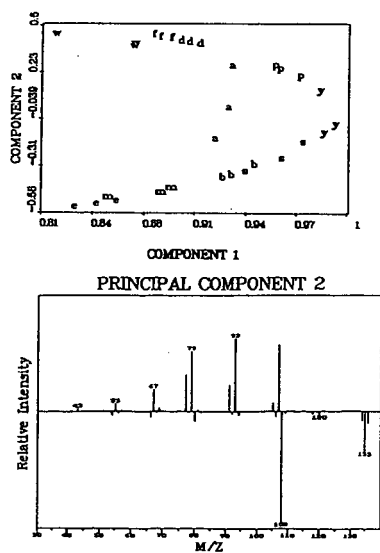


Figure 7. Principal components plot (a) and factor spectrum (b) for daughters of  $m/z$  135

# STABLE CARBON ISOTOPIC COMPOSITION OF INDIVIDUAL PRODUCTS FROM FLASH PYROLYSIS OF KEROGENS

By

Tim Eglinton<sup>1</sup>, Brian D. Fry<sup>2</sup>, Katherine H. Freeman<sup>3</sup> and J.M. Hayes<sup>3</sup>

<sup>1</sup>Dept. of Chemistry, Woods Hole Oceanographic Institution, Woods Hole, MA 02543

<sup>2</sup>Ecosystems Center, Marine Biological Laboratories, Woods Hole, MA 02543

<sup>3</sup>Biogeochemical Laboratories, Depts. of Geological Sciences and of Chemistry, Indiana University, Bloomington, IN 47405

**Keywords:** Kerogen, Flash Pyrolysis, Compound-specific Isotopic Analysis.

## ABSTRACT

Recent analytical developments now allow determination of the stable carbon isotopic compositions of individual compounds eluting from a capillary gas chromatography column. This study describes compound-specific isotope measurements made on aliphatic hydrocarbon products from flash pyrolysis (800°C, 20s) of kerogens representing a range of depositional environments and ages. The carbon isotopic compositions of the major aliphatic pyrolysis products (*n*-hydrocarbons, acyclic isoprenoids and hopanoids), calibrated against those of deuterated *n*-alkane internal standards, were typically measurable to within  $\pm 0.5\text{‰}$ . The data show that for a given sample, *n*-alkenes and *n*-alkanes generally display rather similar values to one another irrespective of carbon number, suggesting a common (bio)polymeric origin. In several cases the average values also reflect the corresponding  $\delta^{13}\text{C}$  TOC value, indicating that (for these samples) the *n*-hydrocarbons are derived from structurally important, or at least isotopically representative, components in the kerogen. Contrastingly, the isotope compositions of *n*-hydrocarbons varied substantially between samples (average values ranged from  $-33\text{‰}$  to  $-14\text{‰}$ ). Differences in isotopic composition were also apparent between the compound classes studied (e.g. hopanoids were isotopically lighter than the *n*-hydrocarbons).

The data obtained allow new deductions to be made regarding the source(s) of the precursor components in the kerogen and their importance in dictating the overall  $\delta^{13}\text{C}$  TOC value. This technique is particularly useful for samples which gives rise to pyrolysis products whose structures are not sufficiently diagnostic to distinguish between biological sources. In these instances, isotopic data in combination with structural information, may prove invaluable in resolving separate carbon sources.

## INTRODUCTION

Determination of the sources and composition of kerogen - the insoluble organic matter which is preserved in sediments and is ultimately responsible for accumulations of oil and gas - is a major goal in organic geochemistry. Kerogens represent a composite of remnants from a wide variety of organisms (algae, bacteria, higher plants) derived from both terrestrial and marine sources and reflect these differing inputs in a number of ways.

Of the approaches used in organic geochemistry flash pyrolysis has become widely accepted as a technique which can provide important and useful information on the structure and composition of kerogen and related geomacromolecules. Much progress has been made in understanding the pyrolysis mechanisms involved and in establishing precursor-pyrolysis product relationships for wide range of biomacromolecules and associated biochemicals. Pyrolytic markers have been established for the major biochemical precursors such as lignins<sup>[1,2]</sup>, aliphatic biopolymers<sup>[3]</sup>, polysaccharides<sup>[4]</sup> etc. as well as materials of secondary origin such as sulfur-bound macromolecules<sup>[5-8]</sup>. From such relationships the potential exists to reconstruct the proportions of different precursor components from the various biological sources which together comprise the kerogen. However, for a large number of sedimentary situations (particularly in diagenetically altered samples) the structure of the products generated upon pyrolysis are not sufficiently diagnostic to resolve individual sources.

Natural variations in the abundance of stable carbon isotopes (as a result of fractionation effects related to atmospheric and dissolved CO<sub>2</sub> equilibria and uptake) potentially may be used to distinguish between carbon sources according to depositional environment<sup>[9]</sup> (e.g. freshwater *versus* marine) and trophic status<sup>[10]</sup> (e.g. aerobic photoautotrophs *versus* methanotrophs). Applications based on this premise are now well established and, typically, the isotopic composition of the gross kerogen is measured (i.e.  $\delta^{13}\text{C}$  TOC) for these purposes. However, since kerogens are usually comprised of a wide variety of components derived from potentially separate sources,  $\delta^{13}\text{C}$  TOC represents a composite value. In order to resolve these separate contributions, the isotopic compositions of each of the individual constituents must be determined.

It has been clear for some time, therefore, that isotopic analyses on a molecular level have the potential to provide much more detailed information. As a result of several analytical developments, it is now possible to obtain stable carbon isotopic compositions of individual compounds eluting from a GC<sup>[11-15]</sup>. Under conditions of optimal chromatography (i.e. baseline separation) and optimum sample size (individual peaks yielding 10<sup>-8</sup> to 10<sup>-9</sup> moles CO<sub>2</sub>) a precision of  $\pm 0.1\text{‰}$  is currently attainable<sup>[14]</sup>. Previously the only practical alternative has been to isolate individual organic compounds using laborious fractionation and purification procedures so that they could be directly analyzed by isotope ratio mass spectrometry<sup>[16,17]</sup>. With this newly available technology for on-line determination of the carbon isotopic composition of individual components eluting from a gas chromatograph it is now feasible to determine the isotopic compositions of individual pyrolysis products.

The combination of pyrolysis with compound-specific isotope analysis therefore holds tremendous possibilities for identifying and quantifying contributions from the various sources according to both structure (biochemical origin) and isotopic composition, with the ability to de-couple marine input from terrigenous sources representing a particularly important application. This paper describes preliminary results from a study designed to assess the viability and utility of this approach for the characterization of kerogens according to organic matter sources and depositional environment.

## EXPERIMENTAL

Six sediments representing a range of depositional environments (marine, estuarine, lacustrine) and ages (Recent to Carboniferous) were chosen for analysis. Selected details are provided in Table 1. Kerogens were isolated from the sediments using established HF/HCl procedures and solvent-extracted prior to analysis.

Off-line flash pyrolysis experiments were performed on the isolated kerogens using a CDS 120 pyrolyser. Samples (1-5mg) mounted in quartz tubes were pyrolyzed (800°C, 20s.) using a coil pyroprobe in a stream of helium carrier gas. Volatile products were swept from a heated zone (200°C) and trapped in a glass U-tube immersed in liquid N<sub>2</sub>. At the end of the pyrolysis experiment the products were retrieved from the U-tube by dissolution in a dichloromethane/hexane (1:1) and transferred to vials. Purified aliphatic hydrocarbon fractions



were isolated from the pyrolyzates by liquid chromatography on short columns (10cm x 5mm) containing activated silica and alumina using hexane as eluant.

Compound identification was achieved by conventional Gas Chromatography-Mass Spectrometry (GC-MS) using a Carlo Erba 4160 GC interfaced to Finnigan 4500 quadrupole MS (EI 50eV).

Compound-specific isotope analysis of the purified pyrolysis products was performed by Gas Chromatography-Combustion-Isotope Ratio Mass Spectrometry (GC-C-IRMS). The instrument set-up consists of a HP 5890 GC linked *via* a combustion interface to a Finnigan Delta-S isotope MS. The interface consists of three major components: a micro-combustion reactor, a non-cryogenic water extractor and an open split interface. As organic compounds elute from the GC they are combusted to CO<sub>2</sub> and H<sub>2</sub>O in the reactor. Subsequently water is removed prior to entry into the mass spectrometer. The entire system is controlled by Finnigan ISODAT software. The stable carbon isotopic compositions of components of interest were calibrated against those of deuterated *n*-alkane standards co-injected with the sample. The isotopic composition of the standards was previously determined by conventional sealed-tube combustion. All isotopic compositions are quoted relative to PDB.

The bulk kerogens were also combusted and analysed separately to provide  $\delta^{13}\text{C}$  TOC values by conventional isotope mass spectrometry using a Finnigan Delta-S mass spectrometer.

## RESULTS

Masses 44 ( $^{12}\text{C}^{16}\text{O}^{16}\text{O}$ ), 45 ( $^{13}\text{C}^{16}\text{O}^{16}\text{O}$ ) and 46 ( $^{12}\text{C}^{16}\text{O}^{18}\text{O}$ ) are simultaneously monitored during the GC-C-IRMS run. The ratio of  $m/z$  45/44 is used to determine the carbon isotopic composition of the compound. A correction is made for  $^{18}\text{O}$ -containing CO<sub>2</sub> from the intensity of  $m/z$  46. Figure 1 shows  $m/z$  44 mass chromatograms from GC-C-IRMS analysis of two of the kerogens studied. Since each compound is combusted to CO<sub>2</sub> on exiting the GC, the  $m/z$  44 trace is analogous to a conventional FID signal. An expanded portion of a chromatogram showing variations in the  $m/z$  45/44 ion current ratio (in addition to the  $m/z$  44 trace) is presented in Figure 2. Compounds enriched in  $^{13}\text{C}$  elute slightly earlier than the corresponding  $^{12}\text{C}$  equivalent, and thus each peak is manifested in the  $m/z$  45/44 trace as an inflection, the  $^{13}\text{C}$ -rich component constituting the leading edge of the peak. The ratio of the magnitude of excursions away from the baseline by the  $^{13}\text{C}$  (+ve inflection) and  $^{12}\text{C}$  (-ve inflection) component gives the isotopic composition.

Four types of hydrocarbons were typically observed to dominate the chromatograms: *n*-alkenes, *n*-alkanes, acyclic isoprenoid and hopanoid hydrocarbons. Average isotopic compositions for these compound classes determined in the manner described above (summed over the appropriate carbon number range) are listed in Table 1 the six kerogens. Results from replicate analyses suggest that most values may be considered accurate to within  $\pm 0.5\text{‰}$ , however, in the worst cases (*i.e.* for samples which display complex chromatograms, or for components which are incompletely resolved) the uncertainty may be  $\pm 1\text{‰}$  or more. Marine kerogens typically proved more difficult to study than lacustrine samples because of the more complex pyrograms they generate. In Figure 3 the stable carbon isotopic compositions of these pyrolysis products are plotted with respect to carbon number for each of the kerogens. The data show that for a given sample the isotopic compositions of *n*-alkenes and *n*-alkanes are generally rather similar (*i.e.* irrespective of carbon number). This finding suggests a common origin, consistent with a (bio)polymeric source. The average values of these components also, in several cases, reflect the corresponding  $\delta^{13}\text{C}$  TOC value (*e.g.* Green River, Westfield), suggesting that they are derived from structurally important, or at least isotopically representative, components in the kerogen. In instances where isotopic compositions of the pyrolysis products do not closely match the  $\delta^{13}\text{C}$  TOC, then alternative components must be considered. Regarding this point it should be borne in mind that the present investigation has only dealt with aliphatic pyrolysis products. The isotopic

compositions of normal hydrocarbons in the Messel kerogen pyrolyzate showed the greatest difference compared to the  $\delta^{13}\text{C}$  TOC value, being up to 10‰ lighter. It has been proposed<sup>[18]</sup> that both the kerogen and the normal hydrocarbon pyrolysis products from this shale derive predominantly from the cell-wall material of the freshwater alga, *Tetradron minimum*. Here, it is found that the hydrocarbon pyrolyzate is depleted in  $^{13}\text{C}$  by ca. 5‰ relative to the total organic carbon (Table 1). Accordingly, the kerogen must contain  $^{13}\text{C}$ -enriched components that do not yield aliphatic hydrocarbons on pyrolysis. It is required either that the visually recognized cell-wall material is isotopically inhomogeneous or that some additional component is present. The alkane/alkene  $\delta$  values observed in this work are very similar to those of acyclic hydrocarbons in extracts of the Messel Shale<sup>[16,19]</sup>.

The isotopic compositions of the various compound classes studied vary substantially from one sample to another. Average values for normal hydrocarbons range from ca. -33‰ (Messel shale) to ca. -14‰ (Westfield). With the exception of the Westfield kerogen, non-marine lacustrine samples (i.e. Messel and Green River kerogens) give lighter average isotope values than marine samples (Monterey, Peru, Spartina). The Westfield shale appears to represent a rather unusual and interesting case. The organic matter in the shale is almost exclusively comprised of the freshwater macroalga, *Botryococcus braunii*. The lack of isoprenoids in the pyrolyzate (Fig. 1) is also a characteristic feature of *B. braunii*-derived kerogens. Whilst the shale represents a freshwater lake deposit, the isotope values (both of the normal hydrocarbons and the TOC) are unusually heavy. This is likely to reflect low concentrations of dissolved  $\text{CO}_2$  in the environment of carbon fixation. In such circumstances, many carbon-fixing organisms utilize special pathways (such as assimilation of  $\text{HCO}_3^-$ ) for accumulation of inorganic carbon. Isotope effects associated with these largely irreversible processes are small in comparison to that of rubisco, and the resulting organic carbon is relatively enriched in  $^{13}\text{C}$ .

Within-kerogen variations in isotopic composition are apparent between different compound classes generated from the samples studied. Isoprenoid hydrocarbons (when present) were found to vary significantly relative to the *n*-hydrocarbons (Fig. 1). In contrast, the hopanoids are in each case substantially lighter than both the TOC and *n*-hydrocarbons, with values as light as -50‰ recorded for hopanoids in the Messel kerogen pyrolyzate. These latter values show good agreement with those reported by Freeman *et al.*<sup>[15]</sup> for hopanoids in solvent extracts of the same shale, indicating a bacterial (methanotrophic?) contribution to the kerogen.

## CONCLUSIONS

Whilst this study contrasts geochemically very different kerogens, the results demonstrate that isotopic compositions may be readily determined for individual pyrolysis products by GC-C-IRMS. The data allow several new deductions to be made regarding the source of these components and their importance in dictating the overall  $\delta^{13}\text{C}$  TOC value of the kerogen. The approach holds much promise, therefore, for assessing the various sources of biological remnants comprising the kerogen, and also for interpreting the overall TOC value in terms of these separate contributions.

## ACKNOWLEDGEMENTS

The isotope-ratio-monitoring GCMS facility at Indiana University has been established and maintained with support from Chevron Oil Field Research Corporation and from Finnigan MAT. We thank Dr. C.G. Johnson for operation of the conventional GC-MS system.

## REFERENCES

1. Obst J.R. *J. Wood Chem. Technol.* 3, 377-397 (1983).
2. Saiz-jimenez C. and de Leeuw J.W. *Org. Geochem.* 10, 869-876 (1986).
3. Tegelaar E.W., de Leeuw J.W., Largeau C., Derenne S., Schulten H.-R., Muller R., Boon J.J., Nip M. and Sprenkels J.C.M. *J. Anal. Appl. Pyrol.* 15, 29-54 (1989).
4. Helleur R.J. *J. Anal. Appl. Pyrol.* 11, 297-311 (1987).
5. Sinninghe Damsté J.S., Kock-van Dalen A.C., de Leeuw J.W. and Schenck P.A. *J. Chromatogr.* 435, 435-452 (1988).
6. Sinninghe Damsté J.S., Eglinton T.L., de Leeuw J.W. and Schenck P.A. *Geochim. Cosmochim. Acta* 53, 873-889 (1989).
7. Eglinton T.L., Sinninghe Damsté J.S., Kohnen M.E.L. and de Leeuw J.W. *Fuel* 69, 1394-1404 (1990).
8. Eglinton T.L., Sinninghe Damsté J.S., Pool W., de Leeuw J.W., Eijkel G. and Boon J.J. *Geochim. Cosmochim. Acta* Submitted (1991).
9. Schoell M. *Advances in Petroleum Geochemistry, Volume 1.* (Eds J. Brooks and D.H. Welte) pp. 215-245. Academic Press, London (1984).
10. Fry B. and Sherr E. *Contributions to Marine Science* 27, 13-47 (1984).
11. Matthews D.E. and Hayes J.M. *Analyt. Chem.* 50, 1465-1473 (1978).
12. Vogler E.A., Meyers P.A. and Moore W.A. *Geochim. Cosmochim. Acta* 45, 2287-2293 (1981).
13. Gilmour I., Swart P.K. and Pillinger C.T. *Org. Geochem.* 6, 665-670 (1984).
14. Hayes J.M., Freeman K.H. and Popp B.N. *14<sup>th</sup> International Meeting on Organic Geochemistry Abstract.* (1989)
15. Freeman K.H., Hayes J.M., Trendel J.-M. and Albrecht P. *Nature* 343, 254-256 (1990).
16. Hayes J.H., Takigiku R., Ocampo R., Callot H.J. and Albrecht P. *Nature* 329, 48-51 (1987).
17. Boreham C.J., Fookes C.J.R., Popp B.N. and Hayes J.M. *Geochim. Cosmochim. Acta* 53, 2451-2455 (1989).
18. Goth K., de Leeuw J.W., Puttman W. and Tegelaar E.W. *Nature* 336, 759-761 (1988).
19. Freeman K.H. unpublished results.

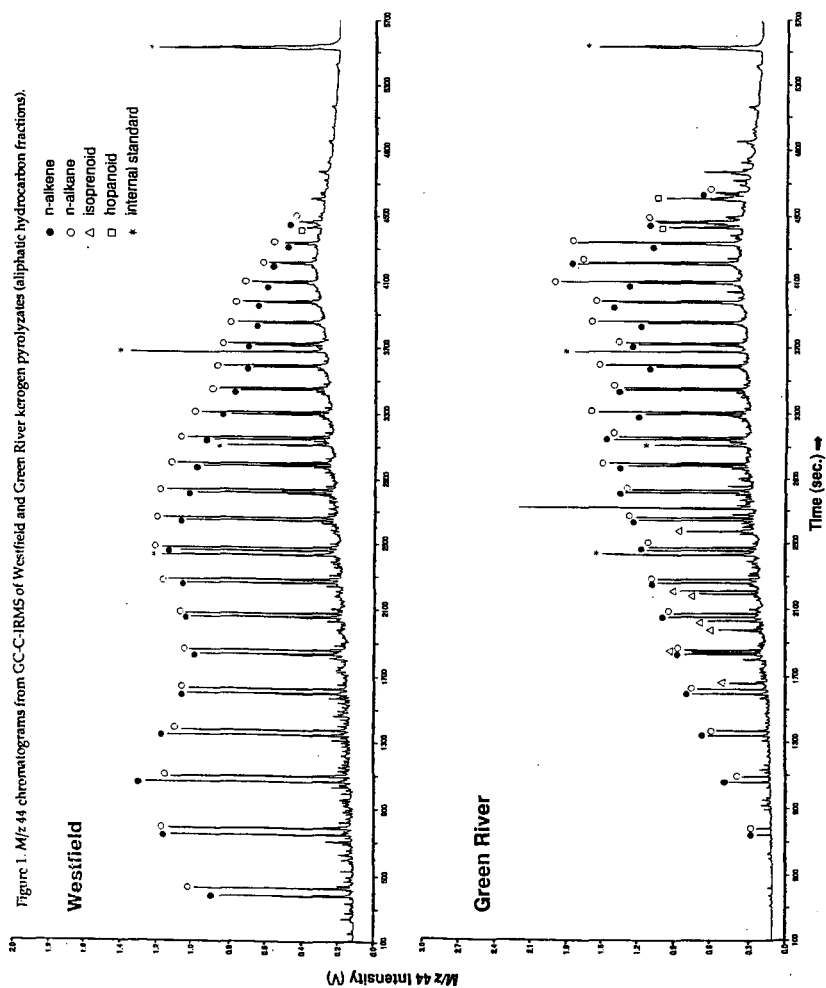
**Table 1. Stable Carbon Isotope Data for Kerogens**

Kerogen	Age	Env.	$\delta^{13}\text{C}$ Value (‰)				
			TOC*	$\Sigma\text{ene}^1$	$\Sigma\text{ane}^2$	$\Sigma\text{isop}^3$	$\Sigma\text{hop}^4$
Westfield, Scotland	Carb.	Lacustrine	-14.26	-14.71	-15.43	n.d.	-23.15
Messel, FRG	Eocene	Lacustrine	-27.69	-32.71	-33.13	-30.83	-45.47
Green River, UT, USA	Eocene	Lacustrine	-29.00	-28.99	-29.96	-31.27	-41.66
Peru, S. America	Contemp.	Marine	-20.47	-23.11	-23.82	-22.90	n.d.
Monterey, CA, USA	Miocene	Marine	-22.17	-23.95	-24.88	-24.64	n.d.
"Spartina", GA, USA	Contemp.	Estuarine	-18.54	-22.69	-23.30	-24.71	n.d.

\*Determined by conventional sealed-tube combustion and MS.

<sup>1</sup>n-alkenes; <sup>2</sup>n-alkanes; <sup>3</sup>isoprenoids; <sup>4</sup>hopanoids.

n.d. = not detected



## Peru Upwelling

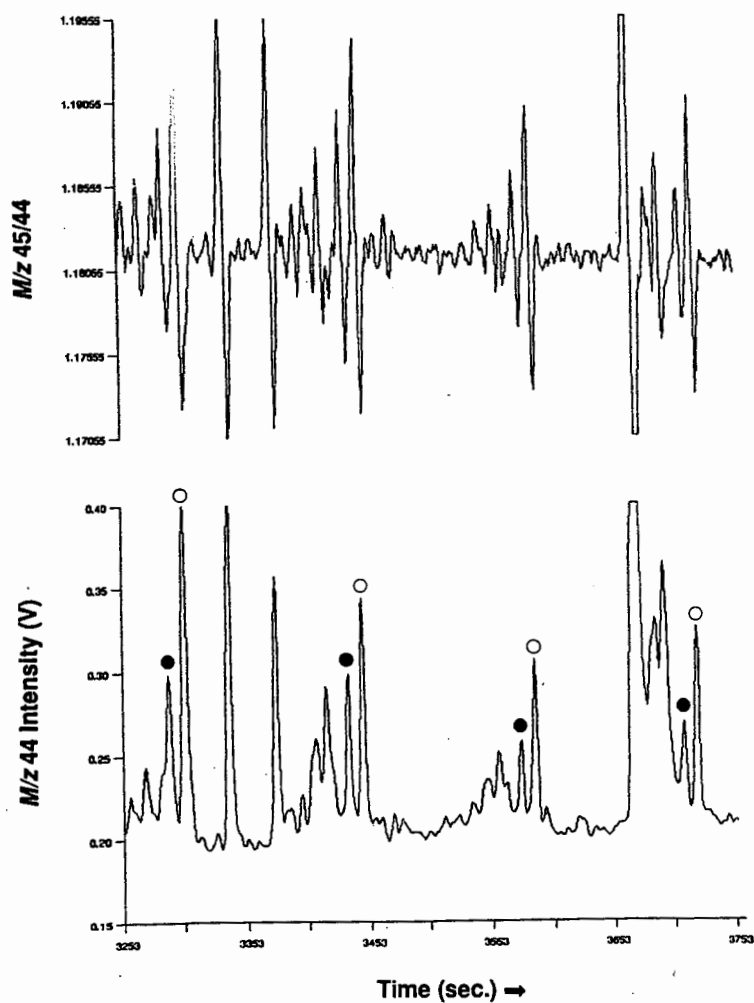


Figure 2. Partial chromatogram of  $m/z$  45/44 ion current ratio (upper) and  $m/z$  44 (lower) from GC-C-IRMS of Peru kerogen pyrolyzate (aliphatic hydrocarbon fraction). Open and closed circles represent  $n$ -alkanes and  $n$ -alkenes respectively.

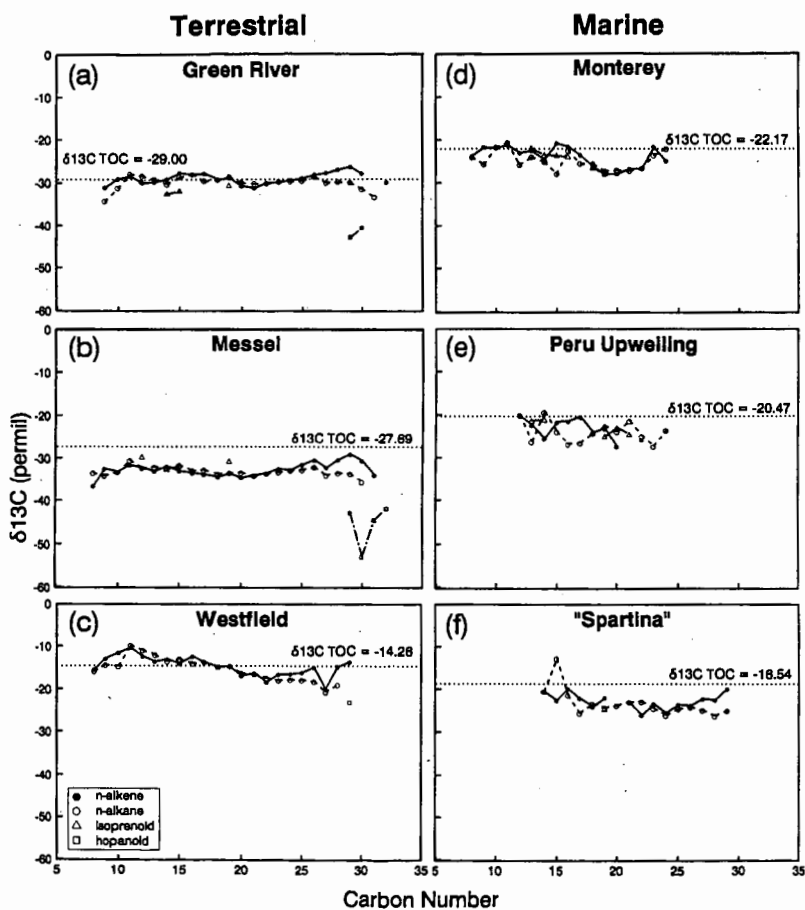


Figure 3. Plots of isotopic composition versus carbon number for different compound classes measured in the kerogen pyrolyzates.

## IN SITU XAFS STUDIES OF SULFUR IN COAL DURING HIGH TEMPERATURE PYROLYSIS AND OXIDATION

M. Mehdi Taghiei, Frank E. Huggins, Naresh Shah and Gerald P. Huffman

233 Mining and Mineral Resources Bldg.  
University of Kentucky  
Lexington, KY 40506

**Keywords:** Sulfur, Pyrolysis, Oxidation, In situ XAFS.

### Abstract:

*In situ* sulfur K-edge XAFS measurements have been performed on Illinois No. 6 and low rank Australian brown coals in order to study the behavior of sulfur forms in coal during pyrolysis and oxidation. The results show that under the relatively slow pyrolysis conditions employed, degradation of organic disulfide starts as low as 200°C while sulfide components degrade at temperatures around 300°C. Pyrrhotite was formed from pyrite during pyrolysis of Illinois No. 6 coal above 400°C. Results obtained during oxidation at temperatures up to 450°C are less well understood. Gradual formation of small amounts of sulfate occurs in both samples, while pyritic sulfur and organic sulfide decrease significantly, with most of the sulfur apparently leaving the sample as SO<sub>2</sub>.

### Introduction

It is well recognized that a full understanding of the behavior of all major forms of sulfur, both inorganic and organic, is essential for the solution of many of the significant research problems involving sulfur in coal. Until very recently, however, information about the different organic forms of sulfur in coal could not be obtained directly, but had to be based on indirect methods involving pyrolysis of the coal. Such pyrolysis techniques include the temperature-programmed reduction ("kinetogram") methods advanced by Attar<sup>[1]</sup>, the flash pyrolysis ("pyroprobe") developed by Calkins<sup>[2,3]</sup>, and a variety of pyrolysis/mass-spectroscopy and gas chromatographic/mass-spectroscopy techniques<sup>[4,5]</sup> that are usually performed on extracts and volatile fractions of the coal, rather than the bulk coal itself. Such pyrolysis methods have provided much useful information about sulfur in coal, but because they do not provide information on the sulfur remaining in the residue materials, the information obtained is not complete.

In the last two years, XAFS spectroscopy has been shown<sup>[6-9]</sup> to be a powerful method for the direct, nondestructive, quantitative determination of all major sulfur forms in coal. In this study, we report some preliminary results from the first *in situ* XAFS spectroscopic investigations of sulfur in coal under conditions of high temperature pyrolysis and oxidation. Emphasis has been given to the quantitative analysis of the various forms of sulfur produced during slow pyrolysis of coal in hydrogen and helium atmospheres as well as oxidation in a helium/oxygen mixture at temperatures up to 600°C.

## Experimental

### *Thermal Analysis:*

The coal samples used in this study were a bituminous Illinois No. 6 coal obtained from Argonne Premium Coal Sample Program Bank and a low rank Australian brown coal (Glencoe). The Illinois No. 6 coal contains 4.83 wt% sulfur of which 2.81 wt% is pyritic sulfur, while the Australian coal contains 5.1% organic sulfur and with very little pyritic sulfur (<0.2 wt%). Some model compounds, such as dibenzylsulfide and dibenzothiophene, have also been examined under similar oxidation conditions.

The X-ray reaction furnace used in this work is modified from the design of Sinfelt and Lytle<sup>[10]</sup>. A chromel-alumel thermocouple is imbedded in a stainless steel backing plate in contact with the sample cell. Temperatures were monitored with a digital voltmeter. Water flow through jackets in the furnace body helps to dissipate heat and prevent the mylar windows of the fluorescent detector from melting. Reactant gases were flowed through the samples which were packed into the cell.

XAFS spectra of samples were obtained while flowing a gas stream of helium or hydrogen in pyrolysis and mixture of 95% helium, 5% oxygen in oxidation at temperatures up to 600°C. Since each spectrum takes approximately 30 minutes to complete, these are considered slow pyrolysis and oxidation processes.

### *XAFS Analysis:*

The XAFS measurements were performed at beam line X19-A at the National Synchrotron Light Source in Brookhaven National Laboratory. Experimental procedure are discussed elsewhere<sup>[6]</sup>.

The least squares method for analysis of X-ray absorption near edge structure (XANES) of the sulfur K-edge spectra is based on the concept that the experimental spectrum can be modelled as the sum of an arctangent function representing the edge step and a number of absorption peaks which arise from 1s→3p electronic transitions of the major forms of sulfur in the coal. The shape of the absorption peaks is modelled as a function of energy by a combined 50:50 Lorentzian:Gaussian function. An example of least-squares curve fitting of the sulfur K-edge XANES spectrum of the Illinois No. 6 coal is shown in Figure 1. This spectrum is fit by one-step arctangent function representing the edge step, six peaks of 50% Gaussian - 50% Lorentzian shape representing three different forms of sulfur, both organic and inorganic, and several scattering resonance peaks<sup>[6]</sup>.

To convert the measurement of relative peak areas to wt% sulfur in the different forms, the calibration method described elsewhere<sup>[8]</sup> was utilized. It has been observed that the 1s→3p transition probability increases with increasing sulfur valence. Therefore, calibration constants for converting XANES peak area percentages to sulfur weight percentages have been experimentally determined for the functional forms of sulfur that occur in coal<sup>[9]</sup>. For this work an additional calibration constant had to be determined for pyrrhotite, which was formed from the degradation of pyrite during pyrolysis. The error in the resulting sulfur percentages is approximately ± 5 - 10%.



## Results and Discussion

*In situ* sulfur XANES spectra obtained during pyrolysis of Illinois No.6 coal are shown in Figure 2. The effect of pyrolysis on different forms of sulfur in this coal as a function of temperature is illustrated in bar-graph form shown in Figure 3. It is evident that between 250°C and 600°C, the organic sulfide component decreases from 19% of total sulfur to about 10%. Simultaneously, pyrite begins to transform to pyrrhotite; this transformation continues as the temperature is raised and appears to be more or less completed at 600°C. No significant differences were observed between the pyrolysis in helium and that in hydrogen.

The results of *in situ* XANES measurements for pyrolysis of Australian (Glencoe) coal under H<sub>2</sub> and He atmospheres are shown in Figures 4 and 5, respectively. It is seen that disulfide compounds start to degrade at about 200°C while sulfide components decrease when the temperature reaches around 400°C. Growth of a peak with a negative valence state was observed as a function of temperature during the pyrolysis of Australian coal in both He and H<sub>2</sub> atmospheres. Since this coal contains virtually no iron (<0.05 wt%) the appearance of this peak may indicate the formation of organic compounds such as thioketones or similar functional groups during the course of experiments. A similar peak was observed during the thermal oxidation of a mixture of 50:50 wt% of dibenzothiophene and dibenzylsulfide.

The changes that occur in the sulfur forms of the Glencoe coal during oxidation under a mixture of 95% He-5% O<sub>2</sub> flowing gas are illustrated in bar-graph form in Figure 6. Decomposition of organic sulfide component occurs at the same temperature as for pyrolysis (above 400°C). The only significant changes during the oxidation of this coal are a gradual increase in the sulfate component and a decrease in the sulfide component. Since the Australian coal is one that contains no pyrite, the sulfate is believed to be either an organic sulfate or possibly CaSO<sub>4</sub>. The latter could result from the reaction of SO<sub>2</sub> released from sulfide groups with carboxyl-bound calcium in the coal macerals. At the conclusion of the experiment, the sample contained 4.2 wt.% sulfur, indicating that about 1 wt.% of the sulfur had left the sample as SO<sub>2</sub> formed by oxidation of the organic sulfides.

Figure 7 shows the percentage of different sulfur forms in Illinois No. 6 coal under oxidation in a mixture of 95% helium - 5% oxygen. Pyrite was partially removed from this sample by centrifugation in carbon tetrachloride prior to the oxidation experiment. The initial sulfur content of the sample was 3.6 wt.%, with a pyritic sulfur content of approximately 1.6 wt.% according to the XANES results. The principal change during oxidation is a significant decrease in pyritic sulfur and a small, gradual increase in sulfate. It should be mentioned that the sample was heated to 500°C, but a spectrum was not obtained because of a loss of the X-ray beam at that temperature. The final bar graph obtained at room temperature therefore is from a sample that had experienced oxidation up to 500°C. Pyrite has disappeared and a small peak from elemental sulfur is observed. Since the final sulfur content of the sample was 1.7%, most of the pyritic sulfur leaves the sample as SO<sub>2</sub>.

### Conclusions

Based on the *in situ* XAFS measurements of the sulfur K-edge of the coal samples reported in this research, the following conclusions can be made:

- *In situ* XAFS high temperature measurements can provide insight into the behavior of sulfur compounds during thermal reactions.
- During pyrolysis, the degradation of disulfide starts to occur at about 200°C, while the organic sulfide decomposes at above 400°C. The conversion of pyrite to pyrrhotite in Illinois No. 6 coal was observed above 400°C.
- During oxidation of an Illinois No. 6 coal at temperatures up to 500°C, pyritic sulfur decreases markedly, while a small and gradual formation of sulfate is observed. A minor amount of elemental sulfur was also formed.
- During oxidation of a brown coal containing no pyrite at temperatures up to 450°C, organic sulfides decreased approximately 50% and a gradual increase of sulfate was observed.

### References

- (1) Attar A.; In Analytical Methods for Coal and Coal Products; Ed, Karr C.; Academic Press: New York, 1979, 1.
- (2) Calkins W. H.; Energy & Fuels; 1987, 1, 59.
- (3) Calkins W. H.; ACS, Div. Fuel Chem.; 1985, 30(4), 450.
- (4) Bakel A. J., Philp R. P., and Galves-Sinibaldi A.; Geochemistry of Sulfur in Fossil Fuels; Eds., Orr W. L. and White C. M.; ACS, 1989, 429, 326.
- (5) Boudou J. P.; Geochemistry of Sulfur in Fossil Fuels; Eds, Orr W. L. and White C. M.; ACS; 1989, 429, 345.
- (6) Huffman, G. P., Huggins F. E., Shah N., Mitra S., Pugmire R. J., Davis B. Lytle F. W., and Greigor R. B.; Energy & Fuels; 1989, 3, 200.
- (7) Gorbaty M. L., George G. N., and Kelemen S.R.; ACS, Div. Fuel Chem., Preprints; 1990, 35(3), 779.
- (8) Huffman G.P., Huggins F. E., Francis H. E., Mitra S., and Shah N.; Processing and Utilization of High-Sulfur Coal III, Elsevier; 1990, 21.
- (9) Huffman G. P., Mitra S., Huggins F. E., and Shah N.; (to be published) Energy & Fuels; 1991.
- (10) Sinfelt J. H., Via G. H., and Lytle F. W.; Chem. Phys.; 1982, 76, 2779.

### Acknowledgement

The authors acknowledge the Electrical Power Research Institute (EPRI) for supporting this research under EPRI contract No. RP-8803. We also are grateful to the U.S. Department of Energy for the use of synchrotron facilities at the National Synchrotron Light Source at Brookhaven National Laboratory.

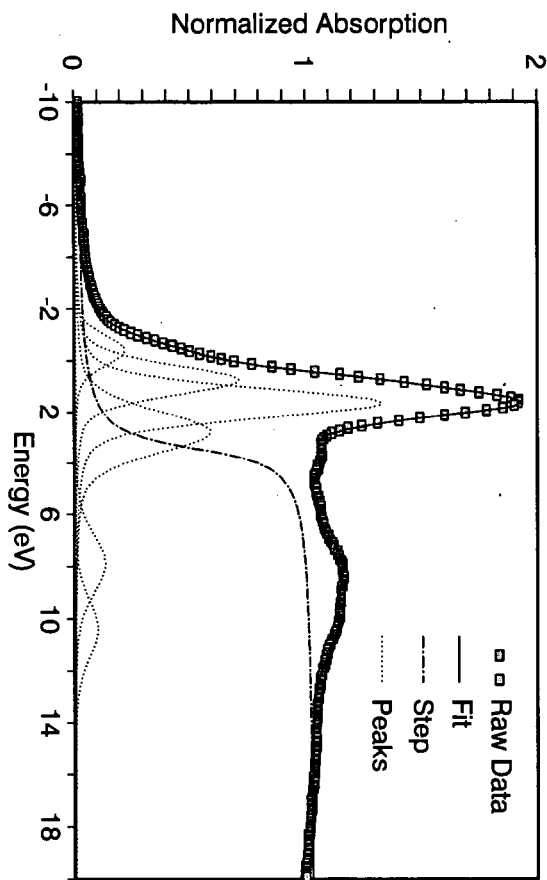


Figure 1. Example of least-squares fitting of the sulfur K-edge XANES spectrum of the Illinois No. 6 coal. The spectrum is fit by one-step arctangent function and a number of peaks of 50% Gaussian - 50% Lorentzian shape.

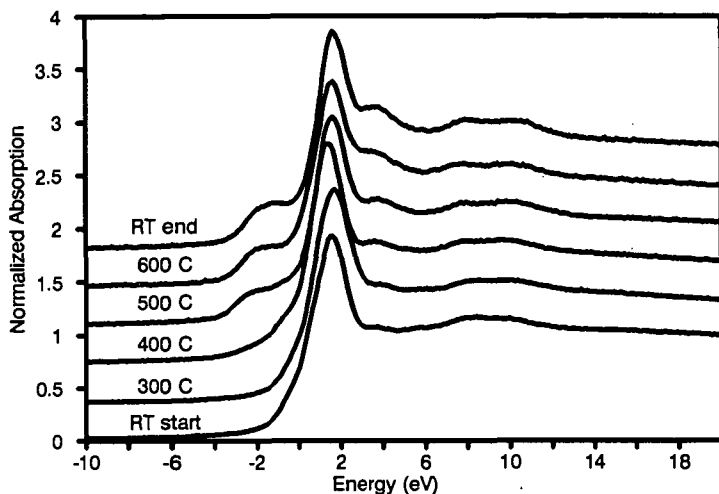


Figure 2. Sequence of sulfur K-edge XANES spectra from Illinois No. 6 at indicated temperatures during pyrolysis in helium.

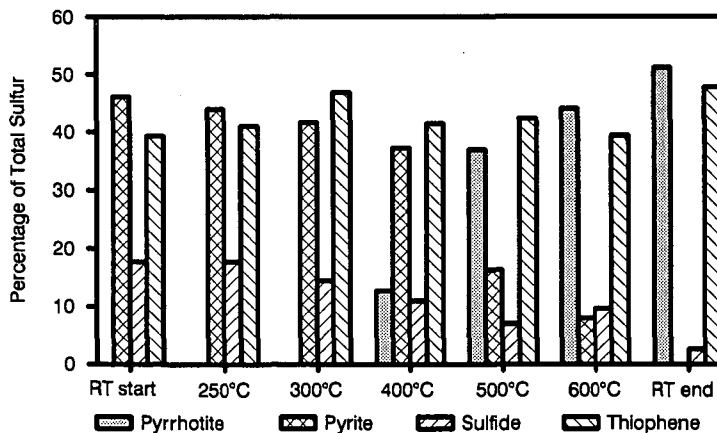


Figure 3. Percentage of different sulfur forms in Illinois No. 6 under pyrolysis in helium obtained by least-squares analysis of the XANES spectra shown in Figure 2.

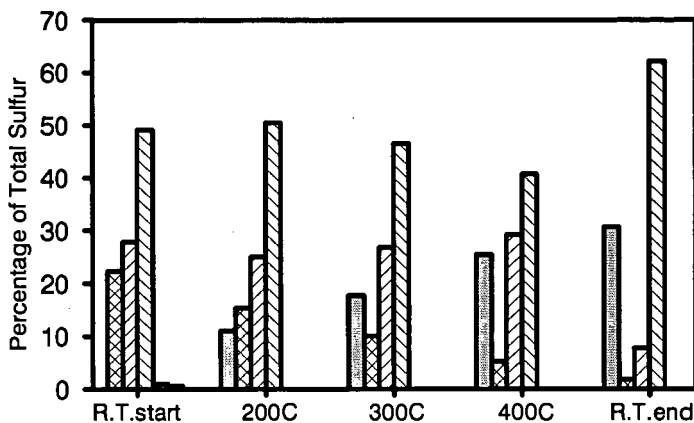


Figure 4. Percentage of different sulfur forms in Australian brown coal (Glencoe) under pyrolysis in hydrogen.

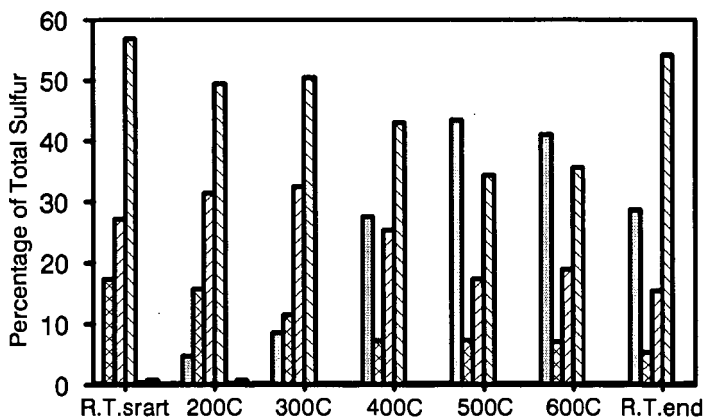


Figure 5. Percentage of different sulfur forms in Australian brown coal (Glencoe) under pyrolysis in helium.

See Text	Disulfide	Sulfide
Thiophene	Sulfone	Sulfate

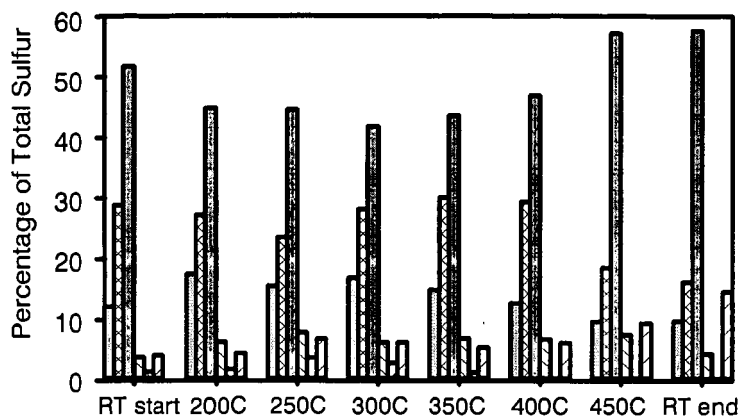


Figure 6. Percentage of different sulfur forms in Australian coal (Glence) under oxidation in 95% helium + 5% oxygen.

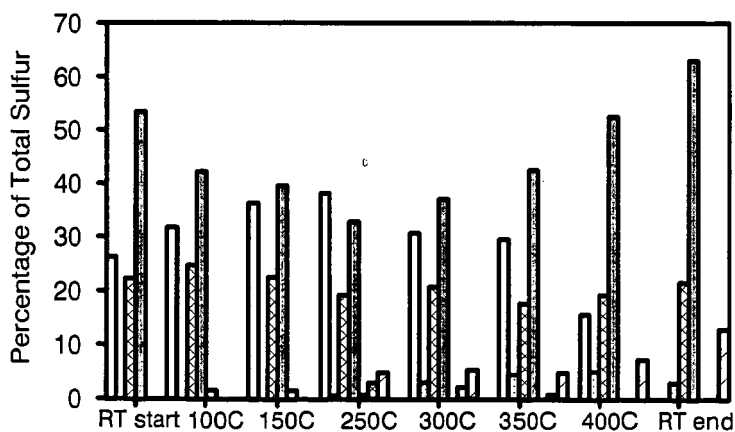


Figure 7. Percentage of different sulfur forms in Illinois No. 6 coal under oxidation in 95% helium + 5% oxygen.

Disulfide    Pyrite    Elemental Sulfure    Sulfide  
 Thiophene    Sulfoxide    Sulfone    Sulfate

## STRUCTURE AND STRUCTURAL DIVERSITY IN RESINITES AS DETERMINED BY PYROLYSIS-GAS CHROMATOGRAPHY-MASS SPECTROMETRY

Ken B. Anderson and Randall E. Winans  
Chemistry Division, Building 200  
Argonne National Laboratory  
9700 S. Cass Avenue  
Argonne, IL, 60439.

Keywords: Resinite, Py-GC-MS, Classification

### INTRODUCTION

A number of workers have reported data concerning the analysis of fossil resins,<sup>1-7</sup> (often referred to as "amber", but referred to herein by their correct general geologic name - resinite). It has become apparent from these data, that a number of chemically distinct forms of resinite exist in the geosphere. At present however, no convention exists for the differentiation of these chemically distinct materials. This problem of nomenclature is further compounded by a degree of ambiguity in the petrographic identification of resinites<sup>8</sup>, and also by the inappropriate use of the term "resin" to describe certain petroleum and source rock components. As a result, the literature concerning the geochemistry of higher plant resins is somewhat confused.

General structural characteristics of a number of different resinites have been established by previous studies. Results of analyses carried out in our laboratory however, indicate that even within closely related samples, a significant degree of variability of composition exists, often as the result of differences in botanical origin and/or level of thermal maturity. We have therefore sought to develop a classification system for resinites, and to establish criteria by which individual resinites may be unambiguously classified.

In order to investigate the nature and extent of variability in resinite structure, we have sought to establish a broadly based resinite sample collection. The results of Pyrolysis-Gas Chromatography-Mass Spectrometric (Py-GC-MS), analyses of a number of different resinite samples from this collection, and the implications of these results to the nomenclature and classification of resinites, are described herein.

### EXPERIMENTAL

Py-GC-MS analyses were carried out using an HP-5890 GC coupled with an HP-5970 MSD. Resinite samples (approx. 1 mg) were subjected to pyrolysis in the presence of excess tetramethylammonium hydroxide (TMAH) to effect in-situ methylation of acidic components,<sup>9</sup> using a C.D.S. "pyroprobe" coil type pyrolyzer. 60m DB-5 and DB-1701 columns were used to obtain adequate chromatographic separation of components.

### RESULTS AND DISCUSSION

A thorough review of the literature, and the results of analysis of our own carefully screened suite of true resinite samples, suggests that three basic structural families of resinites predominate in the geosphere. A small number of less common forms are also known, but are usually restricted to a very small number of sites. The results of Py-GC-MS analyses of examples of each of these resinite classes, illustrated in Figure 1, clearly reflect the compositional differences reported by previous authors. These data also demonstrate that Py-GC-MS is a useful technique for providing detailed information concerning the molecular composition of resinites, especially when used in conjunction with in-situ methylation procedures. As a consequence of these observations, (and parallel spectroscopic data) a preliminary classification system, outlined in Table I and described in detail below, has been developed to rationalize and clarify the nomenclature of resinites, and to enable

researchers to conveniently indicate the specific chemical nature of resinite samples with which their work may be concerned. A more comprehensive description and justification of this classification system will be reported elsewhere.

In addition to resins with structures related to the resinite structures described below, modern plant genus produce numerous other resins, with diverse structural characteristics and compositions. The apparent absence of these resins from geologic strata of significant age however, suggests that these resins are unable to survive diagenetic and/or catagenetic processes in a recognizable form, except perhaps in specialized, rare circumstances.

Class I resinites, which appear to be by far the predominant form of resinite in the geosphere, have been shown by a number of previous workers to be polyditerpenoid structures, based predominantly on the 14,15- polymerization products of labdatriene carboxylic acids, especially communic acid or zanzibaric acid (structures I-IV below).<sup>1-6</sup> Other mono and diterpenoids are often incorporated (or physically occluded) in the structure to a lesser extent. Whilst the results of our analyses concur with these reports, our data indicate that the specific composition of class I resinites, as assessed by Py-GC-MS, varies significantly between samples, and reflects both the botanical origin and maturity of the resinite.

Class I resinites, unlike class II and III resinites which appear to have specific botanical origins, appear to be derived from a number of paelobotanical sources (see Table I). Modern analogues of class I resinites are produced, often in large amounts, by a number botanical genus, including: Araucariaceae, Taxodiaceae, Leguminosae,<sup>10</sup> Cupressaceae,<sup>11</sup> and possibly others. This diversity of sources and often copious production probably accounts for the observed predominance of class I resinites in geologic samples.

Py-GC-MS data (illustrated in Figure II) and other results, suggest that class I resinites may usefully be further divided into divided into three sub-classes on the basis of molecular composition. Resinates based on polycommunic acid can and should be distinguished from those based on polyzanzibaric acid, and for some purposes it may also be useful to further divide communic acid based class I resinites into succinylated and non succinylated forms. A number of class I resinites, including "Baltic amber" (succinite), which together comprise probably the single largest source of resinite, incorporate succinic acid as a cross-linking agent between occasional communal units incorporated into a communic acid based polymeric structure. In other communic acid based class I resinites however, succinic acid is absent, suggesting a related but distinct origin for these materials. These finer sub-categories are useful for distinguishing related resinates of distinct botanical origins, and may also aid in establishing correlations between geographically dispersed samples of closely related structural character. Class I resinites may therefore be sub-divided according to the basic character of the polymeric structure as follows: I(a) Succinylated polycommunic acid; I(b) Non-succinylated polycommunic acid; and I(c) polyzanzibaric acid.

Notable features of the chromatograms illustrated in Figure II are: (i) Significant differences in the distributions of intact diterpenoids (eluting between 55 and 70 minutes in these chromatograms), which reflect the different botanical origins (and possibly also the thermal maturities) of the samples, and (ii) the presence of abundant dimethyl succinate in the pyrolysis products of the class Ia sample. This compound is not observed in the pyrolysis products of class Ib or Ic resinates. A more comprehensive analysis of these data will be presented elsewhere. Slight, but highly significant differences are also observed in the nature of the products eluting between 30 and 55 minutes in these chromatograms. These compounds are predominantly bicyclic carboxylic acids derived from the labdanoid ring system of the parent acids. Preliminary data suggest that differences in these products may be useful for distinguishing class Ia and Ib resinates from class Ic resinates in mature samples, in which no detectable intact diterpenoids remain.

Class II resinates have been shown to be based on polymers of sesquiterpenoid hydrocarbons related to cadinene (V).<sup>6,12,13</sup> Although less common overall than Class I resinates, Class II resinates are very abundant in several locations throughout the world, including the U.S. (specifically Utah) and S.E. Asia (where both modern and fossil deposits occur) and constitute a major resource of resinite. This class of resinite is known to be derived from trees of the Dipterocarpaceae, especially Shorea, modern resins of which, known as Damar, are still commercially exploited, and differ little in structural terms from Class II resinates. Class II resinates are very easily distinguished from Class I and III resinates by pyrolytic techniques (See for example Figures I) on the basis of the nature of the pyrolysis products, especially the absence of significant amounts of carboxylic acids. Spectroscopic data is also often definitive for the classification of resinates of this class.



Class III resinites, which are composed almost entirely of natural polystyrene (VI), are the least common of the three resinite classes defined in Table I, currently identified deposits being restricted to the Eastern US and (possibly) Germany<sup>7,10</sup>. These resinites are believed to be derived from the resins of *Hammelidaceae*, especially *Liquidambar*. Class III resinites are very easily recognized and classified on the basis of spectroscopic and/or pyrolytic data; the principle problem associated with recognition of these materials being confirmation of the provenance of the sample (ie: being sure that the sample is not synthetic polystyrene which has inadvertently been collected as fossil material).

Class II and III resinites are also distinct from Class I resinites in that resinites of these classes are soluble in organic solvents, and hence may be recovered and concentrated by extraction.

As indicated above, although all resinites of a given class share a number of common structural characteristics, the composition of volatile and volatilizable materials produced by pyrolysis varies considerably between samples. These differences reflect variations in the composition of the original resins, and also differences in the thermal maturity of the samples. These differences are particularly important in class I samples, due to the diversity in the botanical origins of these resinites, but are also likely to be important in other resinites.

In immature class I samples, such as those illustrated in Figure 11, abundant, intact diterpenoids are released by volatilization and thermal depolymerization as a result of pyrolysis. These diterpenoids probably reflect the composition and nature of the original resin and hence are of considerable interest. With increasing thermal maturity however, the significance of these compounds decreases, and substituted unsaturated bicyclic carboxylic acids become increasingly predominant in the pyrolysis products. This probably reflects semi-random cross-linking, especially between olefins, and double bond migration to thermodynamically more stable isomers. This results in a thermally more stable polymeric structure, which is less able to thermally "unzip", and which therefore cleaves off naphthenic structures derived from the labdanoid ring system of the precursor, in this case communic acid. The low abundance of tricyclic products in the pyrolyzate of mature resinite samples suggests that cyclization reactions are not an important maturation process in resinites. At high levels of maturity aromatization and elimination of substituents also appear to be significant. This trend is demonstrated in Figure 1, which illustrates Py-GC-MS data for a series of class Ib resinites obtained from New Zealand coals of known maturity. Similar trends are observed in other class I resinites.

## **CONCLUSIONS**

Py-GC-MS is a useful technique for the rapid characterization of resinites, especially when used in conjunction with in-situ methylation procedures, which permit chromatographic analysis of acidic components without complex sample preparation.

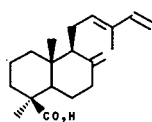
Although significant diversity exists in resinite structures, the majority of resinites may be classified into one of three basic structural groups. Resinites from the largest and most important of these may be further subdivided on the basis of specific structural characteristics into three subclasses. Within these classes, details of specific composition may vary significantly between samples as a consequence of differences in botanical origin and/or level of maturation, but sufficient common structural characteristics exist within these classes to validate application of such a classification system.

## **ACKNOWLEDGMENTS**

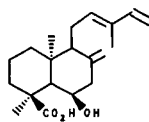
The authors wish to acknowledge Mr. J. Gregar of the Argonne National Laboratory for preparation of specialized glassware. We also wish to express our gratitude to Dr. P. Dunn, and Dr. F. Hueber of the National Museum of Natural History - Smithsonian Institute, Dr. D. Grimaldi of the American Museum of Natural History (ANMH), Dr G. Mustoe of Western Washington University, Dr T.V. Verheyen of the Coal Corporation of Victoria, Dr D. Paris of the New Jersey State Museum (NJSN), Dr A. Criddle of the Natural History Museum (London), Dr J. Crëlling of the University of Southern Illinois, and Dr A. Clemmens of the Coal Research Association of New Zealand (Inc.) for generously providing resinites samples. Reference numbers given in figure captions refer to sample numbers of the organizations indicated. This work was performed under the auspices of the Office of Basic Energy Sciences, Division of Chemical Sciences, U.S. Department of Energy, under contract number W-31-109-ENG-38.

## REFERENCES

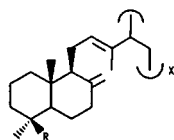
1. (a) Gough, L.J.; Mills, J.S. *Nature* **1972**, *239*, 527-528.  
 (b) Mills, J.S.; White, R.; Gough, L.J. *Chem. Geol.* **1984/85**, *47*, 15-39.
2. Cunningham, A.; Gay, I.D.; Oehlschlager, A.C.; Langenheim, J.H. *Phytochem.* **1983**, *22(4)*, 965-968.
3. (a) Thomas, B.R. *Acta Chem. Scand.* **1966**, *20(4)*, 1074-1081.  
 (b) Thomas, B.R. In *Organic geochemistry - methods and results*; G. Eglinton and M.J.T. Murphy, Eds.; Springer-Verlag: New York, 1969; pp 599-618.
4. (a) Anderson, K.B.; Botto, R.E.; Dyrkacz, G.R.; Hayatsu, R.; Winans, R.E. *Preprint, Fuel Chemistry Div., ACS* **1989**, *34(3)*, 752-758.  
 (b) Anderson, K.B.; Botto, R.E.; Dyrkacz, G.R.; Hayatsu, R.; Winans, R.E. *Fuel* **1990**, *69*, 934-935.
5. Beck, C.W. *Appl. Spec. Rev.* **1986**, *22(1)*, 57-110.
6. Van Aarssen, B.G.K.; Cox, H.C.; Hoogendoorn, P.; De Ieew J.W. *Geochim. Cosmochim. Acta* **1990**, *54*, 3021-3031.
7. Grimaldi, D.; Beck, C.W.; Boon, J.J. *American Museum Novitates* **1989**, *2948*, 1-28.
8. Stach, E.; Mackowsky, M.-T.h.; Teichmuller, M.; Teichmuller, R.; Taylor, G.H.; Chandra, D. In *Stach's Textbook of Coal Petrology*, 3rd edition; Gebruder Borntraeger: Berlin-Stuttgart, 1982; 535 p.
9. (a) Challinor, J.M. *J. Anal. Appl. Pyrol.* **1989**, *16*, 323-33.  
 (b) Dworzanski, J.P.; Berwald, L.; Meuzelaar, H.L.C. *Appl. Environ. Microbiol.* **1990**, *56(6)*, 1717-24.
10. Langenheim, J.H. *American Scientist* **1990**, *78*, 16-24.
11. Mangoni, L.; Belardini, M. *Gazz. Chim. Ital.* **1964**, *94*, 1108-21.
12. Meuzelaar, H.L.C.; Huaying Huai; Lo, R.; Dworzanski, J.P. *Preprint, S.M.E. Meeting, Salt Lake City, Utah*, February 1990.
13. Brackman, W.; Spaargaren, K.; Van Dongen, J.P.C.M.; Couperus, P.A.; Bakker, F. *Geochim. Cosmochim. Acta* **1984**, *48*, 2483-2487.



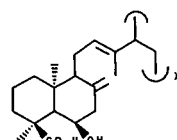
I



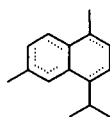
II



III



IV



V



VI

Structures indicated in text: I - Communic acid (trans isomer). II - Zanzibaric acid (trans isomer). III - Basic polymeric structure of class Ia and Ib resinates. (i) R = COOH (polycommunic acid), (ii) R = CH<sub>2</sub>OH (may be succinylated ie: CH<sub>2</sub>O-CO-(CH<sub>2</sub>)<sub>2</sub>-CO-O-R'; R'=H or communol unit of polymer.). IV - Basic polymeric structure of class Ic resinates, polyzanzibaric acid. V - Cadinene (dotted lines indicated double bond isomers). VI - styrene.

TABLE I.

---

Class I

- (a) Basic structural character = polycommunic acid, partially copolymerized with communol. Significant incorporation of succinic acid, probably as a cross linking agent is characteristic.

examples = Succinite (Baltic Amber)

- (b) Basic structural character = polycommunic acid, with varying degrees of copolymerization with communol. Succinic acid is absent.

examples = New Zealand resinites, Victorian Brown Coal resinites.

- (c) Basic structural character = polyzanzibaric acid.

Nearest equivalent modern resins: "Copal" esp. Pontianak, Kauri Resin, Manila Copal  
Brazil Copal, Congo Copal

Most probable botanical affinity\*: (i) Araucariaceae (esp. Agathis)  
(ii) Leguminosae (esp. Hymenaea)  
(iii) Cupressaceae, and possibly others.

---

Class II

Basic structural character = polymer of bicyclic sesquiterpenoid hydrocarbons, esp. cadinene, possibly with some triterpenoid component also present.

examples = Utah resinites, (some) Indonesian resinites.

Nearest equivalent modern resin: "Damar"

Most probable botanical affinity\*: Dipterocarpaceae (esp. Shorea)

---

Class III

Basic structural character = Polystyrene

examples = (some) New Jersey resinites, Montana resinite

Nearest equivalent modern resin: "Storax" (Sometimes = Styra)

Most probable botanical affinity\*: Hammelidaceae (esp. liquidambar)

---

\*Based on equivalent modern resins.

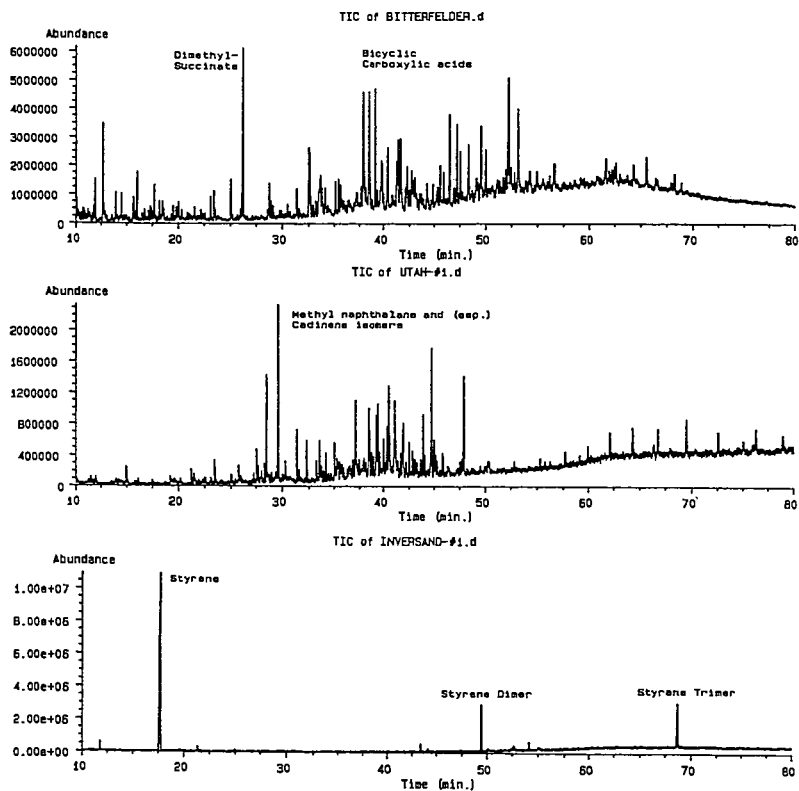


Figure I. Py-GC-MS data for typical examples of Class Ia, II and III resinites. Top: CLASS Ia - Bitterfelder resinite (Germany) [AMNH # B-3]. Centre: CLASS II - Blind Canyon resinite (Utah, U.S.A.). Bottom: CLASS III - Sayrville resinite (New Jersey, U.S.A.) [NJSM #14156].  $T_{\text{pyrolysis}} = 540^{\circ}\text{C}$ , Column = 60m DB-1701.

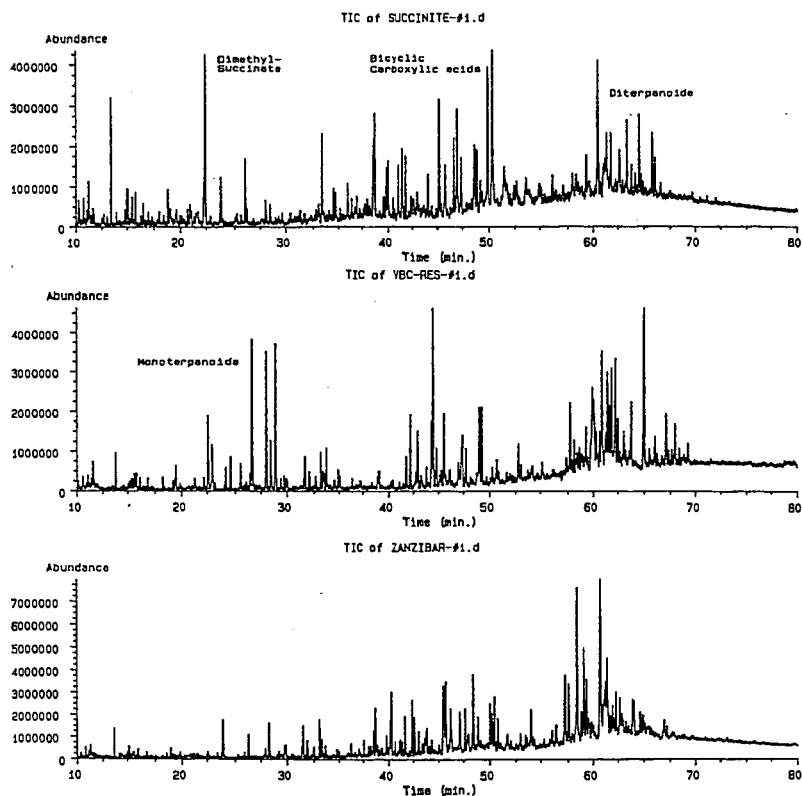


Figure II. Py-GC-MS data for class Ia, Ib, and Ic resinites. Top: Succinite, Baltic region, Eastern Europe [USNM #353431], Centre: Victorian Brown Coal resinite, Latrobe Valley, Victoria, Australia Bottom: Zanzibar resinite, Zanzibar, Africa [AMNH # H252].  $T_{\text{pyrolysis}}=480^{\circ}\text{C}$ , Column = 60m DB-5.

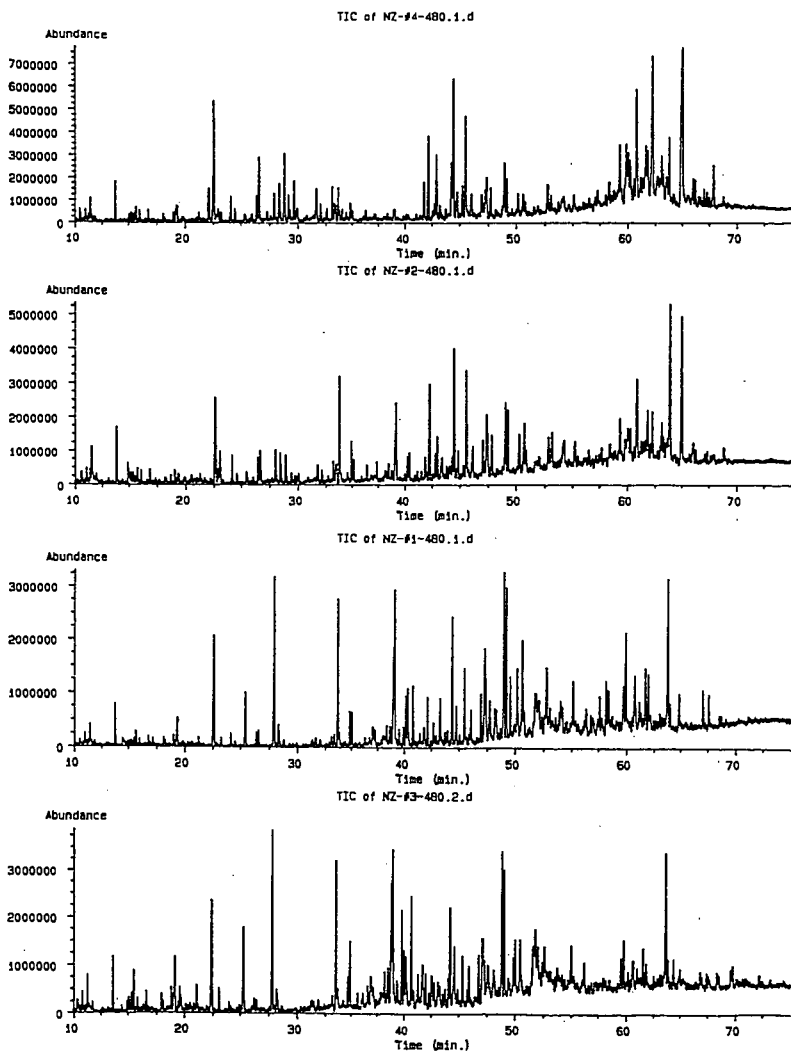


Figure III. Py-GC-MS data for New Zealand Class Ib resinites, showing changes in pyrolysis product distribution as a consequence of increasing thermal maturation.  
 $T_{\text{pyrolysis}} = 480^{\circ}\text{C}$ , Column = 60m DB-5.222

**STRUCTURAL ELUCIDATION OF POLYMERIC DITERPENOIDS  
IN FOSSIL GYMNOSPERM RESINS  
BY MEANS OF PYROLYSIS COMBINED WITH GC-MS.**

**Ben G.K. van Aarssen** and Jan W. de Leeuw.

Delft University of Technology, Faculty of Chemical Technology and  
Materials' Science, Organic Geochemistry Unit, De Vries van  
Heystplantsoen 2, 2628 RZ Delft, The Netherlands

**Keywords:** fossil gymnosperm resins, polymeric diterpenoids, flash-pyrolysis-gas chromatography-mass spectrometry.

## INTRODUCTION

Fossil resins originating from Gymnosperm trees have been the subject of several studies concerning the structure of their high molecular weight fractions <sup>1-4</sup>. Although such resins may be sourced from quite different plant families the structures of the macromolecular moieties have similar features. Formation of these substances is thought to occur *via* a light and/or oxygen induced polymerisation of diterpenoid monomers with a labdane carbon skeleton, such as *communice* acid <sup>1</sup>. Because the polymers are insoluble in common organic solvents, structural studies have been performed using techniques like IR <sup>5</sup>, solid state NMR <sup>3,6,7</sup> and Py-MS <sup>4,8</sup>. In this study we show that Curie point pyrolysis-GC-MS and off-line pyrolysis GC-MS are useful methods to gain information on the structure of the polymeric fractions of fossil resins. For this purpose a fossil resin from the Fushun coal mine in China was analyzed.

## EXPERIMENTAL

Curie-point pyrolysis-gas chromatography-flame ionisation detection (Py-GC-FID) analyses were performed with a Hewlett-Packard 5890 gas chromatograph using a FOM-3LX unit for pyrolysis. The samples were applied to a ferromagnetic wire with Curie temperatures of 770°C (Fe) or 358°C (Ni). The gas chromatograph, equipped with a cryogenic unit, was programmed from 0°C (5 min) to 320°C (20 min) at a rate of 3°C/min. Separation was achieved using a fused-silica capillary column (25m x 0.32mm) coated with CP Sil-5 (film thickness 0.4 µm). Helium was used as the carrier gas.

Curie-point pyrolysis-gas chromatography-mass spectrometry (Py-GC-MS) analyses were performed using the same equipment and conditions as described above for Py-GC-FID connected with a VG 70S mass spectrometer operated at 70 eV with a mass range  $m/z$  40-800 and a cycle time of 1.8 s.

Extraction of the resin was achieved by thoroughly mixing the finely powdered resin ultrasonically several times with a variety of solvents like methanol, dichloromethane, ethylacetate and acetone. The combined extracts were methylated with diazomethane and analysed by GC-MS using the same equipment described for Py-GC-MS (CP Sil-5 column, film thickness 0.32 µm, temperature program from 70°C to 320°C (20 min) at a rate of 4°C/min).

For off-line pyrolysis-gas chromatography-mass spectrometry, an aliquot of the extracted resin was transferred into a quartz tube and heated under a constant flow of nitrogen (100 ml/min) at 425°C for 45 min. The released products were trapped in two flasks with pentane. The first was held at room temperature and the second at -20°C. The trapped pyrolysates were combined and analyzed by GC-MS as described above.

## RESULTS AND DISCUSSION

Extraction of resins is often incomplete because of inclusion of soluble compounds in the insoluble macromolecular matrix. To differentiate between pyrolysis products and evaporated compounds the whole resin was analysed at both a Curie temperature of 770°C and of 358°C. At 358°C no pyrolysis takes place and only volatile compounds are analysed. The chromatograms of both analyses of the whole resin are shown in Figures 1a and 1b. The compounds released were tentatively identified by Py-GC-MS. The most abundant compound present in the mixture obtained at a Curie temperature of 770°C is a mono-unsaturated bicyclic C<sub>15</sub>-carboxylic acid. The mass spectrum and suggested structure for this compound are shown in Figure 2a. Furthermore, a series of C<sub>6</sub>, C<sub>7</sub> and C<sub>8</sub> unsaturated branched acyclic hydrocarbons is present.



Also very abundant are camphor and dehydroabietane. Comparison of the product mixtures obtained at a Curie temperature of 770°C (Fig. 1a) with that of the flash-evaporate (Fig. 1b) shows that both camphor and dehydroabietane are present as such in the resin. This is also true for the  $C_{15}$ -acid. However, at a Curie temperature of 770°C the latter compound is much more abundant, indicating that it is formed upon pyrolysis as well. This is also supported by the presence of a co-eluting similar compound with an additional double bond, which is absent in the flash-evaporate.

To concentrate on the products formed upon pyrolysis, and thus on the structure of the insoluble macromolecule, the resin was thoroughly extracted and the residue was pyrolysed at a Curie temperature of 770°C. The resulting chromatogram is shown in Figure 3a. Compounds like camphor and dehydroabietane are no longer present, showing that the extraction was successful. Flash evaporation at a Curie temperature of 358°C of the residue showed that virtually all the volatile compounds were extracted indeed. From the Py-GC analysis it is clear that the major pyrolysis products are the bicyclic  $C_{15}$ -acid, a similar bicyclic  $C_{14}$ -acid and the series of branched alkenes. Comparison of the chromatogram of the flash-evaporate (Fig. 1b) with that of the methylated extract (Fig. 3b) shows that many diterpenoid methyl esters with an abietane or pimarane carbon skeleton are present in the extract, but not in the evaporate. These  $C_{20}$ -compounds are probably present as free acids in the evaporate and hence not GC-amenable on the apolar column used. This is exemplified by the broadened peak reflecting the  $C_{15}$ -carboxylic acid in the evaporate. It should be noted that no bicyclic  $C_{20}$ -diterpenoids with labdane carbon skeletons could be detected in the pyrolysate nor in the extract. At the end of the chromatogram of the extract a broad hump is visible. Mass spectrometric analysis showed that this hump reflects several badly resolved dimeric diterpenoid acids, probably with labdane carbon skeletons. The mass spectrum of one of these compounds and a possible structure are shown in Figure 2b.

The chromatogram of the GC analysis of the methylated pyrolysate obtained by off-line pyrolysis of the extracted resin is shown in Figure 4. The pyrolysate obtained by off-line pyrolysis resembles the pyrolysate obtained by flash pyrolysis very well. The most abundant compounds are the mono- and disaturated bicyclic  $C_{15}$  methyl esters. Again no bicyclic  $C_{20}$  diterpenoid methyl esters were detected.

The results shown indicate that the fossil resin consists of two fractions. A soluble low-molecular-weight fraction and an insoluble high-molecular-weight fraction. The distinction between these two fractions is however not clear-cut, as shown by the presence of dimeric diterpenoids in the extract. The flash-evaporate obtained at a Curie-temperature of 358°C can however not be taken as representative for the soluble fraction, because of the presence of non GC-amenable acids, which will do show up in the chromatogram. The high-molecular-weight fraction yields upon pyrolysis predominantly an unsaturated bicyclic  $C_{15}$ -carboxylic acid, which is probably the pyrolysis product of a polymeric diterpenoid. As shown in Scheme 1 a pyrolysis mechanism can be conceived starting from a polymeric structure as suggested in literature <sup>1-4</sup>. This mechanism can also explain the presence of unsaturated branched hydrocarbons in the pyrolysate. The acid is also found in the methylated extract as its methyl ester, indicating that some thermal breakdown of the polymer has already occurred in nature. On the other hand, volatile compounds like camphor are still included in the resin, indicating that the resin has not undergone severe diagenesis. No bicyclic  $C_{20}$ -compounds are formed upon pyrolysis of the polymer, as was shown by the off-line pyrolysis. Conclusions about the structure of the polymer in Gymnosperm resins based on the presence of diterpenoid monomers in pyrolysates should therefore be taken with care <sup>4,8</sup>, because they are probably based on included, soluble and volatile compounds and not on pyrolysis products. Because no methyl esters of the  $C_{15}$ -pyrolysis products were detected in the flash pyrolysate, the polymer of the fossil resin used in this study must be built up of non-methylated monomers. The question recently discussed in the literature by several authors <sup>7,8</sup>, as to whether or not Yallourn resinite polymer is methylated for a significant part, can therefore quickly be answered using the analytical methods described above.

## CONCLUSIONS

The results described above support earlier conclusions about the structure of polymers present in fossil and recent gymnosperm resins. The resin studied contains a polymerized bicyclic diterpenoid, probably communic acid. Polymerization has occurred through the side chain, possibly via a 1,2 mechanism. The methods used in this work are relatively fast and simple and the results are complementary to those obtained by spectroscopic methods. Furthermore, they allow for further and more detailed studies of the basic structural units present in such polymers and the way they have polymerized by isolation and structural analysis of dimers and pyrolysis products. Such studies are now in progress.

## REFERENCES

1. Carman R.M., Cowley D.E. and Marty R.A. (1970), *Aust. J. Chem.*, **23**: 1655-1665.
2. Mills J.S., White R. and Gough L.J. (1984/85), *Chem. Geol.*, **47**: 15-39.
3. Wilson M.A., Collin P.J., Vasallo A.M. and Russel N.J. (1986), *Org. Geochem.*, **7**: 161-168.
4. Anderson K.B., Botto R.E., Dyrkacz G.R., Hayatsu R. and Winans R.E. (1989), *Am. Chem. Soc. Div. Fuel Chem. Prepr.*, **34(3)**: 752-758.
5. Beck C.W. (1986), *Appl. Spectr. Rev.*, **22**: 57-110.
6. Cunningham A., Gay I.D., Oehlschlager A.C. and Langenheim J.H. (1983), *Phytochem.*, **22**: 965-968.
7. Wilson M.A., Vasallo A.M., Liu Y.L. and Pang L.S.K., (1990), *Fuel*, **69**: 931-933.
8. Anderson K.B., Botto R.E., Dyrkacz G.R., Hayatsu R. and Winans R.E. (1990), *Fuel*, **69**: 934-936.

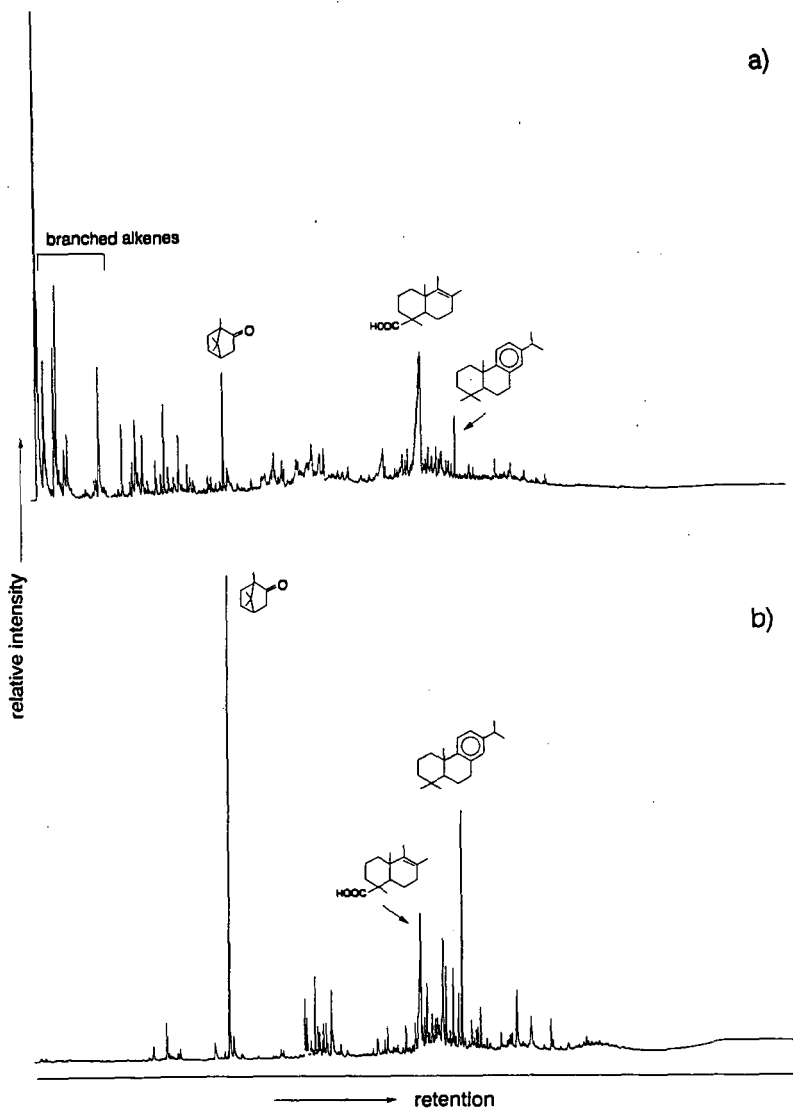


Fig. 1. Py-GC-FID traces of the whole fossil resin at Curie temperatures of a) 770°C and b) 358°C.

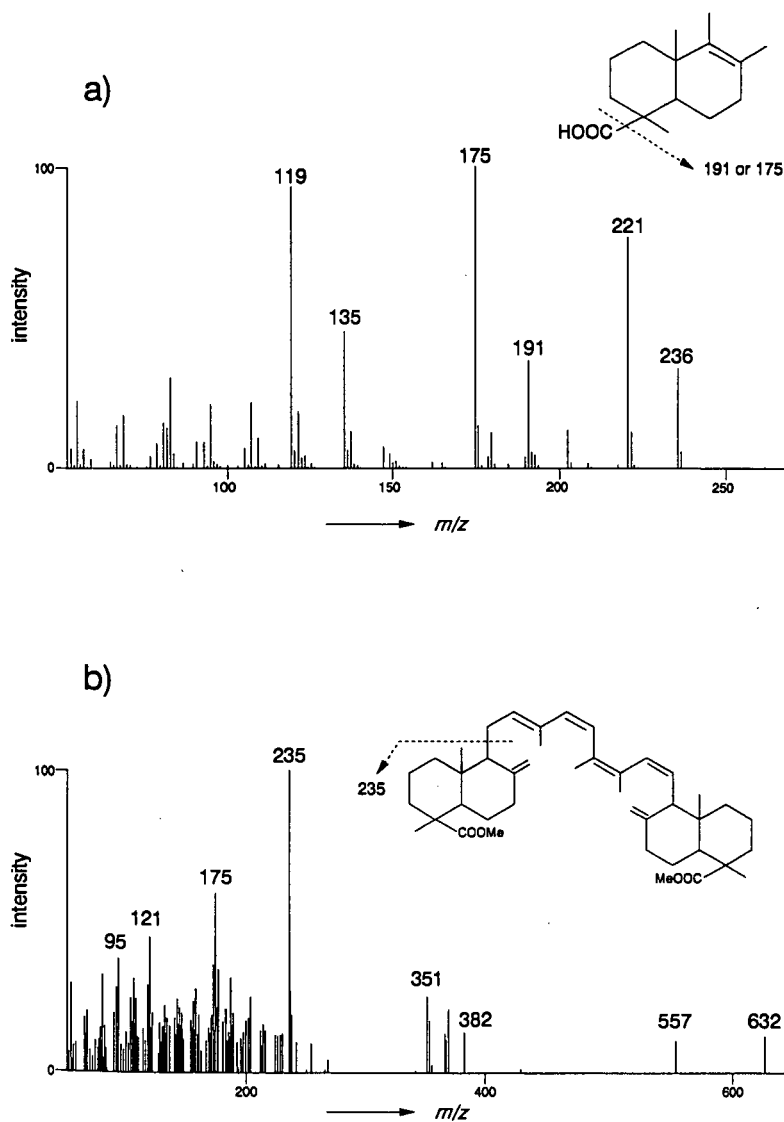


Fig. 2. Mass spectra of a) the major pyrolysis product of the fossil resin at a Curie temperature of 770°C and b) a diterpenoid dimer present in the resin extract.

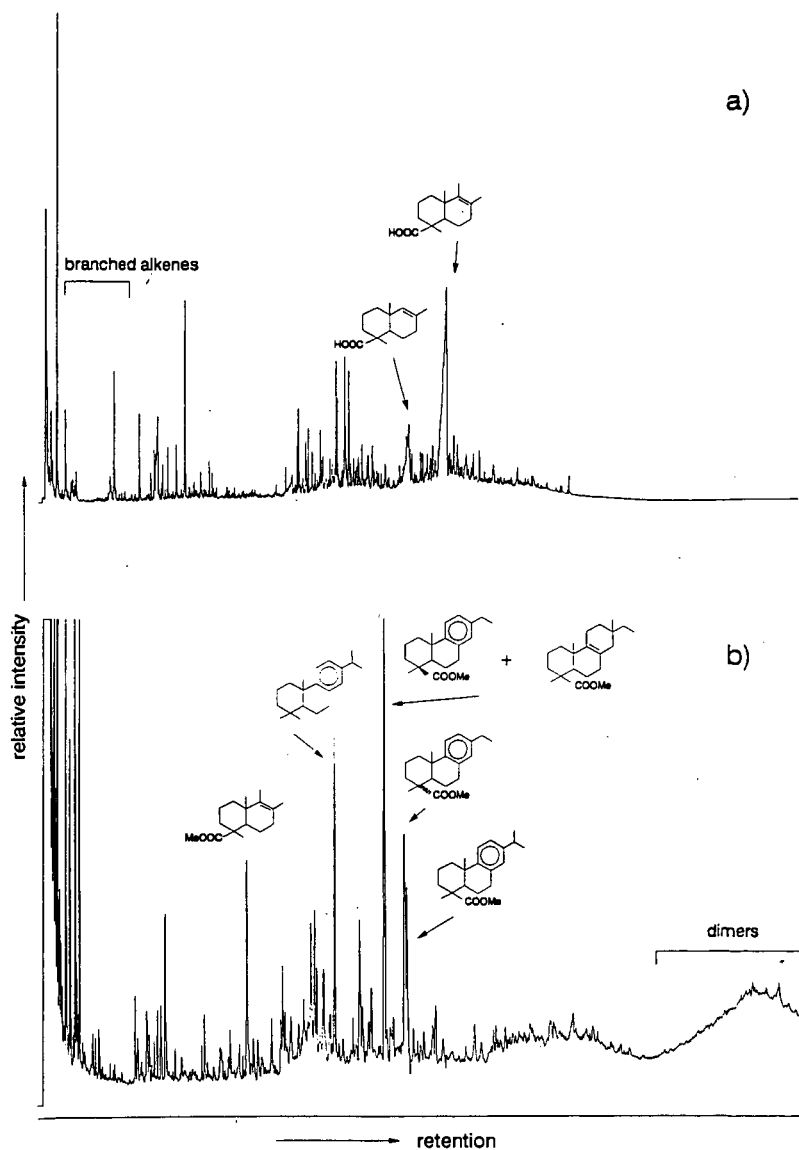


Fig. 3. a) Py-GC-FID trace of the extracted resin at a Curie temperature of 770°C. b) GC-FID trace of the methylated resin extract.

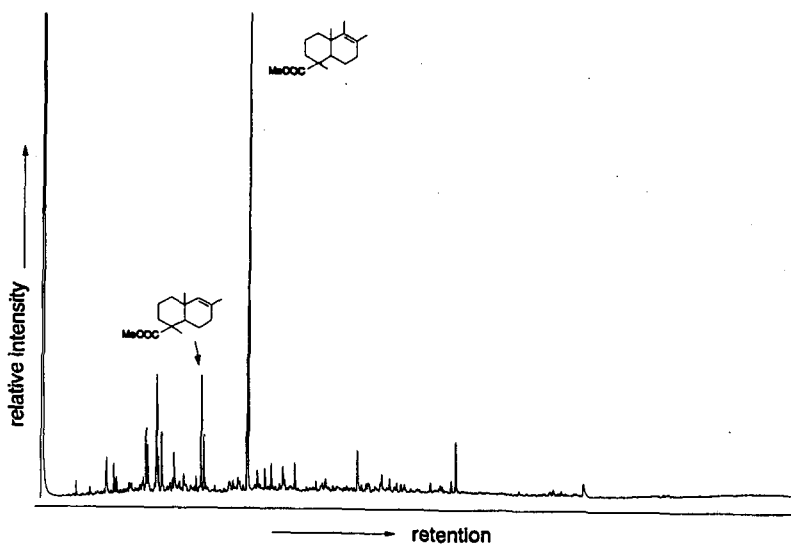
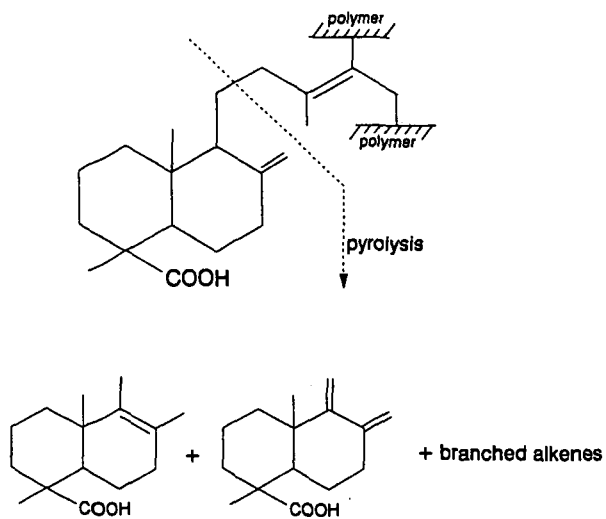


Fig. 4. GC-FID trace of the methylated pyrolysate obtained from the off-line pyrolysis of the extracted resin.

### Scheme 1



## ANALYSIS OF PERU MARGIN SURFACE SEDIMENTS BY PY-MS

By

T.J. Eglinton<sup>1</sup>, M.A. McCaffrey<sup>1</sup>\*, H. Huai<sup>2</sup> and H.L.C. Meuzelaar<sup>2</sup>.

<sup>1</sup>Dept. of Chemistry, Woods Hole Oceanographic Institution, Woods Hole MA 02543.

<sup>2</sup>Center for Micro Analysis and Reaction Chemistry, EMRL, University of Utah, Salt Lake City, UT 84112.

**Keywords:** Peru Upwelling Sediments, Early Diagenesis, Pyrolysis-Mass Spectrometry

### INTRODUCTION

In off-shore Peru high sedimentary organic carbon contents are a direct consequence of the extremely high primary productivity (ca. 1000g Carbon m<sup>-2</sup>.yr<sup>-1</sup>)<sup>[1]</sup> which, in turn, is supported by the upwelling of nutrient-rich waters near the coast. Diatoms represent the major phytoplankton type and give rise to sediments dominated by biogenic silica and planktonic organic matter. The remineralisation of this large flux of organic matter to the bottom waters and sediments results in oxygen depletion over large areas of the shelf which, in turn, promotes organic carbon preservation in the underlying sediments. Sulfide from sulfate reduction is prevalent in the bottom waters<sup>[2]</sup> and with a limited availability of iron (due to the dominant biogenic input coupled with a very low influx of detrital sediments) the excess sulfide is available for reaction with the organic matter. As a result high organic sulfur concentrations are found in the sediments<sup>[3]</sup>.

The coastal Peru upwelling region is believed to be a modern analogue to the depositional environments of petroleum source rocks such as the Miocene Monterey Formation of the California Borderland<sup>[4]</sup>. Because organic matter alteration pathways in surface sediments ultimately influence kerogen type and eventual petroleum yield, there has been interest in characterizing surface sediments such as those off-shore Peru. Lipid<sup>[5-10]</sup>, carotenoid<sup>[11]</sup> and amino acid<sup>[12]</sup> constituents as well as general biogeochemistry<sup>[1,13]</sup> have been studied previously. However, studies of the macromolecular components of the sediments have been less extensive<sup>[3,14]</sup>.

This paper describes results from Py-MS analyses of sediment samples obtained from discrete intervals in a 1-meter core obtained from the upper continental shelf of the Peru Upwelling region. Factor and discriminant analysis of the Py-MS data revealed several distinct changes within this 1-meter section.

### EXPERIMENTAL

#### *Sample Recovery and preparation*

Fifteen sediment samples obtained from a single ca. 1-meter box core were used for this study. The core ("SC3") was taken during a cruise of the R/V Moana Wave in 1987, and was retrieved from Station 4 (15°06.16'S, 75°42.09'W) at a water depth of 253m (within the prevailing oxygen minimum zone). Further information concerning the location and detailed geochemistry of these samples are provided elsewhere<sup>[15]</sup>. General geochemical descriptions of the samples are listed in Table 1.

\* Present address: Chevron Oil Field Research Company, Richmond CA 94802

Wet sediment samples were pre-extracted with isopropanol, followed by a methanol-chloroform mixture (to remove soluble lipid components) and subsequently air-dried prior to further analysis. Organic carbon and nitrogen measurements were made on de-carbonated sediment samples using a Perkin Elmer 2400 CHN analyzer.

#### *Pyrolysis-Mass Spectrometry (Py-MS)*

Similar experimental and mathematical procedures to those described by Metcalf *et al.*<sup>[16]</sup> were adopted for the present investigation. Briefly, dried samples were suspended in methanol (5 mg/ml) and approximately 75 µg of sediment was applied to each wire (Curie temperature, 610°C). Uniform sample coating was achieved by rotation of the wires during air-drying.

Py-MS was performed on an Extranuclear 5000-I quadrupole MS system described by Meuzelaar *et al.*<sup>[17]</sup>. Pyrolysis was started 30 s after introduction of the sample into the mass spectrometer. Py-MS conditions were as follows: temperature rise time 5s, total heating time 10s, electron energy 12 eV, mass range  $m/z$  20-300, scanning rate 2000 amu/s, total number of scans acquired = 70. Each sample was analysed in triplicate.

#### *Multivariate Statistical Analysis*

Multivariate statistical analysis of the Py-MS spectra was performed using the SIGMA (System for Interactive Graphics-oriented Multivariate Analysis) program described by Windig and Meuzelaar<sup>[18]</sup>.

The stored Py-MS data were firstly calibrated and normalized. Subsequently, factor analysis was performed, followed by discriminant analysis. Discriminant analysis was applied on the first seven factors (explaining 82% of the total variance, see Table 2) selected on the basis of Cattell "scree break" criterion<sup>[19]</sup>. As applied here, discriminant analysis involved an orthogonal rotation of factor space aimed at maximising outer/inner variance ratios. Outer variance is a measure of the differences between groups of spectra; inner variance is a measure of the internal variation within replicates as a consequence of experimental scatter or sample heterogeneity. The results are expressed in terms of discriminant scores which provide a quantitative measure of the differences, and in the form of numerically-extracted discriminant spectra<sup>[20]</sup>, which give information about the mass intensity changes involved. The pyrolysis data are interpreted in terms of chemical "components" by means of the "variance diagram" (VARDIA) technique, a method developed for numerical analysis of unknown mixtures<sup>[21]</sup>. The basic principle is that the VARDIA plot shows how strong the correlated behavior of all mass variables is in all possible directions (in steps of 10°). Directions in the discriminant space which can be attributed to such chemical components are called "component axes".

## RESULTS

Figure 1 shows averaged Py-MS spectra of samples from four intervals within the core. In general, the spectra are rather similar, being dominated by low mass ions and containing maxima at similar  $m/z$  values. Major series include ions those due to sulfur compounds such as  $H_2S$  ( $m/z$  34),  $S_2$  or  $SO_2$  ( $m/z$  64), HSSH ( $m/z$  66), and  $S_4$  ( $m/z$  128), as well as sugar products (e.g.  $m/z$  114, 126, 128, 144). Other mass peak patterns reflect contributions from aliphatic hydrocarbons and alkylaromatics (alkylphenols and alkylbenzenes).

Despite the similarity between the traces, factor and discriminant analysis allowed a number of distinctions to be made between the samples studied. Table 2. lists results from factor analysis of the data matrix including all samples and mass peaks. Slightly over 50% of the total variance is explained by the first factor, with the second and third factors accounting for a further 17% and 5% respectively.

The results from discriminant analysis of the data set are presented in Table 3 and Figure 2. Tighter clustering of the replicates and better separation between different samples is observed after discriminant



rotation than in the original score plots (not shown here). It is apparent that Discriminant function 1 (DF1) strongly reflects sediment depth, as clearly revealed by a cross-plot of these two parameters (Fig. 3). Fluctuations which are not directly related to depth are manifested in DF2 (non-depth-related variations are also evident in DFs 3 & 4, Fig. 2b). In addition, three or four "sub-groups" may be identified in Figure 2a (as indicated by the circles). The spectra shown in Figure 1 each correspond to one of these four groups.

In order to determine the chemical variations responsible for these fluctuations, variance diagrams were constructed in which the DFs are kept orthogonal to one another, but may be rotated (in 10° increments) so as to study axes which most clearly reflect differing "chemical components". This is shown in Figure 4(a) in DF1/DF2 space, in which three separate "components" may be identified. A fourth was identified in DF3 (Figure 4b). Mathematically-extracted "discriminant spectra", obtained for each of these chemical "components" from rotation within this framework are presented in Figure 5. Component "A" (DF1 & DF2, 10°) shows a typical pattern derived from sugar moieties. Component "B" (50°) shows strong influence from sulfur-derived compounds as well as some higher mass components ( $m/z$  155, 159, 173 etc.). Component "C" (320°) contains, in addition to sulfur compounds, alkylaromatics including alkylbenzene and phenolic compounds. Component "D" from DF3 & DF4 (70°) contains mass peaks possibly characteristic for terpenoid component(s).

From these data we may conclude that the depth-related variation in "kerogen" reflected in DF1 is primarily the result of a decrease in sugar-containing components together with a corresponding increase in sulfur-containing and alkylaromatic components. The latter is consistent with current concepts concerning sulfur incorporation into organic matter during early diagenesis<sup>22,23</sup>. Other fluctuations independent of depth are presumably a consequence of variations in conditions at the time of deposition. The chemical components responsible for these latter variations are yet to be fully interpreted.

## CONCLUSIONS

Py-MS in conjunction with multivariate statistical analysis of Peru margin sediments has allowed several insights to be made into the formation and transformation of macromolecular organic matter during early diagenesis. Distinctive depth-related changes in chemical composition were observed, including a loss of sugar-containing moieties and an increase in sulfur content. Features reflecting fluctuations due to other influences on organic matter composition were also detected. This study demonstrates the utility of this approach as a rapid method for providing information on macromolecular sedimentary organic matter composition.

## ACKNOWLEDGEMENTS

Drs. J.W. Farrington and D. Repeta are thanked for making these valuable samples available.

## REFERENCES

1. Reimers C.E. and Suess E. *Coastal Upwelling and its sediment record, Part B*. (eds. J. Theide and E. Suess). pp. 311-337. Plenum, New York (1983).
2. Fossing H. (1990) *Continental Shelf Research*. In press.
3. Patience R.L., Clayton C.J., Kearsley A.T., Rowland S.J., Bishop A.N., Rees A.W.G., Bibby K.G. and Hopper A.C. *Proceedings Scientific Results, Leg 112, Ocean Drilling Program*. (Eds. E Suess, R von Huene et al.) pp. 135-153. ODP College Station, Texas (1990).

4. Soutar A., Johnson S.R. and Baumgartner T.R. *The Monterey Formation and related siliceous rocks of California*. pp. 123-147. SEPM Los Angeles (1981).
5. Volkman J.K., Farrington J.W., Gagosian R.B. and Wakeham S.G. *Advances in Organic Geochemistry, 1981* (eds M. Bjoroy et al.) pp. 228-240. Wiley and Sons (1983).
6. Wakeham S.G., Farrington J.W. and Gagosian R.B. *Org. Geochem.* 6, 203-215 (1984).
7. Volkman J.K., Farrington J.W. and Gagosian R.B. *Org. Geochem.* 11, 463-477 (1987).
8. Farrington J.W., Davis A.C., Sulanowski J., McCaffrey M.A., McCarthy M., Clifford C.H., Dickinson P. and Volkman J.K. *Org. Geochem.* 13, 607-617 (1988).
9. McCaffrey M.A., Farrington J.W. and Repeta D.J. *Org. Geochem.* 14, 61-68 (1989).
10. McCaffrey M.A., Farrington J.W. and Repeta D.J. *Geochim. Cosmochim. Acta* 54, 1713-1724 (1990).
11. Repeta D.J. and Gagosian R.B. *Geochim. Cosmochim. Acta* 51, 1001-1009 (1987).
12. Henrichs S.M., Farrington J.W. and Lee C. *Limnol. Oceanogr.* 29, 20-34 (1984).
13. Henrichs S.M. and Farrington J.W. *Limnol. Oceanogr.* 29, 1-19 (1984).
14. Whelan J.K., Kanyo Z., Tarafa M. and McCaffrey M.A. Pre-print (1990).
15. McCaffrey M.A. Ph.D. Thesis. MIT/WHOI, WHOI-90-29 (1990).
16. Metcalf G.S., Windig W., Hill G.R. and Meuzelaar H.L.C. *Int. J. Coal Geol.* 7, 245-268 (1987).
17. Meuzelaar H.L.C., Haverkamp J. and Hileman F.D. *Pyrolysis Mass Spectrometry of Recent and Fossil Biomaterials; Compendium and Atlas*. Elsevier, Amsterdam 294 pp. (1982).
18. Windig W. and Meuzelaar H.L.C. *Proceedings of the 34th ASMS Conference*. Cincinnati, pp. 64-65. (1985).
19. Cattell R.B., *Multivariate Behavioral Research*. 1, 245-276 (1966).
20. Windig W., Kistemaker P.G. and Haverkamp J. *J. Anal. Appl. Pyrol.* 3, 199-212 (1981).
21. Windig W. and Meuzelaar H.L.C. *Anal. Chem.* 56, 2297-2303 (1984).
22. Sinninghe Damsté J.S., Eglinton T.I., de Leeuw J.W. and Schenck P.A. *Geochim. Cosmochim. Acta* 53, 873-889 (1989).
23. Sinninghe Damsté J.S., Rijpstra W.I.C., Kock-van Dalen A.C., de Leeuw J.W. and Schenck P.A. *Geochim. Cosmochim. Acta* 53, 1343-1355 (1989).

Table 1 Geochemical Description of Samples of Peru Sediments from core SC3.

Sample #	Depth (cm)	TOC (%)	%N	Dry wt/wet wt.
1	4-5	11.10	1.26	0.0699
2	9-10	9.20	1.07	0.0640
3	16-17	9.17	1.17	0.0765
4	27-28	9.79	1.19	0.0831
5	30-31	11.02	1.26	0.1115
6	38-39	8.67	1.21	0.1381
7	42-43	8.19	1.03	0.0978
8	46-47	6.19	0.71	0.0859
9	55-56	7.67	0.88	0.1026
10	65-66	7.67	0.92	0.2415
11	70-71	6.81	0.77	0.1467
12	75-76	6.94	0.79	0.2610
13	77-78	7.61	0.87	0.2532
14	85-86	7.00	0.75	0.1717
15	94-96	7.09	0.77	0.1741

Table 2 Results from Factor analysis of normalized Py-MS data.

Factor	Eigen Val.	% Total Var.	% Cum. Var.
1	118.01	50.87	50.87
2	39.91	17.20	68.07
3	12.07	5.20	73.27
4	8.27	3.57	76.84
5	4.94	2.13	78.97
6	3.92	1.69	80.66
7	3.78	1.63	82.29

Table 3 Results from Discriminant analysis of Py-MS data.

Discr. Func.	Eigen Val.	% Outer Var.	% Total Var.	Canonical Corr.
1	40.30	61.88	17.10	0.988
2	11.57	17.77	4.92	0.959
3	7.79	11.96	9.55	0.941
4	3.84	5.89	38.16	0.891
5	1.16	1.77	4.31	0.732
6	0.29	0.45	5.70	0.475
7	0.18	0.27	2.55	0.388

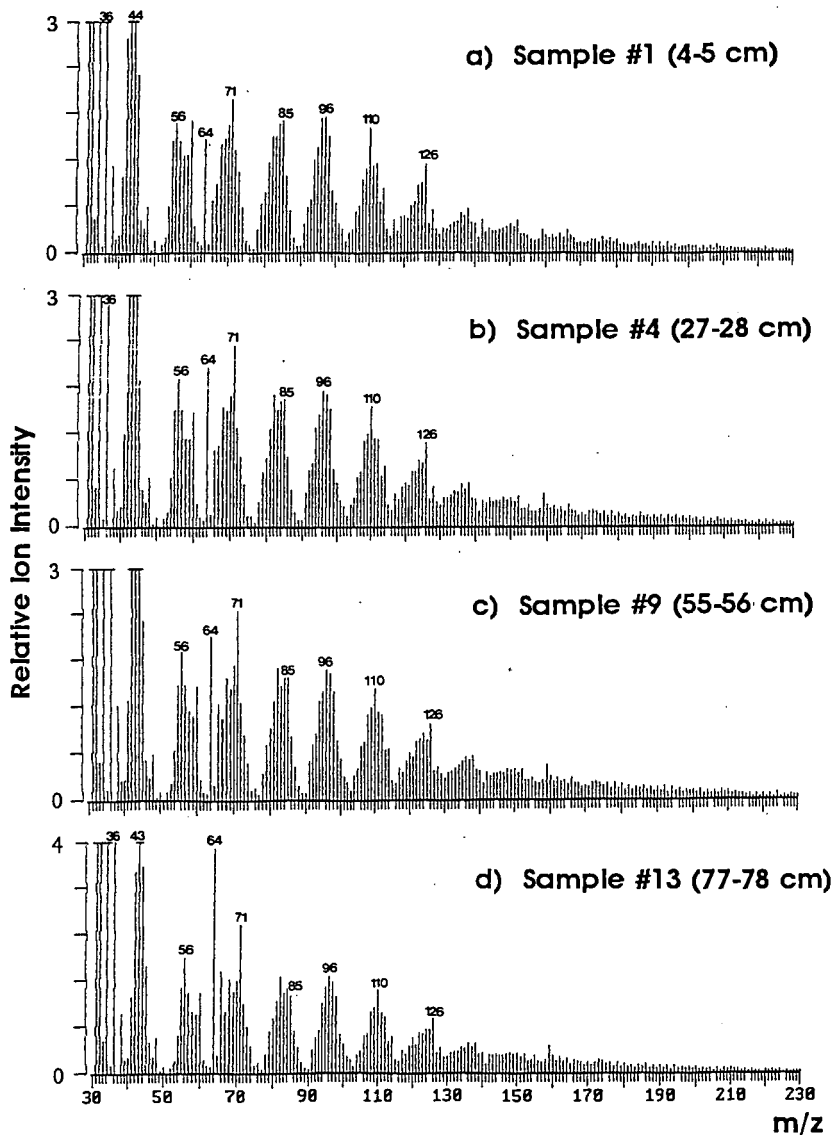


Figure 1. Averaged Py-MS spectra from triplicate analyses of four extracted Peru sediments from core SC3.

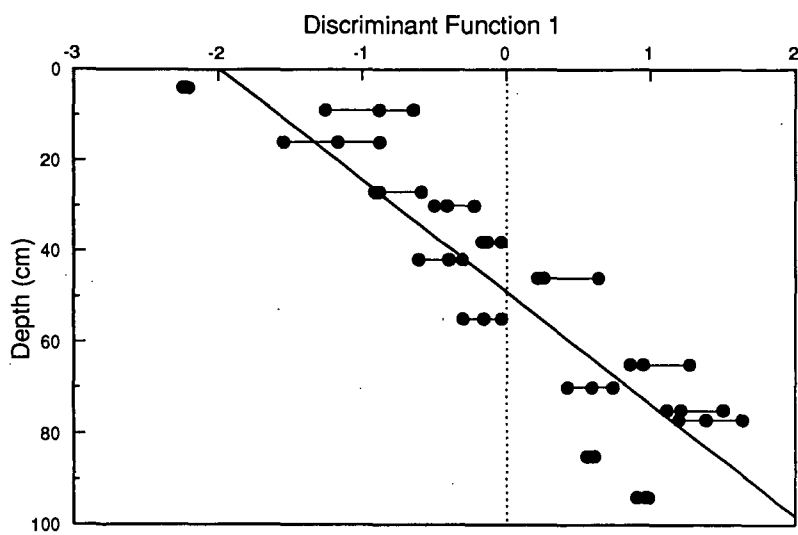


Figure 3. Plot of Discriminant Function 1 versus Depth (cm)

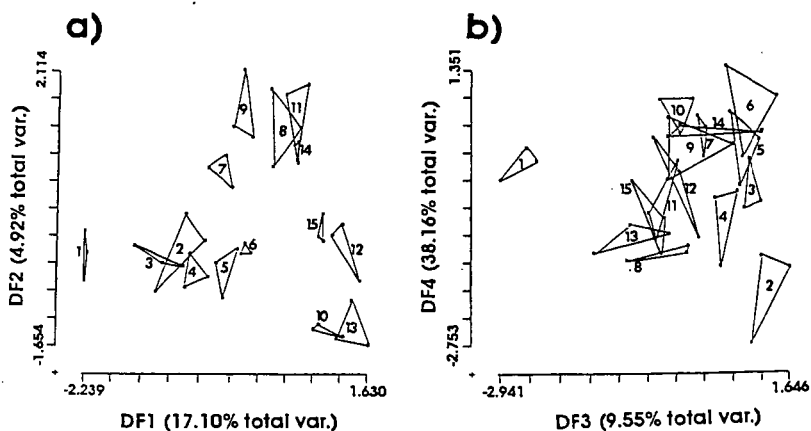


Figure 2. Score plot from Discriminant analysis of normalized Py-MS data:

(a) Discriminant Function 1 versus Discriminant Function 2;

(b) Discriminant Function 3 versus Discriminant Function 4.

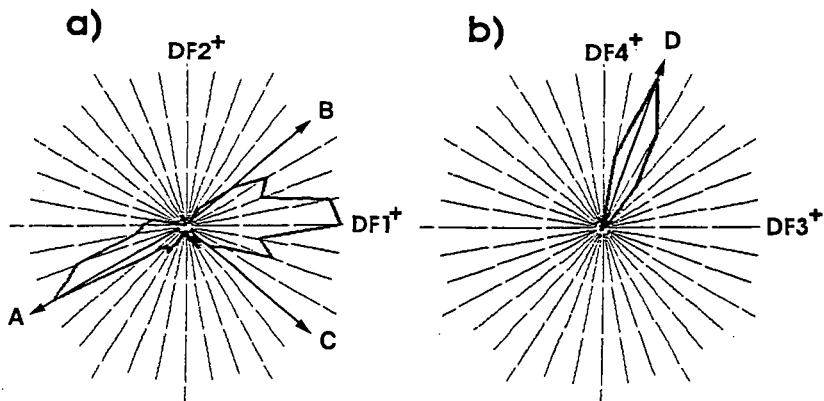


Figure 4. Variance diagram (VARDIA) showing presence of four discrete chemical component axes in the space spanned by discriminant functions 1 and 2 (a) and 3 and 4 (b).

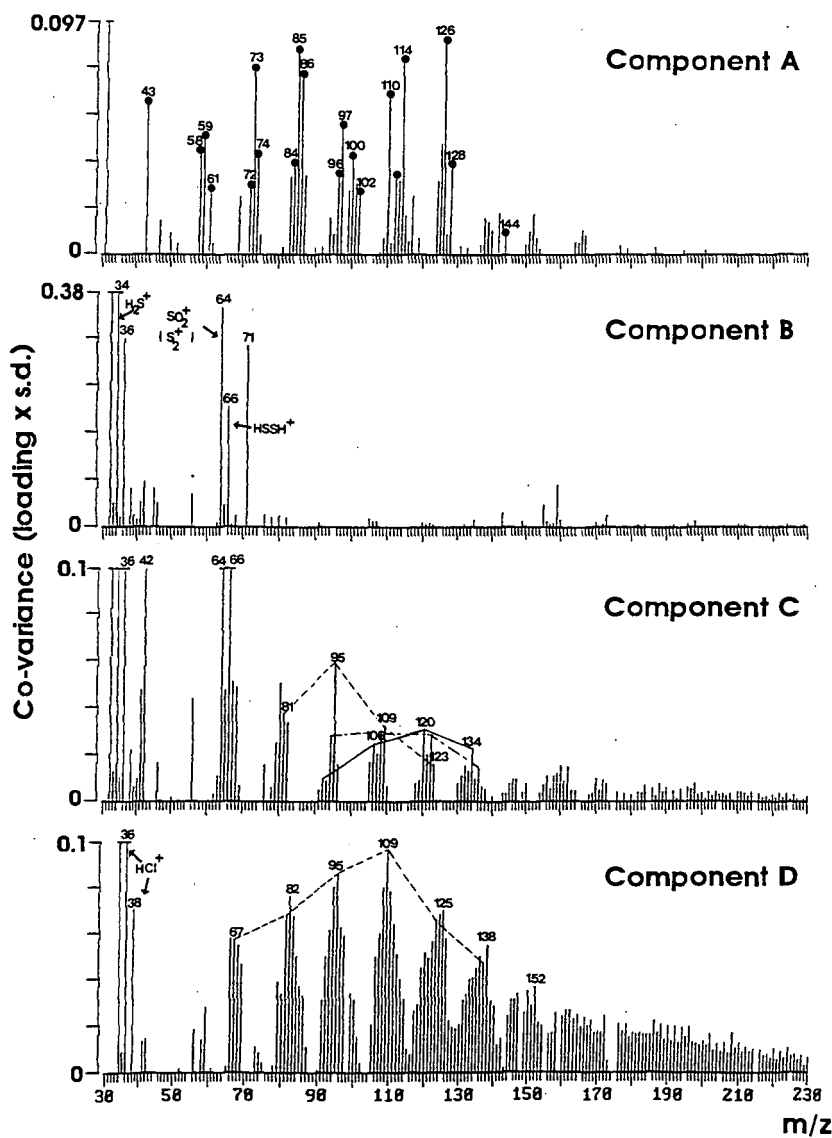


Figure 5. Mathematically-extracted "Discriminant Spectra" of Chemical Components A, B, C and D.

## MECHANISMS OF HYDROCARBON FORMATION DURING FLASH PYROLYSIS OF KEROGEN

Walter A. Hartgers, Jaap S. Sinninghe Damsté and Jan W. de Leeuw

Organic Geochemistry Unit, Faculty of Chemical Technology and  
Materials' Science, Delft University of Technology, De Vries van  
Heystplantsoen 2, 2628 RZ Delft, The Netherlands.

Keywords: alkylbenzenes, fatty acids, sodium salts, aromatic carotenoids

### INTRODUCTION

Geomacromolecules, which account for by far the greatest part of organic matter in sediments, are, due to their physical properties and complex structures, not easily accessible for common spectroscopic methods to elucidate their structure. Therefore, thermal and chemical degradation techniques are often applied to obtain structural information on these substances. Flash pyrolysis (Py) in combination with gas chromatography (GC) and mass spectrometry (MS) has proven to be a useful method of characterizing geomacromolecules (e.g. kerogen) at a molecular level.<sup>1,2</sup> Upon flash pyrolysis of kerogen mixtures of *n*-alkanes, *n*-alk-1-enes, saturated and aromatic (poly)cyclic hydrocarbons are commonly generated.

However, the mechanisms by which these compounds are formed are not completely known. This is surprising since a full understanding of the thermal degradation processes is essential for interpretation of the compound distributions with respect to the macromolecular structure. Therefore, we have flash pyrolysed silicon-bound hydrocarbons, which serve as model compounds for hydrocarbon moieties in kerogen.<sup>3</sup> Although these experiments gave some insight into the thermal degradation of hydrocarbon moieties, the major pyrolysis products were formed by processes involving the O-Si and Si-C bonds and are thus not really representative of hydrocarbon moieties in kerogen.

In this paper we report the C<sub>0</sub>-C<sub>4</sub> alkylbenzene distributions in flash pyrolysates of two kerogens and flash pyrolysis experiments with new model compounds (sodium salts of fatty acids) aimed at the interpretation of the alkylbenzene distributions of the kerogen pyrolysates.

### EXPERIMENTAL

Sediment samples were extracted and decarbonated (Paris Basin shale, G6-2-2<sup>4</sup>) or isolated (Womble shale<sup>5</sup>) and subsequently re-extracted with organic solvents.

Hexadecanoic acid and 12-hydroxy-octadecanoic acid are commercially available (Aldrich) and were converted to their corresponding sodium salts by adding a NaOH solution followed by evaporation of the water. 16-(4'-methylphenyl)hexadecanoic acid was synthesized by a Grignard reaction of 16-oxo-hexadecanoic acid, prepared by oxidation of 16-hydroxydecanoic acid (Aldrich), with 4-bromomagnesium-toluene and subsequent hydrogenolysis<sup>6</sup> of the formed alcohol using triethylsilane and BF<sub>3</sub>·etherate.

The samples were pressed onto ferromagnetic wires. These wires were inductively heated in 0.15 s to their Curie-temperature (610° or 770°C) at which they were held for 10 s. On line gas chromatography (GC) was performed using a Hewlett Packard HP-5890 gas chromatograph equipped with a cryogenic unit and programmed from 0°C (5 min) to 320°C (10 min) at a rate of 3°C/min. The pyrolysate was separated on a 25 m fused silica capillary column coated with chemically bound CP Sil-5 (0.32 mm I.D.; film thickness 0.45 µm).

Py-GC-MS was performed using the same pyrolysis and GC-conditions as mentioned above with a Hewlett Packard HP-5890 gas chromatograph directly coupled to the EI ion source of a VG-70s double focussing mass-spectrometer (mass range *m/z* 40-800; cycle time 1.8 s; ionisation energy 70 eV). C<sub>0</sub>-C<sub>4</sub> alkylbenzenes were identified by comparison of relative retention time and mass spectral data with those of authentic standards.



## RESULTS AND DISCUSSION

### *Alkylbenzenes in flash pyrolysates of kerogen*

Alkylbenzenes are often important pyrolysis products of immature kerogens and coals. They are assumed to be formed *via*  $\beta$ -cleavage of alkylaromatic moieties in the kerogen structure.<sup>1</sup> The origin of these alkylaromatic units in kerogen is far from understood. Therefore, the C<sub>0</sub>-C<sub>4</sub> alkylbenzene distributions of ca. 30 pyrolysates of immature kerogens from different geographical locations and of different types were examined to see whether these are biologically controlled.

Figure 1 shows the alkylbenzene distributions of the flash pyrolysates of two kerogens from the Toarcian Paris Basin and the Ordovician Womble Shale which both contain type II kerogens. Significant differences between the distribution patterns are observed. For example, the abundance of 1,2,3,4-tetramethylbenzene (compound 36, Table 1) in the Womble flash pyrolysate relative to that in the Paris Basin pyrolysate is noteworthy. The substitution pattern of this compound suggests that it is generated by  $\beta$ -cleavage of macromolecularly bound aromatic carotenoid structures. Five major aromatic carotenoids occurring in nature are: renieratene, isorenieratene, isorenierapurpurin, chlorobactene and okenone (figure 2).<sup>7</sup> They all possess 1-alkyl-2,3,4-trimethyl- and 2-alkyl-1,3,4-trimethylbenzene moieties, which are likely to generate 1,2,3,4-tetramethylbenzene upon flash pyrolysis.

Since these aromatic carotenoids are mainly biosynthesized by photosynthetic sulphur bacteria, it is suggested that these bacteria were important contributors to the organic matter of the Ordovician Womble shale. Because of the natural habitat of photosynthetic sulphur bacteria this, in turn, suggests that a part of the photic zone of the water column or sediment was anoxic.

This example shows that alkylbenzenes (and possibly other flash pyrolysis products) contain palaeoenvironmental information. However, to decode this information the mechanisms involved in the formation of these pyrolysis products (*e.g.*  $\beta$ -cleavage in case of alkylaromatic units) need to be known. The study of model compounds is, therefore, a prerequisite to fully understanding kerogen pyrolysis product distributions.

### *Flash pyrolysates of model compounds*

The sodium salt of 16-(4'-methylphenyl)hexadecanoic acid was selected for study because unlike free fatty acids it will not evaporate off the wire without degradation and is, thus, a simple model compound for aromatic moieties in kerogen. It yields upon flash pyrolysis (figure 3A) a homologous series of 4-alkyltoluenes and 4-alkenyltoluenes with a chain length of up to 15 carbon atoms. The series of 4-alkenyltoluenes probably have their double bond in the  $\omega$ -position. These compounds are supposed to be formed by simple homolytic C-C bond cleavage. 1,4-Dimethylbenzene which would be the favoured pyrolysis product resulting from  $\beta$ -cleavage of the aromatic moiety is also a major compound (figure 3A).

However, the presence of 4-methylstyrene as a major pyrolysis product is puzzling. <sup>1</sup>H NMR and TLC of the synthesized product indicated that it is not completely pure and contains a non-GC amenable impurity, which may be responsible for the formation of 4-methylstyrene upon pyrolysis. Alternatively, an uncommon rearrangement reaction of 16-(4'-methylphenyl)hexadecanoic acid sodium salt may also lead to the generation of this compound. Furthermore, the abundance of toluene and benzene in the pyrolysate is remarkable since the formation of these products requires the cleavage of a C-C bond  $\alpha$  to the aromatic ring. Since this degradation pathway is deemed unlikely due to the relatively high bond strength, cyclisation and aromatization of the alkyl chain may be an alternative route to generate these products during flash pyrolysis.

To investigate this phenomenon in more detail, the sodium salts of hexadecanoic acid and 12-hydroxy-octadecanoic acid were also flash pyrolysed (figures 3B and 3C). Flash pyrolysis of hexadecanoic acid generates a series of *n*-alkanes and *n*-alk-1-enes up to C<sub>15</sub> (figure 3B). The lack of hydrocarbons with more than 15 carbon atoms shows that recombination of two radicals is not an important process. The peaks eluting after heptadecane are identified as hexadecanal and hexadecanoic acid, which evaporate from the wire during flash pyrolysis. The results of this experiment are comparable to the flash pyrolysate of Silicon bound *n*-octadecane.<sup>3</sup> Benzene, toluene and other alkylbenzenes were not generated in detectable amounts,

indicating that cyclisation and aromatisation of the *n*-alkyl chain is not occurring during flash pyrolysis.

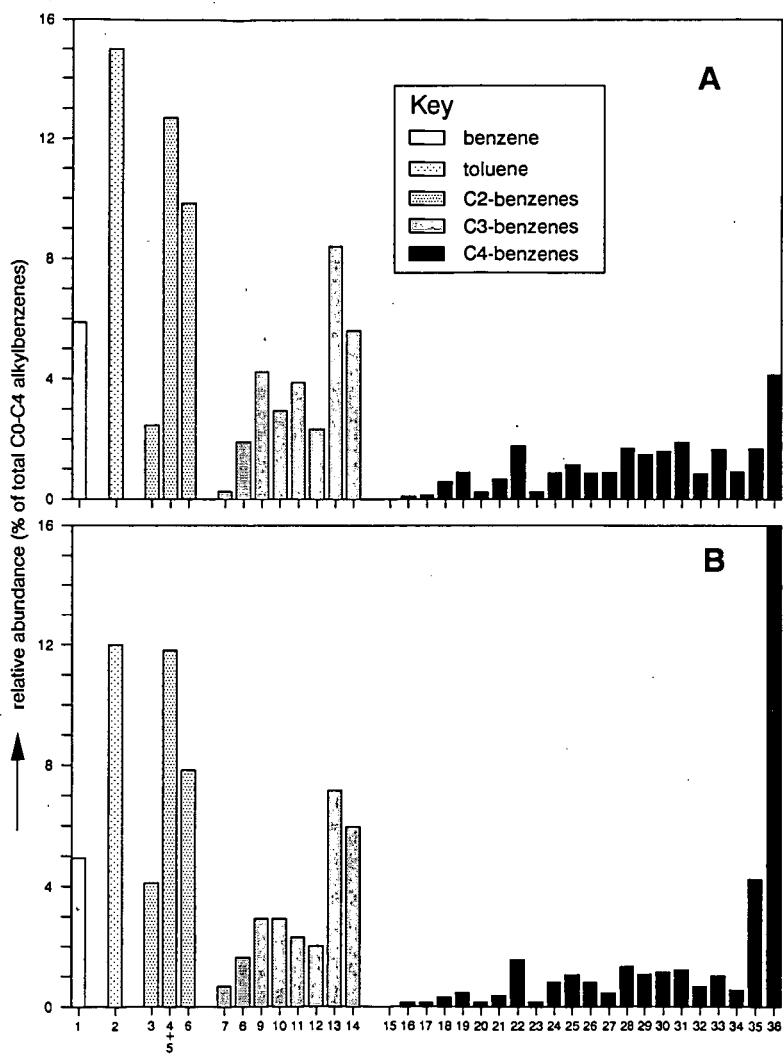
Surprisingly, flash pyrolysis of the sodium salt of 12-hydroxy-octadecanoic acid generates a homologous series of alkan-7-ones and alken-7-ones with the unsaturation in the  $\omega$ -position as the major products. However, more important from our point of view, benzene, toluene and, to a lesser extent, other alkylbenzenes (*i.e.* 1-phenylalkanes, 2-alkyltoluenes) which can be formed by cyclisation and aromatisation of a linear chain are also important pyrolysis products. This indicates that if an alkyl moiety contains at least one functional group alkylbenzenes can be formed *via* cyclisation and aromatisation reactions during flash pyrolysis.

## CONCLUSION

Alkylbenzene distributions in kerogen pyrolysates have a potential to give information on biological contributions and palaeoenvironmental conditions. However, much more work aimed at the understanding of the thermal processes responsible for their formation has to be performed before we can fully decode the information contained in pyrolysis product distributions. Experiments with model compounds are essential in this respect but our preliminary investigations are rather confusing and warrant further investigation.

## REFERENCES

1. Larter, S.R. and Horsfield, B. (1991), In: "Organic Geochemistry", M.H. Engel and S.A. Macko (eds). Plenum Press, New York. In press.
2. Rullkötter, J. and Michaelis, W. (1990), *Org. Geochem.*, **16**: 829-852.
3. Hartgers, W.A., Sinninghe Damsté, J.S. and de Leeuw, J.W. (1991), *J. Anal. Appl. Pyrol.* In press.
4. Mackenzie, A.S., Patience, R.L., Maxwell, J.R., Vandenbroucke, M. and Durand, B. (1981), *Geochim. Cosmochim. Acta*, **45**: 1709-1721.
5. Fowler, M.G. and Douglas, A.G. (1984), *Org. Geochem.*, **6**: 105-114.
6. Parnes, Z.N., Boelestova, G.I. and Kursanov, D.N. (1977), *J. Org. Chem. USSR*, **13**: 434-436.
7. Liaaen-Jensen, S. (1978), In: "Photosynthetic Bacteria", R.K. Clayton and W.R. Sistrom (eds), Plenum Press, New York. pp 233-248.



**Figure 1.** Bar plots showing the distribution of the C<sub>0</sub>-C<sub>4</sub> alkylbenzenes in the flash pyrolysates of the kerogen of (A) Paris Basin G6-2-2 and (B) Womble shale. Numbers refer to compounds listed in Table I.

Table 1: Alkylbenzenes identified in kerogen pyrolysates.

1	benzene	20	1-isopropyl-2-methylbenzene
2	toluene	21	1,3-diethylbenzene
3	ethylbenzene	22	1-propyl-3-methylbenzene
4+5	1,3-/1,4-dimethylbenzene	23	1,4-diethylbenzene
6	1,2-dimethylbenzene	24	1-propyl-4-methylbenzene
7	iso-propylbenzene	25	n-butylbenzene
8	n-propylbenzene	26	1-ethyl-3,5-dimethylbenzene
9	1-ethyl-3-methylbenzene	27	1,2-diethylbenzene
10	1-ethyl-4-methylbenzene	28	1-propyl-2-methylbenzene
11	1-ethyl-2-methylbenzene	29	1-ethyl-2,5-dimethylbenzene
12	1,3,5-trimethylbenzene	30	1-ethyl-2,4-dimethylbenzene
13	1,2,4-trimethylbenzene	31	1-ethyl-3,4-dimethylbenzene
14	1,2,3-trimethylbenzene	32	1-ethyl-2,6-dimethylbenzene
15	t-butylbenzene	33	1-ethyl-2,3-dimethylbenzene
16	iso-butylbenzene	34	1,2,4,5-tetramethylbenzene
17	sec-butylbenzene	35	1,2,3,5-tetramethylbenzene
18	1-isopropyl-3-methylbenzene	36	1,2,3,4-tetramethylbenzene
19	1-isopropyl-4-methylbenzene		

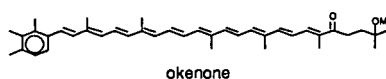
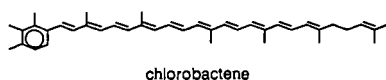
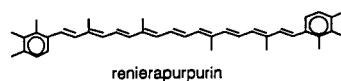
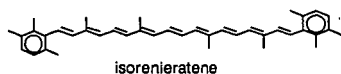
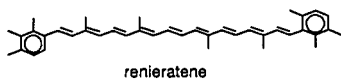
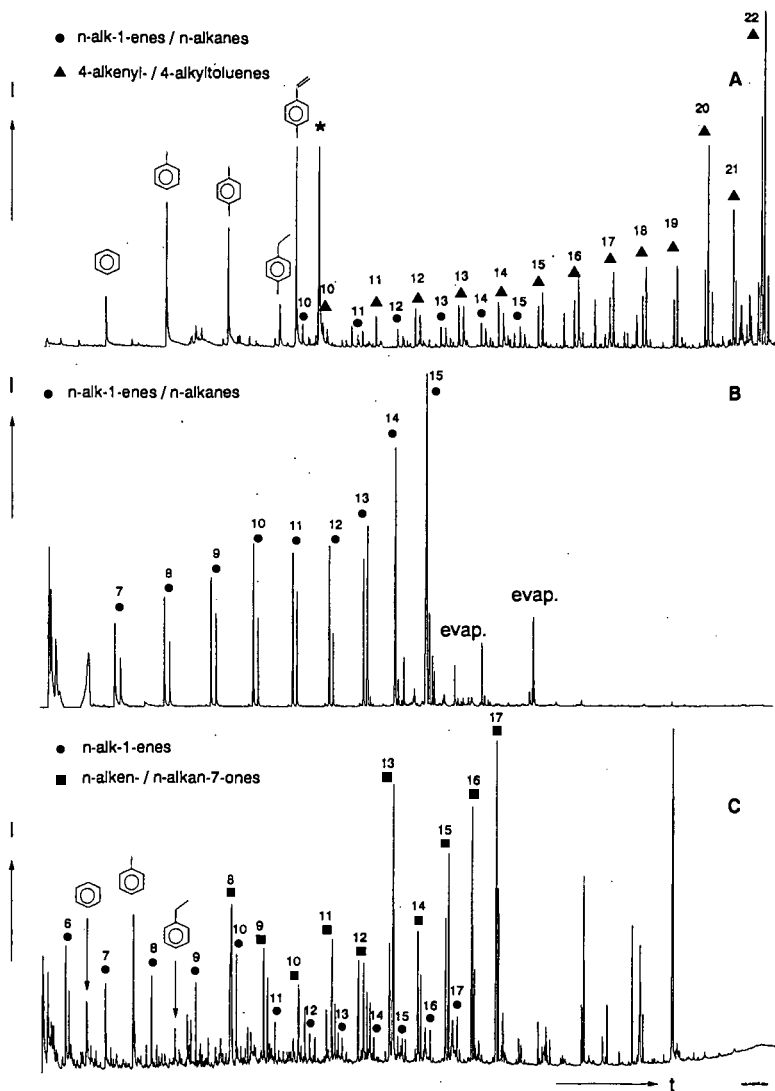


Figure 2. Chemical structures of some aromatic carotenoids.



**Figure 3.** TIC (A, C) and GC (B) traces of the flash pyrolysates (770°C) of the sodium salts of (A) 16-(4'-methylphenyl)hexadecanoic acid, (B) hexadecanoic acid and (C) 12-hydroxy-octadecanoic acid. Numbers indicate total numbers of carbon atoms of compounds identified.

## COAL PYROLYSIS: MEASUREMENTS AND MODELING OF PRODUCT EVOLUTION KINETICS AND CHAR PROPERTIES

Robert M. Carangelo, Michael A. Serio, Peter R. Solomon,  
Sylvie Charpenay, Zhen-Zhong Yu, and Rosemary Bassilakis

Advanced Fuel Research, Inc.  
87 Church Street  
East Hartford, CT 06108

**Keywords:** Coal Pyrolysis, Kinetics, Reactivity

### INTRODUCTION

Thermogravimetric analysis (TGA) has been employed in coal science to perform a number of characterizations including: proximate analysis,<sup>1</sup> kinetics of weight loss,<sup>2</sup> char reactivity,<sup>3-6</sup> and gas adsorption measurements.<sup>7</sup> A complementary technique, evolved product analysis, has been employed to study pyrolysis product distributions and kinetics,<sup>8-11</sup> functional group compositions,<sup>10,12,13</sup> and temperature programmed desorption.<sup>14-15</sup> We have developed a TG-FTIR instrument which combines TGA with evolved product analysis by Fourier Transform Infrared (FT-IR) spectroscopy. FT-IR analysis of evolved products has advantages over mass spectroscopy in allowing analysis of very heavy products, and over gas chromatography in speed.

The application of TG-FTIR to coal and petroleum source rock has recently been described.<sup>16,17</sup> To analyze coal, a sequence of drying, pyrolysis and combustion is employed to obtain: proximate analysis, volatiles composition, volatiles kinetics, and relative char reactivity. By using several different heating rates, kinetic rate constants have been obtained.<sup>18,19</sup> The purpose of this paper is to describe its application in characterizing the volatile evolution kinetics and char reactivities of the Argonne premium coal samples. The technique is being employed to obtain the kinetic and composition parameters for a recently developed general model of coal pyrolysis, called the FG-DVC model,<sup>20</sup> which stands for Functional Group - Depolymerization, Vaporization and Crosslinking model. This is a network model based on an assumed polymeric structure for coal and includes the processes of depolymerization and crosslinking and the formation of char, tar and gases. The reactivity parameters will be included in an extension of the model which is currently under development.

### EXPERIMENTAL

**Apparatus** - A schematic of the TG-FTIR instrument is presented in Fig. 1. Its components are as follows: a DuPont 951 TGA; a hardware interface (including a furnace power supply); an Infrared Analysis 16 pass gas cell with transfer optics; a MICHELSON 110 FT-IR; (Resolution: 4 cm<sup>-1</sup>, Detector: MCT). A helium sweep gas (250 cc/sec) is employed to bring evolved products from the TGA directly into the gas cell. A window purge of 700 cc/sec is employed at each end of the cell. The system is operated at atmospheric pressure. This instrument package is now available commercially as the "TG/plus" from Bomem, Inc.

The most difficult volatiles to analyze are the heavy decomposition products which condense at room temperature, such as tars from coal. In the TG/plus, the high conductivity helium sweep gas and the rapid cooling cause these products to form an aerosol which is fine enough to follow the gas through the analysis cell. The cell is connected without restrictions to the sample area. The aerosol is also fine enough that there is only a little scattering of the infrared beam and it is thus attenuated almost as though the tar was in the gas phase, as shown in Fig. 2. Based on the aerosol's Rayleigh scattering of infrared radiation, the diameter of the aerosol droplets is less than 1.0  $\mu\text{m}$ .

**Procedure** - As an example of the analysis procedure, the pyrolysis and oxidation of a lignite is described. More detail can be found in Refs. 16 - 18. Figure 3a illustrates the weight loss from

this sample and the temperature history. A 35 mg sample of Zap lignite, loaded in the sample basket of the DuPont 951, is taken on a 30°C/min temperature excursion in the helium sweep gas, first to 150°C to dry for 240 sec, then at 30°C/min to 900°C for pyrolysis. Upon reaching 900°C, the sample is immediately cooled to 250°C over a twenty minute period. After cooling, a small flow of O<sub>2</sub> (0.3 cc/sec) is added to the helium sweep gas at the 57 minute mark and the temperature is ramped to 700°C at 30°C/min (or as high as 1000°C) for oxidation.

During this excursion, infrared spectra are obtained once every thirty seconds. As shown in Fig. 2, the spectra show absorption bands for CO, CO<sub>2</sub>, CH<sub>4</sub>, H<sub>2</sub>O, SO<sub>2</sub>, COS, C<sub>2</sub>H<sub>4</sub>, and NH<sub>3</sub>. The spectra above 250°C also show aliphatic, aromatic, hydroxyl, carbonyl and ether bands from tar. The evolution of gases derived from the IR absorbance spectra are obtained by a quantitative analysis program which employs a database of integration regions and calibration spectra for different compounds<sup>16-18</sup>. The routine employs regions of each calibration spectrum which permit the best quantitation with the least interferences. The routine is fast enough to allow the product analysis to be displayed on the computer screen during the actual experiment.

Figure 3b illustrates the integral of the evolution curves to obtain cumulative evolved product amounts. Because the data are quantitative, the sum of these curves match the weight loss as determined by the TGA balance. Discrepancies occur in this match because of missing components such as H<sub>2</sub> which cannot be seen by IR. Also, when O<sub>2</sub> is introduced, the balance shows a net gain in weight due to O<sub>2</sub> chemisorption.

**Reactivity Measurements** - Initial char reactivity measurements were made using the isothermal measurement developed at Pennsylvania State University in which the time for 50% burnoff ( $\tau_{0.5}$ ) was measured.<sup>4</sup> In our char characterization work, we had difficulty applying the isothermal technique to chars formed over a wide range of conditions. A temperature level selected for one char was inappropriate for another. The temperature was either too high for the rate to be chemically controlled or too low for the  $\tau_{0.5}$  to be reached in a reasonable time period.

In order to overcome this difficulty, a non-isothermal technique was developed.<sup>3,5</sup> A Perkin-Elmer TGA 2 was initially used for this method. Recent measurements have been made using the TG-FTIR instrument discussed above and good agreement has been found between these two systems. The sample is heated in air at a rate of 30 K/min until a temperature of 900°C is reached. The TGA records the sample weight continuously and, at the end of the experiment, the weight and derivative are plotted.

The "critical" temperature ( $T_{cr}$ ) at which the derivative of the fractional weight loss with respect to time reaches a value of 0.065 wt. fraction/min = 0.001 wt. fraction/s was chosen as an index of reactivity to be compared with the  $\tau_{0.5}$  values measured by the isothermal technique. The actual critical slope used is arbitrary. A value is chosen which is large enough to be unambiguously determined, but small enough so that reaction occurs in the chemically controlled regime. Values of  $\ln \tau_{0.5}$  were plotted against  $1/T_{cr}$  and a good correlation was observed.<sup>3</sup>

**Temperature Programmed Desorption** - Temperature programmed desorption (TPD) has proved to be a valuable tool for characterization of surfaces of carbonaceous materials such as coal chars.<sup>14,15</sup> An example of the application of this technique to the characterization of chars from two coals is shown in Figure 4. This work was done in our TG-FTIR system described above by operation in a slightly different mode. The chars were prepared by programmed pyrolysis at 30° C/min to 1000° C, then cooled to 200° C, exposed to air for ten minutes, and then reheated to 1000° C. Samples which have a high oxidation reactivity have a larger increase in weight due to O<sub>2</sub> uptake and desorb CO<sub>2</sub> much more readily. In Figure 4, a comparison is made between a highly reactive char produced from a low rank (Zap lignite) coal (solid line) compared with a relatively unreactive char produced from a high rank (Pocahontas) coal (dashed line). The differences between these samples can be rapidly and easily assessed using this technique.

**Samples** - The coals analyzed were Argonne premium coal samples. The characterization of these samples has appeared elsewhere.<sup>21</sup>

## RESULTS

**Char Properties** - The results from the application of the TG-FTIR instrument to measurements of  $T_g$  and oxygen chemisorption capacity on the Argonne Premium coals are shown in Fig. 5. As expected, the values of  $T_g$  decrease with decreasing rank which indicates that lower rank coals are more reactive. This variation in reactivity with rank is primarily due to mineral contributions to reactivity.<sup>3,5</sup> The measurements of oxygen chemisorption capacity (OCC), which are related to the active site concentration, are inversely related to  $T_g$  and are also shown in Fig. 5. In our work, we have found that the value of  $T_g$  is a more useful correlative parameter for reactivity than the OCC.<sup>22</sup>

**Kinetics** - The TG-FTIR system was used to conduct programmed pyrolysis experiments on the Argonne premium coals over a range of heating rates (3, 30, 50, 100°C/min).<sup>18,19</sup> When comparing the multi-peak evolution curves of a given specie in different coals, an interesting feature was observed. As the coal is increased in rank, the leading edges and the early peaks shift to higher temperatures while the trailing edges remain at the same temperature. An example of this is shown for water for five coals in Fig. 6.<sup>23</sup> From this figure it appears that this feature can be explained in the light of the geological aging process of coal formation. With increasing aging temperature and time, the maturation process gradually evolves the loosely bound functional groups and leaves the tightly bound groups intact. The FG-DVC model has been used to successfully simulate the shifts in the evolution curves as a function of rank.<sup>23</sup> This was done by extrapolating the kinetics determined in the TG-FTIR experiments at moderate heating rates (3-100°C/min) to geological conditions and assuming that the coals of increasing rank are the products from lower rank coals pyrolyzed under natural conditions at increased times and temperatures.

**Relationships between Kinetic Rates of Different Volatile Species** - It was also found that some pools in the different gas species have peak evolution rates at the same temperature and those peaks have the same shifts when the heating rate changes. The Utah Blind Canyon coal gives a good example as shown in Fig. 7. The TG-FTIR measurements indicate that the tar evolution, the CO<sub>2</sub>-Loose, CO-Loose, and the H<sub>2</sub>O-Loose pools all show very close peak temperatures at about 480° C for 30° C/min., at about 519° C for 100° C/min. and at about 430° C for 3° C/min. runs. This feature implies that these volatile pools can be fit with the same kinetic parameters. This may also imply that there is some common chemistry.

**Model Predictions** - The kinetic parameters for the functional group pools from the eight Argonne premium coals have been determined using a set of rules that were developed to allow a systematic method of establishing the rank variations (e.g., the frequency factors were fixed at values of less than 10<sup>15</sup>/sec. and only the activation energies were allowed to vary with rank). The details will be provided in a future publication. A typical comparison of theory and TG-FTIR experiments is shown in Figs. 8 and 9 for two widely spaced heating rates. The agreement between the theory and experiment is generally quite good except for CO<sub>2</sub>. For this specie, residual oxygen in the TG-FTIR causes some oxidation at the slowest heating rate and minerals contribute evolved CO<sub>2</sub> which is not modeled. CO also shows some differences in the predicted amplitude, while the agreement is good for water, weight-loss, CH<sub>4</sub>, tar and H<sub>2</sub>O. The kinetic parameters obtained from the TG-FTIR method extrapolate well to very low heating rates, as in natural maturation processes,<sup>23</sup> as well as to the high heating rates of importance in most coal gasification and combustion processes.<sup>19</sup>

## CONCLUSIONS

The TG-FTIR instrument provides a simple, fast and reliable method for providing information on product evolution kinetics and char reactivity for coals and other polymeric materials. The information from this test has been used to provide validated kinetic and composition



parameters for a general model of coal pyrolysis, called the FG-DVC model. This model can make accurate predictions of both very low and very high heating rate pyrolysis events.

## ACKNOWLEDGEMENTS

This work was supported under U.S. DOE Contract No. DE-AC21-86MC23075 through the Morgantown Energy Technology Center. Richard Johnson is the Project Manager.

## REFERENCES

1. Ottaway, W.; *Fuel*, **1982**, *61*, 713.
2. Ciuryla, V.T.; Weimer, R.F.; Bivans, A.; and Motika, S.A.; *Fuel*, **1979**, *58*, 748.
3. Solomon, P.R.; Serio, M.A.; and Heninger, S.G.; *ACS Div. of Fuel Chem. Preprints*, **1986**, *31*, (3), 200.
4. Best, P.E.; Solomon, P.R.; Serio, M.A.; Suuberg, E.M.; Mott, W.R., Jr.; and Bassilakis, R.; *ACS Div. of Fuel Chem. Preprints*, **1987**, *32*, (4), 138.
5. Serio, M.A.; Solomon, P.R.; Bassilakis, R.; and Suuberg, E.M.; *ACS Div. of Fuel Chem. Preprints*, **1989**, *34*, (1), 9.
6. Mahajan, O.P., R. Yarab, and P.L. Walker, Jr., *Fuel*, **57**, 643, (1978).
7. Suuberg, E.M.; Calo, J.M.; and Wojtowicz, W.; *ACS Div. of Fuel Chem. Preprints*, **1986**, *31*, (3), 186.
8. Winans, R.E.; McBeth, R.L.; and Neill, P.H.; *ACS Div. of Fuel Chem. Preprints*, **1988**, *33*, (3), 85.
9. Chakravarty, T.; Windig, W.; Hill, G.R.; and Meuzelaar, H.L.C.; *Energy & Fuels*, **1988**, *2*, (4), 400.
10. Solomon, P.R. and Hamblen, D.G.; Finding Order in Coal Pyrolysis Kinetics, Topical Report submitted to U.S. Department of Energy under Contract No. DE-AC21-FE05122, (1983), also *Progress in Energy and Combustion Science*, **1983**, *9*, 323.
11. Burnham, A.K.; Oh, M.S.; Crawford, R.W.; and Samoun, A.M.; *Energy & Fuels*, **1989**, *3*, 42.
12. Attar, A. and Hendrickson, G.G.; *Coal Structure*, (R.A. Meyers, Ed.), Academic Press, NY, **1982**; Chapter 5, p. 131.
13. LaCount, R.B.; Anderson, R.R.; Friedman, S.; and Blaustein, B.D.; *Fuel*, **1987**, *66*, 873.
14. Hall, P.J. and Calo, J.M.; *Energy & Fuels*, **1989**, *3*, 370.
15. Zhang, Z.G.; Kyotani, T.; and Tomita, A.; *Energy & Fuels*, **1989**, *3*, 566.
16. Carangelo, R.M.; Solomon, P.R.; and Gerson, D.G.; *Fuel*, **1987**, *66*, 960.
17. Whelan, J.K.; Solomon, P.R.; Deshpande, G.V.; and Carangelo, R.M.; *Energy and Fuels*, **1988**, *2*, 65.
18. Carangelo, R.M., Solomon, P.R., Bassilakis, R., Gravel, D., Baillargeon, M., Baudais, F., and Vail, G., Applications of TG-FTIR in the Analytical Lab, American Laboratory, p. 51, (1990).
19. Serio, M.A., Solomon, P.R., Charpenay, S., Yu, Z.Z., and Bassilakis, R., Kinetics of Volatile Product Evolution from the Argonne Premium Coals, ACS Div. of Fuel Chem. Preprints, **35**, (3), 808, (1990).
20. Solomon, P.R.; Hamblen, D.G.; Carangelo, R.M.; Serio, M.A.; and Deshpande, G.V.; *Energy & Fuels*, **1988**, *2*, 405.
21. Vorres, K.S.; Users Handbook for the Argonne Premium Coal Sample Program, Supported by US DOE, Contract No. W-31-109-ENG-238 (1989).
22. Serio, M.A., Solomon, P.R., Yang, Y.P., and Suuberg, E.M., "The Use of TG-FTIR Analysis to Determine Char Combustion Properties", presented at the AIChE Annual Meeting, Chicago, Ill, (Nov. 11-16, 1990).
23. Solomon, P.R., Serio, M.A., Carangelo, R.M., Bassilakis, R., Yu, Z.Z., Charpenay, S., and Whelan, J., Analysis of Coal by TG-FTIR and Pyrolysis Modeling, presented at the Pyrolysis '90 Meeting in Holland, June 1990, to be published in *Journal of Analytical and Applied Pyrolysis*.

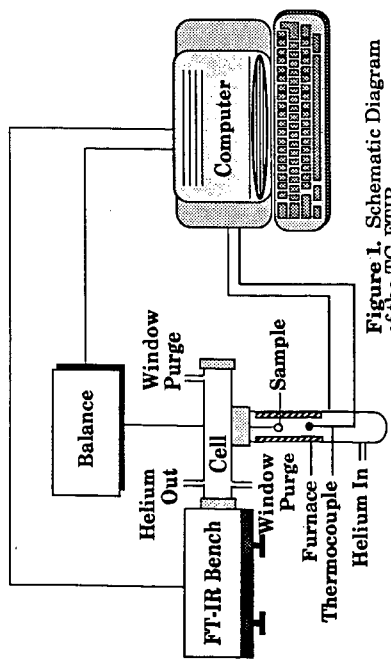


Figure 1. Schematic Diagram of the TG-FTIR.

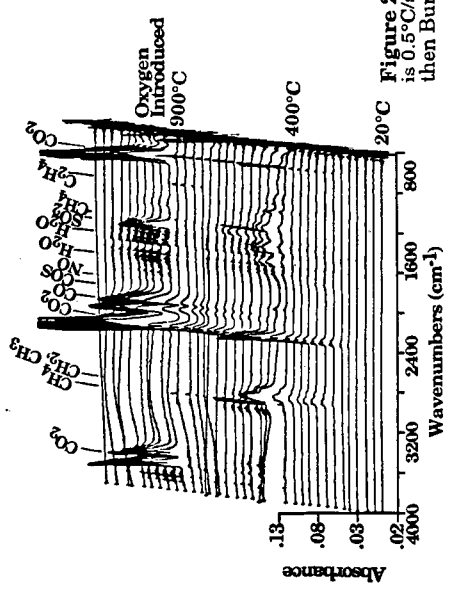


Figure 2. Spectra from TG-FTIR of Coal. Heating Rate is  $0.5^\circ\text{C/s}^{-1}$  from 20 to  $900^\circ\text{C}$ . The Remaining Char is then Burned at  $700^\circ\text{C}$ .

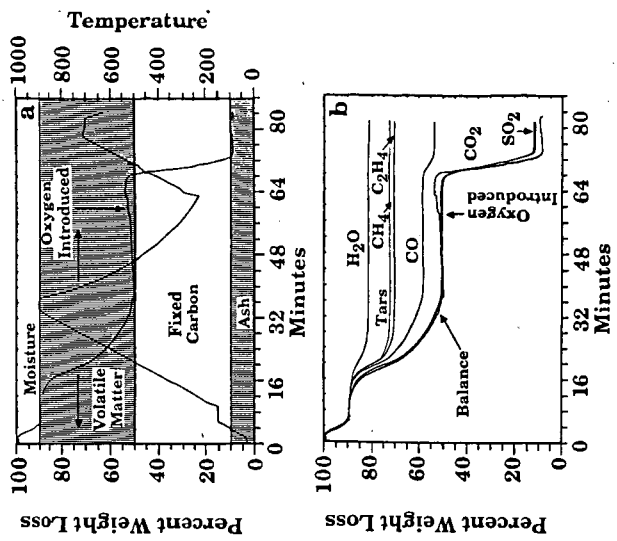


Figure 3. TG-FTIR Analysis of a Lignite. a) Temperature History and Weight Loss; b) Species Contributions to Weight Loss.

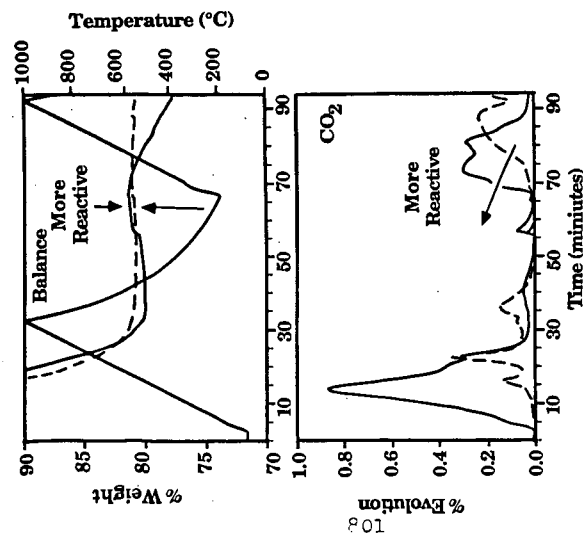


Figure 4. Temperature Programmed Desorption Curves for Pocahontas (---) and Zap Lignite (—).

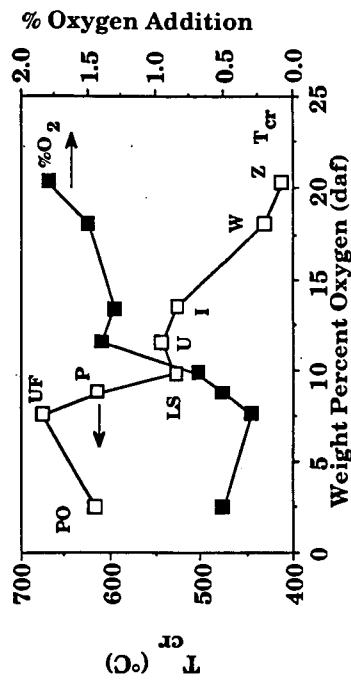


Figure 5. Rank Variation of  $T_{cr}$  and Oxygen Chemisorption Capacity (as-received basis).

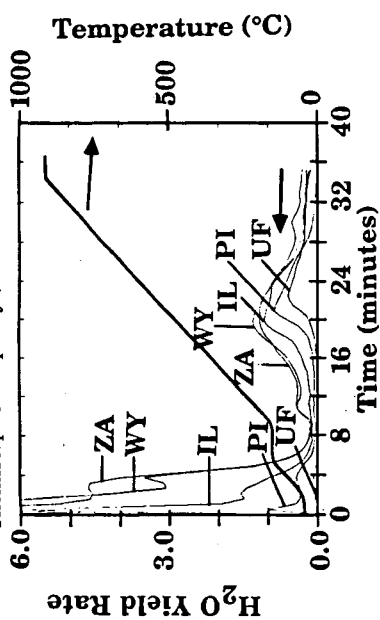


Figure 6. Evolution Curves for  $H_2O$  Measured in a TG/Plus for Five Coals from the Argonne Premium Samples Collected at  $30^\circ C/min$  (UF: Upper Freeport, PI: Pittsburgh, IL: Illinois, WY: Wyodak, ZA: Zap Lignite)

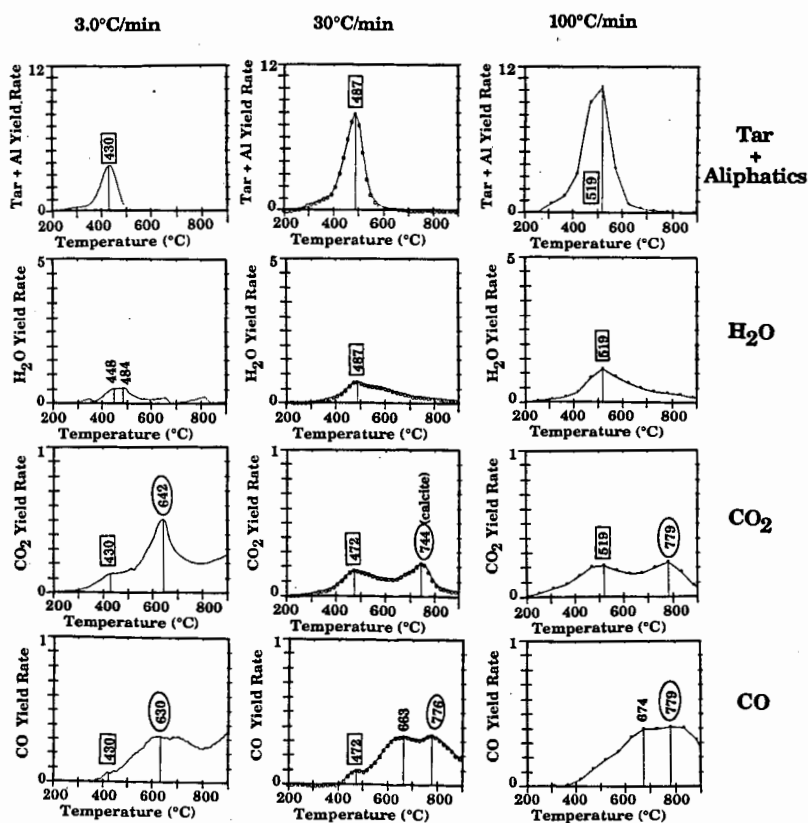


Figure 7. Evolution of Tar, H<sub>2</sub>O, CO<sub>2</sub>, and CO from Utah Blind Canyon Coal at Three Heating Rates.

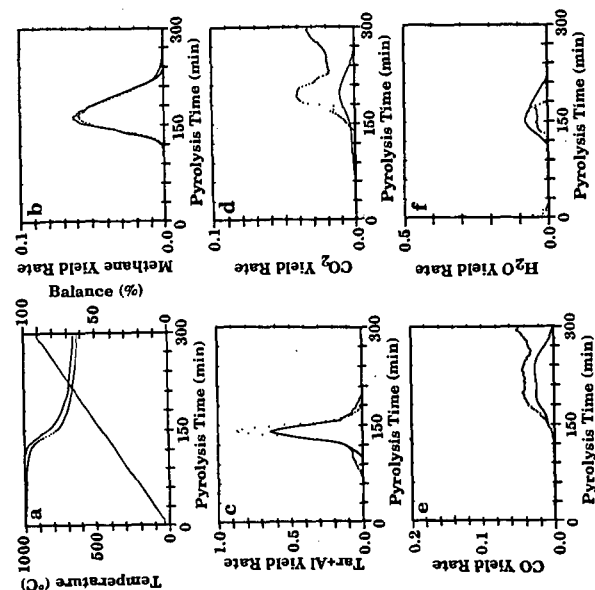


Figure 8. Data from TG-FTIR Heating Rates (---) and Predictions of FG-DVC Model for Pittsburgh No. 8 Bituminous Coal at 3°C/min. a) Weight Loss and Temperature; b) Methane; c) Tar + Aliphatic Gases; d) CO<sub>2</sub>; e) CO; f) H<sub>2</sub>O.

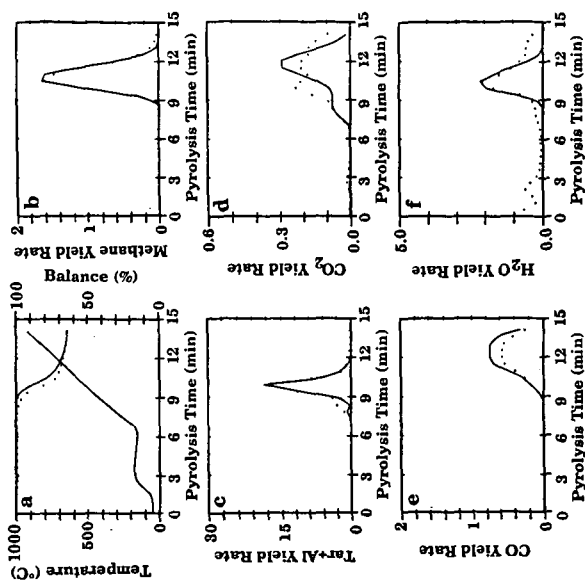


Figure 9. Data from TG-FTIR Heating Rates (---) and Predictions of FG-DVC Model for Pittsburgh No. 8 Bituminous Coal at 100°C/min. a) Weight Loss and Temperature; b) Methane; c) Tar + Aliphatic Gases; d) CO<sub>2</sub>; e) CO; f) H<sub>2</sub>O.